Advancing Ground-Based Water Vapor Profiling through Synergy of Microwave Radiometer and Dual-Frequency Radar

Inaugural-Dissertation

zur Erlangung des Doktorgrades
der Mathematisch-Naturwissenschaftlichen Fakultät
der Universität zu Köln

vorgelegt von

Sabrina Schnitt
aus Berlin

September 2020

Berichterstatter: Prof. Dr. U. Löhnert
Prof. Dr. R. Neggers

Tag der mündlichen Prüfung: 20. November 2020

Abstract

Continuous water vapor profiling methods are crucial for advancing the understanding of the role of clouds and water vapor in Earth's climate system. Particularly in the maritime trade wind driven environment, where shallow cumulus clouds prevail, the interplay between cloud and convection processes is not quantified satisfactorily. Current instrumentation techniques are limited by low temporal resolution in the case of soundings, signal saturation at cloud boundaries in the case of optical methods, or too coarse vertical resolutions in the case of passive microwave measurements. Therefore, in this thesis, the feasibility of a novel synergy concept is assessed by combining synthetic microwave radiometer (MWR) and dual-frequency radar measurements.

The synergy benefits are evaluated for a combination of seven MWR K-band brightness temperatures (TBs) with a Ka- and W-band radar combination (KaW), e.g. available at Barbados Cloud Observatory (BCO), and a Differential Absorption Radar (DAR) frequency combination of 167.0 and 174.8 GHz (G2). An optimal estimation framework retrieving the absolute humidity profile was selected to evaluate the synergy concept by deriving the retrieval uncertainty, information content through Degrees of Freedom of Signal (DFS), as well as the accuracy of the retrieved profile and partial water vapor amount. By varying the observation vector configuration to include both MWR TBs and radar Dual-Wavelength Ratio (DWR) in the synergistic configuration, or only TBs or only DWR in the single-instrument runs, the synergistic impacts were analyzed for an idealized single-cloud scenario frequently observed at BCO, and for three selected, more complex cases observed during the EUREC^{4}A field study. Additional 2 m humidity and cloud boundary measurements further constrain the retrieval.

Based on the single-layered cloud scenario with varying water vapor conditions, the analyses show that the total information content of a MWR+KaW combination only increases marginally by less than 6 %, while the DFS in case of the MWR+G2 synergy increases by 1.2 DFS on average compared to the MWR-only configuration.

While the sub- and in-cloud information content is increased by 1 DFS, driven by the radar measurements, the synergistic information content above the cloud layer is enhanced by 13.5 % compared to the MWR-only configuration. Meanwhile, the synergistic MWR+G2 retrieval uncertainty decreases around cloud base to 1.0 g m^{-3}, corresponding to a 28 % reduction compared to the MWR-only configuration. The synergistic benefits are most sensitive to the assumed radar measurement error, leading to an uncertainty increase of 0.1 g m^{-3} in the cloud layer when the DWR error is doubled, as well as to radar signal saturation before reaching cloud top.

Case study analyses of two double-layered cloud scenarios confirm the findings of the single-cloud layer case as the information content above each cloud layer is increased in all cases by up to 0.3 DFS. A modified retrieval concept serves to evaluate the role of the synergy when reconstructing the atmospheric state at 12 hours between 24-hour spaced operational radiosondes based on the EUREC^{4}A case scenarios. While the total synergistic information gain is reduced to 0.2 - 0.6 DFS due to the more accurate prior assumptions, the derived dry free tropospheric water vapor amount agrees better, by up to 3.6 kg m^{-2}, with the observed sounding reality than the interpolated prior amount. As expected, the addition of synthetic Raman lidar measurements improves the retrieval performance particularly in the sub-cloud layer, leading to increasing sub-cloud information content of 0.8 - 1.3 DFS, and decreasing optimal to prior uncertainty ratio of 13.6 - 26.2 percentage points compared to the MWR+G2 retrieval. A modified observation vector configuration including the simulated in-cloud humidity, as would e.g. be available by an independent direct inversion retrieval, further decreases the retrieval uncertainty in respect to the prior by 11.4 percentage points between the cloud layers.

Under realistic instrument deployment, the simulated measurements suggest that current G-band radar signal sensitivity would impair profiling the whole vertical cloud extent for the simulated thin liquid clouds in the trades. First simulated cases show similar restrictions for an airborne deployment in the trades, for example on HALO. Simulated radar measurements for an idealised mixed-phase cloud scenario in the drier Arctic environment as observed at Ny-Ålesund, Spitsbergen, suggest that current G-band radar sensitivities would allow evaluating the concept in drier conditions than observed in the tropics. The analysed benefits suggest that a synergy of MWR and G-band DAR could contribute to closing the current observational gap of continuous high-resolution water vapor profile measurements.

Contents

List of Figures

List of Tables

1 Introduction

1.1 Scientific Motivation

Water Vapor and Cloud Observations Throughout the Centuries

Weather phenomena, clouds, and water vapor have fascinated and served as inspiration for generations of scientists, artists, writers, and dreamers. While weather observations can be traced back to civilizations as early as the Babylonians and several ancient peoples in India, the earliest conveyed essay known to date summarizing the state of the art of atmospheric knowledge is Aristotle's *De Meteorologica*, written around 340 BC (Frisinger, 1972). Clouds and water vapor play a fundamental role in Aristotle's theories and observations, as he describes the cycle of evaporating water forming clouds from which precipitating liquid or ice closes what now is referred to as the hydrological cycle[1].

Aristotle's work on meteorology shaped western thinking about meteorology until the 17^{th} century, when scientists like Galileo and Pascal designed first scientific experiments to understand nature phenomena, as opposed to the observation-based scientific thinking that dominated the centuries before (Frisinger, 1973). In the 18^{th} and 19^{th} century, fundamental processes were discovered in pioneering experiments regarding basic physical laws in thermodynamics and astronomy. For example, in 1856, Foote (1856) first discovered that water vapor and CO_2 could absorb and emit heat, leading to warming effects in the atmosphere. Tyndall further specified in 1859 that specifically longwave infrared radiation caused the warming effect (Tyndall, 1859); see also Hulme (2009) and Jackson (2020). Arrhenius (1896) found that emitting CO_2 to the Earth's atmosphere would lead to increasing surface temperatures. The role of clouds in influencing the Earth's radiation budget was first noted by Abbott and Fowle (1908).

[1] Translation of Aristotle's *De Meteorologica* available by Webster (2020); the cycle between clouds and precipitation is mentioned in book 1, part 9; and book 2, part 2.

Since initial measurements documenting increasing atmospheric CO_2 concentrations (Keeling, 1960), scientists have warned of the implications of increasing CO_2 emissions leading to a globally changing climate (Charney et al., 1979) and major efforts have been undertaken to understand the present climate system and evaluate future, changing climate scenarios. The Intergovernmental Panel on Climate Change (IPCC) therefore assesses the current state of changing climate regularly, evaluating observations and models (current report: IPCC (2013), next one expected for 2021). Since General Circulation Models (GCM) have emerged as a tool to model current and predict future global climate scenarios (e.g. Smagorinsky, 1963), modeling and forecasting capacities have tremendously improved over the past decades (Bauer et al., 2015). Yet, uncertainties remain, for example due to the characterisation and parametrisation of feedback processes that amplify or dampen the response of the climate system to forcing (Hansen et al., 1984; Held and Soden, 2000; Bony et al., 2006, most recent review: Sherwood et al. (2020)). Processes related to water vapor show large positive feedback throughout models (Held and Soden, 2006), while the role and magnitude of cloud feedback has been known as very important, but not yet clearly quantified in its magnitude (Cess et al., 1990; Hartmann et al., 1992; Stephens, 2005; Boucher et al., 2013). Subgrid-scale processes driving water vapor and cloud feedback are not resolved in GCM models, but rely on parametrisation schemes (e.g. Tiedtke, 1989; Arakawa, 2004; Jakob, 2010).

Water Vapor Structure and Shallow Clouds in the Trades

In particular, the representation of low tropical marine boundary layer clouds in the subtropical subsidence zones leads to major inter-model spreads (Bony and Dufresne, 2005; Dufresne and Bony, 2008; Nuijens and Siebesma, 2019). These clouds are small in size and ubiquitous over the tropical oceans. At Barbados, shallow maritime cumulus clouds can be observed year-round, and they are representative for tropical marine boundary-layer clouds (Medeiros and Nuijens, 2016).

The clouds and structure of the trade wind driven atmosphere have been of interest since the first coordinated observation periods of the Northern Atlantic trades (e.g. Malkus, 1958). Characterized by strong surface easterlies, the trade winds, the vertical moist structure is characterized by a moist convective layer, a transition zone characterized by the typical increase of temperature ("trade inversion") with an associated strong moisture gradient ("hydrolapse"), and the dry free troposphere resting above the trade inversion (see Fig. 1.1). The lower structure of the moist layer

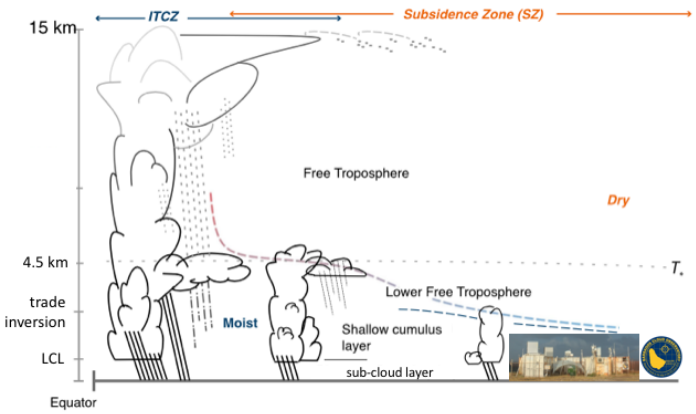

Figure 1.1 – Structure of water vapor and clouds in the (sub-)tropics, adapted from Stevens et al. (2017). The sub-cloud layer is limited by the LCL, while shallow clouds between LCL and the trade inversion height. The lower free troposphere ranges between trade inversion and freezing level below the dry free troposphere. The Barbados Cloud Observatory is located in the sub-tropical subsidence zone.

is marked by a well-mixed sub-cloud layer, driven by evaporation and turbulences (e.g. Betts and Albrecht, 1987). The convective potential of the moist layer is determined by the water vapor amount in the sub-cloud layer (e.g. Stevens et al., 2017). The Lifting Condensation Level (LCL) varies little over time and, at Barbados, is usually located between 600 m to 800 m (Nuijens et al., 2014; Stevens et al., 2017). Cumulus clouds form between LCL and the trade inversion layer (ranging around 2000 m), transporting and distributing water vapor vertically. Clouds appear as shallow cumulus humilis clouds, and can grow to large towers of cumulus congestus, often sheared horizontally due to strong winds, sometimes pushing through the trade inversion, transporting moist air into the dry lower free tropospheric environment. Vertical cloud development is capped by the trade inversion. Therefore, moisture is trapped below the inversion, and stratiform cloud outflow layers can form (e.g. Lock, 2009). Recent observational studies found that the highest variability of cloud fraction is observed around LCL and around the stratiform outflow below the trade inversion (Nuijens et al., 2015; Brueck et al., 2015; Lamer et al., 2015). The dry free troposphere is characterized by dry air, often characterized by large-scale subsidence. This air originates from the Intertropical Convergence Zone (ITCZ), and is transported polewards by the Hadley circulation. Varying on the circulation conditions, elevated moisture layers can be advected to the trade wind driven regions often associated with altocumulus or -stratus clouds, or Saharan dust layers impacting the radiative heating profiles (Gutleben et al., 2019).

The moisture structure is driven by moist convective processes that are closely intertwined with cloud and circulation processes (Derbyshire et al., 2004; Stevens, 2004; Sherwood et al., 2010). Local convective processes and shallow cloud formation interact with their immediate local environment e.g. through entrainment or precipitation, but interplay with large-scale circulations (e.g. Riehl and Malkus, 1957; Nuijens and Siebesma, 2019). Mesoscale convective aggregation and organization further affect the cloud and water vapor distribution (Bretherton et al., 2005; Tobin et al., 2012; Holloway et al., 2017). Not only is the amount of water vapor important for clouds and convection and, thus, feedback processes, but also is its distribution and variability.

The structure of lower-tropospheric water vapor mixing and moisture transport are crucial for determining low cloud feedback processes (Sherwood et al., 2014). Convective precipitation amounts strongly relate to the total vertical moisture content, but particularly to water vapor variability in the lower troposphere above LCL (e.g. Bretherton et al., 2004; Holloway and Neelin, 2009; Nuijens et al., 2009; Stevens et al., 2017). The variability of tropospheric water vapor amount is largest around cloud base (Stevens et al., 2001), where it influences the cloud amount and, thus, low cloud feedback processes (e.g. Brient et al., 2016; Vial et al., 2017). Important water vapor feedback processes result from radiative cooling. A substantial enhancement of cooling can be induced by water vapor variations in the dry subsiding free troposphere (e.g. Pierrehumbert, 1995; Spencer and Braswell, 1997; Gutleben et al., 2019). Variations in the moist layer can lead to the formation of cold pools, which further enhance cooling and drive circulation patterns (Zuidema et al., 2012b).

Shallow Clouds, Convection and Circulation

Yet fundamental questions remain unanswered for a thorough understanding of how shallow clouds and related convection and circulation processes will change in a changing climate (e.g. Stevens and Bony, 2013; Bony et al., 2006; Marotzke et al., 2017). While it is generally acknowledged that water vapor amounts in the troposphere increase with warming temperatures (Trenberth et al., 2005), it is not clear whether increasing temperature will lead to a reduction of low-level clouds and thus amplify warming (e.g. Rieck et al., 2012; Webb and Lock, 2013), or whether increasing Sea Surface Temperature (SST) will lead to an increase of low cloudiness due to enhanced clear-sky radiative cooling and convection (Wyant et al., 2009). Which cloud-controlling processes will be dominant in a warming climate

under different future radiative forcing scenarios (Bretherton et al., 2013)? How do moisture mixing processes in the lower troposphere influence cloud feedback, and how will mixing processes change in a warming climate (Sherwood et al., 2014)? Which processes and their representation through parametrization are particularly responsible for the discrepancy between observed and modeled tropospheric water vapor mixing and amounts (Pierce et al., 2006; Bony et al., 2015)?

Field Study Observations in the Northern Atlantic Trades

In order to shine a light on these questions, to improve the understanding of underlying feedback, and in order to evaluate parametrization schemes, thorough observations of the interplay of convection, clouds, and large-scale circulation are crucial in areas with prevailing shallow clouds, such as the trades. The trades and their clouds have been of scientific interest since the pioneering landmark studies by J. Malkus and H. Riehl (Riehl and Malkus, 1957; Malkus, 1958). Airborne observations during BOMEX (*Barbados Oceanographic and Meteorological EXperiment*; Holland, 1970; Friedman et al., 1970), as well as shipborne measurements during ATEX (*Atlantic Trade-Wind EXperiment*; Augstein et al., 1974) increased the observational understanding significantly, and provided observational data for many modeling studies (e.g. Stevens et al., 2001).

While the *Rain In shallow Cumulus over the Ocean*-experiment (RICO; e.g. Rauber et al., 2007; Davison et al., 2013) targeted measurements of key processes around precipitation, the *Barbados Aerosol Cloud EXperiment* BACEX (Jung et al., 2016) and the CARRIBA-project (*Cloud, Aerosol, Radiation and tuRbulence in the trade wInd regime over BArbados*, Siebert et al., 2013) focused on aerosol-cloud-precipitation interaction. More recently, the interplay of clouds, convection and circulation was further studied during the NARVAL field studies, in which the research aircraft HALO was equipped as a cloud observatory (Stevens et al., 2019). The measurements build the foundation for characterizing cloud properties (e.g. Schnitt et al., 2017; Jacob et al., 2019), water vapor structure (Naumann and Kiemle, 2020) and large-scale convergence (Bony and Stevens, 2019). The EUREC^{4}A (Bony et al., 2017; Stevens et al., 2020a) field study took place in 2020 to further elucidate the couplings between clouds, convection, and circulation, including interaction with the ocean surface and eddies, respectively. The coordinated measurements of four research aircraft and four research ships were complemented by a high temporal resolution upper air sounding network (Stephan et al., 2020, and Sec. A.1), high

temporal resolution dropsonde activity, and intensive remote sensing and in-situ observations.

Global Radiosonde Network

While intensive periods of observations during field studies offer valuable testbeds for model parametrization development and evaluation, as well as process understanding of interplay between small- and large-scale environments, long-term stationary observations are crucial for observing trends on longer time scales (Wulfmeyer et al., 2015). In the tropics, long-term observations are mainly available from radiosondes and spaceborne remote sensing observations. Launched within a globally connected network every 6, 12, or 24 hours, regular radiosonde launches at coordinated times worldwide are a crucial pillar of global atmospheric observations. Each sounding is timed such that it reaches the 100 hPa-level at coordinated UT times, generally at 00, 06, 12, or 18 UT. At Barbados, soundings have been launched every 12 or 24 hours from Grantley Adams International Airport (GAIA, station identifier: TBPB) for the 00 and 12 UT times since 1973.

Equipped with a humidity, temperature, and GPS-sensor, modern soundings record vertical profiles of temperature, humidity, pressure, wind speed and direction, as well as position and altitude. Sounding measurements can be affected e.g. by solar radiation, varying with pressure level and sun elevation; by different sensor response times, varying with pressure; by sensor icing and wetness when ascending through cloud layers; and by horizontal drifting depending on the wind conditions. Different correction algorithms need to be applied depending on the type of radiosonde used (Vömel et al., 2007; Turner et al., 2003; WMO et al., 2011). Challenges in the analysis of longterm trends or re-analysis data are introduced by different sounding types used worldwide and over time, and by differently strong horizontal drifting depending on the launch location (Finger and Schmidlin, 1991; Ross and Elliott, 2001; Durre et al., 2006).

Satellite Observations

Even though satellite observations cannot reach the vertical resolution that soundings provide, observations are available with broad global coverage, particularly providing measurements over remote, inaccessible regions of the world. Long records, e.g. by the Special Sensor Microwave Imager/(Sounder) (SSMI/(S)) instrument on the

Defense Meteorological Satellite Program (DMSP) satellites, in space since 1978, help to diagnose worldwide trends and observations of water vapor conditions under changing climate (e.g. Schulz et al., 1993). Longterm trends can be analyzed once the biases between the different sensors are corrected for (Trenberth et al., 2005; Sohn and Smith, 2003), and can be used to evaluate water vapor representation in climate models (e.g. Chen et al., 1996; Pierce et al., 2006).

Since data assimilation procedures have moved forward to 4D-var algorithms, the humidity observations over oceans provided by microwave satellite sounders such as SSMI/S or the Microwave Humidity Sounder (MHS) have been significantly improving forecasts up to multiple days (e.g. Geer et al., 2017). Recent efforts have been made to include more satellite radiances into all-sky data assimilation (Geer et al., 2019) for ECMWF forecasts and re-analyses. Boundary layer moisture structure is a key to successful assimilation strategies, particularly in the tropics, and requires bias free observations for model evaluation (Andersson et al., 2007).

However, while low revisiting times of twice per day in case of polar orbiters prohibit the quantification of short-term processes, instruments on geostationary orbits with higher temporal resolution operate in the visible or infrared, but cannot penetrate clouds (e.g. Wulfmeyer et al., 2015, for overview). Humidity observations are therefore only available above the highest cloud layer, and large portions of the available water vapor in the boundary-layer are missed in the presence of clouds. Microwave sounders like the Advanced Microwave Sounding Units (AMSU)-A or -B can penetrate clouds, but suffer from low vertical resolutions due to broadening weighting functions towards the lower troposphere where highest water vapor amounts and variability are expected in the trades. Often, satellite footprints are larger than the actual observed clouds. Active remote sensing instruments on satellites forming the A-Train like CloudSat (Stephens et al., 2002) and the Cloud-Aerosol Lidar and Infrared Pathfinder Satellite Observations (CALIPSO Winker et al., 2010) complement the picture of passive sensors. Spaceborne lidar observations by CALIOP (Cloud-Aerosol Lidar with Orthogonal Polarization,) on CALIPSO, and the Cloud Profiling Radar on CloudSat, offer high vertical resolution, and advance the monitoring of the vertical structure and properties of clouds and aerosols (Stephens et al., 2018). Yet the detection of shallow maritime clouds is challenged by radar instrument sensitivities (Lamer et al., 2020). Spaceborne water vapor profile observations can be advanced by combining active and passive instruments on one satellite, such as is planned for the future EarthCARE mission (Illingworth et al., 2015b).

Ground-based Remote Sensing Observatories

Even though spaceborne remote sensing applications cover a larger area than radiosondes and can capture large-scale conditions, the characterization of water vapor and cloud interplay requires a higher horizontal, vertical, and temporal resolution than what is feasible with current satellite sensors (e.g. Wulfmeyer et al., 2015). In order to overcome these observational constraints, ground-based remote sensing observatories such as the Barbados Cloud Observatory (BCO, Stevens et al., 2016) in the subtropics, or the ARM facilities (Ackerman and Stokes, 2003) and the Jülich ObservatorY of Cloud Evolution (JOYCE, Löhnert et al., 2015) located in the mid-latitudes can monitor the atmospheric column continuously. Ground-based remote sensing networks can fill observational gaps between operationally launched soundings (Löhnert et al., 2007), and can be integrated reliably into data assimilation to improve numerical weather prediction (NWP) (Illingworth et al., 2015a; Cimini et al., 2012; De Angelis et al., 2017).

While passive remote sensors capture natural thermal emissions of atmospheric constituents, active sensors transmit a beam of radiation and receive the backscattered signal. In case of the radar, the transmitted signal is at microwave frequencies, and backscattering targets are cloud or precipitation hydrometeors; lidars transmit a visible or near-infrared signal, which scatters on aerosols and molecules. While remote sensing applications based on visible or infrared radiation mostly cannot penetrate clouds, microwave remote sensing like the microwave radiometer or radar can profile through cloud layers.

Microwave radiometers sense atmospheric emissions mainly originating from energy state transitions of water vapor, oxygen, and liquid water. These emissions can be expressed as brightness temperatures according to Planck's law. By combining the brightness temperatures measured in different frequencies, the Integrated Water Vapor (IWV), Liquid Water Path (LWP), and coarse humidity and temperature profiles can be derived, given precipitation-free conditions (Westwater, 1978; Löhnert and Crewell, 2003). In order to solve the ill-posed inverse problem of linking the measured radiometric measurements to atmospheric states, multiple retrieval methods are available (Solheim et al., 1998): statistical regression retrievals (Crewell and Löhnert, 2003); physical retrievals such as the optimal estimation framework introduced by Rodgers (2000); or neural network retrievals (Cadeddu et al., 2009). Yet, due to coarse weighting functions of the channels, the vertical resolution of the

temperature and humidity profiles is limited (e.g. Güldner and Spänkuch, 2001), such that strong humidity gradients or temperature inversions are likely not resolved.

Generally, active sensors can achieve a higher vertical resolution than passive sensors. Water vapor profiles derived from lidar instruments reach vertical resolutions of a few meters in cloud-free situations given long integration times, but cannot profile the whole atmospheric column in the presence of clouds. While cloud radars, for example using Ka- or W-band frequencies, can profile through clouds with short integration times of a few seconds and single-frequency applications can deduct cloud and precipitation properties, the water vapor distribution cannot be derived. Combining two frequencies in a differential absorption approach can overcome some of these limitations. By locating one channel in the center of an absorption line, and a second channel on its wing, the height-resolved concentration of atmospheric gases can be measured. The differential absorption principle has been used for decades using visible frequencies with lidar instruments (DIfferential Absorption Lidar (DIAL) to derive the vertical structure of water vapor (Schotland, 1966) in clear conditions or until signal saturation at cloud base. Recently, frequencies in the microwave spectrum around the 183.31 GHz (G-band) water vapor absorption line (Differential Absorption Radar (DAR); Battaglia et al., 2014; Lebsock et al., 2015) have been used to determine the water vapor profile in cloud layers in the boundary layer (Roy et al., 2020) and to assess the potential for ice cloud profiling (Battaglia and Kollias, 2019). While DIAL gives accurate profiles up to cloud base, DAR can deliver accurate humidity profiles within each cloud layer, and the partial water vapor amount between radar and the lowest cloud base. Both techniques are insensitive to the water vapor structure above the highest cloud top due to signal saturation or lack of backscattering targets.

Ground-based Sensor Synergy

In order to overcome the restrictions of each sensor, synergistic retrievals can be used to make use of the complementary potential of different remote sensing applications available at ground-based observatories (Stankov, 1998). In particular, the combination of passive and active instruments is beneficial. The Cloudnet algorithm (Illingworth et al., 2007), operational at multiple cloud observatories like JOYCE or BCO, combines ceilometer, radar, and MWR observations to retrieve cloud boundaries and properties, and offers a target classification product as well as thermodynamic profiles. The integrated profiling technique (Löhnert et al., 2004, 2007) combines

MWR, Ka-radar, and ceilometer in an optimal estimation approach to derive humidity, temperature, and liquid water content profiles in cloudy and drizzling conditions, as well as effective radius (Ebell et al., 2017). Barrera-Verdejo et al. (2016) and Foth and Pospichal (2017) combine Raman lidar and MWR, enhancing the retrieval performance in clear and cloudy conditions. Combing MWR and a ground-based infrared spectrometer (Atmospheric Emitted Radiance Interferometer, AERI) decreases retrieval errors for lower tropospheric temperature and humidity profiling in clear conditions (Löhnert et al., 2009) and below cloud boundaries (Blumberg et al., 2015). A combination of ground-based MWR and spaceborne infrared (IR) instruments enhances the information content for temperature and humidity profiles in clear conditions (Ebell et al., 2013), and for IWV and atmospheric stability (Toporov and Löhnert, 2020).

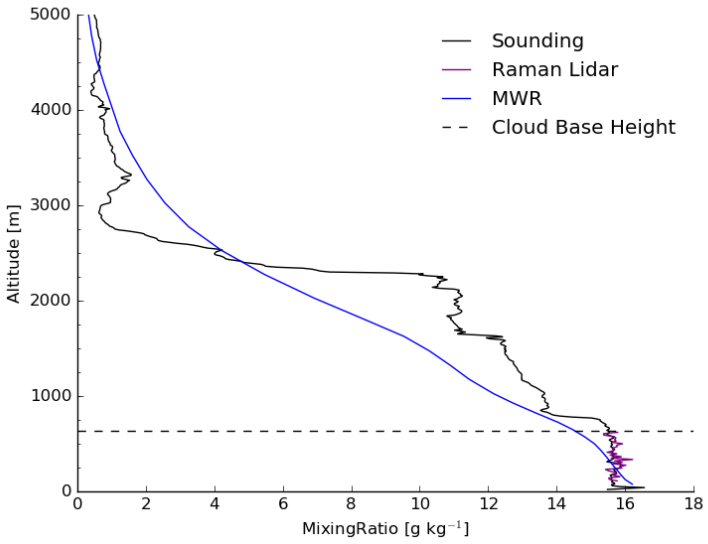

Figure 1.2 – MWR (blue), Raman-Lidar (purple) and radiosonde (black) measurements of water vapor mixing ratio at BCO, 02.02.20. The sounding was launched at 10:51 UTC, and the MWR and lidar observations were averaged within a ± 2 minute window around the sounding launch. A shallow cloud formed above LCL with cloud base located at 620 m (black dash).

However, so far, no reliable remote sensing technique exists for retrieving the whole column water vapor profile, particularly the lower tropospheric profile, in the presence of one or multiple cloud layers with sufficient vertical and temporal resolution (Nehrir et al., 2017; Stevens et al., 2017; Pincus et al., 2017). This observational gap has been identified as critical atmospheric variable for NWP by the World Meteorological Organisation (WMO, 2014). Figure 1.2 illustrates this observational gap, based on

the remote sensing and sounding measurements at BCO for a shallow Cumulus case example during the EUREC^{4}A campaign. The MWR-derived profile, limited by a rather coarse vertical resolution, does not resolve the sharp moisture gradients, particularly occurring around the trade inversion (on this day located at around 2300 m). The derived profile suggests an underestimation of the moisture content in the moist layer, and an overestimation of the moisture in the free troposphere. The profile derived from the Raman-Lidar represents the conditions below the cloud layer very accurately. Above cloud base, however, no profile can be retrieved as the lidar beam cannot penetrate the liquid targets. Additionally, an accurate profile cannot be derived within the overlap region of the instrument, reaching up to 100 m. The illustrated case implies the necessity for an observational method that can profile through clouds, can continuously monitor the full atmospheric column, and can achieve a sufficiently high vertical resolution to improve the representation of the typical strong humidity gradients observed in the trades.

1.2 Research Questions and Thesis Outline

In this thesis, the potential of closing this observational gap is assessed by combining MWR and dual-frequency radar observations. The proposed instrument synergy combines the advantages of each instrument, such as sketched in Fig. 1.3: while the MWR provides information about the integrated column water vapor amount, and a coarse water vapor profile, the dual-frequency radar constrains the retrieval within the cloud layer(s), and the amount of water vapor below the lowest cloud layer. The proposed synergistic retrieval approach is further constrained by supplemental 2m absolute humidity measurements $\rho_{2\mathrm{m}}$, as well as cloud boundary observations. A synergy between the two instruments offers more impact than just combining each single retrieval with another, as in a combined retrieval, information from the one instrument can be supplemented with the other instrument's information.

In the following studies, an optimal estimation framework (Rodgers, 2000) is chosen to analyze the synergistic benefits of MWR and dual-frequency radar based on the retrieval uncertainties, information content expressed as Degrees of Freedom of Signal (DFS), and retrieved profile. The passive MWR channels are selected based on the K-band channels of the HATPRO instrument (Rose et al., 2005). The frequencies of the dual-frequency radar are chosen for the Ka- and W-band radar, available at ground-based observatories such as BCO or JOYCE. A second frequency combination

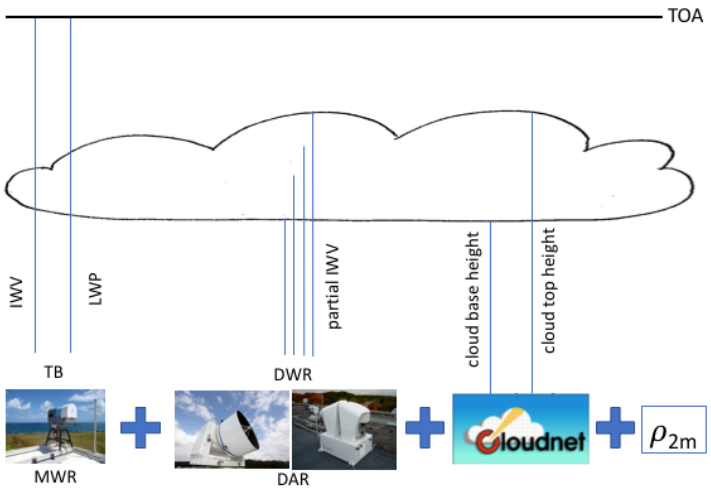

Figure 1.3 – Concept, instruments and their observations used in the synergistic retrieval approach: MWR brightness temperature TB for IWV, LWP, coarse water vapor profile; DWR for partial IWV quantification below cloud base and in-cloud profiling; cloud base and top height provided by e.g. Cloudnet (Illingworth et al., 2007); and 2 m absolute humidity ρ_{2m} observations. Blue lines represent the vertical range of the instruments' observations.

in the G-band was chosen according to the operational G-band VIPR-instrument (*Vapor In-cloud Profiling Radar*, Roy et al., 2020), so far the only such instrument in operation. As no simultaneous observations are available of all instruments, synthetic observations have been generated using the Passive and Active Microwave TRAnsfer (PAMTRA) forward simulator (Mech et al., 2020) for typically observed conditions at BCO. Atmospheric profiles measured by radiosondes are combined with idealistic single- and double-layered cloud properties to generate brightness temperatures, radar reflectivities, atmospheric attenuation, and the radar differential Dual-Wavelength Ratios (DWR).

The following research questions of this thesis will be addressed in two main studies. They will structure the potential analysis of the benefits, limitations and applicability of the proposed synergy concept in this thesis.

1. Which synergy potential is available when combining MWR with KaW and G2, respectively, analyzed for a single-cloud scenario in various moisture conditions observed in the trades? In which vertical levels is the synergy most beneficial?
2. How sensitive are the synergistic retrieval uncertainties and information content to the assumed measurement errors, as well as radar sensitivity limits?

3. How much would an instrument synergy of MWR and DAR G2 improve the retrieval performance in zones of highest water vapor variability, shown for representative cases observed during the EUREC^{4}A field study?
4. Does the synergistic MWR+DAR G2 retrieval improve the reconstruction of an atmospheric state between 24-hour spaced operational radiosondes compared to the temporal interpolated sounding profile, and, if so, at which heights?
5. Expanding the concept to including synthetic Raman lidar measurements, how does the retrieval benefit in the sub-cloud layer, and which modified retrieval configurations lead to an optimized performance between and above the cloud layers?

Before addressing the research questions, I will give a brief overview of the scientific background for microwave remote sensing applications for water vapor profiling in chapter 2. I will address the microwave radiative transfer theory, the underlying instrument principles of the microwave radiometer and radar, and give an overview of radar-based water vapor observation techniques. Outlining observations and the inverse method applied for the later analyses in chapter 3, I will first give an overview of the continuous remote sensing measurements at BCO (Sec. 3.1), including a brief overview of the intense observation period during the EUREC^{4}A field study and the associated sounding network observations. Section 3.2 will then describe the concept behind the synthetically generated observations. The optimal estimation setup used to retrieve water vapor profiles from the observations will be introduced in Sec. 3.3.

In study 1, summarized in chapter 4 and published as Schnitt et al. (2020), the potential of the synergy concept will be investigated by combining MWR with the two different radar frequency pairs. Based on an idealized single-layered liquid cloud scenario, the synergistic benefits will be analyzed in different water vapor conditions guided by research question 1. Their sensitivity to measurement errors and radar reflectivity detection thresholds will be evaluated within research question 2.

Study 2, presented in chapter 5, will expand the potential analysis to more realistic and, thus, increasingly complex atmospheric conditions as observed during the EUREC^{4}A campaign. Based on three case studies representing the main water vapor structures occurring at BCO in trade wind driven conditions, the synergy of MWR and G-band radar will be analyzed for a single-layered boundary layer cloud case, a double-layer liquid cloud case, and for a scenario of an elevated moisture layer associated with the formation of a higher, ice-containing altocumulus cloud layer. In

Sec. 5.2, I will analyze the synergistic benefits and their vertical distribution using a standard climatological prior in the optimal estimation retrieval, discussing research question 3. The added value of the synergy to deriving the atmospheric state between 24-hour spaced operational sounding measurements will be investigated in Sec. 5.3, answering research question 4. Furthermore, the retrieval concept will be expanded to include synthetic Raman Lidar measurements in Sec. 5.4. The impacts on the sub-cloud layer retrieval, as well as tools for further optimizing the retrieval between and above the cloudy layers will be analyzed, resolving research question 5.

A first insight into the potential of extending the concept feasibility study to an airborne application, or to the dry Arctic environment will be given in chapter 6 based on first synthetic measurements. In chapter 7, all findings will be summarized, limitations of the study will be discussed, and concluding remarks will be given regarding the potential for advancing ground-based water vapor profiling through a synergy of MWR and dual-frequency radar.

2 Microwave Remote Sensing of Water Vapor and Clouds

This chapter presents a brief overview of the fundamentals regarding radiative transfer in the microwave part of the electromagnetic spectrum (Sec. 2.1), as well as the principles of operation and application examples of the remote sensing instruments used in this thesis (Sec. 2.2). More specifically, the MWR, the radar, and radar applications for water vapor profiling will be discussed.

2.1 Microwave Radiative Transfer

The following overview on radiative transfer will answer the following questions: How can radiation be quantified? Which processes alter the radiation along its ray path throughout the atmosphere? Which atmospheric constituents are mainly responsible for absorption and emission? Which scattering processes are important? Deeper insights than what is presented in the following can be found in many atmospheric science textbooks, as for example in Petty (2006), Liou (2002), and Ulaby (2014).

Radiation and Extinction

The spectral radiance B emitted by a medium at a particular frequency ν is described by Planck's law (Eq. (2.1.1)) and is a function of the emitting body's temperature T, the medium's speed of light c, Planck's constant h and the Boltzman constant k_B[1]. For frequencies in the microwave spectrum, Planck's law can be linearized by

[1] speed of light c in air: $c = 3 \cdot 10^8 \mathrm{m\,s^{-1}}$; Planck's constant h = 6.626 $\cdot 10^{-34}$ J s; Boltzman constant $k_B = 1.38 \cdot 10^{-23} \mathrm{J\,K^{-1}}$.

the Rayleigh-Jeans approximation (Eq. (2.1.2)).

$$B(\nu, T) = \frac{2h\nu^3}{c^2} \frac{1}{e^{\frac{h\nu}{k_B T}} - 1} \tag{2.1.1}$$

$$B_{RJ}(\nu, T) \approx \frac{2k_B\nu^2}{c^2} T \tag{2.1.2}$$

Planck's law describes the radiation of a so-called blackbody medium, which describes a perfect absorbing body. According to Kirchhoff's law, an absorbing body is also an emitting body, given it is in local thermodynamic equilibrium. In other words, a thin layer of e.g. air absorbs radiation, and also emits radiation according to Planck's law, depending on its temperature. Yet, in reality, bodies often are not perfect absorbers or emitters. The so-called grey bodies emit only a part $I(\nu, T)$ of the maximum possible radiation $B(\nu, T)$, scaled by the emissivity factor $\epsilon(\nu) = I(\nu, T)/B(\nu, T)$.

When radiation propagates through the atmospheric medium, it interacts with atmospheric constituents such as gas molecules and hydrometeors. Radiation can be absorbed e.g. by molecules or hydrometeors, meaning that it stimulates an energy state transition, or it can be scattered, that is redirected in direction. All different gases' and hydrometeors' volume absorption and scattering coefficients β_a and β_s sum up to the volume extinction coefficient β_e (Eq. (2.1.3)). Each one of the volume coefficients β_a and β_s can be related to the mass absorption or scattering coefficients κ_a or κ_s by multiplying with the hydrometeor or gas density ρ. For example, the water vapor absorption coefficient β_a^{WV} equals to the product of water vapor mass absorption coefficient κ_a^{WV} and absolute humidity ρ_v. The mass extinction coefficient is a function of frequency ν, temperature T and pressure p

$$\beta_e(\nu) = \beta_a(\nu) + \beta_s(\nu) \tag{2.1.3}$$

$$= \sum_i \rho_i \cdot (\kappa_{a,i} + \kappa_{s,i}). \tag{2.1.4}$$

Beer's law states that the initial radiation $I(\nu)$ is attenuated when propagating through a medium (Eq. (2.1.5)) depending on the optical depth τ, that is the integral over all extinction coefficients, or the layer's transmissivity $t(\nu)$ (Eq. (2.1.6)). In the microwave spectrum, the atmosphere is generally semi-transparent, which means

that radiation can propagate through clouds and $t(\nu)$ is never zero.

$$I(s_2) = I(s_1) \cdot \exp(-\tau(s_1, s_2)) \quad \text{with} \quad \tau(s_1, s_2) = \int_{s_1}^{s_2} \beta_e(\nu) ds \tag{2.1.5}$$

$$= I(s_1) \cdot t(\nu, s_1, s_2) \quad \text{with} \quad t(\nu, s_1, s_2) = \exp(-\tau(s_1, s_2)) \tag{2.1.6}$$

Along its propagation path ds, the initial radiation $I(\nu)$ is reduced by absorption processes to I_a, while temperature-dependent grey-body emissions I_e add up along the path. According to Kirchhoff's law, the thermal emissions can again be quantified by Planck's law (Eq. (2.1.1)). The transition of dI along its path through the atmosphere ds is described by the radiative transfer equation (Eq. (2.1.8)), and is in its presented form valid for a non-scattering volume ($\beta_e \approx \beta_a$).

$$\frac{dI}{ds} = \frac{dI_a + dI_e}{ds} \tag{2.1.7}$$

$$= \beta_a \cdot (-I(\nu) + B(T, \nu)) \tag{2.1.8}$$

Absorption Spectrum

Absorption and emission varies throughout the microwave spectrum between 3 and 200 GHz. The main absorbing gases are water vapor and oxygen, while absorption by other atmospheric constituents like nitrogen or ozone are of order of magnitudes smaller. In addition to the broadened absorption lines, continuum absorption by water vapor increases throughout the spectrum. The absorption spectrum is illustrated in Fig. 2.1. The spectrum is characterized by the rotational absorption lines of water vapor at 22.24 GHz (K-band) and 183.31 GHz (G-band), the oxygen absorption band between 50 and 60.0 GHz (V-band) and at 118 GHz (F-band), as well as the increasing absorption with increasing frequency due to water vapor continuum absorption. The liquid water absorption increases throughout the spectrum with frequency squared (not shown). Atmospheric pressure leads to a broadening of the respective absorption lines as molecules are forced to collide. The absorption and, thus, also the emission at different frequencies varies depending on temperature, humidity, and pressure.

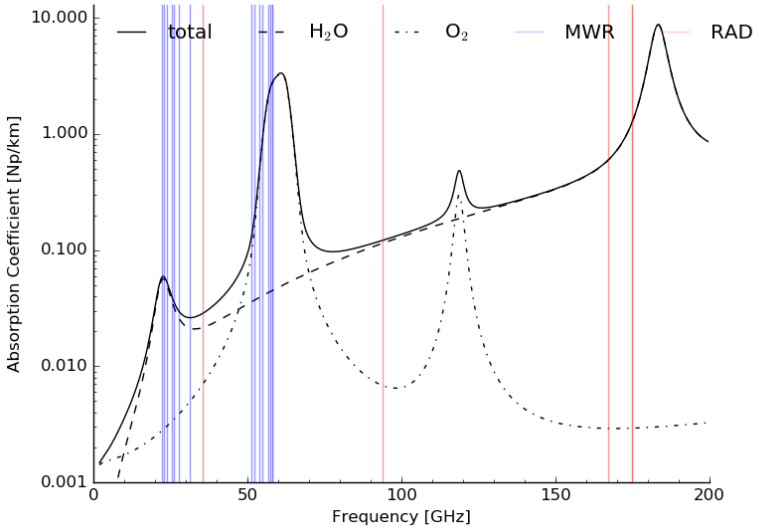

Figure 2.1 – Clear air absorption spectrum for lower microwave frequency range below 200 GHz calculated using PAMTRA (Mech et al., 2020). Water vapor (dash), oxygen (dash-dot) and total absorption (solid) were calculated at 1000 hPa for an atmosphere with a temperature of 293.15 K and an absolute humidity of $10\,\mathrm{g\,m^{-3}}$. The MWR HATPRO channels are marked in red, and the used radar frequencies are marked in blue.

Scattering

In addition to absorption and emission processes, scattering also alters the radiation on its propagation path throughout the atmosphere. The impact of scattering depends on the radiation wavelength λ (Petty, 2006, Sec. 12.1.2), as well as the volume- or size-equivalent radius of the scatterer r. The size parameter $x = 2\pi r/\lambda$ provides a first estimate about the scattering regime of the respective wavelength used. When $x \ll 1$ and assuming spherical particles, scattering processes can be described by Rayleigh scattering (e.g. Petty, 2006), and the scattering cross section σ_s is proportional to the radius of the scatterer to the power of six, and the inverse wavelength to the power of 4. Otherwise, Mie scattering (Mie, 1908) describes the scattering phase function of each particle, depending on the particle's shape and phase. σ_s then depends on the particular backscattering cross section σ_{bsc}. In the lower microwave spectrum below 100 GHz, including the K-band frequencies used in the MWR, scattering impacts of molecules or small hydrometeors are an order of magnitude smaller than the occurring thermal emission at these frequencies. In case of larger precipitating particles, the scattering impact can no longer be neglected (Bobak and Ruf, 2000).

2.2 Remote Sensing Instruments

Emission and scattering of radiation throughout the atmosphere can be used to study water vapor and cloud properties through remote sensing instruments. Remote sensing instruments can be divided into passive and active sensors. While passive instruments receive the natural radiation $I(\nu)$ propagating through the atmosphere and altered along its path as described in Eq. (2.1.8), active sensors transmit a beam of radiation at a frequency ν and receive the back-scattered, attenuated signal. In the following sections, the basic operational principles of the passive MWR (Sec. 2.2.1), and the active radar (Sec. 2.2.2) will be illustrated with a particular focus on applications for water vapor and cloud remote sensing. The state-of-the-art for water vapor profiling using dual-frequency radar applications will be summarized in Sec. 2.2.3.

2.2.1 Microwave Radiometer

The radiation that a zenith-pointing ground-based MWR senses in its different frequency channels can be quantified by integrating the radiate transfer equation Eq. (2.1.8) from the top of the atmosphere (TOA) to the ground as shown in Eq. (2.2.1)

$$I_0(\nu) = I_{\cos} \cdot \exp(-\tau) + \int_0^{\infty} B(\nu, T(z)) \cdot \beta_a \cdot \exp(-\int_0^{z} -\beta_a(z')dz')dz. \qquad (2.2.1)$$

The overall signal $I_0(\nu)$ combines the initial cosmic background radiation $I_{\cos} = B(T = 2.7\,\mathrm{K})$, attenuated by the total column optical depth $\tau = \int_0^{\infty} \beta_a dz$, and the thermal emissions $B(\nu, T(z))$ originating from each vertical atmospheric layer at height z[2]. The emitted radiation $B(\nu, T(z))$ depends on the layer's temperature $T(z)$, the gases' and hydrometeors' emission coefficients $\beta_a(z)$, and is further attenuated by the absorption between the emitting layer and the ground by the transmissivity on the way to the ground. In case of an air- or spaceborne MWR, additional radiation reflected from the ground impacts the received $I(\nu)$.

In microwave remote sensing applications, generally the brightness temperature TB is used as opposed to the radiance I. TB describes the radiative-equivalent temperature a body would have to emit I, and can be obtained by inverting the

[2]Note that z here refers to altitude above ground level as opposed to the radar reflectivity z introduced in Sec. 2.2.2.

Planck law or the Rayleigh-Jeans approximation (Eq. (2.1.1) or (2.1.2)). By applying inverse methods to Eq. (2.2.1), such as statistical (e.g. Westwater, 1978; Crewell and Löhnert, 2003) or physical (e.g. Rodgers, 2000; Maahn et al., 2020) retrieval algorithms, the total column water vapor amount (IWV) and the Liquid Water Path (LWP) can be quantified.

Coarsely resolved profiles of temperature and humidity can be derived from K- and V-band TBs (Güldner and Spänkuch, 2001; Liljegren et al., 2005; Crewell and Löhnert, 2007), for example available in the Humidity And Temperature PROfiler (HATPRO; Rose et al., 2005). Accuracies of 0.8 to 1.0 $\mathrm{g\,m^{-3}}$ (Güldner and Spänkuch, 2001) and 1.0 to 1.5 K (Crewell and Löhnert, 2007) can be reached throughout the lower troposphere in non-precipitating conditions with degrading vertical resolutions of 500 m to 1000 m. Synergies with other remote sensing instruments can further improve the retrieval performance by incorporating radar (e.g. Löhnert et al., 2004, 2008), infrared-radiometer (e.g. Löhnert et al., 2009) or lidar measurements (Barrera-Verdejo et al., 2016; Foth and Pospichal, 2017).

2.2.2 Radar

Radar instruments transmit a microwave signal and receive the radiation that is scattered back into the direction of the instrument's antenna. Backscattering targets include cloud or precipitation droplets, ice or snow particles, birds or insects, depending on the radar's frequency. Radars have been used for meteorological purposes since the mid-20th century, and radar theory has been summarized in many books (e.g. Battan, 1973; Rinehart, 2010; Rauber and Nesbitt, 2018).

The received power p_r at the radar (Eq. (2.2.2)) depends on the distance r between scattering medium and instrument, the radar reflectivity factor z[3], as well as instrument-specific constants summarized in c_1. The received signal p_r decreases with the squared distance between radar and target

$$p_r = \frac{c_r z}{r^2}. \tag{2.2.2}$$

The radar constant c_r includes the radar wavelength λ, the beam's volume described by the horizontal and vertical beamwidth θ and ϕ respectively, the gain factor g and the transmitted power p_t.

[3]Reflectivity factor will be referred to as reflectivity in the following.

For spherical particles in Rayleigh-scattering regime, the radar reflectivity z can be described by Eq. (2.2.3), or by Eq. (2.2.4). Depending on the representation used, z thus depends on the particle size distribution $N(D)$ and the scatterer's diameter D to the power of six for Rayleigh scattering mediums; or, more generally, on the summarized volume backscattering coefficient of the target $\eta = \sum \sigma_i$, the medium's dielectric factor $|\mathrm{K}|^2 \approx 0.93$ for liquid targets, and the radar wavelength λ to the power of four.

$$z = \int_0^\infty N(D) D^6 dD \tag{2.2.3}$$

$$= \frac{\eta \lambda^4}{\pi^5 |K|^2} \tag{2.2.4}$$

As the particle size distributions in clouds are wide, z spans a wide range of numbers and is therefore generally converted to logarithmic units using Eq. (2.2.5). The equivalent logarithmic reflectivity, that is the reflectivity for equivalent spherical particles, is the un-attenuated reflectivity Z_e^{th} expected purely from scattering processes (Eq. (2.2.6)).

$$Z_e^{\mathrm{th}}[\mathrm{dBz}] = 10 \log_{10} z \tag{2.2.5}$$

$$= P_r[\mathrm{dBm}] + 10 \log_{10}(r) + \log_{10}(c) \tag{2.2.6}$$

Yet, in reality, the radar beam experiences further attenuation on its path through the atmosphere according to Beer's law (Eq. (2.1.6)). Therefore, the measured attenuated reflectivity z_e^{att} can be calculated (Eq. (2.2.7)) by introducing the additional two-way attenuation factor $T(\nu, r) = 2 \cdot t(\nu, r)$, specific to the radar's frequency and range (Eq. (2.2.7), also see Lhermitte, 1990). The height-specific transmissivity $t(\nu)$ depends on the extinction coefficients β_a of the respective absorbing gases and hydrometeors (see Sec. 2.1), and the specific frequency (see Fig. 2.1). The logarithmic reflectivity signal Z_e^{th} is reduced to Z_e^{att} by the corresponding logarithmic transmissivity.

$$z_e^{\mathrm{att}} = T(\nu, r) \cdot z \tag{2.2.7}$$

$$Z_e^{\mathrm{att}} = Z_e^{\mathrm{th}} - \log_{10} T(\nu, r) \tag{2.2.8}$$

For simplicity, all future mentioned z_e or Z_e will refer to the attenuated signal without additional specification.

Most cloud and precipitation radars operate in window frequencies away from the main absorption lines to minimize signal attenuation. With increasing operation frequency, e.g. from Ka-band to W-band radar, the sensitivity to smaller particles increases, and smaller cloud droplets can be detected. Yet, also the attenuation increases with increasing frequency due to increasing absorption of water vapor continuum and liquid water. At ground-based remote sensing observatories such as BCO or JOYCE, pulsed (e.g. Görsdorf et al., 2015) and Frequency-Modulated Continuous Wave (FMCW) radars (e.g. Küchler et al., 2017) are in operation.

2.2.3 Radar Strategies for Water Vapor Profiling

Radar measurements cannot only be used to derive cloud and precipitation properties, but can also be used to measure partial water vapor amounts between adjacent radar range gates. Fabry et al. (1997) propose to use S-band radar phase information from natural ground targets to infer the refractive index of the surrounding, horizontal atmosphere, linked to the 2D-structure of temperature and moisture around the radar. Ellis and Vivekanandan (2010) compare non-attenuated S-band with attenuated Ka-band radar measurements to derive the total water vapor attenuation at Ka-band along the ray path. Through scanning techniques, they successfully derive a low-tropospheric humidity profile with a 2 % to 6 % relative error compared to sounding in-situ measurements. Airborne return signals of a Ku- and W-band combination are used by Tian et al. (2007) to infer water vapor attenuation in a light rain field. Meneghini et al. (2005) explore the feasibility of deriving water vapor profiles based on three frequencies around the 22 GHz absorption line.

Differential Absorption Radar

Only recently, Lebsock et al. (2015) proposed a dual-frequency combination of radar frequencies along the wing of the strong water vapor absorption line at 183.31 GHz to derive water vapor profiles based on differential reflectivity signals. By placing one frequency close, and one frequency further away from the line center (*online* and *offline*), the Differential Absorption Radar (DAR) technique can be related to the water vapor concentration, similarly to the DIAL technique, but is applicable in

cloudy situations. This technique can be used to study e.g. the boundary layer water vapor structure (Millán et al., 2016; Roy et al., 2018), or water vapor throughout ice clouds (Battaglia and Kollias, 2019).

The Dual-Wavelength Ratio (DWR) at distance r, that is the differential reflectivity signal in the corresponding range gate, can be determined by the ratio of the attenuated linear reflectivities $z_e(\nu_1, r)$ and $z_e(\nu_2, r)$ for the off- and online frequency, respectively, or the difference between the corresponding logarithmic reflectivities (Eq. (2.2.9))[4]. Assuming that the difference between off- and on-line un-attenuated z_e (Eq. (2.2.4)) is small, and that no differential scattering occurs, DWR (Eq. (2.2.9)) simplifies to Eq. (2.2.10), the ratio of transmissivities at the corresponding frequencies and range gates. Due to the strong water vapor absorption along the 183.31 GHz-line, it is valid to assume that the water vapor absorption is on order of magnitudes higher than the liquid hydrometeor attenuation. Using Eq. (2.1.6) to calculate the 2-way transmissivity, the resulting DWR signal then only depends on the water vapor specific properties as seen in Eq. (2.2.11). The differential DWR signal relates to the layer's water vapor concentration ρ_v, assumed constant in the respective volume, as well as the water vapor mass absorption coefficients κ_v at the two respective frequencies (also see Eq. (2.1.4)).

$$\mathrm{DWR}(\nu_1, \nu_2, r) = \frac{z_e^{\mathrm{offline}}(\nu_1, r)}{z_e^{\mathrm{online}}(\nu_2, r)} = Z_e^{\mathrm{offline}}(\nu_1, r) - Z_e^{\mathrm{online}}(\nu_2, r) \tag{2.2.9}$$

$$= \frac{T(\nu_1, r)}{T(\nu_2, r)} \tag{2.2.10}$$

$$= \exp(-2 \cdot \int_{r_0}^{r} [\rho_v(r) \cdot (\kappa_v(\nu_1, r) - \kappa_v(\nu_2, r))] dr) \tag{2.2.11}$$

Profiles of partial water vapor can be inferred throughout cloud layers in-between adjacent range gates r_0 and r, with the vertical resolution depending on the radar range gate spacing and signal processing. Additionally, the partial water vapor amount between the instrument's location and the first backscattering target along the beam path can be derived. In a ground-based application, this partial water vapor amount could be the sub-cloud layer water vapor amount. In an air- or spaceborne application, the ground return signal can be used to derive the full-column water vapor in clear-sky conditions, the boundary layer water vapor amount below the

[4]Equations have been summarized using the notation in Lebsock et al. (2015), as well as the derivation in Roy et al. (2018) and Battaglia and Kollias (2019).

cloud layer, and the partial water vapor amount between air-/spacecraft and cloud top.

Even though the potential of G-band radars for atmospheric studies has been known for a while (Battaglia et al., 2014), only very recently, the first prototype was successfully built and tested with a tunable frequency range between 183 and 193 GHz (Cooper et al., 2018; Roy et al., 2018). The frequencies of the Vapor In-cloud Profiling Radar (VIPR) used in Roy et al. (2020) were changed to 167.0 and 174.8 GHz due to frequency restriction laws. Roy et al. (2020) use VIPR's differential measurements at the ARM-Southern Great Planes site to retrieve 180 m-resolved in-cloud humidity profiles with a root-mean square error (RMSE) of $0.8\,\mathrm{g\,m^{-3}}$, and the sub-cloud layer water vapor amount with a RMSE of $1.2\,\mathrm{kg\,m^{-2}}$ compared to radiosoundings.

3 Observations and Inverse Method

The following chapter introduces the observations and inverse method used in this thesis. First, in Sec. 3.1.1, the continuously running measurements at BCO will be introduced with a focus on the MWR BCOHAT, the CORAL Ka-band radar and lidar, the Cloudnet algorithm, as well as a Vaisala weather station. The operational soundings launched at Grantley Adams International Airport (GAIA) will be described. The observations of the intensive measuring activities performed during EUREC^{4}A will be presented in Sec. 3.1.2, illustrating briefly the synoptic conditions during the field study, as well as the sounding data from BCO and GAIA. The forward simulation setup to obtain synthetic measurements of the K-band MWR channels, as well as the reflectivities at 35.5, 94.0, 167.0 and 174.8 GHz will be illustrated in Sec. 3.2. The optimal estimation inverse method will be summarized in Sec. 3.3 by presenting the basics of the approach, as well as the setup and assumptions used in the later analyses.

3.1 Measurements at Barbados

3.1.1 Continuous Observations at BCO

The Barbados Cloud Observatory (BCO) has been operating since 2010 off the coast of Barbados at 13.2 °N and 59.4 °W, exposed to the North Atlantic trades (Stevens et al., 2016; Medeiros and Nuijens, 2016). The observatory is equipped with a suite of remote sensing instruments, including a Raman lidar, a Ka-band radar, a W-band radar, two wind lidars, a MWR HATPRO, a weather station, a disdrometer, and

Figure 3.1 – Barbados Cloud Observatory in February 2019. While the Raman lidar and the Ka-band radar are located on the containers to the left, the MWR HATPRO is installed further to the right next to the ceilometer, and the W-band radar is located on top of the middle container. The radiosonde preparing station is located in the center, while soundings are launched from outside of the fenced area.

solar radiation sensors.[1] As illustrated on the photo shown in Fig. 3.1, all instruments are mounted on top of containers about 30 m away from the coastline-cliffs and 20 m above mean sea level.

Microwave Radiometer BCOHAT

BCOHAT is a HATPRO microwave radiometer Generation 5 (Rose et al., 2005). The radiometer has 14 channels: 7 channels in the K-band, sensitive to water vapor and liquid water, and 7 channels in the V-band, sensitive to oxygen absorption and usable for temperature profiling. Calibration uncertainties can affect the measured TBs with an uncertainty of 0.4 K in the K-band channels (Maschwitz et al., 2013). At BCO, a similar statistical retrieval as presented in Löhnert and Crewell (2003) and Steinke et al. (2015) is used to retrieve IWV, LWP, temperature and absolute humidity profiles from the 14 measured TBs, using a quadratic least square regression method following Eq. (3.1.1) (*var* representing the to-be-retrieved quantity)

$$var = c_0 + \mathbf{c}_1 \cdot \mathbf{TB} + \mathbf{c}_2 \cdot \mathbf{TB}^2. \tag{3.1.1}$$

In order to derive the retrieval coefficients c_0, c_1, and c_2, a training dataset of 10871 quality-controlled soundings launched at GAIA between 1990 and 2018 have

[1] Most recent instrument status and data availability at `barbados.mpimet.mpg.de`. Data copyright at Max-Planck-Institute for Meteorology, Hamburg, Germany, made available by Friedhelm Jansen and Ilya Serikov (Raman lidar).

been included using the criteria described in Nörenberg (2008). The retrieved LWP values are corrected by the closest clear-sky LWP offset: $\mathrm{LWP_{corrected}} = \mathrm{LWP_{ret}} - \mathrm{LWP_{clear\text{-}sky}}$. Retrieval results are available with a temporal resolution of 2 s in non-precipitating conditions, given that the radiometer radome is dry. IWV values can be retrieved with an error of 0.5 to 0.8 $\mathrm{kg\,m^{-2}}$ (Steinke et al., 2015), while the LWP accuracy can be estimated around 15 to 25 $\mathrm{g\,m^{-2}}$ (Crewell and Löhnert, 2003).

CORAL Ka-band Radar and Lidar

The CORAL Ka-band radar is a pulsed, polarized Doppler cloud radar, continuously operating in zenith-pointing mode at 35.5 GHz. The radar is operated in zenith-only mode reaching a vertical range gate spacing of 31.2 m (Klingebiel et al., 2019). Data processing is done following Görsdorf et al. (2015), leading to radar sensitivities of −70 dBz at 500 m. Görsdorf et al. (2015) estimate a reflectivity uncertainty of 1.3 dB to account for various uncertainties in system-relevant parameters.

Complementing the suite of active remote sensing instruments, the CORAL Raman lidar transmits signals at 355, 532, and 1064 nm (comparable to the lidar used in Schulz and Stevens, 2018). The signal at 355 nm stimulates the Raman vibrational energy state transition of water vapor and nitrogen molecules, detectable at 407.5 and 387.7 nm, respectively. The high-resolution data provides profiles of particle backscatter and water vapor mixing ratio, temperature and relative humidity, as well as a cloud mask with a vertical resolution of 15 m below 3000 m. High-temporal resolution profiles are available every 4 s, or over longer integration times of 10, 20 or 60 minutes. Systematic errors associated with the sensor overlap affect the measurements in the lowest 100 m with high uncertainty. Yet, above 100 m throughout the sub-cloud layer, water vapor mixing ratio measurements can be deducted with an uncertainty ranging around 1.0 $\mathrm{g\,kg^{-1}}$ in clear-sky situations at night. During the day, the uncertainty increases due to sunlight disturbances.

Cloudnet

The suite of available remote sensing instruments at BCO allows data processing with the synergistic Cloudnet algorithm (Illingworth et al., 2007). The output includes e.g. a cloud target classification based on the measurements of the MWR HATPRO, CORAL Ka-band radar, and the available ceilometer together with GDAS-1 (Global

Data Assimilation System) thermodynamic profiles. The temporal resolution of the output is 30 s.

Ground Weather Station

The weather station, a Vaisala WXT-520 ground station, measures standard meteorological variables such as temperature, humidity, pressure, wind speed and direction, as well as rain rate. The station operates continuously with a temporal resolution of 10 s. The manufacturer provides a relative uncertainty of 3 % for the humidity measurements (Vaisala, 2012).

Operational Soundings at GAIA

At Grantley Adams International Airport (GAIA), 30 km southwest of BCO, operational soundings are launched every 12 or 24 hours for the 00UT and 12UT sounding times with the station identifier name TBPB (78954). The available sounding record goes back to 1973 and is available at `http://weather.uwyo.edu/upperair/sounding.html`. As the sounding data available before 1990 only comprises standard pressure levels, only sounding data launched 1990 and later have been used in the analyses.

3.1.2 EUREC^{4}A

The EUREC^{4}A field study comprised an intensive period of observation and modelling activities in January and February 2020 to investigate the coupling of clouds, convection and circulation in the shallow convective maritime trade wind environment over the North Atlantic off the coast of Barbados (Bony et al., 2017; Stevens et al., 2020a). The airborne observations of up to four simultaneous aircraft were focused around a corridor northeast of Barbados. Ship-borne activity by four research vessels was centered around the flight area, as well as further South in a corridor northeast of the South American continent. An overview of the many other measurements made is given in Stevens et al. (2020a) or on `http://eurec4a.eu`. The air- and ship-borne in-situ and remote sensing observations were complemented by an upper air sounding network measuring the atmospheric conditions every four hours throughout the month of coordinated measurements (Stephan et al., 2020, see Sec. A.1). Remote

sensing observations at BCO (Stevens et al., 2016), as well as the operation of a C-band weather radar on Barbados, complemented the array of observations.

Synoptic Conditions

Most coordinated measurements were made between 20.01. and 17.02.20. While the first and last week (20. - 27.01.20 and 10. - 17.02.20) were associated with middle and higher cloud formation and elevated moisture layers, the second and third week (27.01. - 10.02.20) were characterized mainly by shallow convection and low clouds (see Figs. 7 and 8 in Sec. A.1). Using the mesoscale cloud pattern classification by Stevens et al. (2020b), the Sugar and Gravel pattern were prevailing in these weeks with occasional Flower clouds forming. Prevailing cloud types in these weeks were shallow Cumuli forming at LCL, and stratiform outflow layers trapped under the trade inversion, facilitated by the conditions associated with the Flower pattern. While increased moisture and rainfall in the first week was associated with a Fish cloud transporting moisture northwards (see Fig. 9 in Sec. A.1), higher Altocumulus and -stratus clouds formed in the last week of the field study due to enhanced moisture between 3 and 9 km in the dry free troposphere. These different large-scale cloud patterns also were associated with changes in the lower tropospheric humidity profiles as seen in Fig. 10 in Sec. A.1.

Humidity Conditions at BCO

As seen in Sec. A.1 (Stephan et al., 2020) and previously, a variety of synoptic conditions was observed by the upper air sounding network. The temperature and humidity conditions as observed by the soundings launched at BCO during EUREC^{4}A are illustrated in Figs. 3.2a and b. The sub-cloud layer reaching between ground and LCL, usually located between 600 and 800 m (Nuijens et al., 2014), is characterized by an on average well-mixed humidity profile with increasing relative humidity towards cloud base. The trade temperature inversion ranged between 1900 and 2400 m as seen by the decreased temperature gradient in Fig. 3.2b. The temperature profile varied little throughout the lower troposphere, and reached a variability of around 1.5 K between 2000 m to 3000 m. Both the absolute and relative humidity variability as illustrated by the shading in Fig. 3.2a increases particularly in these heights, as the strong humidity gradient associated with the trade inversion changes in altitude depending on the atmospheric conditions.

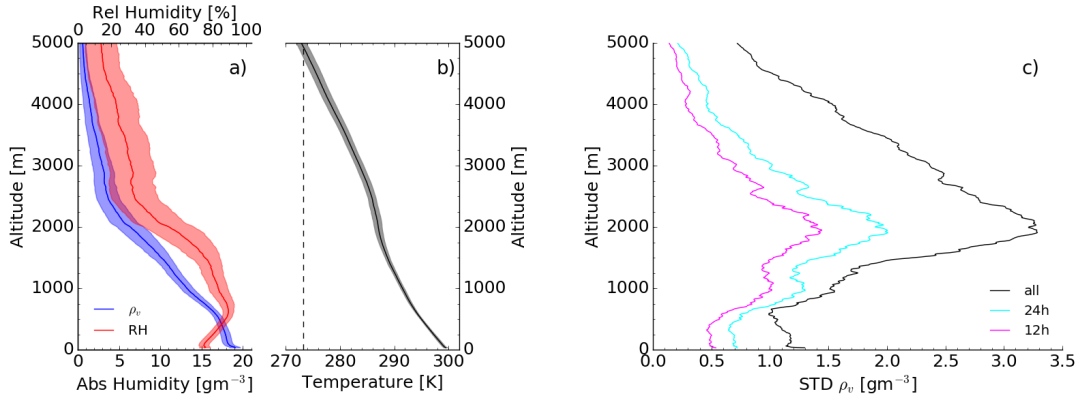

Figure 3.2 – Mean (solid) and STD (shaded) of (a) relative (red) and absolute (blue) humidity and (b) temperature (black) calculated from all 182 ascending soundings at BCO during EUREC^{4}A , as well as (c) standard deviation of absolute humidity profile for all (black) soundings, as well as mean standard deviation in time windows of 12 (magenta) and 24 (cyan) hours.

The absolute humidity profile varied most between 1900 and 2100 m as seen in Fig. 3.2c. The sub-cloud layer as well as the dry free troposphere above 4 km are the least variable over time, with the absolute humidity standard deviation in a 24-hour window reaching 0.5 and 0.7 g m^{-3}, respectively. Local maxima of the variability are observed around LCL and the trade inversion layer, independent of the analyzed time window, reaching a standard deviation of 1.6 and 3.3 g m^{-3} respectively, when considering all soundings. The areas of highest variability correspond to the levels of highest cloud fraction, with shallow boundary layer cloud formation at LCL, as well as stratiform outflow layers trapped under the trade inversion as found in observational (Nuijens et al., 2014) and modelling (Vial et al., 2019) studies.

3.2 Synthetic Observations

Synthetic measurements of MWR K-band TBs and radar reflectivities Z_e at 35.5, 94.0, 167.0, and 174.8 GHz were generated based on the radiative transfer model PAMTRA (Mech et al., 2020). Sounding measurements of pressure, temperature, relative humidity and, in the case of airborne simulations, wind speed, were used to constrain the atmospheric thermodynamic profile input. All forward simulations were made on a height grid resembling a weather model vertical grid which has been used for retrieval studies before (Löhnert et al., 2004), evolving from a 50 – 75 m resolution below 800 m to a lower resolution of 100 – 250 m up to 5000 m, and 500 – 1000 m

up to 20 km. In order to facilitate the positioning of cloud layers, and in order to prevent partially filled radar volumes, cloud base and top heights always correspond to grid levels, and were added to the grid correspondingly. DWR measurements were calculated following Eq. (2.2.9).

All considered liquid cloud Droplet Size Distributions (DSD) were assumed to follow a log-normal distribution with an effective radius r_{eff} of 10 µm and a σ of 0.3, motivated by Miles et al. (2000). Droplet diameters in the liquid DSDs were limited to below 500 µm. Ice hydrometeors such as considered in chapter 5 and Sec. 6.2 were modeled using a mono-disperse particle size distribution (PSD) as used in the ICON model (Mech et al., 2020), parametrized based on the mass mixing ratio input.

The LWP was assumed to be 50 g m^{-2} in case of the single-layered cloud scenario simulated in chapter 4, motivated by typical trade wind conditions as found in Schnitt et al. (2017) and Jacob et al. (2019). In order to account for a more realistic representation of the cloud conditions in chapter 5 for the EUREC^{4}A scenarios, the average BCOHAT LWP around each respective sounding launch was considered. In all simulations, the LWC profile was assumed to be distributed constantly throughout all liquid cloud layers accounting for the high sub-adiabaticity of the observed clouds (Abel and Shipway, 2007). Partitioning of LWP in case of multiple liquid cloud layers was performed based on the depth of each cloud layer. The choice of Ice Water Path (IWP) for scenario 3 simulated in chapter 5 was motivated by the median IWP derived from ICON model runs during the NARVAL studies (personal communication with M. Jacob), and the Ice Water Content (IWC) was kept constant throughout the ice cloud layer.

All simulated measurements were noised by a number generated randomly from a normal distribution with a standard deviation of σ_y and mean value of 0. The MWR TB σ_y was assumed to be 0.4 K in all K-band channels, accounting for radiometric noise and calibration uncertainties (Maschwitz et al., 2013). One random number was generated for each channel. Based on the uncertainties given by the Cloudnet algorithm in comparable scenarios, σ_{Ze} was assumed to be 0.4 dB for all simulated radar frequencies. The same random error was added to Z_e in each range gate. All observations and their associated errors and products are summarized in Tab. 4.1. Full-cloud penetration was assumed in all analyses unless noted differently, as reflectivity thresholds are unique to each respective radar instrument and respective signal processing, and are expected to change with further instrument development. Yet G-band measurements and synergy results are also discussed and evaluated for

a potential radar sensitivity threshold of −50 dBz at 1 km range, motivated by the G-band radar VIPR for 150 m resolution (Roy et al., 2020).

3.3 Optimal Estimation

Background

A remote sensing measurement $\boldsymbol{y}$ is specific to the measured atmospheric state $\boldsymbol{x}$. Assuming a moderately linear forward function F, the state $\boldsymbol{x}$ is mapped to a measurement $\boldsymbol{y}$ by Eq. (3.3.1). $\mathbf{K}$ is called the Jacobian matrix, which elements describe the sensitivity of each $\boldsymbol{y}$ to a certain state $\boldsymbol{x}$: $\mathbf{K}_{mn} = \partial \boldsymbol{y}_{mn}/\partial \boldsymbol{x}_{mn}$ with n and m describing the number of elements in $\boldsymbol{x}$ and $\boldsymbol{y}$, respectively. In microwave radiative transfer applications, the forward mapping can be influenced by a variety of factors, such as the DSD, which are summarized in the forward function parameters $\boldsymbol{b}$

$$\boldsymbol{y} = F(\boldsymbol{x}, \boldsymbol{b}). \tag{3.3.1}$$

Yet the inverse problem of deriving $\boldsymbol{x}$ from a measured $\boldsymbol{y}$ is usually an ill-defined problem.

Bayes' theorem gives the joint probability density function $P(\boldsymbol{x}|\boldsymbol{y})$ given a specific $\boldsymbol{x}$ and a certain measurement $\boldsymbol{y}$ (Eq. (3.3.2)). The joint probability function $P(\boldsymbol{x}|\boldsymbol{y})$ depends on the prior knowledge $P(\boldsymbol{x})$ of the state, the probability function $P(\boldsymbol{y}|\boldsymbol{x})$ of measuring $\boldsymbol{y}$ given $\boldsymbol{x}$, and a scaling constant $P(\boldsymbol{y})$

$$P(\boldsymbol{x}|\boldsymbol{y}) = P(\boldsymbol{y}|\boldsymbol{x})P(\boldsymbol{x})/P(\boldsymbol{y}). \tag{3.3.2}$$

The optimal estimation (OE) equations (Rodgers, 2000) can be derived from Bayes' theorem when assuming Gaussian probability distribution functions for $P(\boldsymbol{x}|\boldsymbol{y})$, $P(\boldsymbol{x})$ and $P(\boldsymbol{y}|\boldsymbol{x})$. In case of Gaussian probability distributions, the prior state $\boldsymbol{x}_a$ is associated with a covariance $\mathbf{S}_a$, and the measurement $\boldsymbol{y}$ is associated with the measurement covariance matrix $\mathbf{S}_e$. The Gaussian solution function $P(\boldsymbol{x}|\boldsymbol{y})$ can then be described by the covariance $\mathbf{S}_{op}$ (Eq. (3.3.3)), and the expected value, which in the Gaussian case equals the most probable state $\boldsymbol{x}_{op}$ (the *solution*)

$$\mathbf{S}_{op} = \mathbf{S}_a - \mathbf{S}_a\mathbf{K}^T \cdot (\mathbf{S}_e + \mathbf{K}\mathbf{S}_a\mathbf{K}^T)^{-1} \cdot \mathbf{K}\mathbf{S}_a. \tag{3.3.3}$$

The most probable solution, i.e. the maximum of $P(\boldsymbol{x}|\boldsymbol{y})$, is located at a local minimum of the derivative of Eq. (3.3.2). Replacing $P(\boldsymbol{x})$, $P(\boldsymbol{y}|\boldsymbol{x})$ and $P(\boldsymbol{y})$ with their respective Gaussian distribution function gives Eq. (3.3.4), which is referred to as the cost function

$$\begin{aligned}\frac{\partial P(\boldsymbol{x}|\boldsymbol{y})}{\partial \boldsymbol{x}} &= \frac{\partial}{\partial \boldsymbol{x}}[\boldsymbol{y} - F(\boldsymbol{x}, \boldsymbol{b})]^T \cdot \mathbf{S}_e^{-1} \cdot [\boldsymbol{y} - F(\boldsymbol{x}, \boldsymbol{b})] + [\boldsymbol{x} - \boldsymbol{x}_a]^T \cdot \mathbf{S}_a^{-1} \cdot [\boldsymbol{x} - \boldsymbol{x}_a] \\ &= 0.\end{aligned} \tag{3.3.4}$$

Solving Eq. (3.3.4) gives the most probable solution $\boldsymbol{x}_{op}$ through Eq. (3.3.5), which is physically consistent with the measurement $\boldsymbol{y}$, the associated measurement errors $\mathbf{S}_e$, as well as the prior state $\boldsymbol{x}_a$ and its covariance $\mathbf{S}_a$. In order to find the numerical solution $\boldsymbol{x}_{op}$ to this minimization problem, Eq. (3.3.5) is iterated with i as iteration parameter, until convergence is found

$$\boldsymbol{x}_{i+1} = \boldsymbol{x}_a + (\mathbf{S}_a\mathbf{K}_i^T \cdot (\mathbf{K}_i\mathbf{S}_a\mathbf{K}_i^T + \mathbf{S}_e)^{-1} \cdot (\boldsymbol{y} - F(\boldsymbol{x}_i, \boldsymbol{b}) + \mathbf{K}_i \cdot (\boldsymbol{x}_i - \boldsymbol{x}_a))). \tag{3.3.5}$$

Here, convergence is found if the step size of the forward-modeled measurements $F(\boldsymbol{x}_{i+1}, \boldsymbol{b}) - F(\boldsymbol{x}_i, \boldsymbol{b})$ is an order of magnitude smaller than its estimated uncertainty $\mathbf{S}_{\delta y}$ (Eq. (3.3.6); Rodgers, 2000, Sec. 5.6.3)

$$\mathbf{S}_{\delta y} = \mathbf{S}_e \cdot (\mathbf{K}\ \mathbf{S}_a\mathbf{K}^T + \mathbf{S}_e)^{-1} \cdot \mathbf{S}_e. \tag{3.3.6}$$

True convergence can be verified based on a χ^2 test. The null hypothesis describes that δ_y is a member of a Gaussian distribution characterized by a covariance $\mathbf{S}_{\delta y}$ and a mean of zero (see Rodgers, 2000, Sec. 12.3.2). A true test verifies that the null-hypothesis cannot be rejected with a significance level of 95 %. In that case, $\boldsymbol{x}_i = \boldsymbol{x}_{op}$.

The sensitivity of the retrieved state $\boldsymbol{x}_{op}$ to the real atmospheric state $\boldsymbol{x}$ is given by the Averaging Kernel matrix $\mathbf{A}$ (Eq. (3.3.7); Rodgers, 2000, Sec. 2.4.2). The Degrees of Freedom for Signal (DFS), that is the number of independent pieces of information of a measurement used for signal, can be derived as the trace of the Averaging Kernel (Eq. (3.3.8)).

$$\mathbf{A} = \mathbf{S} \cdot (\mathbf{K}^T \mathbf{S}_e^{-1} \mathbf{K}) \tag{3.3.7}$$

$$\mathrm{DFS} = \mathrm{trace}(\mathbf{A}) \tag{3.3.8}$$

The DFS as well as the retrieval uncertainty, that is the square root of the $\mathbf{S}_{op}$ diagonal elements, can be used as a mean to evaluate the retrieval performance. Therefore, optimal estimation retrievals provide the necessary framework to evaluate synergistic measurement combinations of active and passive remote sensing instruments to retrieve profiles of liquid cloud water (e.g. Löhnert et al., 2001), humidity and temperature profiles (e.g. Löhnert et al., 2009), or PSDs (e.g. Posselt et al., 2017). The synergistic impact is evaluated by comparing the retrieval results using the synergistic observation vector to the results when only the single instruments are used as measurements.

Setup and Parameters

The synergy algorithm developed in this thesis is based on the optimal estimation core routines made available by Maahn et al. (2020)[2]. With the OE equations at its core, the algorithm is structured such that the user can modify various OE and measurement related parameters through a control-file. The forward model PAMTRA (Mech et al., 2020) is integrated as forward function F, and is called in order to derive the Jacobian $\mathbf{K}$ in each iteration step. The state vector $\boldsymbol{x}_i$ comprises the absolute humidity on each level defined in the height grid used for the synthetic observations (see Sec. 3.2), decreasing in resolution with height. As the OE equations require a quasi-normal distribution of the states, the natural logarithm of the absolute humidity was retrieved (Maahn et al., 2020). The observation vector $\boldsymbol{y}$ comprised of the seven MWR HATPRO K-band TBs, DWR in each layer within the cloud boundaries, and the 2 m absolute humidity measurement ρ_{2m}, depending on the respective retrieval configuration. The synergistic retrieval configuration included all observations, whereas the MWR-only and DAR-only configurations combined $\rho_{2\mathrm{m}}$ with the MWR TBs or the DWRs, respectively. Depending on the specific cloud scenario and location, the number of DWR measurements varied correspondingly.

[2]For this work, a code version from September 2017 has been used and further customized.

Within each forward function call, PAMTRA needs profiles of pressure, relative humidity and temperature as input to generate the TBs and Z_es. Temperature and pressure profiles are taken from the radiosonde that was used to initially generate the synthetic observations, while the relative humidity profile is calculated based on the temperature profile and the respective state $\boldsymbol{x}_i$ in each forward function call. Cloud microphysical parameters like r_{eff}, DSD, maximal diameter and LWC used for the synthetic observations are included through the forward parameters $\boldsymbol{b}$. An estimation of the forward model parameter error introduced this way is given in Sec. 4.5.2. In order to account for the liquid attenuation particularly in the Ka- and W-band reflectivities, LWP was added to the state vector $\boldsymbol{x}$ in the feasibility study presented in chapter 4. In the setup used in chapter 5, G-band reflectivities were simulated, and liquid attenuation was estimated from LWP set as forward parameter.

The prior state $\boldsymbol{x}_a$ and its associated covariances $\mathbf{S}_a$ were derived using operational soundings launched at GAIA. More specifically, for the analyses in chapter 4, soundings launched between 2002 and 2017 were used to calculate $\boldsymbol{x}_a$ and $\mathbf{S}_a$ for the dry and wet seasons including December to May and June to November, respectively (Stevens et al., 2017). Quality control excluded soundings that did not reach 20 km altitude, or where the recorded pressure, temperature or humidity profiles were not complete, resulting in 1862 and 2758 available soundings for the dry and wet season, respectively (also see Sec. 4.2.2). In order to further condition the prior to the expected conditions observed during EUREC^{4}A, the prior used in chapter 5 was further customized to include only soundings launched in the months of January and February. In order to expand the statistical sample, soundings launched between 1990 and 2017 were used.

The measurement errors defining the diagonal elements of the $\mathbf{S}_e$ matrix are set to the squared σ_y defined as measurement uncertainties in Sec. 3.2. For the MWR TBs, uncertainties of $\sigma_{TB} = 0.4\,\text{K}$ are assumed. The DWR measurement error was calculated based on error propagation laws of the σ_{Ze} with $\sigma_{DWR} = 0.56\,\text{dB}$. The $\rho_{2\text{m}}$ uncertainty was assumed to be a 10 and 3 % relative error in chapter 4 and chapter 5, respectively. All measurement uncertainties are assumed to be uncorrelated. Sensitivities of the retrieval concept to the assumed measurement uncertainties σ_y as well as forward model parameters $\boldsymbol{b}$ are analyzed in Sec. 4.5.2.

In the following analyses, evaluation of the retrieved state is performed based on the discrepancy between sounding reality and the retrieved profile $\boldsymbol{x}_{op}$ (chapter 4), as well as the partial water vapor amount below, in, between and above all respective cloud

layers (chapter 5). Furthermore, the information content available to the retrieval, quantified through the DFS, and the retrieval uncertainty calculated from $\mathbf{S}_{op}$ are quantified to evaluate the synergy potential. Synergistic benefits are analyzed based on running the retrieval in the synergy configuration, that is an observation vector including all measurements, and in the respective observation vector configurations only including the respective single instrument's measurements.

4 Study 1: Assessing Synergy Potential and Sensitivities in Single-Layered Cloud Conditions

The following chapter presents a feasibility study to analyze the synergistic benefits of combining MWR and dual-frequency radar measurements based on a synthetic single-layered cloud scenario. Simulated observations of MWR and two radar frequency pairs are analyzed: a KaW combination, available e.g. at BCO, and a combination of G-band frequencies available in the VIPR-instrument prototype. The synergistic benefits of the MWR and radar, MWR-only and radar-only retrieval configurations are analyzed for both frequency pairs based on the respective retrieved profile, retrieval uncertainty and information content, assessing research question 1. These benefits will be assessed regarding various sources of uncertainties, as summarized in research question 2.

Remarks and Contributions

All analyses and text presented in the following chapter have been accepted as Schnitt et al. (2020).

Sabrina Schnitt took the leading role in conducting the presented analysis, preparing and processing all graphics, and writing the manuscript. SaS and UL conceptualized this study. Both UL and RP provided support in the editing and review process of the manuscript.

Contextualization

The following analyses present the potential of combining MWR and dual-frequency radar for a single-cloud scenario under varying water vapor conditions as frequently observed at BCO. The synergistic benefits of two radar frequency pairs, namely KaW and G2, were analyzed based on synthetic observations. An optimal estimation algorithm was used to retrieve the absolute humidity profile, and to compare the retrieval uncertainties and information content for the synergistic, MWR-only and radar-only observation vector configurations. The analyses revealed larger synergistic benefits in case of a MWR+G2 synergy compared to the MWR+KaW combination, as the total information content increases by 38.7 % and 5.3 %, respectively, compared to the MWR-only approach. One cause is the increased sensitivity to water vapor conditions in the differential radar signal using the G2 frequency pair, while the KaW differential signal is affected by the ambiguity of liquid and water vapor attenuation. Referring to research question 1, the synergistic benefit is revealed above the cloud layer where the synergistic information content is enhanced on average by 0.2 DFS compared to the MWR-only retrieval, even though the DAR observations do not provide any information. This increase of information content goes along with decreasing retrieval uncertainties of up to $0.2\,\mathrm{g\,m^{-3}}$ above cloud top. Below and in the cloud layer, the profile, retrieval uncertainty and information content are guided by the DAR observations, leading to a 28 % uncertainty reduction compared to the MWR-only configuration. The revealed synergistic benefits are sensitive to the assumed measurement uncertainties (see research question 2). Largest impacts are seen when the radar uncertainties are varied, as a doubling of the DWR uncertainty to 1.1 dB increases the sub- and in-cloud uncertainty by $0.1\,\mathrm{g\,m^{-3}}$, while assuming perfect channel intercalibration decreases the retrieval uncertainty by $1.0\,\mathrm{g\,m^{-3}}$ right below cloud top compared to the initial MWR+G2 configuration. While full-cloud profiling was assumed in the whole study, current G-band radar sensitivity thresholds might limit the profiling to only parts of the cloud layer, or lead to signal saturation before reaching cloud base. In this case, the synergistic benefits are reduced, depending on where the sensitivity limit is reached.

As discussed in Sec. 4.6, this potential analysis can be extended in many ways. While the MWR+KaW concept seems to be promising e.g. for a synergistic LWC-retrieval, the MWR+G2 water vapor retrieval will be extended in the following chapter 5 to more complex cloud scenarios as observed during the EUREC^{4}A field study. Therein, the presented three selected cases were chosen to represent the

expected variability of water vapor and cloud conditions at BCO in trade wind driven synoptic conditions occurring during the dry season. Real BCO observations will be used to constrain the simulated observations to reality as much as possible.

4.1 Introduction

Water vapor is the driving constituent of the global hydrological cycle, and cloud and precipitation formation. It plays a key role in the characterization of the global radiation budget (Held and Soden, 2006; Hartmann et al., 2013). In the trades, the maximum variability of atmospheric water vapor is found in the lower part of the troposphere within the boundary layer where it influences shallow convection, cloudiness, and circulation processes (Holloway and Neelin, 2009; Sherwood et al., 2010). Thus, precise observations of the low-tropospheric moisture structure in trade wind driven regions are particularly important to better understand the mechanisms controlling shallow convection, the intensity of cloud feedbacks and, hence, climate sensitivity (Pincus et al., 2017; Nehrir et al., 2017).

Currently, profiles of the atmosphere are available through the operational radiosonde network with ascents typically every 6, 12 or 24 hours. However, these observations are not only sparse in temporal and spatial resolution, but also expensive in operation (e.g. Nehrir et al., 2017). Spaceborne sensors provide broad global coverage, but lack the horizontal and vertical resolution needed for quantifying processes in the boundary layer (Ebell et al., 2013; Stevens et al., 2017; Schröder et al., 2019). Ground-based microwave remote sensing instruments are a promising alternative to these methods (Westwater et al., 2004), as the atmosphere is semi-transparent in the microwave spectral region. Passive microwave radiometers (MWRs) and radars can, thus, penetrate clouds and measure in clear, cloudy, and, in case of the radar, precipitating conditions. MWRs, such as the Humidity And Temperature PROfiler (HATPRO; Rose et al., 2005), accurately provide integrated quantities such as Integrated Water Vapor (IWV) and Liquid Water Path (LWP), and, using the different weighting functions of the channels, can be used for deriving temperature and humidity profiles (Crewell and Löhnert, 2007). However, the profiles' vertical resolution, which reaches about 1 km at 500 m height, further degrades with height and is too low to accurately quantify the before-mentioned processes. On the other hand, active instrument measurements, such as by the lidar or radar, are characterized by high vertical resolutions, but need backscattering targets like

aerosols or cloud droplets to gain information about the profile of the atmosphere. In case of the lidar, a profile can only be derived below cloud base, as the signal is saturated within the cloud layer.

Compensating for disadvantages of each individual instrument, synergistic retrieval approaches that combine passive and active remote sensing instruments increase the information content about the state of the atmosphere (e.g. Stankov, 1998; Löhnert et al., 2001; Wagner et al., 2018). Synergistic ground-based water vapor retrievals have thus far been developed using the combination of various remote sensing instruments: e.g. MWR and lidar (Barrera-Verdejo et al., 2016; Foth and Pospichal, 2017), infrared hyperspectrometer and MWR (Turner and Löhnert, 2014), or MWR, ceilometer, and Ka-band radar (Löhnert et al., 2004). Optimal estimation-based retrieval algorithms provide the necessary framework for data evaluation (Rodgers, 2000; Maahn et al., 2020).

The potential of dual-frequency radar for water vapor profiling has been previously explored using the difference in water vapor continuum absorption (Ellis and Vivekanandan, 2010; Tian et al., 2007), and frequencies in the 183.31 GHz band (Battaglia et al., 2014; Battaglia and Kollias, 2019). Analog to the Differential Absorption Lidar (DIAL) technique, Differential Absorption Radar (DAR) uses one radar frequency close to the absorption line's center (*online*), and a second frequency on the complex's wing (*offline*). Evaluating the Dual-Wavelength Ratio (DWR), i.e. the difference between the logarithmic equivalent reflectivity factors, gives information about the partial integrated water vapor amounts along the ray path. Due to the difference of water vapor attenuation in the two frequencies, the partial water vapor amount can be derived between radar and the backscattering volumes (Lebsock et al., 2015; Millán et al., 2016) . Only recently, Roy et al. (2020) presented the Vapor In-cloud Profiling Radar (VIPR), the first ground-based DAR system operating at 167 and 174.8 GHz along the wing of the 183.31 GHz absorption line. With the VIPR-system, the water vapor profile throughout the cloud layer can be retrieved with an uncertainty of smaller than $1\,\mathrm{g\,m^{-3}}$.

In this paper, we assess the synergistic benefits of a combined retrieval of dual-frequency radar and MWR for a typical trade wind driven cloud scene. We analyze a combination of synthetic ground-based MWR K-band brightness temperatures (TBs) with simulated differential radar signals for two frequency pairs: the Ka- and W-band frequencies at 35.5 and 94 GHz, later referred to as KaW, which are available at e.g. at the Barbados Cloud Observatory (BCO; Stevens et al.,

2016); and a hypothetical G-band frequency combination motivated by the novel VIPR instrument with frequencies at 167 and 174.8 GHz, in the following referred to as G2. The resulting DWR of these two frequency pairs is mainly affected by different absorption features due to their location in the microwave spectrum. In case of KaW, the DWR signal is driven by differential continuum absorption, including contributions due to water vapor as well as liquid water; in case of G2, the signal is mainly affected by the difference in absorption strength on the absorption line wing at 183.31 GHz.

As observations of both frequency pairs are not available for simultaneous cases, we use synthetic observations generated by the Passive and Active Microwave TRAnsfer model (PAMTRA; Mech et al., 2020). Specifically, we simulate radar reflectivities at Ka-, W-, and G2 frequencies, as well as of the MWR TBs in the seven HATPRO K-band channels distributed between 22.24 and 31.4 GHz. Then, we apply an optimal estimation algorithm to these observations to retrieve the column water vapor profile as well as the LWP. To assess the synergistic benefits of this novel approach, we vary the constellation of the observation vector using MWR-only TBs; radar-only DWRs; and the combination of both. DWR is analyzed for both KaW and G2 frequency pairs. In all configurations, a 2 m humidity observation is used to constrain the retrieval. The synergistic benefit is evaluated based on the total Degrees of Freedom of Signal (DFS; Rodgers, 2000) and the resulting retrieval error, and compared to the results of the MWR-only and radar-only retrieval.

The paper is organized as follows: the instruments, the simulation method, and the retrieval concept are introduced in Sec. 4.2. The synthetic observations, their sensitivity to varying water vapor and liquid water conditions, as well as limitations due to radar detection thresholds are presented in Sec. 4.3. Based on a typical case study example, we analyze the synergistic retrieval potential in Sec. 4.4. Expanding the results of the case study to a larger number of scenes, Sec. 4.5 quantifies the synergistic benefits compared to the MWR-only and radar-only retrievals, underlining differences between the two radar frequency pairs. Furthermore, sensitivities to assumed observation and forward model uncertainties are analyzed, and the impacts of radar sensitivity thresholds on the retrieval are discussed. Section 4.6 summarizes the findings, and gives an outlook on future application potential of this novel approach.

4.2 Synergy Concept and Algorithm Methodology

4.2.1 Instruments and Observation Simulations

Exposed to the North Atlantic trade winds, BCO is located at the eastern point of the Barbados island (Stevens et al., 2016). Observing trade wind clouds since 2010, the observatory is equipped with a suite of state-of-the art remote sensing instruments, including a W-band radar recently complementing the suite.

The microwave radiometer HATPRO measures incoming radiation in 14 channels distributed throughout the lower microwave spectrum. In this work, we use the brightness temperature of the 7 water vapor sensitive K-band channels. Six of these channels are located in the center and on the wing of the water vapor absorption line at 22.24 GHz. IWV and LWP can be retrieved when including the measurements of a window channel located at 31.4 GHz. As the opacity of the atmosphere increases towards the absorption line center, the K-band HATPRO TBs can also be used for humidity profiling, such as described in e.g. Löhnert et al. (2009). Water vapor profiles can be retrieved with an uncertainty of about $1\,\mathrm{g\,m^{-3}}$, a temporal resolution of 2 to 4 seconds, and a vertical resolution of 1 to 2 km, degrading with height. Two to three independent pieces of information can be derived. Due to the limited vertical resolution of the retrieved profile, retrievals based on only MWR observations are not able to resolve strong humidity gradients typical for the trade wind driven atmosphere observed e.g. at BCO.

Cloud radars can profile the atmosphere reaching increased vertical resolutions. One of the measured quantities, the equivalent radar reflectivity factor Z_e (further referred to as reflectivity), depends on the scatterer's diameter to the power of six when Rayleigh-scattering only is assumed. The observed Z_e is further affected by two-way attenuation due to gas and hydrometeor extinction along the beam path. Microwave attenuation is frequency-dependent: liquid water and water vapor attenuation generally increase with frequency (continuum absorption), and attenuation due to water vapor is particularly enhanced within the water vapor absorption lines around 22.24 and 183.31 GHz. Further attenuation can occur due to other atmospheric gases like oxygen and nitrogen, which, in the G-band, is smaller than the attenuation due to water vapor. Attenuation is also influenced by the broadening of the absorption lines due to temperature and pressure changes.

The DAR technique, in analogy to the DIAL technique, makes use of the frequency dependent difference in radar attenuation described by the Dual-Wavelength Ratio (DWR [dB] = Ze_1 [dBz] - Ze_2 [dBz]) when locating one frequency near the absorption line center (*online*) and one on the absorption line wing (*offline*). According to Lebsock et al. (2015) and Millán et al. (2016), the differential signal can be related to the amount of water vapor located between the radar and the target when neglecting multiple scattering; assuming that water vapor absorption is order of magnitudes stronger than absorption due to other gases; and when neglecting the temperature and pressure dependency. However, this relation is only valid if non-Rayleigh-scattering either does not impact the reflectivity signal, or if it impacts Z_e of both frequencies the same way. The former we can assume for the pure liquid clouds observed at BCO in case of the MWR and KaW signals; the latter we assume for the frequencies used in the G-band.

Whereas typical Ka-band radars are pulsed radar systems, W-band radar systems typically are nonpulsed frequency modulated continuous wave (FMCW) radars (see e.g. Küchler et al., 2017). Due to the FMCW principle, the vertical resolution, sensitivity, and Nyquist velocity are height-dependent and can be adjusted through the chirp table settings. At BCO, these settings are chosen such that the range bins of the two radar systems match with a vertical resolution of 30 m throughout the boundary layer. With this range resolution, the pulsed Ka-band radar system reaches a sensitivity threshold of −69 dBz at 1 km height (Görsdorf et al., 2015). Typical W-band settings at BCO lead to a detection threshold of −51 dBz at 1000 m, operating with an integration time of 0.9 s.

Roy et al. (2020) present the first operational G-band DAR system and a least-squares inversion method to derive the water vapor profile throughout the cloud layer. With a system output power of 0.2 W, a range resolution of 15 m and a nominal chirp duration time of 1 ms, VIPR reaches a single-pulse reflectivity detection threshold of −40 dBz at 1000 m. Decreasing the vertical range resolution to 150 m would lead to a sensitivity improvement of 10 dB to −50 dBz (personal communication R. Roy). Non-coherent signal processing would similarly improve the detection sensitivity while decreasing the temporal resolution.

Using the profiling capabilities of the dual-frequency radar, as well as the advantages of the MWR, a synergy concept such as illustrated in Figure 4.1 promises increasing information content compared to a MWR-only or radar-only retrieval setup. In the instrument synergy, the MWR provides information about the full-column

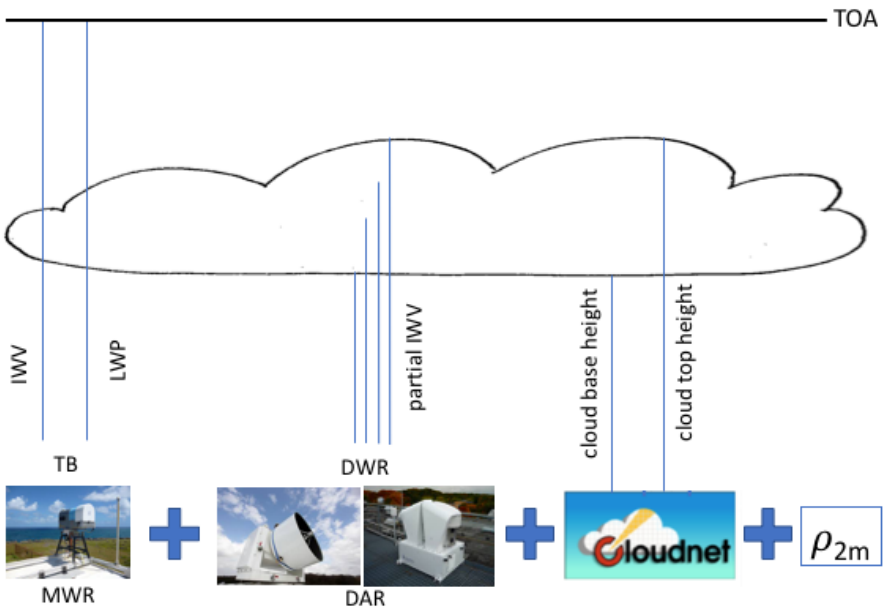

Figure 4.1 – Concept, instruments and their observations used in the synergistic retrieval approach: MWR brightness temperature TB for IWV, LWP, coarse water vapor profile; DWR for partial IWV quantification below cloud base and in-cloud profiling; cloud base and top height provided by e.g. Cloudnet (Illingworth et al., 2007); and 2 m humidity ρ_{2m} observations. Blue lines represent the vertical range of the instruments' observations.

water vapor path, the LWP, and a coarse water vapor profile throughout the whole atmospheric column. The dual-frequency radar observations provide information about the partial water vapor amounts between each backscattering volume. Thus, the amount of partial water vapor located between ground and cloud base can be derived, as well as a finely resolved water vapor profile within the cloud layer. In this retrieval approach, we assume that cloud base and top height observations and 2 m humidity observations are available, for example through Cloudnet observations, and use this extra information to constrain the retrieval.

We present a feasibility study based on simulated observations to test the retrieval concept under ideal conditions, as simultaneous observations of all considered instruments are not available. By simulating the instruments' observations, unknown instrument uncertainties or biases of real observational data are eliminated, and a fair comparison between all different retrieval setups and both frequency pairs is possible. The radiative transfer model PAMTRA is used to simulate MWR TBs and radar reflectivity factor Z_e. In order to model a typical single-layered liquid trade wind cumulus cloud scenario, we use quality-controlled pressure, temperature, and relative humidity profiles of the 00 and 12 Z radiosondes launched

at Grantley Adams International Airport (`http://weather.uwyo.edu/upperair/sounding.html`), approximately 15 km southwest of BCO. We only consider soundings that reached 20 km altitude, and have complete pressure, temperature, and humidity profiles. The lowest available humidity measurement of each radiosonde profile is assumed as 2 m humidity observation.

Specifically, we assign a LWP of $50\,\mathrm{g\,m^{-2}}$ to the cloud layer as motivated from previous studies analyzing the distribution of LWP in trade wind driven conditions around Barbados (e.g. Jacob et al., 2019; Schnitt et al., 2017). Due to the high sub-adiabaticity of these clouds (e.g. Abel and Shipway, 2007), we distribute the LWP such that the Liquid Water Content (LWC) is constant with $0.05\,\mathrm{g\,m^{-3}}$ throughout the cloud layer. Simulating typical cloud conditions observed at BCO (e.g. Nuijens et al., 2014), cloud base and top height are assumed to be 1000 and 2000 m, respectively. We assume a cloud droplet effective radius (r_{eff}) of 10 µm, and a log-normal droplet size distribution (DSD) with a shape parameter σ of 0.3 (Miles et al., 2000). Using this simplified approach, we neglect potential challenges due to non-Rayleigh-scattering of drizzle or ice particles affecting the radar observations. The sensitivity of our results to the assumed cloud parameters is analyzed in Sec. 4.5.2.

To model expected measurement uncertainties, we add a random Gaussian noise to each simulated measurement. We assume a TB accuracy of 0.4 K for all seven K-band channels taking into account uncertainties due to radiometric noise and calibration (Maschwitz et al., 2013). For the radar reflectivities, we assume an uncertainty of 0.4 dB for all frequencies and heights, based on the errors given by the Cloudnet algorithm (Illingworth et al., 2007) in comparable situations. All considered measurements and their assumed characteristics are summarized in Tab. 4.1.

4.2.2 Optimal Estimation Methodology

Finding a solution to linking an atmospheric state $\boldsymbol{x}$ to a remote sensing measurement $\boldsymbol{y}$ by $\boldsymbol{x} = F^{-1}(\boldsymbol{y})$ is typically an ill-posed problem. Hence, multiple atmospheric states $\boldsymbol{x}$ can lead to the same observation $\boldsymbol{y}$. Bayes' theorem manifests a general way of finding the most probable solution considering $\boldsymbol{y}$ and a given prior state. The optimal estimation equations derived by Rodgers (2000) fulfill this theorem, assuming a moderately non-linear forward function $F(\boldsymbol{x})$, and given that the uncertainties of $\boldsymbol{x}$ and $\boldsymbol{y}$ follow a Gaussian distribution. The prior state $\boldsymbol{x}_a$ and its covariance matrix $\mathbf{S}_a$ constrain the solution in state space while the solution is physically consistent:

Table 4.1 – Characteristics of Observations. The observations forming the OE observation vector are highlighted in bold-print. Radar sensitivity thresholds are given at 1 km height for a 30 m (Ka, W) and 150 m (G2) vertical resolution, and an integration time of 0.9 s (W) and 1 ms (G2), respectively.

	MWR	dual-frequency radar				2m
	HATPRO	Ka	W	G2		humidity
Channels [GHz]	22.24, 23.44 23.84, 25.44 26.24, 27.84 31.4	35.5	94.0	167.0	174.8	
Measurement	Brightness Temperature **TB**	Equivalent Reflectivity Factor (Z_e [dBz]); **DWR** [dB]				$\rho_{\mathbf{2m}}$
Uncertainty	0.4 K	$\Delta Z_e = 0.4$ dB ΔDWR $= 0.56$ dB				10 %
Sensitivity 1 km		−69 dBz	−51 dBz	−50 dBz		

applying the forward function to the retrieved state $\boldsymbol{x}$ leads to the original observation $\boldsymbol{y}$ within the corresponding measurement uncertainties given by the error covariance matrix $\mathbf{S}_e$ and the prior covariance matrix $\mathbf{S}_a$.

The optimal solution $\boldsymbol{x}_{op}$ is found when iterating Eq. (4.2.1) until a minimum of the cost function is found and convergence is reached

$$\boldsymbol{x}_{i+1} = \boldsymbol{x}_a + (\mathbf{S}_a\mathbf{K}_i^T \cdot (\mathbf{K}_i\mathbf{S}_a\mathbf{K}_i^T + \mathbf{S}_e)^{-1} \cdot (\boldsymbol{y} - F(\boldsymbol{x}_i) + \mathbf{K}_i \cdot (\boldsymbol{x}_i - \boldsymbol{x}_a))). \quad (4.2.1)$$

The Jacobian matrix $\mathbf{K}_i$ gives the sensitivity of each observation to each changing state, and is calculated per retrieval iteration.

$$\mathbf{S}_i = \mathbf{S}_a - \mathbf{S}_a\mathbf{K}_i^T \cdot (\mathbf{S}_e + \mathbf{K}_i\mathbf{S}_a\mathbf{K}_i^T)^{-1} \cdot \mathbf{K}_i\mathbf{S}_a \quad (4.2.2)$$

The diagonal elements of the a posteriori retrieval error matrix $\mathbf{S}_{op}$ give the uncertainty of each retrieved state, and depend on the prior covariances $\mathbf{S}_a$, the Jacobian matrix $\mathbf{K}_i$, and the error covariances $\mathbf{S}_e$. Here, $\mathbf{S}_e$ includes uncertainties from observations, as well as the forward model parameters.

Retrieval convergence requires the residuum of $\boldsymbol{y}_{i+1} - \boldsymbol{y}_i$ to be an order of magnitude smaller than the estimated error given by the a posteriori covariance matrix $\mathbf{S}_{op}$ of

the derived state $\boldsymbol{x}_{op}$ (Eq. (4.2.2)). Whether the converged solution $\boldsymbol{x}_{op}$ is physically consistent can be tested with a χ^2-test (e.g. Rodgers, 2000; Ebell et al., 2017). A true test verifies, here with a significance level of 95 %, that the null-hypothesis cannot be rejected. In other words, true convergence is reached if the distribution of the difference δ_y between forward-modeled retrieval results $F(\boldsymbol{x}_{op})$ and original observations $\boldsymbol{y}_{obs}$ is a member of a Gaussian distribution with zero mean and covariance of $\mathbf{S}_{\delta_y} = \mathbf{S}_e \cdot (\mathbf{K}\mathbf{S}_a\mathbf{K}^T + \mathbf{S}_e)^{-1} \cdot \mathbf{S}_e$.

The Averaging Kernel Matrix $\mathbf{A}$ describes the sensitivity of the retrieved state $\boldsymbol{x}_{op}$ to the original state following $\mathbf{A}_i = \mathbf{S}_i(\mathbf{K}_i^T\mathbf{S}_e^{-1}\mathbf{K}_i)$. The diagonal elements of $\mathbf{A}$ provide the DFS, that is the independent pieces of information, per retrieved state element; the trace of $\mathbf{A}$ gives the total DFS, describing the total information content available in the retrieval.

In the presented retrieval approach, the state vector $\boldsymbol{x}$ consists of absolute humidity on 45 height levels with decreasing vertical resolution, and the LWP. We retrieve the natural logarithm of the absolute humidity in order to maintain a quasi-Gaussian distribution of the retrieval states. The retrieved LWP is used to calculate the liquid attenuation of the radar signal in each retrieval iteration. In this paper, the observation vector $\boldsymbol{y}$ comprises the seven HATPRO K-band brightness temperatures, complemented by the 2 m humidity observation, as well as the DWR calculated in each layer within the cloud boundaries. For the cloud scene simulated in this study, seven DWR observations were included with a vertical spacing of 150 to 200 m. Linking the observations $\boldsymbol{y}$ with the state vector $\boldsymbol{x}$, the radiative transfer model PAMTRA (Mech et al., 2020) is used as forward function $F(\boldsymbol{x})$.

In order to find a consistent solution, the prior profile should represent the natural atmospheric conditions around Barbados. Therefore, we built an absolute humidity profile prior climatology from all operationally available radiosonde ascents launched at 00Z or 12Z at Grantley Adams International Airport located 30 km southwest of BCO from 2002 until 2017. We control the sounding quality by excluding sondes with incomplete temperature, pressure or relative humidity measurements, as well as those not reaching 20 km height, and, hence, consider 4620 sondes. The prior state and covariance are derived for the dry and the wet season, respectively, as described in Stevens et al. (2017). 1862 sondes are available for the dry season in December through May, and 2758 sondes for the wet season stretching from June through November. As in the approach presented by Turner and Löhnert (2014), the prior

LWP is assumed to be $0\,\mathrm{g\,m^{-2}}$ with a variance of $50\,\mathrm{g\,m^{-2}}$, excluding correlations with the water vapor states. Here, the prior state is also used as first guess.

We assume that the measurement errors are uncorrelated, and use a TB uncertainty of $\Delta\mathrm{TB} = 0.4\,\mathrm{K}$ in each of the microwave channels, and a Z_e uncertainty of $\Delta Z_e = 0.4\,\mathrm{dB}$ for all radar frequencies (see Sec. 4.2.1). According to error propagation, the un-correlated Z_e errors lead to a DWR uncertainty of 0.56 dB. The 2 m humidity measurement $\rho_{2\mathrm{m}}$ is assumed to be affected by a 10 % relative error. For simplicity reasons, we neglect possible errors due to forward model assumptions like the DSD parameters, the effective radius or the LWC profile shape, but give estimates of the sensitivity of our results to these parameters, as well as the assumed measurement uncertainties ($\mathbf{S}_e$) and prior covariances ($\mathbf{S}_a$) in Sec. 4.5.2.

In the following analyses, we will use three criteria to estimate the quality of the retrieved profile $\boldsymbol{x}_{op}$, and to quantify the synergistic benefit: the DFS; the a posteriori error of each state, given by the diagonal entries of the $\mathbf{S}_{op}$ matrix; and the comparison of the retrieved profile to the original radiosonde absolute humidity profile used to generate the synthetic observations.

4.3 Synthetic Observations

Synthetic observations of MWR K-band TBs and radar reflectivities Z_e for Ka-, W-, and G2 were generated by forward simulating 633 quality-controlled radiosonde profiles from 2018, using the method described in Sec. 4.2.1.

All simulated radar reflectivities as well as the resulting DWRs are presented as function of height above cloud base in Fig. 4.2. Shown are the attenuated reflectivities, that is the 2-way attenuation of the signal due to liquid and water vapor attenuation along the path subtracted from the un-attenuated simulated reflectivity. The DWR were calculated for the KaW and G2 combination by subtracting the respective reflectivities from another. A random measurement error was added to the simulated Z_e as described in Sec. 4.2.1.

The reflectivity in each frequency decreases with height due to cumulating water vapor and liquid attenuation along the ray path. The attenuation strength depends on the frequency, and is strongest nearest the water vapor absorption line at 183.31 GHz. Thus, between 1000 and 2000 m, Ka and W-band reflectivities only decrease by less than 1 dB due to continuum absorption, whereas the G-band reflectivities, located

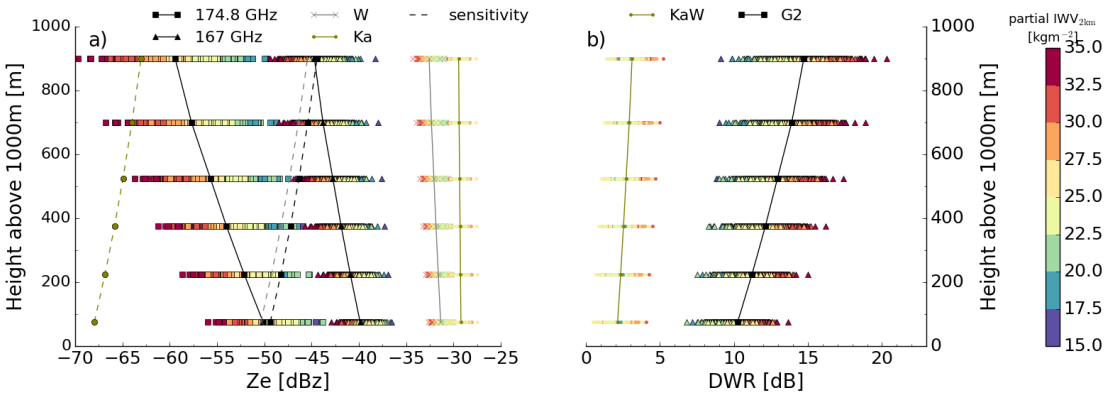

Figure 4.2 – Simulated (a) radar reflectivity Z_e at 35.5 GHz (dots), 94 GHz (x), 167.0 GHz (triangles), 174.8 GHz (squares) and (b) resulting DWR for KaW (dots, olive) and G2 (squares, black) frequency combination. Z_e and DWR are plotted as function of height above an assumed cloud base of 1000 m, and color-coded by water vapor amount below 2000 m. The mean Z_e and DWR are shown (solid line), as well as the respective radar sensitivity thresholds given in Tab. 4.1 (dashed). Simulations were based on 633 radiosonde profiles from 2018 with cloud base and top height assumed at 1000 and 2000 m, respectively. A cloud LWP of 50 g m^{-2} with constant LWC of 0.05 g m^{-3} was assumed.

on the wing of the absorption line, decrease on average by 4.8 and 9.3 dB in 167 and 174.8 GHz, respectively. Lower water vapor amounts below 2000 m, thus weaker water vapor attenuation, lead to higher reflectivities per range bin, an effect that is particularly pronounced in the water vapor sensitive G-band frequencies.

Not only does the attenuation strength change depending on the frequency, but so does the differential attenuation between Ka-W and the G2 frequencies. As attenuation increases strongly along the wing of the 183 GHz water vapor line, the resulting attenuation gradient is higher compared to the respective gradient of the continuum absorption between Ka and W. Therefore, the DWR G2 signal is higher than the KaW-signal, and also increases stronger with height, as attenuation cumulates along the ray path. Between 1000 and 2000 m, the DWR increases on average by 1.0 dB (KaW) and 6.6 dB (G2). Lower water vapor amounts reduce the vertical dynamical range of the DWR signal.

The influences of water vapor and liquid water to the DWR signals are illustrated in Fig. 4.3a. Shown for the synthetic cloud scenario used in this study, the KaW and G2 DWRs depend linearly on the water vapor path between radar and targets. For both frequency combinations, the Pearson correlation coefficient is nearly one. An increase of partial IWV of 1 kg m^{-2} leads to an increase of DWR at cloud top of 0.1 dB (0.6 dB) for KaW (G2), as denoted by the slope m of a linear fit function.

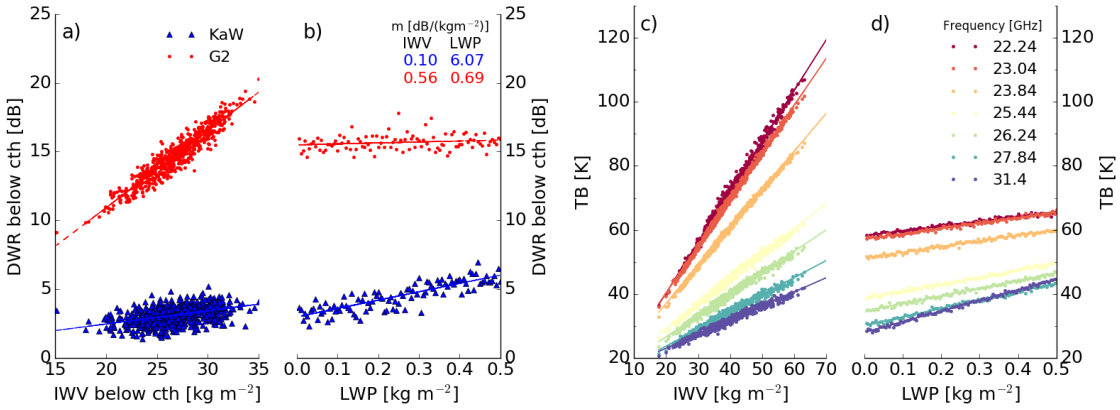

Figure 4.3 – DWR in radar range gate right below cloud top for KaW (blue) and G2 (red) frequency combination, and simulated MWR K-band TBs (frequency color-coded) as function of (a), partial IWV below cloud top (2000 m), (c) total IWV, and (b), (d) LWP. Depicted DWRs and TBs are (a), (c) the same synthetic observations shown in Fig. 4.2 for a LWP of 50 g m^{-2}, and (b), (d) for one radiosonde profile with partial IWV below cloud top of 27.6 kg m^{-2} (total IWV of 32.6 kg m^{-2}) and varying LWP. In all simulations, cloud base and top height were located at 1000 and 2000 m, respectively, and LWC was constant with 0.05 g m^{-3}. The DWR increase per water vapor and liquid amount is given by the slope of the respective linear fit function.

Fig. 4.3b shows that the DWR KaW at cloud top increases with cloud LWP, leading to a gain of signal of 6.1 dB per 1 kg m^{-2} added liquid, whereas the G2 DWR only increases by 0.7 dB per 1 kg m^{-2}. The MWR TBs vary as expected: whereas the TB in the channel 22.24 GHz increases most (1.58 K/(kg m^{-2})) with increasing IWV, the TB in the window channel at 31.4 GHz is most sensitive to changes in LWP (33.3 K/(kg m^{-2})).

The sensitivities of KaW and G2 DWR, as well as the MWR TBs, give an initial impression about the synergy potential of these observations for the retrieval. Whereas the DWR G2 signal shows an enhanced sensitivity to varying partial IWV along the beam path, the differential liquid attenuation contribution to DWR G2 is small. In case of DWR KaW, however, differential liquid attenuation contributions are of similar magnitudes than the signal sensitivity due to changing water vapor conditions. The MWR TBs are sensitive to both water vapor and liquid water.

Even though these results suggest that the G2 synergy would be particularly beneficial for water vapor profiling retrievals, sensitivity thresholds of current G-band technology might prohibit the penetration of the entire cloud layer. With the current potential of the VIPR system, a single-pulse sensitivity threshold of −40 dBz is reached at 1 km with a 15 m range resolution and 1 ms integration time. Given these technical constraints, the assumed cloud top at 2000 m (see Fig 4.2) would

not be detected at 167 or 174.8 GHz, and cloud base would be undetectable with the 174.8 GHz-channel for all simulated cases. Decreasing the vertical resolution to 150 m or applying non-coherent signal processing could improve the sensitivity to −50 dBz at 1 km (see Tab. 4.1), which would lead to a detection of 33.3 % of the simulated cloud bases at 174.8 GHz. Assuming a detection threshold of −60 dBz for future radar systems with increased transmitter power would allow detection of all simulated cloud bases. In 60.0 % of all simulated cases, the modeled cloud would be profiled up to 1500 m.

Therefore, in the following synergy analysis, the retrieval grid spacing was selected such that the retrieval resolution varies between 150 to 200 m in the cloud-layer. As G-band technology is only at the early stage of development and sensitivities might change in future systems, no sensitivity threshold was applied to the synthetic radar observations in the synergy analyses, and full cloud profiling potential was assumed. The impact of different sensitivity thresholds and, thus, different cloud penetration depths on the retrieval is analyzed in Sec. 4.5.2 by reducing the number of DWRs in the observation vector.

4.4 Case Study

The selected case study is based on a radiosonde launched at BCO on February 19, 2019, at 14:06 UTC (10:06 local time). On that day, the atmosphere showed typical features for a trade wind driven scene: a strong temperature inversion layer located between 2350 and 2600 m with a temperature increase of 4 K; a strong absolute humidity gradient of 8.5 to 0.2 g m^{-3}, corresponding to 97 % and 0 % relative humidity change within the inversion layer; the Lifting Condensation Level (LCL) located at 660 m; and a shallow cloud layer located below the inversion layer with cloud base around 1000 m and cloud top around 2300 m. The sonde measured a column IWV of 32.6 kg m^{-2}. Using the simulation setup described in Sec. 4.2 with cloud top height located at 2300 m, the simulated MWR TBs decrease from 59.2 K (22.24 GHz) to 30.2 K (31.4 GHz). At cloud base, Z_e reaches −30.5 dBz (−32.7 dBz) for the Ka- (W-) frequency, and −40.6 dBz (−51.5 dBz) at 167 GHz (174.8 GHz), respectively. The observed 2 m humidity $\rho_{2\mathrm{m}}$ was 18.9 g m^{-3}.

Figures 4.4a and 4.4b show the radiosonde absolute humidity profile, as well as the retrieval results using MWR-only, the synergistic MWR+radar approach, and

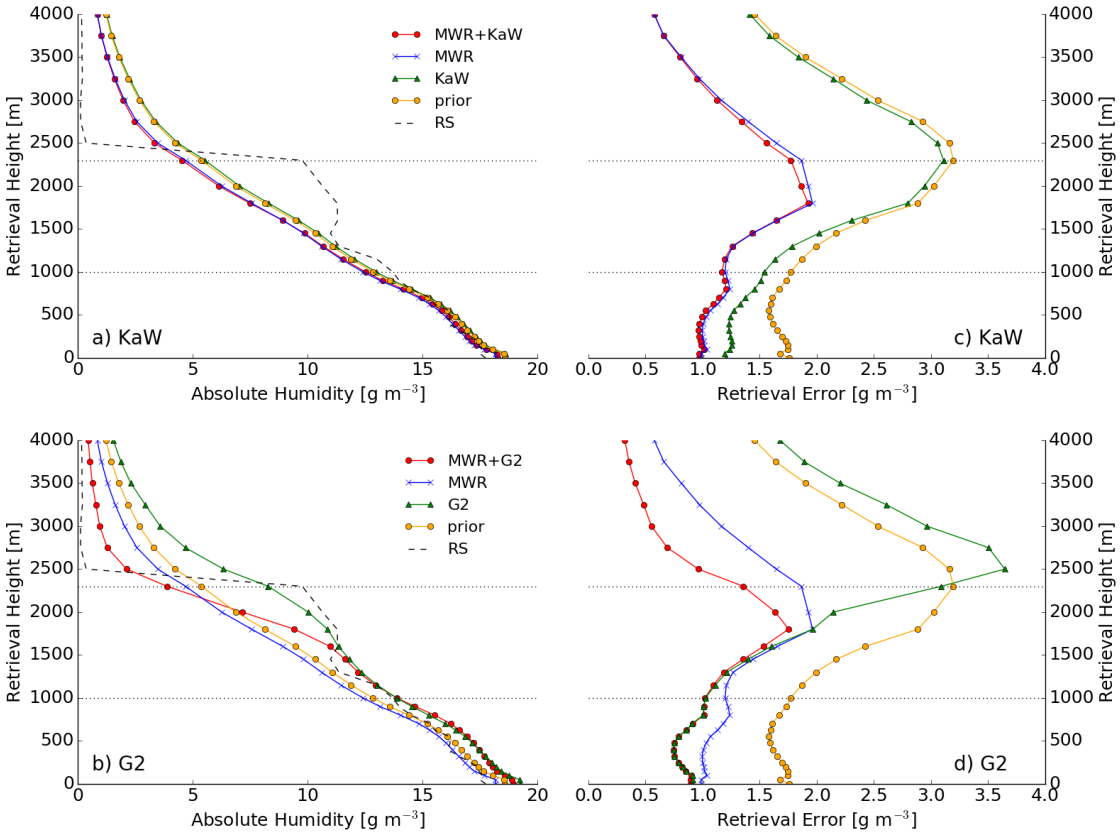

Figure 4.4 – Case study results for (a, b) retrieved absolute humidity profile and (c, d) a posteriori retrieval error. Different retrieval setups were used: MWR-only (blue), radar-only (green), and MWR+radar (red) for (a, c) KaW radar frequencies, and (b, d) G2 radar frequencies; case study radiosonde profile (black dashed) and prior profile and error (orange) are shown for comparison. Cloud base and top height are located at 1000 and 2300 m (black-dotted), respectively.

radar-only for both frequency combinations. All setups converge and pass the χ^2 test.

The retrieved profile using the MWR-only setup agrees well with the original radiosonde below the inversion layer. Within and above the inversion layer, the retrieval does not resolve the strong humidity gradient, but smooths the profile. The difference between retrieved and radiosonde absolute humidity at cloud top is $5.1\,\mathrm{g\,m^{-3}}$ in case of the MWR-only retrieval setup, with the retrieval underestimating the radiosonde water vapor amount below cloud top. Above the inversion layer, the retrieval overestimates the radiosonde measurements by about the same amount. The retrieved IWV of $31.7\,\mathrm{kg\,m^{-2}}$ matches the radiosonde IWV by a difference of $1\,\mathrm{kg\,m^{-2}}$ within the associated uncertainty range. This case nicely illustrates the restrictions of profiling retrievals based on pure MWR observations: whereas the IWV

amount of the retrieved profile matches the observed state of the atmosphere, the retrieved profile does not represent the vertical distribution of water vapor correctly particularly around the inversion layer.

When combining the MWR and radar observations using the synergistic KaW setup (see Fig. 4.4a), we expect the discrepancy between radiosonde and retrieval profile to decrease within the cloud layer due to the information added by the radar. At cloud base, the difference between radiosonde and retrieved profile reduces to $1.2\,\mathrm{g\,m^{-3}}$. The profiles of both setups agree with the radiosonde profile within the range of uncertainty. Throughout the cloud layer, the addition of KaW does not lead to an improved agreement between retrieved and radiosonde profile. When adding the DAR G2 observations to the retrieval as shown in Fig. 4.4b, however, the retrieved profile agrees with the radiosonde profile within the retrieval uncertainties, particularly within the lower part of the cloud. In the upper part of the cloud, the humidity gradient is not fully captured, but better represented than in the MWR-only setup. The G2-only retrieval performs well within the cloud layer, but cannot capture the profile above the cloud.

As shown in Fig. 4.4c, the a posteriori error of the retrieved MWR-only profile increases from 1.0 and 1.2 to $1.9\,\mathrm{g\,m^{-3}}$ from ground level to cloud base and top, respectively. Adding KaW observations to the retrieval decreases the error at cloud top slightly, by $0.1\,\mathrm{g\,m^{-3}}$. As shown in Fig. 4.4d, the error of the synergistic MWR+G2 retrieval is similar to the error of the DAR G2-only approach below cloud base, reducing the error to $0.7\,\mathrm{g\,m^{-3}}$ at 400 m. Towards cloud top, the error of the DAR G2-only setup increases, while the synergistic error further decreases compared to the MWR-only retrieval setup. The synergistic benefit of combining MWR and DAR G2 is pronounced particularly in these layers with an improvement of error compared to the MWR-only setup of up to $1.0\,\mathrm{g\,m^{-3}}$ at 3000 m.

The information gain through the instrument synergy, and the vertical distribution of the available information can be analyzed through the DFS summarized in Tab. 4.2. The MWR-only setup reaches 3.06 DFS in total. When adding KaW to MWR, the total DFS do not increase considerably, but the addition of DAR G2 to the MWR increases the available DFS to 4.28. In both synergistic combinations as well as the MWR-only setup, one piece of information is used for LWP. The KaW-only configuration contains reduced information about the LWP, whereas the G2-only does not give any information about the LWP.

Table 4.2 – Case study DFS for different retrieval setups: synergistic approach with MWR and dual-frequency radar observations, MWR-only configuration, and dual-frequency radar-only. Dual-frequency radar observations were evaluated for KaW and G2 frequency pairs. The synergistic and DAR-G2 only retrieval were also run with a reduced observation vector setup only taking into account DWR measurements if both simulated radar reflectivities were above a sensitivity limit of −60 dBz at 1000 m. Given are the total DFS, the DFS for the LWP state, the sum of DFS for all water vapor (WV) states, and the partial water vapor DFS for below, within, and above the cloud layer.

	synergistic MWR+			MWR	dual-radar		
DFS	KaW	G2	$G2_{-60}$		KaW	G2	$G2_{-60}$
total	3.20	4.28	3.67	3.06	1.52	2.34	1.21
LWP	0.99	1.00	0.99	0.99	0.88	0.01	0.01
WV	2.21	3.28	2.67	2.07	0.64	2.33	1.21
WV_{below}	0.57	0.89	0.87	0.52	0.57	0.89	0.90
WV_{in}	0.44	1.17	0.83	0.40	0.07	1.44	0.31
WV_{above}	1.18	1.23	0.97	1.15	0.0	0.0	0.0

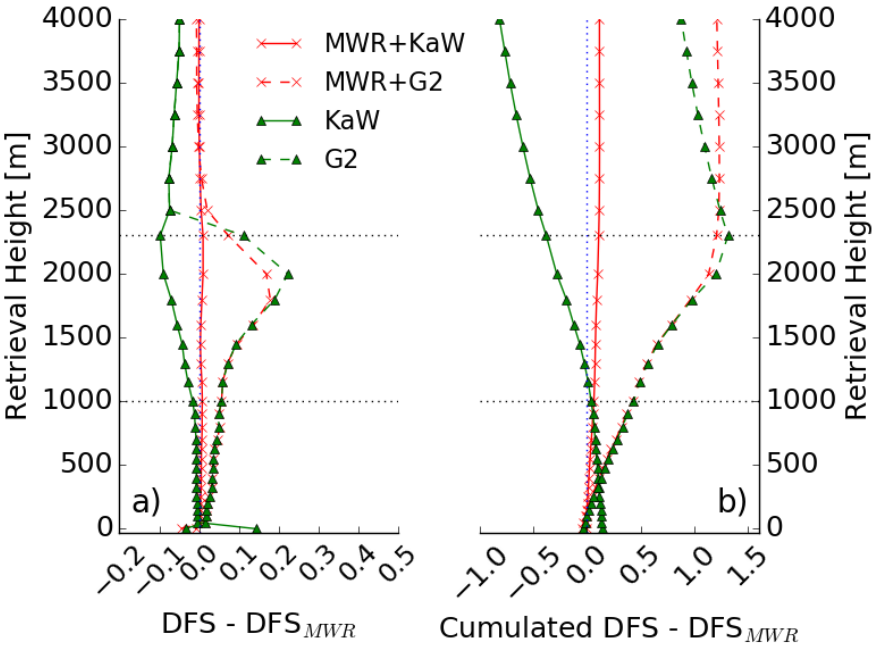

Figure 4.5 – Relative DFS to MWR-only retrieval of the case study retrieved profiles (a) per retrieved state and (b) vertically cumulated. Shown are the synergistic retrieval setups (red) and the radar-only setups (green) for both frequency pairs KaW (solid) and G2 (dashed). Note that the cumulative DFS in (b) include the DFS for ρ_{2m} and the DFS up to 4 km height.

Table 4.2 and Fig. 4.5 illustrate the vertical partitioning of the information content in respect to the cloud layer, plotted relative to the MWR-only setup. Below the cloud layer, the synergistic retrieval information in both setups originates from the

radar observations, with the DAR G2 combination providing a higher information content compared to the KaW frequencies (0.89 vs 0.57 DFS, respectively). In the cloud layer, the synergy of MWR+G2 increases the available information by 0.77 DFS compared to the MWR-only setup, but shows a slightly reduced information content compared to the G2-only approach. The synergistic benefit of the joint MWR+G2 retrieval is pronounced above cloud, where the information content is further enhanced compared to the MWR-only approach. Increasing information content correlates with a reduced retrieval error for the respective states (compare Figs. 4.4c and d). In case the G-band radar system's reflectivity sensitivity threshold were −50 dBz at 1000 m, cloud base at 1000 m would not be detected, and the synergistic approach would not enhance the information content compared to the MWR-only approach. If a sensitivity threshold of −60 dBz at 1000 m were assumed, however, cloud base would be detectable, but not the full cloud would be profiled. The synergistic observation vector, thus, would comprise of TBs, $\rho_{2\mathrm{m}}$, and the DWR measurements at three height levels from cloud base up to 1450 m. Using this reduced setup, the total synergistic information content would be enhanced compared to the MWR-only approach, but the synergistic benefit for the water vapor states above the cloud layer would be reduced compared to the full-cloud profiling application (see Tab. 4.2). Full-cloud profiling in this particular scene would require a sensitivity threshold in the G2 frequencies of better than −70 dBz at 1000 m, given the assumptions made in the forward modeling (see Sec. 4.2.1).

In case of the MWR+KaW synergy, only little information is provided by the radar observations, as can be explained by the stronger differential liquid attenuation component in the DWR KaW signal, and the resulting lower Signal-to-Noise Ratio (SNR) with respect to changing water vapor conditions. This dependency, however, is beneficial when looking at the LWP DFS: in case of KaW-only, 0.88 of the total 1.52 DFS are attributed to LWP, whereas DAR G2 contains no information about the LWP.

4.5 Retrieval Statistics and Sensitivity

4.5.1 Statistics For Varying Water Vapor Conditions

Expanding the case study analysis to a statistics of varying water vapor conditions, we evaluate all observations presented in Section 4.3 based on 633 atmospheric profiles and forward simulated with the method described in Section 4.2.1. The vertical absolute humidity profiles together with the LWP are retrieved from the synthetic observations with varying observation vector configuration: MWR-only, radar-only, and the synergistic setup. Even though the assumption of a cloud between 1000 and 2000 m might not be represented by each of the atmospheric moisture conditions, we assume that the synergistic benefits regarding the information content and retrieval error will, however, qualitatively not change.

Both the synergistic and MWR-only retrieval setup reach convergence rates of nearly 100 %. The retrieval based on pure dual-frequency radar observations shows lower convergence rates due to missing radar observations above cloud layer: there, all information content is determined by the prior climatology. Therefore, in the following, we analyze a reduced sub-sample of 212 cases that converge and pass the χ^2-test in all different retrieval configurations.

All retrieval setups cover the expected spread of IWV below cloud base given by the radiosondes as shown in Fig. 4.6a. The median values agree with the RS within $0.5\,\mathrm{kg\,m^{-2}}$. The setups using radar-only observations show application potential for retrieving the partial IWV amount below cloud base. The setups including the G2 observations show an increasing correlation r to 0.9, and a decreasing RMS compared to the MWR-only retrieval runs. In case of the MWR+KaW-combination, the opposite is true with the RMS increasing to $1\,\mathrm{kg\,m^{-2}}$. As shown in Fig. 4.6b, the medians of both synergistic retrieved LWPs agree with the assumed LWP of $50\,\mathrm{g\,m^{-2}}$ due to the information included by the MWR. 50 % of the results lie within the range of $\pm 20\,\mathrm{g\,m^{-2}}$. However, the LWP retrieved from radar-only observations disagrees significantly with the assumed LWP of $50\,\mathrm{g\,m^{-2}}$. KaW-only overestimates the LWP, showing a large spread of the retrieved values of about $100\,\mathrm{g\,m^{-2}}$; DAR G2 underestimates the LWP significantly, and the spread of the data is low. This discrepancy can be explained by the different sensitivity of the DWR signal to differential liquid water and water vapor attenuation (see Fig. 4.2). In case of KaW, the signal is similarly affected by both liquid water and water vapor attenuation:

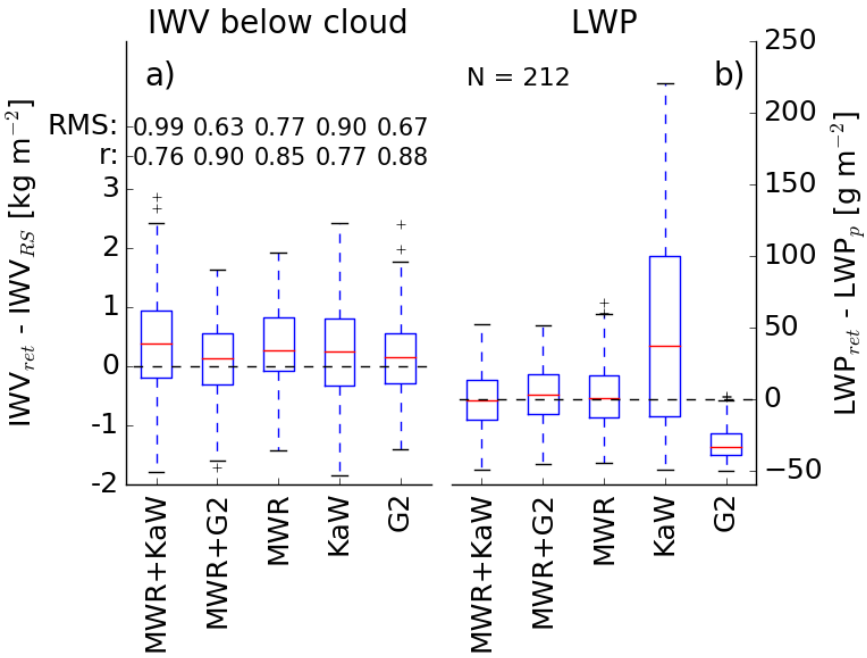

Figure 4.6 – Difference between (a) retrieved partial IWV to RS partial IWV, and (b) retrieved LWP to assumed LWP for all different retrieval setups. Shown are median (red), 10 %, 25 %, 75 %, 90 %-percentiles (blue) and outliers (black) of MWR-only, radar-only, and synergistic setups analyzed for KaW and G2 DAR pairs. The numbers in (a) refer to the Pearson correlation coefficient r and the RMS error. All physical converging cases of quality-controlled radiosonde profiles from 2018 were analyzed, resulting in 212 analyzed cases that converged in all different retrieval configurations.

the retrieval overcompensates the lack of variation in DWR signal under changing water vapor conditions by increasing the LWP state in order to find a converging solution. In contrast, the sensitivity of DWR G2 to liquid water is smaller, and the LWP result is driven by the prior state.

The distribution of total available information content is shown in Fig. 4.7 for all retrieval setups. The MWR-only retrieval contains on average 3.2 DFS. Using the synergistic approach of combining MWR and KaW (DAR G2) observations, the total DFS increase on average by 5.3 % (38.7 %) to 3.4 (4.5). In case of using the radar-only observations, the total DFS using the DAR G2 frequencies are on average higher (DFS = 1.8) than the DFS using KaW (DFS = 1.4). In the synergistic setups, larger water vapor contents below cloud top generally lead to higher DFS.

Figure 4.8 and Tab. 4.3 provide information about the vertical distribution of the information content available to the different retrieval configurations. Below and within the cloud layer, the information content of the synergistic MWR+G2 retrieval originates from the DAR G2 observations, as the DAR G2 and the synergistic

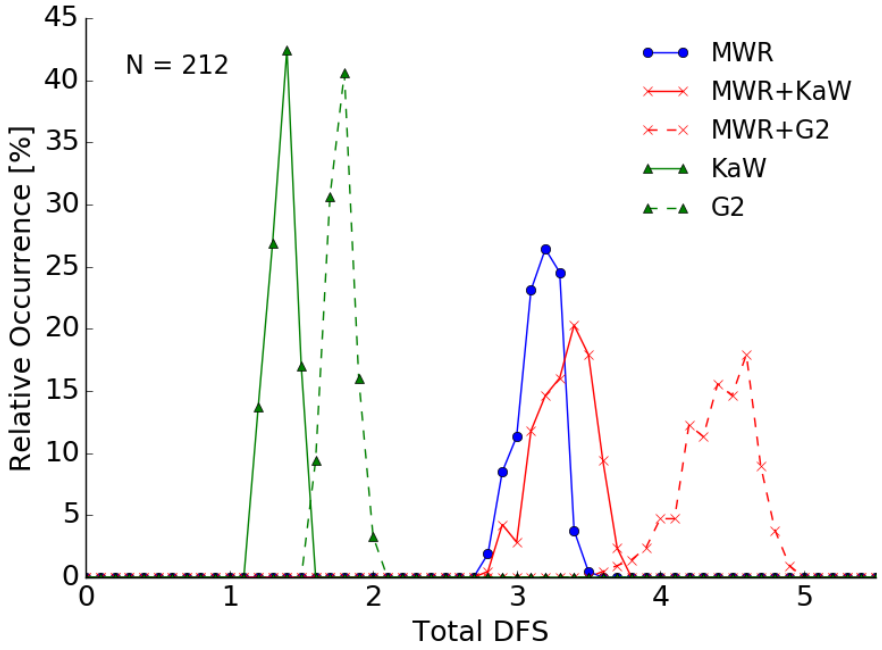

Figure 4.7 – Frequency of occurrence of total DFS, including DFS for LWP and all water vapor states. All 212 cases analyzed in Fig. 4.6 were considered using the MWR-only (blue), dual-frequency radar-only (green), and the synergistic retrieval setup (red); dual-frequency radar observations were evaluated for the KaW frequencies (solid), and DAR G2-frequencies (dashed).

setup both reach 1.8 DFS at 2000 m. Above cloud top, the synergy increases the information content by 0.2 DFS compared to the MWR-only setup. In case of KaW, this synergy effect is not pronounced due to the DWR KaW signal attenuation ambiguities (see Section 4.3). However, this sensitivity to liquid attenuation leads to an information gain for the LWP state: in case of KaW-only to about 0.9 DFS, whereas DAR G2 contains no information about the LWP. In both synergistic and the MWR-only retrievals, the MWR provides one DFS for the LWP.

Corresponding to the areas of increased information content, the retrieval error is reduced particularly above and in the upper cloud layer when combining MWR with DAR G2 as shown in Fig. 4.9. This synergistic effect is most pronounced between cloud top and 3500 m, resulting in an error decrease of up to $0.2\,\mathrm{g\,m^{-3}}$ compared to the MWR-only retrieval. Below and in the lowest cloud layers, the MWR+G2 error is similar to the G2-only retrieval error, leading to a reduction compared to the MWR-only approach of 28 % from 1.4 to $1.0\,\mathrm{g\,m^{-3}}$. Combining KaW and MWR observations leads to a small error decrease around cloud base of less than 5 %, but not to a significant improvement in other areas.

Table 4.3 – Mean DFS for 212 cases converging in all varying retrieval configurations using MWR and KaW or DAR G2 observations. Given are the total DFS, the LWP DFS, the sum of DFS for all water vapor (WV) states, and the partial water vapor DFS for below, within, and above the cloud layer.

	MWR+		MWR	dual-radar	
DFS	KaW	G2		KaW	G2
total	3.38	4.45	3.21	1.42	1.82
LWP	0.99	0.99	0.99	0.88	0.02
WV	2.39	3.45	2.21	0.53	1.8
WV_{below}	0.51	0.83	0.45	0.48	0.84
WV_{in}	0.42	1.00	0.36	0.04	0.96
WV_{above}	1.45	1.63	1.41	0.0	0.0

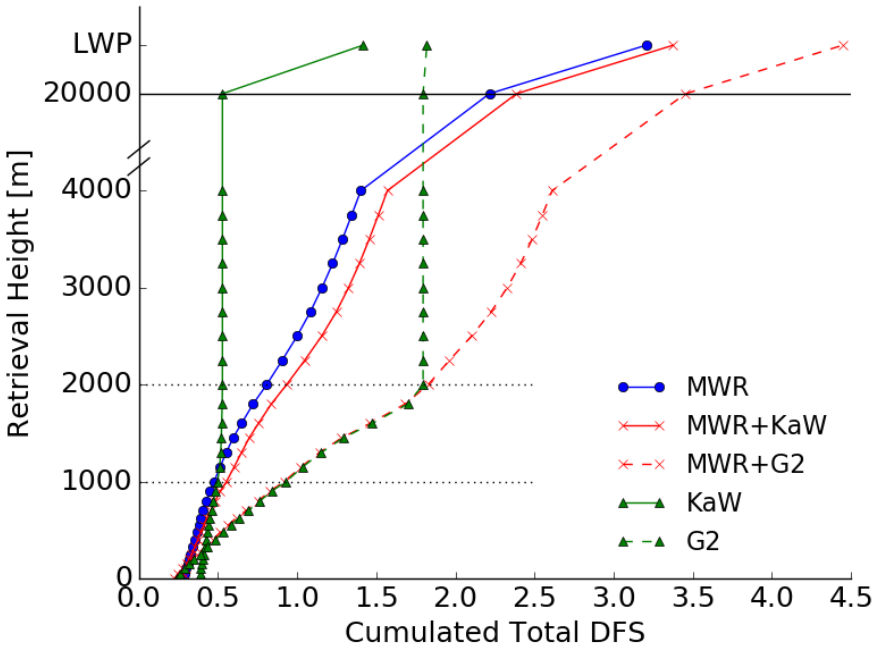

Figure 4.8 – Mean DFS, vertically cumulated and depicted per retrieval state. Experiment setup, colors and line style as in Fig. 4.6. Note that states between 4000 and 20 000 m are not resolved for figure clarity, but are considered in the calculation.

Even though the increase of DFS and the decrease of error is small in case of a synergy of MWR and KaW, a combination of the instruments adds valuable information to the humidity profile retrieval, as passive observations alone cannot successfully partition the retrieved water vapor profile in sub-, in-, and above-cloud layers. Additionally, KaW can add information about LWP and LWC as shown by Hogan et al. (2005). As opposed to KaW, DAR G2 is almost insensitive to liquid water, and contains information about the water vapor distribution below and

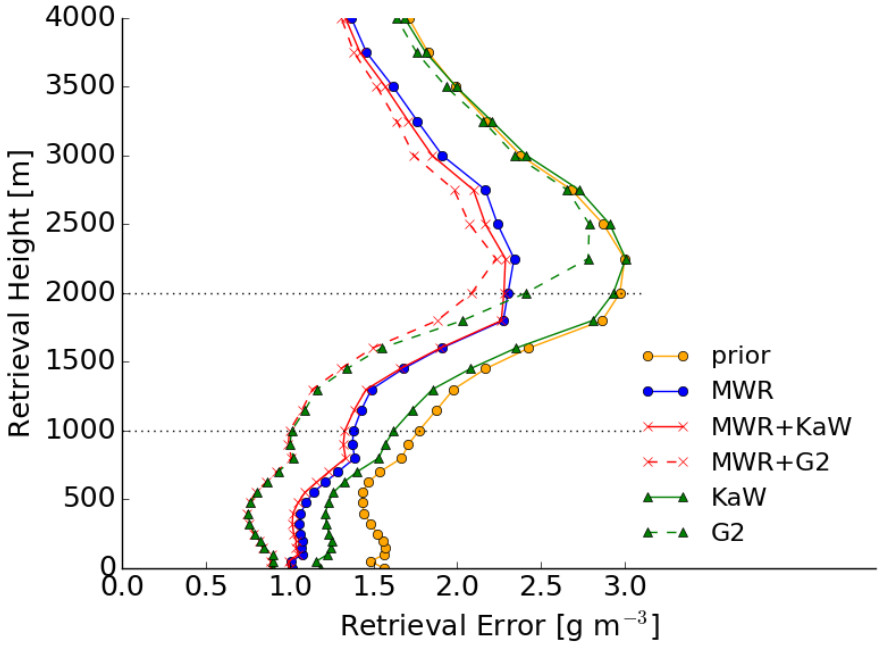

Figure 4.9 – Mean a posteriori retrieval error of retrieved absolute humidity per retrieval grid step, shown here up to 4000 m. Experiment Setup, colors, and line style as in Fig. 4.6; prior uncertainty shown in orange.

throughout the cloud layer. Therefore, the MWR provides the information about LWP in the synergistic MWR+G2 setup. Compared to the MWR-only approach, the water vapor information content is increased above the cloud layer due to the instrument synergy.

4.5.2 Synergistic Retrieval Sensitivity to Forward Model, Observation Errors and Prior

After analyzing the retrieval error and information content for varying water vapor conditions, we now investigate the synergistic MWR+G2 retrieval sensitivity to changing forward model assumptions, observation errors, prior covariances, and radar detection thresholds.

The error associated with the forward model assumptions on LWC profile shape, effective radius, and DSD can be estimated following Rodgers (2000) if the parameter errors are uncorrelated. Therefore, we independently compare the observations resulting from the standard setup as described in Sec. 4.2.1 to simulations with an adiabatic-like linearly increasing LWC profile; an increased effective radius r_{eff} of

15 µm; and a decreased DSD shape parameter σ_{DSD} of 0.2. The LWP of $50\,\mathrm{g\,m^{-2}}$ is maintained in all simulations. Based on the case study profile presented in Sec. 4.4, we also evaluate the retrieval errors induced by the change of each parameter in the forward function when retrieving from the standard simulated observations.

We find that varying the LWC profile shape produces variabilities in the DWRs of less than 1 % in case of the KaW pair and leaves the DWR G2 invariable. These variations induce changes in the total DFS of less than 0.1, and of less than $0.1\,\mathrm{g\,m^{-3}}$ in the retrieval error, respectively. Varying $\mathrm{r_{eff}}$ or σ_{DSD} does not impact the observations or the retrieval error significantly. Thus, we neglect these error contributions under the condition that the non-Rayleigh scattering regime is not reached. Additional uncertainties to the MWR TB introduced by absorption model uncertainties as discussed in Cimini et al. (2018) are assumed to be within the range of the before-mentioned analyses performed for doubled TB errors.

In order to quantify the synergistic benefit under varying observational error magnitudes, we repeat the statistical synergistic MWR+G2 analysis while varying the diagonal elements of the y-covariance matrix, as well as the noise of the respective observations accordingly: doubled TB-error, doubled DWR-error and halved relative $\rho_{2\mathrm{m}}$ error. Modeling an optimally intercalibrated dual-frequency radar instrument, we also investigate the impact of adding the same random noise factor to both Z_e, and reducing the DWR noise to 0.05 dB. Additionally, we test the sensitivity of the MWR+G2 retrieval to the magnitude of the prior covariance matrix by multiplying all elements of $\mathbf{S}_a$ by various factors (here shown for 200) while conserving the correlation between all elements. In all setups, the measurement errors are assumed to be uncorrelated. Figure 4.10a shows the mean square-root of all $\mathbf{S}_{op}$ diagonal elements for a sub-sample of 203 cases which reach true convergence in all different retrieval configurations.

Doubling the TB-error leads to an increase of the retrieval uncertainty above cloud top by $0.1\,\mathrm{g\,m^{-3}}$. Doubling the DWR-error, which would correspond to a lowering of the radar SNR, leads to an increase of error in and under the cloud layer of around $0.1\,\mathrm{g\,m^{-3}}$. Halving the $\rho_{2\mathrm{m}}$ uncertainty improves the retrieval performance by $0.1\,\mathrm{g\,m^{-3}}$ in the layers just above ground. The largest impact is seen when the radar system is assumed to be perfectly inter-calibrated. Then, the retrieval error decreases particularly within the cloud layer and, right below cloud top, reduces by $1.0\,\mathrm{g\,m^{-3}}$ compared to the original MWR+G2 setup. Simultaneously, the DFS nearly double within the cloud layer (not shown). The retrieval error is insensitive to magnitude

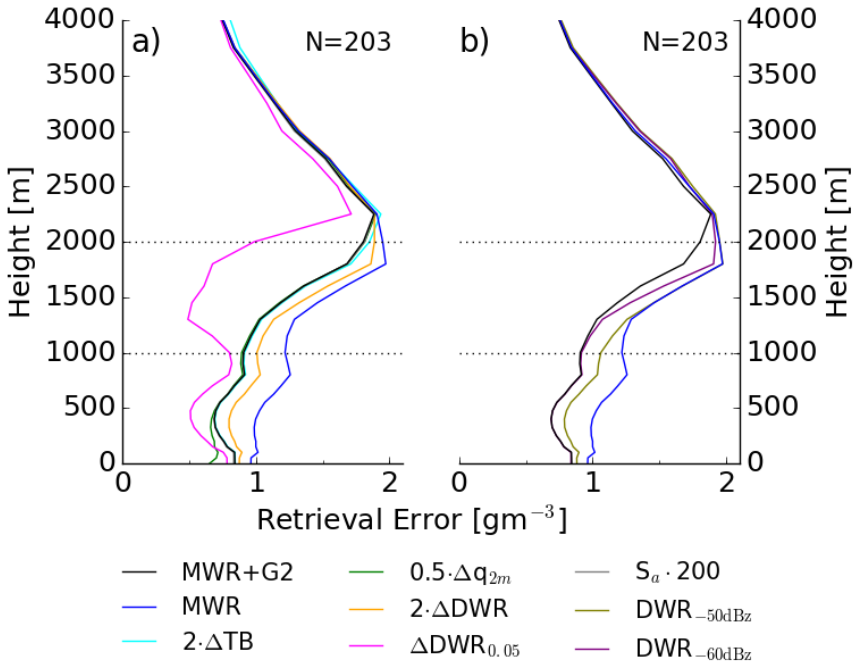

Figure 4.10 – Mean synergistic a posteriori retrieval error for synergistic MWR+G2 retrieval calculated based on 203 converging cases with different retrieval setups: a) the standard retrieval with varying $\mathbf{S}_e$ and $\mathbf{S}_a$ components, and b) a setup with a reduced observation vector setup with MWR TBs, DWR above the respective radar sensitivity threshold, and $\rho_{2\mathrm{m}}$. Shown are the mean errors for the standard synergistic retrieval (black), the MWR-only configuration (blue), as well as a) doubled TB-uncertainty (cyan), halved $\rho_{2\mathrm{m}}$ error (green), doubled DWR error (orange), reduced and coupled DWR error (magenta), as well as inflated prior covariance (gray); b) a reduced observation vector setup using MWR TBs and DWR calculated for layers with Z_e above -50 dBz (olive) and above -60 dBz (purple).

changes of the prior covariance matrix as long as the correlations between all elements are conserved. The presented error sensitivity study is particularly important when moving from synthetic to real observations. The DWR uncertainty in particular could be enhanced for real instruments to account for sensor misalignment and non-uniform beam filling effects, as well as due to the vertical dependence of the radar's SNR. Hogan et al. (2005) further describe how to quantify these errors.

As discussed in Sec. 4.3, current G-band radars might only be able to penetrate the lowest cloud layers. While the analyses before assumed that the entire cloud layer is penetrated independent from radar sensitivity thresholds, the dependence of the MWR+G2 synergy retrieval to partial cloud profiling is now investigated. We therefore run the retrieval with a different observation vector configuration which consists of all TBs, $\rho_{2\mathrm{m}}$, and the DWR calculated only for those layers, where the reflectivity in both frequencies lies above the respective sensitivity limit. As the

received power is inversely proportional to the square of the range, the respective thresholds were calculated for each cloud layer. A threshold of −50 dBz at 1000 m was selected based on the single-pulse VIPR sensitivity with a range resolution of 150 m, whereas a sensitivity of −60 dBz is assumed to be achievable with future, more powerful transmitters.

Only 33.3 % of the simulated 174.8 GHz-reflectivities at 1000 m reach a reflectivity of larger than −50 dBz. In 96 % of these cases, only the lowest cloud layer right above cloud base is detected, and, thus, only one DWR measurement is added to the observation vector. With a sensitivity threshold of −60 dBz, the lowest cloud layer can be observed for all simulated cases. Towards cloud top, the number of detected cases reduces to 60.0 % at 1500 m, and 7.6 % at cloud top. Thus, the number of DWR in the observation vector varies depending on each specific case. The retrieval error and information content of the same subset of 203 cases were analyzed, and are summarized in Fig. 4.10b and Tab. 4.4. For comparison, the error and information content for the retrieval without detection thresholds are added to the analysis.

Table 4.4 – Mean DFS for 203 converging cases, calculated for MWR+G2 synergistic setup without sensitivity restrictions, with a radar sensitivity of −50 dBz and −60 dBz applied, and the MWR-only retrieval setup.

DFS	MWR	MWR+G2	MWR+G2$_{-60\,\mathrm{dBz}}$	MWR+G2$_{-50\,\mathrm{dBz}}$
total	3.09	4.16	3.94	3.50
LWP	0.99	0.99	0.99	0.99
WV	2.10	3.17	2.95	2.50
$\mathrm{WV_{below}}$	0.51	0.85	0.85	0.77
$\mathrm{WV_{in}}$	0.39	0.90	0.72	0.46
$\mathrm{WV_{above}}$	1.20	1.43	1.38	1.27

When a sensitivity of −50 dBz is assumed, the retrieval error of the synergy setup is mainly reduced below and within the lowest cloud layer, as no DWR observations above are available. The reduction of error compared to a MWR-only setup is accompanied by a gain of information content for the water vapor profile below the cloud. Compared to the optimal MWR+G2 setup, the slightly reduced information content below cloud leads to an increase of retrieval error of 1.0 g m^{-3}. Throughout the cloud layer, the retrieval error blends with the MWR-only error, as no additional observations are available. The synergistic information content gain above the cloud layer is reduced.

When applying a threshold of −60 dBz, DWR observations are available deeper into the cloud layer. Therefore, the information content is reduced particularly throughout the cloud layer compared to the optimal setup, and the retrieval error increases towards cloud top with decreasing availability of observations. However, the synergistic information gain above the cloud layer is only marginally reduced compared to the optimal setup, leading to an increase of total DFS by 0.9 compared to the MWR-only retrieval (vs 1.1 DFS for the original MWR+G2).

Even though the synergistic benefits are less pronounced when a sensitivity threshold is considered, our results suggest that a synergistic deployment of MWR and DAR G2 would be beneficial even with current technological detection thresholds.

4.6 Conclusions and Future Studies

Continuous, high-resolution water vapor profile observations in the lower troposphere are essential for quantifying shallow convective processes and characterizing cloud and precipitation formation. Especially in the trade wind regions, high resolution observations are needed, for example to evaluate the representation of shallow convective cloud parametrization in models. Synergistic retrievals using ground-based active and passive remote sensing observations can help close this observational gap, e.g. in-between regular radiosonde network launch times. In clear sky cases, lidar systems give very accurate profiles of water vapor; in cloudy conditions, however, these observational methods fail to reproduce the atmospheric state within and above the cloud layer due to signal saturation. In these cases, the approach presented in this study can help to complement the picture.

In this paper, we present the potential of a novel synergistic, optimal estimation-based retrieval approach combining microwave radiometer and dual-frequency radar observations. Specifically, we use synthetic observations of TB and DWR to quantify the synergistic benefits of combining MWR with either the Ka- and W-band radars (KaW), e.g. available at BCO, or with a novel differential absorption radar prototype VIPR (Roy et al., 2020) using frequencies of 167 and 174.8 GHz (G2). The simulated G2 radar reflectivities and resulting dual-wavelength ratios show a higher sensitivity to changing water vapor conditions than the KaW simulations. However, the simulated observations suggest that full-cloud profiling might in reality

be impaired by current G-band radar sensitivity thresholds in shallow cloud scenarios such as modeled in this study.

We retrieve the full column absolute humidity profile as well as the LWP for a single-layered liquid cloud scenario typical for the atmospheric conditions observed at BCO, assuming full-cloud profiling. The synergistic approach combines the advantages of both instruments: the high potential of the MWR for retrieving integrated quantities such as IWV, LWP and coarse water vapor profiles throughout the column; and the high profiling potential of dual-frequency radar, providing the partial water vapor amounts between the radar range gates in the presence of backscattering targets.

Based on case study results and the statistical analysis of different water vapor conditions, we find that the combination of MWR+KaW only marginally increases the total retrieval information content compared to the retrieval based on pure MWR observations (3.4 vs 3.2 DFS). Within the cloud layer, the increasing ambiguity of separating liquid and water vapor impacts in the DWR signal leads to reduced DWR signal ranges for varying water vapor conditions. The addition of KaW radar observations to the retrieval could, however, be beneficial for deriving cloud base and top height, partial IWV amount up to cloud base, and the LWC profile (e.g. Hogan et al., 2005; Zhu et al., 2019). The analysis could also be further expanded to drizzling clouds by combining the presented algorithm with the modified Frisch approach presented by Küchler et al. (2018).

The combination of DAR G2 and MWR, on the other hand, increases the information content on average by 1 DFS to 4.4, particularly below and within the cloud layer. There, the radar observations provide all information for the water vapor states. The full potential of this synergy is seen above the cloud layer where the synergistic information content is enhanced compared to the MWR-only and DAR G2-only setup.

The results show sensitivity to the assumed measurement errors, particularly to the radar uncertainties. In order to gain the full synergistic potential of this approach, more sensitive G-band radars are needed for future applications. Increasing sensitivity, for example through increased transmitter power, is required in order to fully profile the shallow clouds observed at BCO. Albeit, when applying the retrieval to real observations, further sources of uncertainty will have to be quantified: beam-mismatching of the instruments; mis-alignment of the radar antennas; inter-calibration discrepancies of the radars; horizontal spacing between

the instruments (Küchler and Löhnert, 2019); and non-uniform beam filling effects. By operating the VIPR-instrument (Roy et al., 2020) at BCO in close vicinity of the HATPRO, these uncertainties could be further quantified, and the detection limits, as well as the synergistic retrieval, could be further evaluated.

This synthetic study will be expanded to more complex cloud scenarios observed at BCO. The synergistic benefit will be further analyzed for cases of double-layered liquid clouds, as well as overlying ice cirrus clouds, expanding the presented study to a larger variation of more realistic scenarios. For these cases, we expect the synergistic benefit analysis to be more complicated due to assumptions about the partitioning of LWP per cloud layer, as well as non-Rayleigh-scattering effects influencing the radar observations. In cases of multiple-layer clouds, however, we also expect the synergy to be more pronounced due to increased information content between the cloud layers.

In order to further customize this retrieval to typical trade wind boundary layers and enhance the synergistic effects, the effects of additional constraining tools will be analyzed: reducing retrieval states by parametrizing the profiles in sub-, in-, and above-cloud; including the surface temperature and the assumption of a well-mixed boundary layer under cloud base; forcing humidity saturation within the cloud layer through a simultaneous temperature profiling retrieval; using cloud top height as a proxy for the inversion layer height; and analyzing the retrieval performance for circulation-dependent prior conditions. Further analyses will investigate the potential of including the direct inversion approach presented by Roy et al. (2020) into the synergy concept.

In order to overcome current G-band radar sensitivity constraints in high moisture and shallow cloud conditions such as observed in the trades, current detection limits would have to be enhanced. However, the application of this synergy concept is not limited to the trade wind region: a synergy application of MWR and current high frequency radar instruments would be particularly beneficial in drier environments, such as at mid-latitude observatories like the Jülich ObservatorY for Cloud Evolution JOYCE (Löhnert et al., 2015), or in the Arctic environment. Further analyses, including the air- and spaceborne application, will also contribute to assimilation strategies in numerical weather models, as well as to both satellite calibration and product evaluation campaigns. Synergy concepts of passive and active microwave sensors such as discussed in this study will contribute to closing the current gap of continuous, high-resolution water vapor observations in the cloudy boundary layer.

5 Study 2: Exploring the Synergy Concept in Increasingly Complex Cloud Situations: EUREC^{4}A Case Studies

The real conditions observed at BCO are more complex than the single-layered cloud scenario analyzed in the previous chapter. As the previous analyses revealed a higher potential for the MWR+G2 synergy compared to the MWR+KaW combination, this chapter will expand the synergistic analyses of the MWR+G2 combination to more realistic cloudy conditions based on synthetic measurements. The synergistic information content, retrieval uncertainty and performance will be evaluated based on three selected scenarios as observed during the EUREC^{4}A campaign. Furthermore, the synergy concept will be expanded to include synthetic Raman Lidar (RL) measurements. Based on all available measurements, different modification tools will be evaluated to enhance the synergistic performance between and above cloud layers.

First, Sec. 5.1 will introduce the three chosen cases, which are representative for re-occurring cloud scenarios observed at BCO in trade wind driven conditions. Using a similar retrieval approach as presented in chapter 4 with a climatological sounding prior, the synergistic results of MWR+G2 will be analyzed and discussed in Sec. 5.2 for the selected scenarios. The analysis will be centered around research question 3, assessing if the synergistic benefits align with the vertical levels of highest water vapor variability. Based on a modified retrieval approach as presented in Sec. 5.3, the effects of the synergistic retrieval will be explored for reconstructing the atmospheric humidity profile between 24-hourly operational sounding launches. Research question 4 will be addressed by analyzing the vertical distribution of information gain. In Sec. 5.4, the synergy concept will be expanded to include synthetic RL measurements, responding to research question 5 by analyzing the synergistic benefits compared to

the MWR+G2 approach. The expected benefits on the sub-cloud layer information content and retrieval uncertainty will be evaluated for all three scenarios in Sec. 5.4.1. By modifying the retrieval concept in Sec. 5.4.2, different tools will be investigated to optimally use all available measurements to maximize the information content between and above the cloud layers as analyzed based on scenario 2. Sec. 5.5 will summarize and discuss the findings regarding the potential of the synergy concept in increasingly complex cloudy conditions, as well as the expansion and modification of the concept when including additional RL measurements.

5.1 Selected EUREC⁴A Cases

Three substantially different yet typically re-occurring cases of water vapor structure and associated cloud formation were selected to investigate the potential of the proposed synergy concept for typical, realistically occurring conditions observed at BCO. The selection of the first two cases was motivated by the cloud variability observed at BCO, summarized in Nuijens et al. (2014), while the third case emerged from the importance of quantifying elevated moisture layers for radiative heating profiles (Gutleben et al., 2019; Stevens et al., 2017). Suitable cases observed during the EUREC⁴A campaign were selected, favored by the sampled synoptic conditions summarized in Sec. A.1 as measured by the upper-air sounding network (also see Sec. 3.1.2).

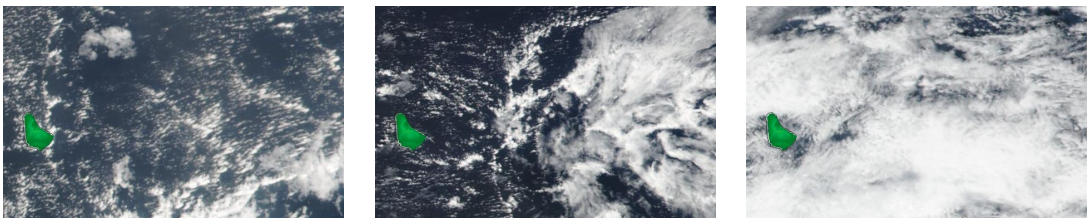

(a) 10.02.20 **(b)** 12.02.20 **(c)** 13.02.20

Figure 5.1 – Aqua MODIS corrected reflectance RGB composites[1] of the area covering 12.5 °N to 14.2 °N and −59.8 °W to −57.1 °W with Barbados highlighted in green.

Many days during the EUREC⁴A field study were characterized by shallow cumulus clouds forming at LCL (see Figure A8). Usually, these shallow clouds organize in scattered fields as seen in Fig. 5.1a and classified as Sugar or Gravel cloud fields in Stevens et al. (2020b). The atmospheric profile recorded by the sounding launched

[1] Satellite images acquired from `worldview.earthdata.nasa.gov`.

on 10.02.20 at 10:46 UTC (see Fig. 5.2a) provides a representative example of these conditions. As seen in Nuijens et al. (2014), stratiform outflow layers trapped under the trade inversion manifest the second most observed cloud appearance. On 12.02.20, the sounding launched at 02:47 UTC as well as the simultaneous radar observations at BCO captured two distinct cloud layers (see Fig. 5.3), associated with more stratiform large-scale cloud patterns as seen in Fig. 5.1b. A third case was chosen in order to represent the formation of an elevated moisture layer in the normally dry free troposphere, as observed during the last week of EUREC^{4}A . This moist layer was associated with the formation of higher altocumulus and -stratus decks as seen on the satellite image Fig. 5.1c, while shallow clouds formed further below around LCL. A representative sounding was launched on 13.02.20 at 22:52 UTC (see Fig. 5.4).

Synthetic observations for the MWR and G-band radar were generated using the approach introduced in Sec. 3.2 based on the PAMTRA model (Mech et al., 2020). For the synthetic EUREC^{4}A observations, however, more realistic cloud conditions as measured at BCO were included. Cloud base and top heights were derived from the Ka-band radar measurements by averaging the respective signal around the sounding launch, and the sounding humidity profile. The LWP of the cloud scenario was derived from the statistical BCOHAT retrieval described in Sec. 3.1.1. Constant LWC profiles, as well as an effective radius of 10 µm were assumed for the liquid droplets as motivated in Sec. 3.2. The temperature profile of the respective sounding was used to determine the phase of the modelled cloud, assuming only liquid hydrometeors for all clouds but the altocumulus cloud in case 3, where temperatures were below freezing and ice hydrometeors only were assigned. In scenes with multiple cloud layers, cloud LWP was partitioned based on the respective cloud layer depth. The $\rho_{2\mathrm{m}}$ observations were derived from the ground weather station (see Sec. 3.1.1) measurement closest to the launch-time. In the following analyses, it will be assumed that the radar signal would not saturate before reaching cloud top as instrument sensitivity thresholds are expected to improve in future instrumentation. A currently feasible G-band radar sensitivity threshold of $-50\,\mathrm{dBz}$ at 1000 m, decreasing with the distance squared (see Sec. 3.2, Sec. 4.3; Battaglia and Kollias, 2019), was considered as reference to evaluate the simulated reflectivities. Expected limitations due to this assumption will be discussed in Sec. 5.5.

On 10.02.20 around the sounding launch at 10:46 UTC, a shallow cumulus cloud formed between 700 and 1000 m as recorded by the radar (see Fig. 5.2b) and in the

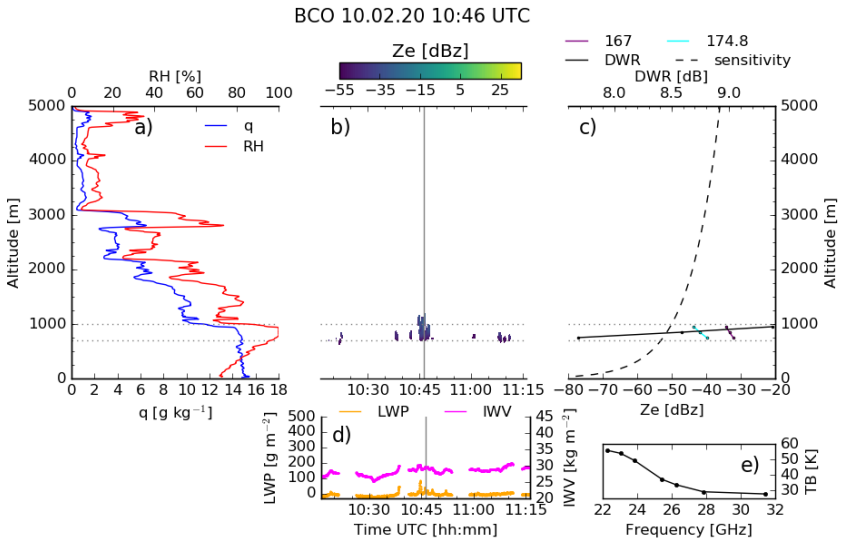

Figure 5.2 – (a) Sounding specific (blue) and relative humidity (red) profiles, (b) Ka-band radar reflectivities (color-coded) and (d) MWR IWV (magenta) and LWP (orange) as measured at BCO, as well as simulated (c) G-band reflectivities at 167 GHz (purple) and 174.8 GHz (cyan) with resulting DWR profile (black) and (e) MWR TBs (black) for scenario 1, 10.02.20, 10:46 UTC. The estimated G-band radar sensitivity at each radar range gate is added (dashed).

sounding relative humidity profile (Fig. 5.2a). A temperature inversion accompanied by a drop in humidity of 4.5 g kg^{-1} over 100 m capped the vertical expansion of the cloud. The measured 2 m absolute humidity ρ_{2m} was 17.0 g m^{-3}. BCOHAT recorded a LWP of 43 g m^{-2} in an IWV environment of 30.5 kg m^{-2} (Fig. 5.2d). The simulated G-band reflectivities shown in Fig. 5.2c decrease from -39.8 and −32.2 dBz to -43.6 and −34.3 dBz from cloud base to top at 174.8 and 167 GHz, respectively. The resulting DWR-signal increases from 7.7 to 9.4 dB throughout the cloud layer. In this case, an assumed radar sensitivity threshold of −50 dBz at 1000 m would allow full-cloud profiling as illustrated in Fig. 5.2c.

The atmospheric conditions recorded in the sounding launched on 12.02.20 at 02:47 UTC were moister than in case 1, shown by the increased IWV of 38.4 kg m^2 (Fig. 5.3d), as well as the increased ρ_{2m} of 18.6 g m^{-3}. Two distinct cloud layers formed: (i) around LCL ranging between 500 and 700 m; and (ii) below the trade inversion between 1900 and 2250 m as seen in Fig. 5.3b. The top height of the second cloud layer here represents the boundary between moist cloud layer and dry free troposphere. In the simulations, the LWP of 40 gm^{-2} retrieved from the BCOHAT measurements (see Fig. 5.3d) was partitioned equally between the first and second cloud layers. The humidity profile recorded by the sounding is associated with a

well-mixed sub-cloud layer characterized by a constant q-profile. The trade inversion located right above the upper cloud top is accompanied by a humidity gradient reducing the specific humidity by $8\,\mathrm{g\,kg^{-1}}$ until 3000 m, marking the separation between moist and dry troposphere (see Fig. 5.3a). Increased water vapor contents compared to case 1 led to increased simulated TBs of 70 K in the channels near the water vapor absorption line at 22.24 GHz (Fig. 5.3e). The simulated reflectivities of -32.5 and −38.4 dBz at the lower cloud base are further attenuated aloft towards the base of the second cloud layer, reaching -45.0 and −60.9 dBz at 167 and 174.8 GHz, respectively (Fig. 5.3c). Due to accumulating water vapor attenuation along the beam path, DWR increases with increasing height, increasing from 5.9 to 7.3 dB within the first cloud layer, and gaining 10 dB signal in the second cloud layer. A radar sensitivity threshold of −50 dBz at 1000 m would allow the profiling of the first cloud layer, but high signal attenuation throughout the lower troposphere would not allow a detection of the second cloud layer as seen in Fig. 5.3c.

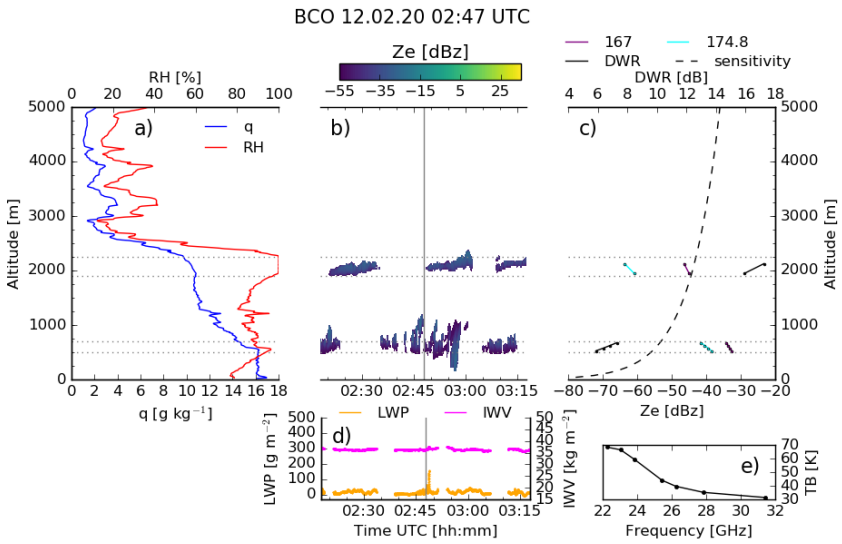

Figure 5.3 – As Fig. 5.2, but for scenario 2, 12.02.20, 02:47 UTC.

The formation of an elevated moisture layer and the associated middle and high clouds were captured in the sounding launched on 13.02.20, 22:52 UTC and the radar observations at BCO as illustrated in Fig. 5.4a and b. Winds made the sounding go through the upper cloud features that passed BCO 10 to 15 minutes after the sounding launch. A first shallow cloud layer formed around the higher LCL between 900 and 1000 m above a well-mixed sub-cloud layer. A $\rho_{2\mathrm{m}}$ of $16.9\,\mathrm{g\,m^{-3}}$ was measured. Above the first cloud layer, the humidity recorded by the sounding decreased from $11.2\,\mathrm{g\,kg^{-1}}$ to $1.3\,\mathrm{g\,kg^{-1}}$ below the trade inversion, between 1500 and

2000 m (Fig. 5.4a). Within the free tropospheric dry subsidence zone, an elevated moisture layer formed between 2500 and 4200 m, increasing the specific humidity up to 6.6 g kg^{-1} at 3200 m. Above the elevated moisture layer, an ice-phase dominated altocumulus cloud formed between 5700 and 9000 m (Fig. 5.4b). The retrieved BCOHAT LWP at the time of the cloud passing was estimated with 120 g m^{-2} based on the median within a 5-minute window (Fig. 5.4d). In the simulations, 120 g m^{-2} were assigned as liquid hydrometeor content to the lower cloud layer, while an Ice Water Path (IWP) of 100 g m^{-2} was assigned to the upper cloud layer. Similar IWPs were observed in the ICON model runs during the Narval campaigns (personal communication M. Jacob). For simplicity, only the ice phase was considered in the forward simulations, assuming a mono-disperse PSD and neglecting the presence of potential supercooled liquid.

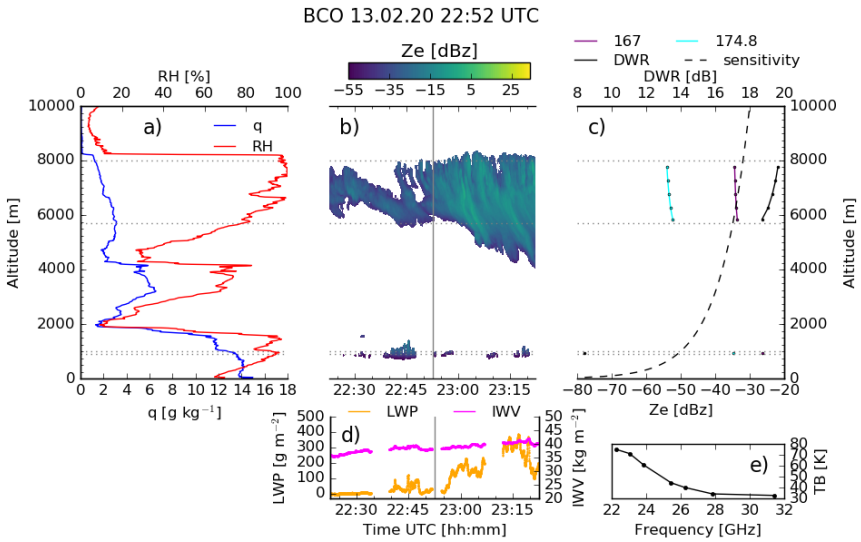

Figure 5.4 – As Fig. 5.2, but for scenario 3, 13.02.20, 22:52 UTC.

In this case, similar conditions in the lower troposphere result in similar simulated reflectivities and DWRs compared to the measurements in case 1. The DWRs simulated in the upper cloud layer increase from 18.6 to 19.5 dB (see Fig. 5.4c) due to a higher cloud position and increased cumulated water vapor attenuation along the radar beam. As the humidity gradient and mean absolute humidity within the second cloud layer is reduced compared to further below in the boundary layer, the DWR gradient throughout the cloud is reduced. While the cloud layer would still be detected at 167 GHz with a −50 dBz radar sensitivity threshold at 1000 m, it would not be detectable at 174.8 GHz (see Fig. 5.4c).

As the selected cases cover a majority of the range of expected trade wind driven conditions at BCO in the dry season and, thus, the expected water vapor structure variability, the following sections will focus on the benefits and limitations of applying the synergy concept to these cases. In particular the information content and retrieval uncertainty of the synergistic configuration will be assessed in comparison to the MWR-only or DAR-only configuration. The retrieval uncertainty will be quantified relatively to the prior, expressing the ratio of the square-root of the diagonal elements of $\mathbf{S}_{op}$ and $\mathbf{S}_a$ in percent as done in Maahn et al. (2020). The retrieved profile and partial water vapor amounts, even though specific to each of the convergences, will additionally be used to evaluate the synergistic impact.

5.2 Synergy Performance Based on Climatological Sounding Prior

A retrieval method similar to the one presented in chapter 4 will be applied to the three selected cases to expand the synergistic benefits analysis to more complex cloud conditions, centered around research question 3. The logarithmic humidity profile will be retrieved based on the observation vector with the respective measurement errors summarized in Sec. 3.2. As opposed to the setup used previously, however, LWP will be assumed as forward model parameter as the effects on the DWR are small (see Fig. 4.3). Furthermore, the partitioning of the cloud liquid and ice water paths is estimated based on the vertical extent of the cloud layers as described in Sec. 5.1. The synergistic benefits will be evaluated based on the retrieval DFS and retrieval uncertainty decrease compared to the prior uncertainties. The derived profile and partial water vapor amounts will be compared to the original sounding profile.

In order to customize the prior to the EUREC^{4}A conditions, 928 quality-controlled soundings launched at Grantley Adams International Airport (GAIA) in the months of January and February 1990 - 2017 were used to derive a mean climatological prior profile, as well as the prior covariance and correlation matrix illustrated in Fig. 5.5. The matrix illustrates the different water vapor regimes and their correlations nicely: all states in the moist layer below the trade inversion are highly correlated, as well as the free troposphere above the trade inversion. The moist layer and free troposphere, however, are de-coupled by the trade inversion.

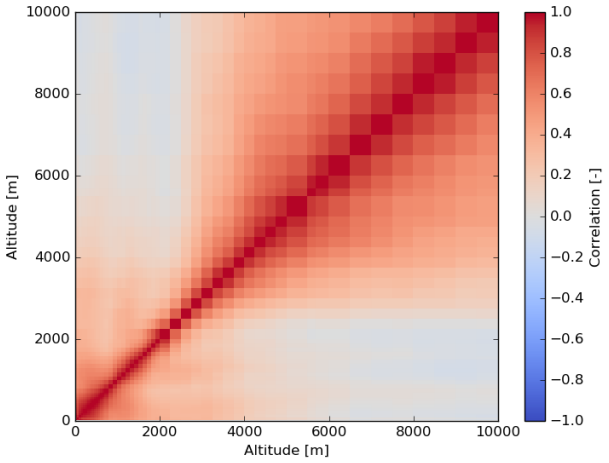

Figure 5.5 – Correlation matrix derived from GAIA soundings using 928 quality controlled soundings available from January and February 1990 to 2017 with red and blue shading representing positive and negative correlation coefficients, respectively.

Case 1: 10.02.20, 10:46 UTC

Case 1 is characterized by a single shallow liquid cloud layer forming at LCL just below a strong humidity gradient. While the prior profile is very close to the actual observed profile, the synergistic and DAR-only retrieval setup capture the sub- and in-cloud profile as well as the humidity gradient more accurately than the MWR-only configuration (Fig. 5.6a) which also reduces the discrepancy of the partial water vapor amount below and in the cloud layer (Fig. 5.7). In the sub-cloud and in-cloud layers, the synergistic results are dominated by the information originating from the DAR measurements, reducing the synergistic and DAR-only retrieval uncertainty compared to the MWR-only configuration by 11.3 and 10.3 percentage points at 350 and 850 m (see Fig. 5.6b). The $\rho_{2\mathrm{m}}$ observations constrain the retrieved humidity in the lowest levels. The synergistic impact increases between cloud base and top, and is most pronounced towards the top of the cloud, even though small. There, at 850 m, the synergistic retrieval error as seen in Fig. 5.6b is reduced by 10.3 and 8.1 percentage points compared to the MWR-only and DAR-only configuration, respectively. The in-cloud information content is enhanced by 0.1 DFS compared to the MWR-only retrieval (see Fig. 5.6c and Fig. 5.7a). Cumulating the DFS above the cloud layer results in 0.1 DFS improvement compared to the MWR-only DFS (see Fig. 5.7a).

Compared to the findings in Sec. 4.4, where the DFS above cloud on average increased by 13.0 percentage points compared to the MWR-only setup, the synergistic

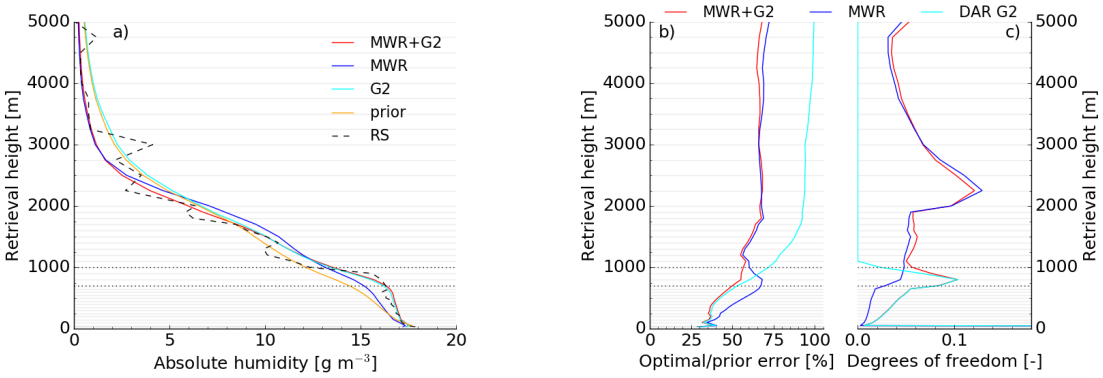

Figure 5.6 – Case 1, 10.02.20, 10:46 UTC: (a) Retrieved absolute humidity profiles, (b) optimal to prior uncertainty ratio and (c) DFS illustrated for synergistic MWR+G2 (red), MWR-only (blue), DAR-only (cyan) retrieval configurations. The prior (orange) and original sounding (black) profiles were added for reference.

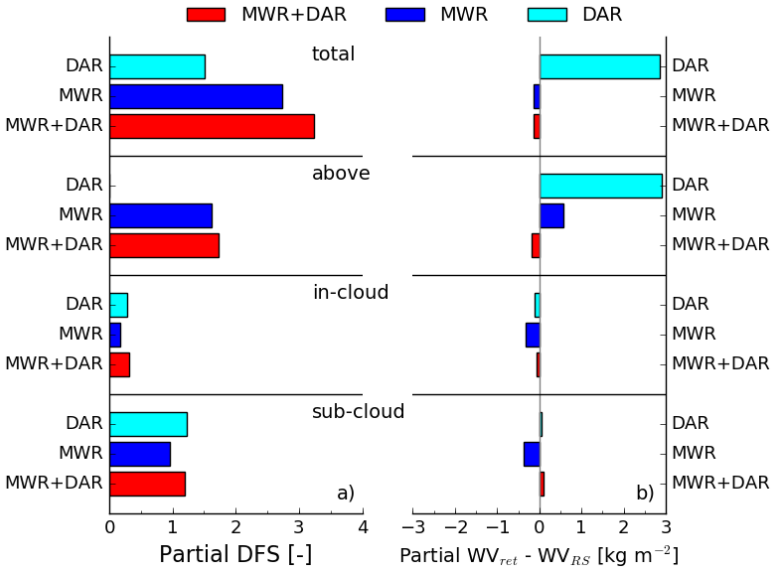

Figure 5.7 – Case 1, 10.02.20, 10:46 UTC: (a) Partial DFS and (b) partial water vapor amount discrepancy compared to sounding for sub-, in-cloud and above cloud layers for synergistic MWR+G2 (red), MWR-only (blue), DAR-only (cyan) retrieval configurations.

benefits here are reduced to 6.4 % improvement compared to the MWR-only (see Fig. 5.7a). This effect might be due to the thinner cloud layer and, thus, a reduced number of DWR measurements. Due to the correlation of the states, more DWR measurements due to a thicker cloud layer would lead to additional information from the signal in the cloud, and the information of the MWR measurements could be used for different non-cloudy states. Yet the partial water vapor amounts above the

cloud layer approach the actual observations of the sounding in case of the synergistic deployment, which could be an effect related to the specific solution. While the total IWV retrieved from both the MWR-only and synergistic setup matches the sounding IWV better than $0.2\,\mathrm{kg\,m^{-2}}$ as seen in Fig. 5.7b, the synergistic impact is seen in the improvement of the derived partial water vapor amount in all layers. In the synergistic approach, the underestimation of the in-cloud water vapor amount is reduced by $0.3\,\mathrm{kg\,m^{-2}}$ compared to the MWR-only configuration (Fig. 5.7b).

Case 2: 12.02.20, 02:47 UTC

Similarly to the performance of case 1, the sub-cloud humidity profile is captured more accurately in the synergistic setup compared to the MWR-only retrieval as illustrated in Fig. 5.8a. The added sub-cloud information of increased 0.2 DFS compared to the MWR-only approach (Fig. 5.9c) originates from the additional DAR observations as the vertically resolved DFS (Fig. 5.8c) align between synergistic and DAR-only configuration. The discrepancy between the retrieved partial water vapor amount and the sounding reduces by $0.3\,\mathrm{kg\,m^{-2}}$ compared to the MWR-only configuration (Fig. 5.9b). While the synergistic configuration was expected to improve the profiles of the in-cloud humidity, only an improvement of partial water vapor amount of $0.2\,\mathrm{kg\,m^{-2}}$ is seen between the cloud layers (Fig. 5.9a). Yet this result does necessarily contradict the expectation that DAR-measurements would improve the in-cloud water vapor profile, but could be related to this particular case and the prior and measurement error assumptions. While all information content below the second cloud layer originates from the DAR measurements as MWR+G2 and DAR-only have the same DFS (Fig. 5.8c), the synergistic information content increases between cloud top and 3500 m, in total by 0.3 DFS compared to the MWR-only configuration (Fig. 5.9b). This increase of information content is aligned with reducing retrieval uncertainties as seen in Fig. 5.8b, as the synergistic optimal to prior retrieval uncertainty ratio is decreased by up to 11.1 percentage points compared to the MWR-only configuration, here specified for the level above cloud top.

By combining MWR+G2, the total information content is increased by 1.0 and 1.6 DFS compared to the MWR-only, and DAR-only approach, respectively (see Fig. 5.9a). This increase in information content is distributed such that the absolute water vapor amount discrepancies are reduced below, between and above the cloud layers by 0.1, 0.2 and $0.4\,\mathrm{kg\,m^{-2}}$, respectively (see Fig. 5.9b).

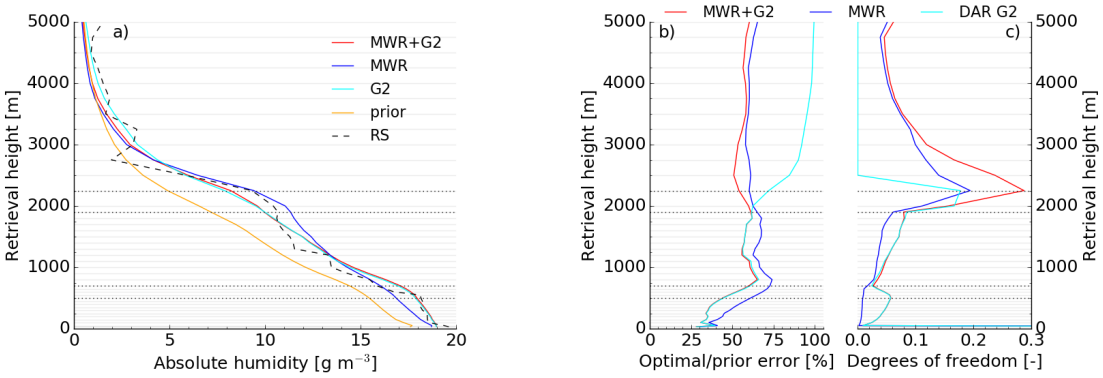

Figure 5.8 – Case 2, 12.02.20, 02:47 UTC: (a) Retrieved absolute humidity profiles, (b) optimal to prior uncertainty ratio and (c) DFS. Experiment setup and colors as in Fig. 5.6.

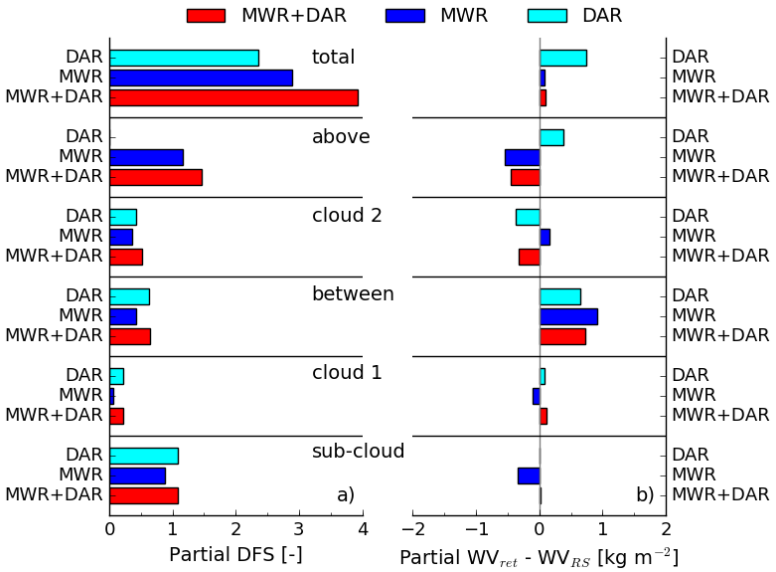

Figure 5.9 – Case 2, 12.02.20, 02:47 UTC: (a) Partial DFS and (b) partial water vapor amount discrepancy compared to sounding for sub-, in-cloud, between and above cloud layers. Experiment setup and colors as in Fig. 5.7.

Case 3: 13.02.20, 22:52 UTC

Scenario three is associated with an extra moist layer located in the dry free troposphere, characterized by the increased sounding humidity above the trade inversion between 2500 and 4200 m (Fig. 5.6a). Similarly to the cases analyzed above, the information content in and below the first cloud is driven by the DAR observations as seen in Fig. 5.10c. Similarly to the previous cases, the synergistic benefit increases throughout the cloud layer, marked by an error reduction of 6.1

and 6.7 percentage points compared to the MWR-only and DAR-only run at cloud base (Fig. 5.10b).

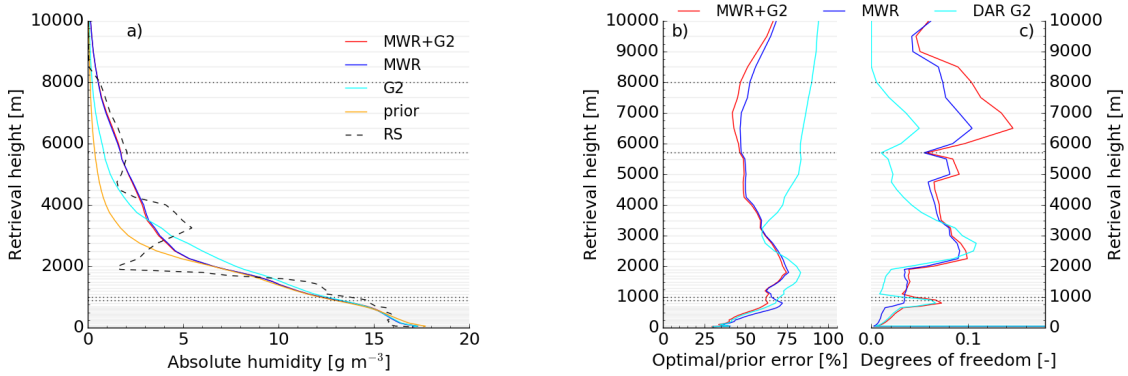

Figure 5.10 – Case 3, 13.02.20, 22:52 UTC: (a) Retrieved absolute humidity profiles, (b) optimal to prior uncertainty ratio and (c) DFS. Experiment setup and colors as in Fig. 5.6.

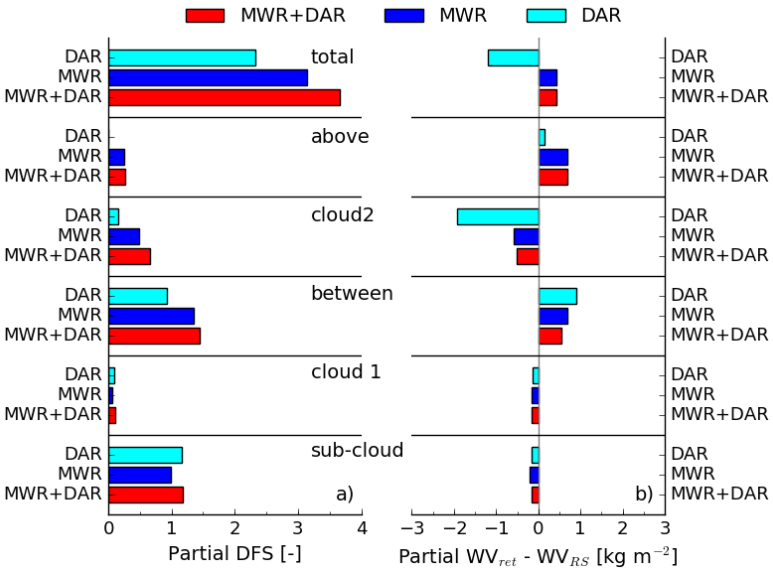

Figure 5.11 – Case 3, 13.02.20, 22:52 UTC: (a) Partial DFS and (b) partial water vapor amount discrepancy compared to sounding for sub-, in-cloud, between and above cloud layers. Experiment setup and colors as in Fig. 5.7.

No configuration resolves the humidity gradients associated with the elevated moisture layer (Fig. 5.6a). Yet the partial water vapor amount between the cloud layers as illustrated in Fig. 5.11b is best represented by the synergistic configuration, reducing the discrepancy between retrieved and sounding water vapor amount by 0.2 kg m^{-2} compared to the MWR-only configuration. The synergistic information

content gain between the cloud layers is marginal, with 0.1 DFS compared to the MWR-only setup (Fig. 5.11a), but increases up to 0.2 and 0.5 DFS in the second cloud layer compared to the MWR-only and DAR-only configuration, respectively.

Overview of All Cases

Summarizing all cases, Tab. 5.1 gives an overview of the gain of DFS of the MWR+G2 synergy compared to the MWR-only and DAR-only configurations, respectively, as well as the improvement of retrieval uncertainty compared to the MWR-only configuration, partitioned in respect to the cloud layers. The uncertainty reduction is given for the height bin half-way between ground and cloud base representative for the sub-cloud layer, for the middle height within each cloud layer, half-way between the cloud layers, as well as for the height level above the upper cloud top.

Table 5.1 – Gain of synergy DFS compared to the MWR-only and DAR-only configuration, as well as optimal to prior uncertainty ratio reduction compared to the MWR-only configuration, specified for all cases below, in, between and above the cloud layers(s). The uncertainty reduction is given for the height bin half-way between ground and cloud base for the sub-cloud layer, for the middle height within each cloud layer, half-way between the cloud layers, as well as in the height level above the upper cloud top. Note that the subscript *syn* refers to the MWR+G2 synergistic configuration.

	$DFS_{syn\ -\ MWR}$			$DFS_{syn\ -\ DAR}$			$S_{op}/S_{a\ MWR\ -\ syn}$ [%]		
case	1	2	3	1	2	3	1	2	3
total	0.50	1.0	0.51	1.72	1.57	1.3	n/a	n/a	n/a
above	0.11	0.29	0.03	1.72	1.46	0.27	1.80	11.11	4.78
cloud 2	-	0.16	0.17	-	0.10	0.50	-	15.81	5.46
between	-	0.23	0.09	-	0.0	0.52	-	7.81	0.69
cloud 1	0.15	0.16	0.04	0.0	0.0	0.0	10.33	2.67	4.60
sub-cloud	0.24	0.20	0.19	0.0	0.0	0.0	11.30	10.30	7.50

When combining MWR+G2, the total DFS are increased by 0.5 - 1.0 DFS and by 1.3 - 1.7 DFS compared to the MWR-only and DAR-only configurations, respectively. While in all cases, the information content in the sub- and first cloud layer originates from the DAR measurements (as the synergistic DFS are not increased compared to the DAR-only DFS), the DFS in the sub-cloud and within the first cloud layer is increased by 0.2, and between 0 and 0.2 DFS, respectively, compared to the MWR-only. The optimal to prior uncertainty ratio, correspondingly, decreases by 7.5 to 11.3 percentage points in the sub-cloud layer, and by 2.7 to 10.3 percentage points within the first cloud layer. While in case 2, the DFS between the clouds

is driven by the DAR measurements and enhanced by 0.2 DFS compared to the MWR-only configuration, a synergistic benefit of the information content in case 3 is seen due to 0.1 and 0.5 DFS increase compared to the MWR- and DAR-only configuration, respectively. In the second cloud layer, the synergistic benefit is clearly visible as DFS increase compared to both the MWR-only and DAR-only information content, precisely by 0.2 and by 0.1 - 0.5 DFS, respectively. The retrieval uncertainty decreases by 7.8 - 0.7 percentage points. Above the upper cloud layer, the synergistic benefit is most distinct as the synergistic DFS are increased by 0.1 - 0.3 DFS (6.4 - 19.7 %) compared to the MWR-only configuration, associated with an uncertainty reduction of 1.8 to 11.1 percentage points. The water vapor variability is highest around LCL and associated cloud formation, as well as around the trade inversion (see Sec. 3.1.2). The increasing information content particularly in and above each cloud layer in case 1 and 2 improves the retrieval performance in these heights.

5.3 Reconstructing the Gap between 24-hour Spaced Operational Soundings

In this section, the potential of the synergistic concept is analyzed for reconstructing the humidity profile between two 24 hour-spaced operational soundings at the 12-hour temporal interpolation point. Using a modified retrieval approach following Löhnert et al. (2007), the same cases as above are used as a testbed to not only evaluate the retrieval performance compared to an interpolated sounding profile, but also to identify the vertical areas of highest information gain as summarized in research question 4. This method can be used when trying to reconstruct a past atmospheric state with an associated uncertainty, e.g. between operational sounding launches.

The prior profile $\boldsymbol{x}_a$ represents the temporally interpolated profile at 12 hours between two 24-hour spaced soundings. Thus, the prior profile is closer to the observed reality, and the information gain is expected to be smaller than in the climatological prior case. The corresponding covariances in the $\mathbf{S}_a$ matrix thus describe the variation and correlation between the actual observed absolute humidity profile ρ_v and the corresponding interpolated profile $\boldsymbol{x}_a$, calculated for 12 hours past the initial launch. For example, soundings launched at 10:45 UTC and 10:45 UTC on the next day would be temporally interpolated and compared to the actual sounding launched at 22:45 UTC. The EUREC^{4}A sounding array launched at BCO provides

the necessary dataset to derive $\mathbf{S}_a$, as 182 soundings were launched with a 4-hour spacing. While $\boldsymbol{x}_a$ changes for each respective case, the corresponding covariances were calculated based on N=182 BCO ascending soundings using Eq. (5.3.1) with i, j denoting the altitude levels, and k the respective sounding number

$$\mathbf{S}_a(i,j) = \frac{\sum_{k=1}^{N}(\boldsymbol{x}_a(i) - \rho_v(i))_k \cdot (\boldsymbol{x}_a(j) - \rho_v(j))_k}{N-1}. \tag{5.3.1}$$

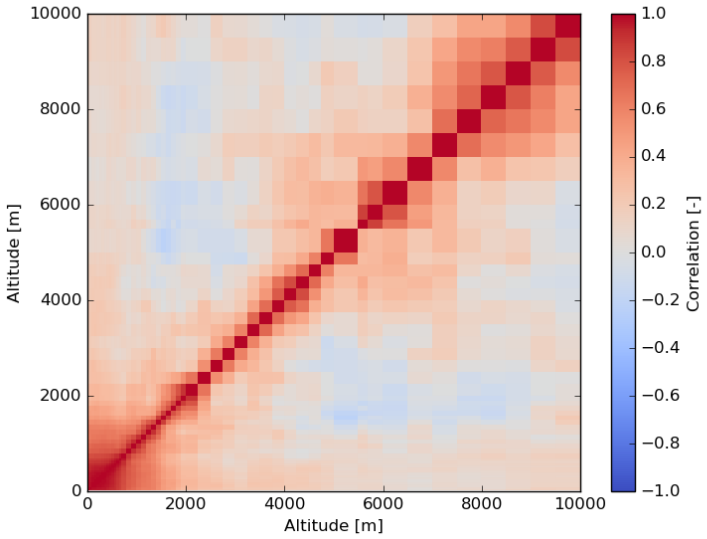

Figure 5.12 – Correlation matrix derived from error covariances of the temporal interpolation 12 hours after initial sounding calculated following Eq. (5.3.1) based on 182 soundings launched at BCO during EUREC^{4}A . Red and blue shading represent positive and negative correlation coefficients, respectively.

The resulting error correlations due to temporal interpolation, illustrated in Fig. 5.12, show similar features as the error correlations derived from the sounding climatology used in Sec. 5.2 (Fig. 5.5). Yet Fig. 5.12 suggests a stronger error de-coupling between moist and dry troposphere compared to the climatological correlations. The sounding specific humidity analyses in Sec. 3.1.2 revealed that the highest temporal water vapor variability in a 24-hour window is expected around the trade inversion with a standard deviation of $3.3\,\mathrm{g\,m^{-3}}$, and around LCL with a standard deviation of $1.6\,\mathrm{g\,m^{-3}}$, respectively.

The retrieved profiles, the optimal to prior uncertainty ratio, as well as the vertical resolved DFS are illustrated for all configurations and all cases in Fig. 5.13.

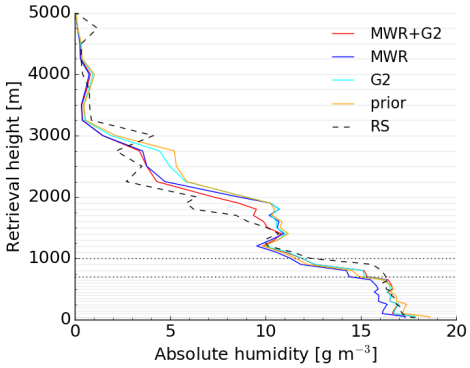

(a) Case 1, 10.02.20, 10:46 UTC

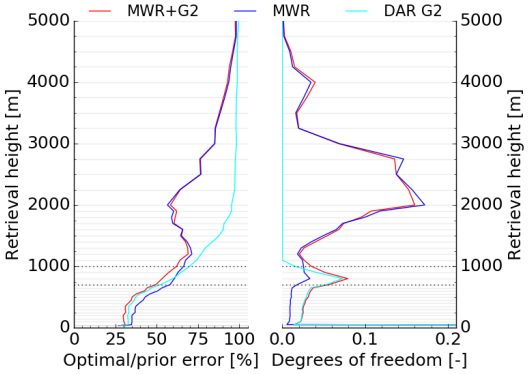

(b) Case 1, 10.02.20, 10:46 UTC

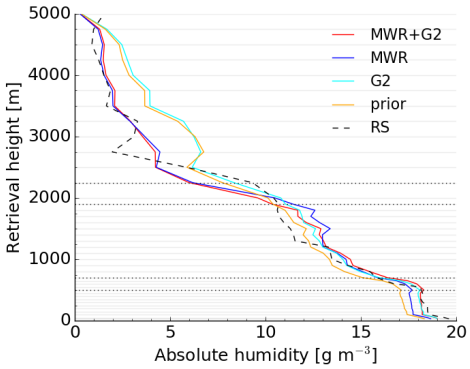

(c) Case 2, 12.02.20, 02:47 UTC

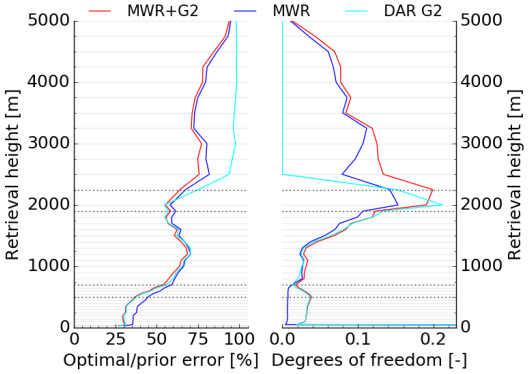

(d) Case 2, 12.02.20, 02:47 UTC

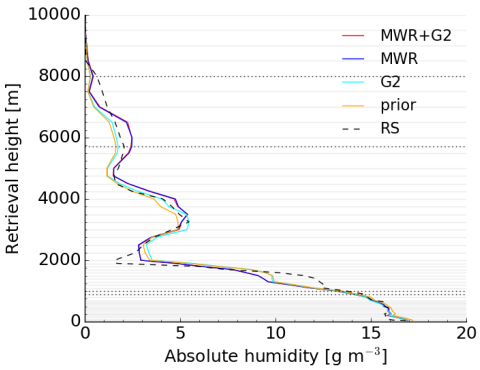

(e) Case 3, 13.02.20, 22:52 UTC

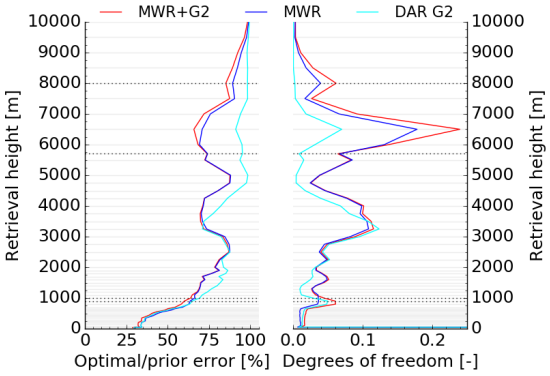

(f) Case 3, 13.02.20, 22:52 UTC

Figure 5.13 – (a, c, e) Retrieved absolute humidity profiles, (b, d, f) optimal to prior uncertainty ratio (left panel) and DFS (right panel) illustrated for synergistic MWR+G2 (red), MWR-only (blue), DAR-only (cyan) retrieval configurations for (a, b) case 1, 10.02.20, 10:46 UTC, (c, d) case 2, 12.02.20, 02:47 UTC, (e, f) case 3, 13.02.20, 22:52 UTC. The prior (orange) and original sounding (black) profiles were added to (a, c, e) for reference.

The sub-cloud layer did not vary much within the 24-hour window in all cases as the prior profiles seen in Fig. 5.13a, c, e correspond to the actual observed sounding profiles within $1.5\,\mathrm{g\,m^{-3}}$. In all retrieval configurations, the sub-cloud information content is driven by the DAR observations, as the synergistic and DAR-only DFS illustrated in Fig. 5.13b, d, f agree (also see Tab. 5.2). Compared to the MWR-only configuration, the sub-cloud DFS is enhanced by 0.1 DFS, leading to an error reduction half-way between ground and cloud base of 3.1 - 6.7 percentage points (Fig. 5.14 and Tab. 5.2).

Within the cloud layers in case 1 and case 2, the synergistic DFS increase by up to 0.1 DFS compared to the MWR-only configurations, driven by the DAR-observations (see Fig. 5.13b, d, f and Tab. 5.2). In case 3, a synergistic gain of 0.1 DFS can only be seen in the upper cloud layer. The retrieval uncertainties half-way through the cloud layer are marginally reduced by 2.9 - 6.7 percentage points compared to the MWR-only configuration. Similarly to the results using a climatological prior in Sec. 5.2, the retrieval uncertainty reduction increases towards cloud top.

Between and above the cloud layer, where no DAR measurements are available, no synergistic information gain compared to the MWR-only configuration is seen in case 1 or 3, while the DFS in case 2 increase by 0.1 and 0.2, respectively (see Fig. 5.13b, d, f and Tab. 5.2). This gain in DFS leads to an uncertainty decrease ranging between 1.5 - 6.1 percentage points compared to the MWR-only configuration.

Table 5.2 – Gain of synergy DFS compared to the MWR-only and DAR-only configuration, as well as optimal to prior uncertainty ratio reduction compared to the MWR-only configuration, specified for all cases below, in, between and above the cloud layers(s). The uncertainty reduction is given for the height bin half-way between ground and cloud base for the sub-cloud layer, for the middle height within each cloud layer, half-way between the cloud layers, as well as in the height level above the upper cloud top. Note that the subscript *syn* refers to the MWR+G2 synergistic configuration.

	$DFS_{syn\ -\ MWR}$			$DFS_{syn\ -\ DAR}$			$S_{op}/S_{a\ MWR\ -\ syn}$ [%]		
case	1	2	3	1	2	3	1	2	3
total	0.24	0.55	0.30	1.36	1.10	0.98	n/a	n/a	n/a
above	0.0	0.16	0.01	1.34	1.03	0.04	3.40	6.14	2.96
cloud 2	-	0.11	0.12	-	0.02	0.49	-	2.93	3.91
between	-	0.10	0.04	-	0.04	0.40	-	1.46	1.15
cloud 1	0.11	0.10	0.03	0.04	0.04	0.03	6.46	6.71	2.95
sub-cloud	0.11	0.09	0.09	0.0	0.0	0.0	6.36	6.71	3.12

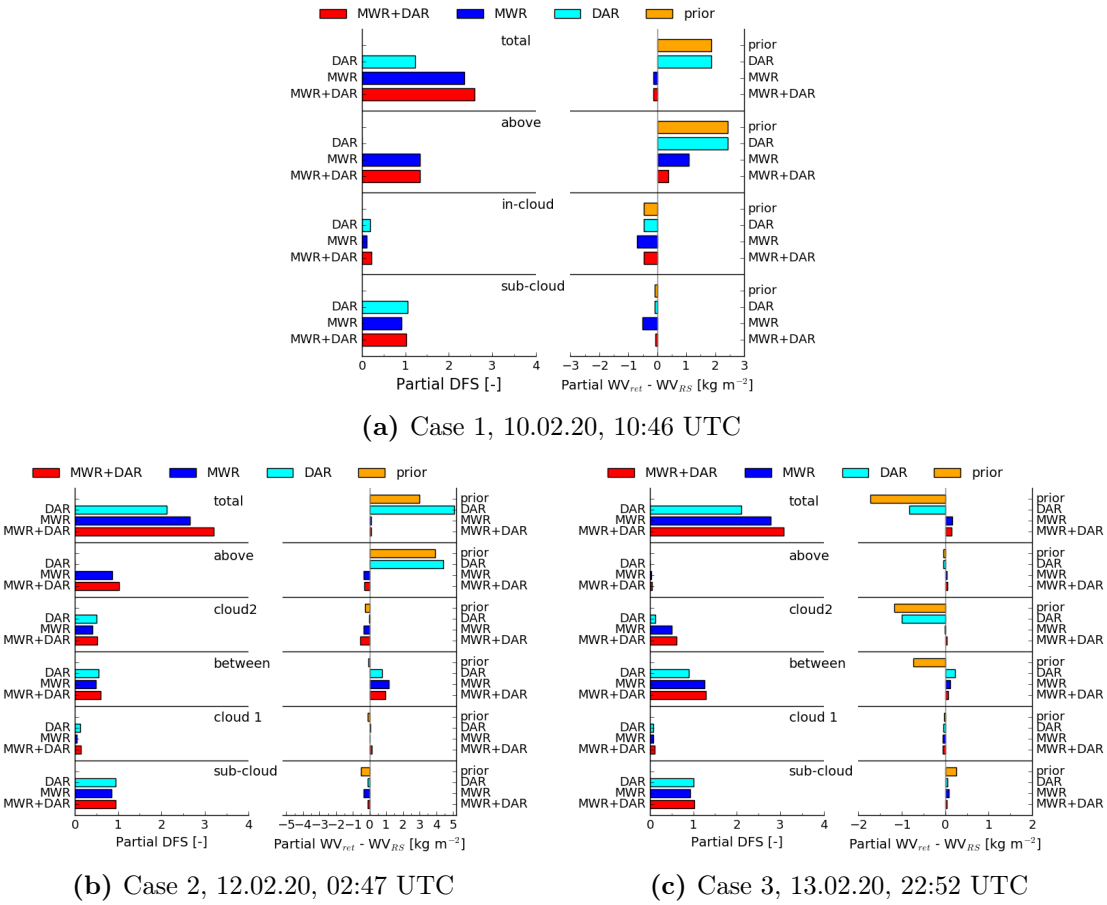

(a) Case 1, 10.02.20, 10:46 UTC

(b) Case 2, 12.02.20, 02:47 UTC

(c) Case 3, 13.02.20, 22:52 UTC

Figure 5.14 – Total and partial DFS (left panel), and total and partial water vapor amount discrepancy compared to sounding (right panel) for sub- and in-cloud, as well as between and above cloud layers for synergistic MWR+G2 (red), MWR-only (blue), DAR-only (cyan) retrieval configurations and prior (orange) for (a) case 1, 10.02.20, 10:46 UTC, (b) case 2, 12.02.20, 02:47 UTC, (c) case 3, 13.02.20, 22:52 UTC.

The total available information content increases by 0.2, 0.3 and 0.6 DFS compared to the MWR-only retrieval (see Tab. 5.2 and Fig. 5.14). Compared to the results using the climatological prior, the information gain is generally reduced, as expected, as the prior in this case is better and more conditioned to the expected atmospheric state than in the climatological assumptions.

When assessing the benefits of the synergy regarding the reconstruction of the atmospheric humidity conditions, the accuracy of the retrieved profile (Fig. 5.13) as well as the partial water vapor amounts (Fig. 5.14) can also be considered. In case 1, the discrepancy between synergistic retrieved partial water vapor amounts and sounding measurements decreases throughout the whole column by up to 0.5 kg m^{-2} compared to the MWR-only retrieval results (see Fig. 5.14b right panel). In case 2

and 3, only marginal improvements to the MWR-only configuration of lower than $0.1\,\mathrm{kg\,m^{-2}}$ can be seen. Yet the synergistically derived dry free tropospheric water vapor amount above the trade inversion as derived in case 2 and 3 agrees by up to $3.6\,\mathrm{kg\,m^{-2}}$ better with the sounding measurements than the interpolated prior amount (Fig. 5.14b right panel). The derived profile and partial water vapor amount, however, directly depend on the particular solution that only represents one most probable solution of all possible solutions. Thus, the presented tendencies are subject to the particular measurements and their errors, but can still be used to identify first tendencies. The identified improvements will have to be confirmed based on a larger statistical dataset.

The synergistic measurements add more information of 0.2 - 0.6 DFS to the reconstruction of the water vapor structure conditions between 24-hour spaced operational soundings particularly in the vertical heights of highest water vapor variability, seen around the cloud layers forming at LCL and below the trade inversion. The derived free tropospheric water vapor agrees by up to $3.6\,\mathrm{kg\,m^{-2}}$ better with the actual observed conditions compared to the interpolated sounding prior, driven by the MWR information.

5.4 Expanding and Modifying the Synergy Concept

At BCO, a Raman lidar (RL) measures continuously in close vicinity of the MWR HATPRO instrument. In this section, therefore, the impacts of additional RL measurements when added to the MWR+G2 synergy will be analyzed based on the three selected scenarios, assessing research question 5. The analyses in Sec. 5.4.1 are centered around the impacts of the RL measurements to the sub-cloud layer information content, retrieval uncertainty, and partial water vapor derivation. All three scenarios will be analyzed to additionally test at which other heights the RL measurements could lead to additional synergistic benefits compared to the initial MWR+G2 concept. In Sec. 5.4.2, different retrieval configurations using MWR, DAR G2 and RL will be assessed for the double-layered cloud scenario 2. Based on the resulting information content, retrieval error and partial water vapor, the modified configurations will be evaluated around the question of how to optimize the retrieval performance between and above the cloud layers.

5.4.1 Adding Raman Lidar Measurements

In this section, the effects of adding synthetic Raman Lidar (RL) measurements to the retrieval will be explored by analyzing the effects on the retrieved profile, water vapor amounts, retrieval error and information content by expanding the standard retrieval approach with a climatological sounding prior as introduced in Sec. 5.2. In order to simulate the measurements of the CORAL lidar at BCO (see Sec. 3.1.1), the sounding humidity measurements above the overlap zone of 100 m were noised by a random Gaussian error factor with $\sigma_{RL} = 1.0\,\mathrm{g\,m^{-3}}$, an error estimated from real instrument deployment at night time (e.g. Schulz and Stevens, 2018). All synthetic RL measurements below cloud base were taken into account to simulate signal saturation at cloud base. σ_{RL} is added to the $\mathbf{S}_e$ matrix and is assumed to be un-correlated with different measurement errors, as previously done in Barrera-Verdejo et al. (2016). The lidar observations are expected to dominate the sub-cloud layer retrieval, but the following analyses will additionally evaluate if the Raman lidar measurements also act on the retrieval uncertainty and information content at different height levels.

Table 5.3 – Gain of synergy DFS and optimal to prior uncertainty ratio reduction compared to the MWR+G2 configuration, specified for all cases below, in, between and above the cloud layers(s). The uncertainty reduction is given for the height bin half-way between ground and cloud base for the sub-cloud layer, for the middle height within each cloud layer, half-way between the cloud layers, as well as in the height level above the upper cloud top. Note that the subscript *syn* refers to the MWR+G2+RL synergistic configuration.

	DFS_{syn} - DFS_{MWR+G2}			$S_{op}/S_{a\ MWR+G2}$ - $S_{op}/S_{a\ syn}$ [%]		
case	1	2	3	1	2	3
total	1.27	0.76	1.83	n/a	n/a	n/a
above	0.04	0.0	0.0	0.87	0.67	1.03
cloud 2	-	0.0	0.0	-	1.99	1.18
between	-	0.0	0.0	-	0.14	-0.29
cloud 1	0.0	-0.09	0.0	3.79	8.29	10.09
sub-cloud	1.30	0.83	1.82	16.86	13.60	26.20

The retrieved profiles, the optimal to prior uncertainty ratio, as well as the vertical resolved DFS are illustrated for all configurations and all cases in Fig. 5.15. As expected, the addition of the lidar measurements increases the DFS in the sub-cloud layer by 1.3, 0.8 and 1.8 DFS in scenarios 1, 2, and 3, respectively, compared to the initial MWR+G2 configuration (see Fig. 5.15 b, d, f and Tab. 5.3).

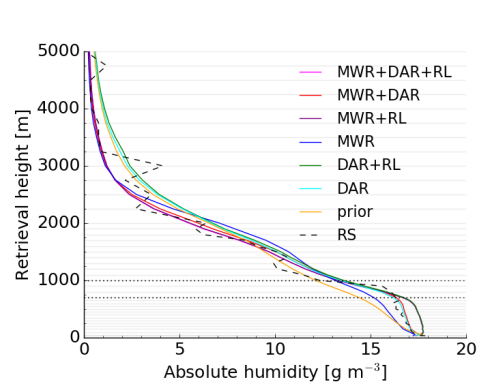

(a) Case 1, 10.02.20, 10:46 UTC

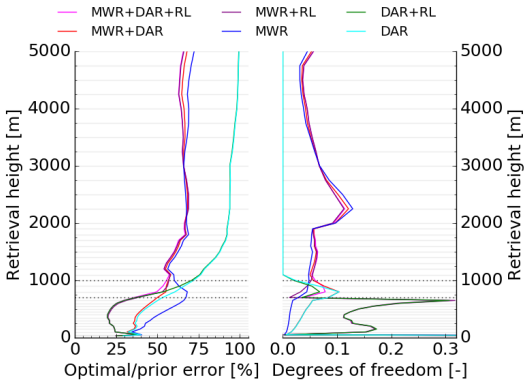

(b) Case 1, 10.02.20, 10:46 UTC

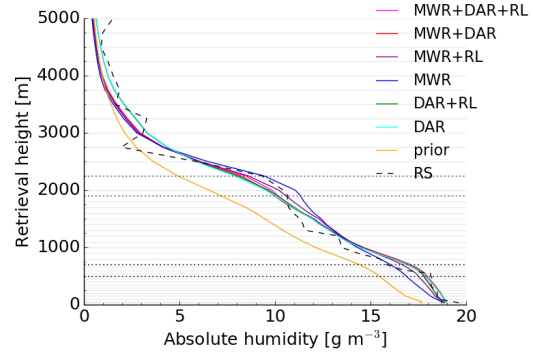

(c) Case 2, 12.02.20, 02:47 UTC

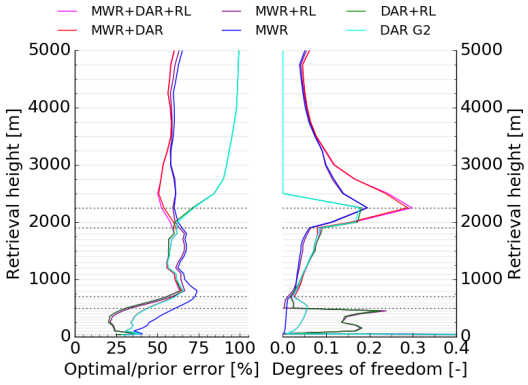

(d) Case 2, 12.02.20, 02:47 UTC

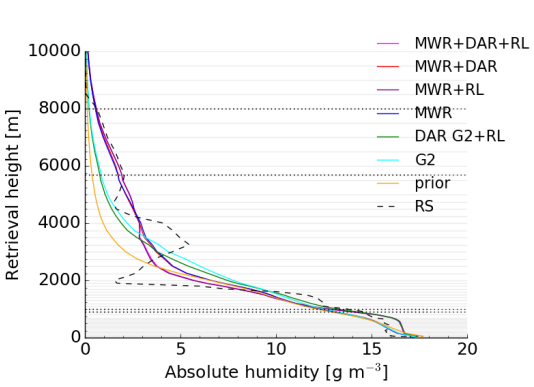

(e) Case 3, 13.02.20, 22:52 UTC

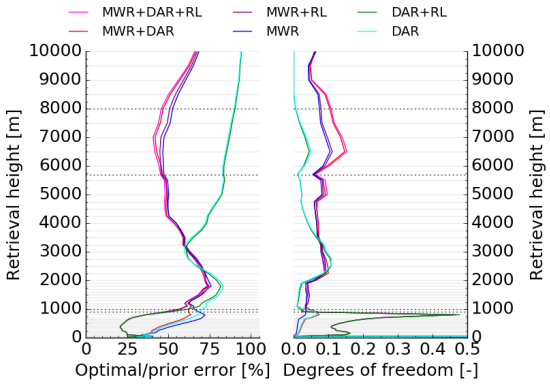

(f) Case 3, 13.02.20, 22:52 UTC

Figure 5.15 – (a, c, e) Retrieved absolute humidity profiles, (b, d, f) optimal to prior uncertainty ratio (left panel) and DFS (right panel) illustrated for synergistic MWR+DAR+RL (magenta), MWR+G2 (red), MWR+RL (purple), MWR-only (blue), DAR+RL (green), DAR-only (cyan) retrieval configurations for (a, b) case 1, 10.02.20, 10:46 UTC, (c, d) case 2, 12.02.20, 02:47 UTC, (e, f) case 3, 13.02.20, 22:52 UTC. The prior (orange) and original sounding (black) profiles were added to (a, c, e) for reference.

The sub-cloud layer information gain increases with the height of cloud base, i.e. the amount of added RL measurements. Corresponding to the increased information content, the optimal to prior uncertainty ratio decreases by 16.9, 13.6 and 26.2 percentage points compared to the initial MWR+G2 configuration in case 1, 2 and 3, respectively (see Fig. 5.15 b, d, f right panel and Tab. 5.3). Due to correlations, the synergistic error reduction propagates into the lowest cloud layer, further reducing the in-cloud MWR+G2 uncertainty by 3.8, 8.3 and 10.1 percentage points, respectively.

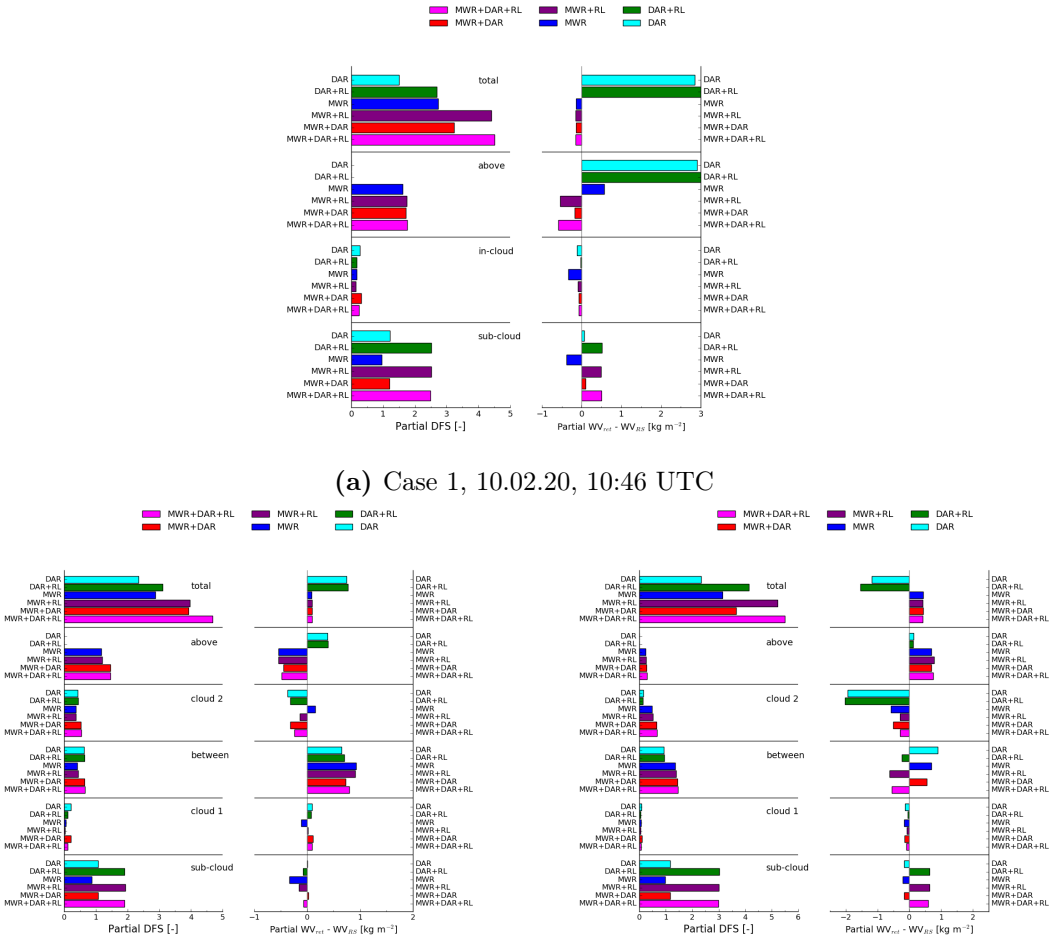

(a) Case 1, 10.02.20, 10:46 UTC

(b) Case 2, 12.02.20, 02:47 UTC

(c) Case 3, 12.02.20, 22:52 UTC

Figure 5.16 – Total and partial DFS (left panel), and total and partial water vapor amount discrepancy compared to sounding (right panel) for sub- and in-cloud, as well as between and above cloud layers for synergistic MWR+DAR+RL (magenta), MWR+G2 (red), MWR+RL (purple), MWR-only (blue), DAR+RL (green), DAR-only (cyan) retrieval configurations and prior (orange) for (a) case 1, 10.02.20, 10:46 UTC, (b) case 2, 12.02.20, 02:47 UTC, (c) case 3, 13.02.20, 22:52 UTC.

The addition of the lidar measurements reduces the information content in the cloud layer by up to 0.1 DFS (see Tab. 5.3), presumably because the DAR information regarding the sub-cloud partial water vapor amount is constrained due to the RL measurements. The retrieval uncertainty and information content in the height levels further above are not affected by the addition of the RL measurements. Adding RL measurements to the synergy also acts on the retrieved profile in the sub-cloud layer as seen in Fig. 5.15a, c, e. The well-mixed sub-cloud layer profile shape is better represented in case 1 and 3, but the introduced random σ_{RL} error leads to a bias of the profile within the assumed error margin. Therefore, also the retrieved sub-cloud layer partial water vapor amount is biased by 0.5 and 0.6 $\mathrm{kg\,m^{-2}}$ in case 1 and 3, respectively.

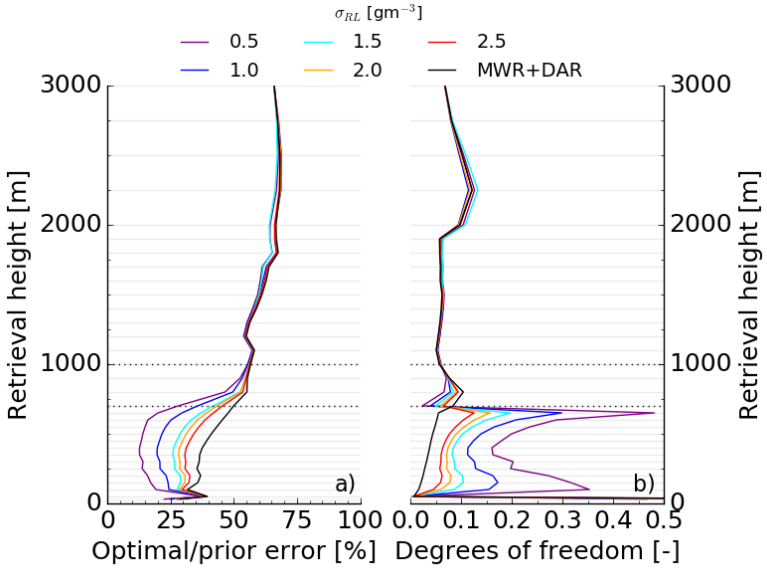

Figure 5.17 – (a) Optimal to prior uncertainty ratio, as well as (b) DFS for MWR+DAR+RL synergistic configurations assuming an RL measurement error σ_{RL} of 0.5 $\mathrm{g\,m^{-3}}$ (purple), 1.0 $\mathrm{g\,m^{-3}}$ (blue), 1.5 $\mathrm{g\,m^{-3}}$ (cyan), 2 $\mathrm{g\,m^{-3}}$ (orange) and 2.5 $\mathrm{g\,m^{-3}}$ (red). The results of the MWR+G2 configuration are added for comparison (black).

The sensitivity of the MWR+DAR+RL synergy to the assumed lidar measurement error σ_{RL} is tested using the single-layered scenario 1 by increasing the random noise factor and the $\mathbf{S}_e$ matrix diagonal elements in 0.5 $\mathrm{g\,m^{-3}}$ increments from 0.5 to 2.5 $\mathrm{g\,m^{-3}}$. As shown in Fig. 5.17, an increased lidar uncertainty leads to decreasing sub-cloud layer information content and increasing retrieval uncertainty, as expected as the RL observations dominate the sub-cloud layer retrieval. With the highest assumed error of 2.5 $\mathrm{g\,m^{-3}}$, the sub-cloud DFS would reduce to 1.6 DFS, a reduction of 0.9 DFS compared to the initial error assumption of 1.0 $\mathrm{g\,m^{-3}}$. The sub-cloud

information content would still be increased by 0.4 DFS compared to the MWR+G2 synergy. Correspondingly, the retrieval uncertainty half-way through the sub-cloud layer at 350 m would be increased by 11.0 percentage points compared to a RL error of 1.0 g m^{-3}, but still reduced by 5.9 percentage points compared to the initial MWR+G2 synergy. Due to the correlations with the lowest cloudy levels, the error at cloud base is reduced by up to 22.0 percentage points compared to the MWR+G2 configuration assuming a minimal RL uncertainty of 0.5 g m^{-3}. Throughout the cloud layers, the MWR+G2+RL uncertainty merges the initial MWR+G2 configuration. Depending on the error characteristics of the used Raman lidar system and its integration time, the analyzed uncertainties could be on the lower end, particularly when deploying the instrument at day time.

5.4.2 Evaluating Alternative Retrieval Setups

As seen in the previous section, expanding the observation vector $\boldsymbol{y}$ by additional RL measurements increases the sub-cloud layer information content and decreases the sub-cloud retrieval uncertainty, as expected. As additional synergistic benefits were found only in the lowest cloud layer, this section will focus on the evaluation of different retrieval configurations to optimize the retrieval performance between and above the cloud layers, based on all available MWR, DAR G2, RL and $\rho_{2\mathrm{m}}$ measurements. The analyses will be based on scenario 2, which allows the additional evaluation of the different configurations' performance for representing the moist versus free tropospheric water vapor conditions.

Several different observation vector $\boldsymbol{y}$ configurations, forward model parameters b, as well as a saturation constraining tool are evaluated as summarized in Tab. 5.4. All configurations include the $\rho_{2\mathrm{m}}$ measurement in the observation vector. The initial concept of combining MWR+G2 is added for comparison (Sec. 5.2) to the analysis (configuration (*i*)). The observation vector expansion by RL measurements (see Sec. 5.4.1) is represented by configuration (*ii*). In configuration (*iii*), the retrieval states were reduced to the height levels between and above the cloud layers. The humidity profile below and within the cloud layers was introduced to the retrieval configuration in the forward calculations as forward parameters $\boldsymbol{b}$ by fixing the respective states to the radiosonde humidity. The humidity profile information here could originate from an independent direct inversion retrieval of the DAR or RL measurements. The observation vector $\boldsymbol{y}$ here only comprises the MWR TBs and $\rho_{2\mathrm{m}}$.

Configuration (*iv*) introduces a saturation constraint to the MWR+DAR+RL setup which forces the in-cloud profile in each retrieval iteration to the observed reality as represented by the radiosonde measurements. As opposed to adding the DAR DWR measurements to the MWR+RL retrieval as in configuration (*ii*), configuration (*v*) represents the results for a configuration where the DAR in-cloud ρ_v and RL sub-cloud ρ_v are added to the observation vector $\boldsymbol{y}$ with a measurement uncertainty of $1.0\,\mathrm{g\,m^{-3}}$. The DAR humidity profiles could e.g. be derived by applying a direct inversion approach as presented in Roy et al. (2020).

Table 5.4 – Different retrieval configurations used to evaluate the optimal configuration for enhancing the DFS above and between the cloud layers, summarizing the measurements forming the observation vector $\boldsymbol{y}$, the additional forward model parameters $\boldsymbol{b}$, and whether the retrieval grid was reduced or a humidity saturation constraint was added to the retrieval. Also see text for more details.

configuration	observation vector $\boldsymbol{y}$	additional $\boldsymbol{b}$	retrieval grid	saturation
(*i*)	TB; DWR; $\rho_{2\mathrm{m}}$		full	no
(*ii*)	TB; DWR; $\rho_{2\mathrm{m}}$; RL		full	no
(*iii*)	TB; $\rho_{2\mathrm{m}}$	DAR ρ_v; RL	reduced	no
(*iv*)	TB; DWR; $\rho_{2\mathrm{m}}$; RL		full	yes
(*v*)	TB; DAR ρ_v; RL		full	no

When analyzing the retrieved profiles as illustrated in Fig. 5.18, only marginal differences of less than $1.0\,\mathrm{g\,m^{-3}}$ exist between the different configurations. As expected, the in-cloud humidity profiles of configuration (*iv*) and (*v*) correspond to the radiosonde profile. As shown in the previous Sec. 5.4.1, adding RL measurements to the observation vector acts primarily on the retrieval performance in the sub-cloud layer. Thus, as illustrated in Fig. 5.18, the optimal to prior uncertainty ratio in this configuration (*i*) decreases by 14.5 percentage points at e.g. 300 m, where the information content is increased by up to 0.1 DFS compared to the initial MWR+DAR concept. Presumably due to the correlations of the in-cloud and sub-cloud layer states, the retrieval error is further reduced by up to 6.3 percentage points throughout the first cloud layer compared to the initial concept, and merges the MWR+DAR uncertainty above the first cloud layer. A marginal error decrease of 2.0 percentage points is seen in the upper cloud layer at 2000 m.

As opposed to adding the RL humidity measurements to the observation vector $\boldsymbol{y}$, they can also be added to the forward model parameters $\boldsymbol{b}$ (see Rodgers, 2000; Maahn et al., 2020). Similarly, DAR in-cloud humidity profiles obtained e.g. through a direct inversion approach as presented in Roy et al. (2020) are added to $\boldsymbol{b}$ in

configuration (*iii*), fixing the humidity profile to the observed sounding profile. Then, the observation vector $\boldsymbol{y}$ consists of the MWR TBs and $\rho_{2\mathrm{m}}$, and the retrieval states can be reduced to the layers between and above the cloud layers. Correspondingly, the reduction of states also reduces the prior covariances and correlations, e.g. between sub- and in-cloud layers. No error correlations $\mathbf{S}_b$ were added to the $\mathbf{S}_e$ matrix.

The effects of missing correlation between sub- and in-cloud, as well as in-cloud and above-cloud layers lead to increasing retrieval errors around the cloud edges compared to a full retrieval grid as seen in Fig. 5.18. While the error and information content between the cloud layers at 1500 m is comparable to the general configuration (*i*) or (*ii*), a reduction of states does not seem to improve the retrieval performance above the upper cloud layer. As the lack of correlations additionally worsens the performance around the cloud edges, this tool does not seem suitable to optimize the retrieval performance, particularly as the uncertainties would further increase if $\mathbf{S}_b$ was specified.

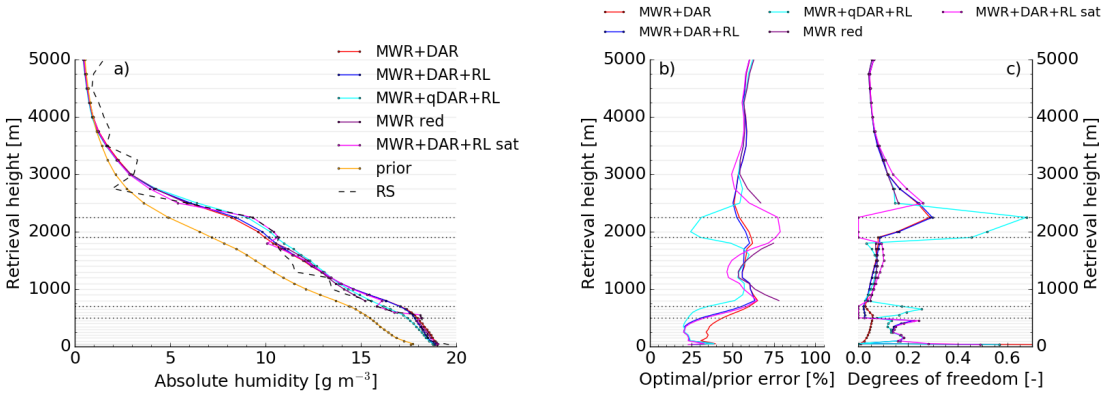

Figure 5.18 – Case 2, 12.02.20: (a) Retrieved absolute humidity profiles, (b) optimal to prior uncertainty ratio and (c) DFS illustrated for synergistic MWR+G2 (red; configuration (*i*)), MWR+DAR+RL (blue, configuration (*ii*)), MWR-only with reduced retrieval grid (purple, configuration (*iii*)), MWR+DAR+RL with saturation constraint (magenta, configuration (*iv*)), and MWR+DAR ρ_v+RL (cyan, configuration (*v*)) retrieval configurations. The prior (orange) and original sounding (black) profiles were added for reference.

As in reality the in-cloud humidity, particularly towards the cloud core, reaches saturation, this additional knowledge can be supplied to the retrieval by constraining saturation to the in-cloud humidity states as tested in configuration (*iv*). This saturation constraint requires the knowledge of the temperature profile, which, in this case, is given by the sounding profile. Practically speaking, this constraint forces the retrieved profile $\boldsymbol{x}_i$ in each iteration to the sounding humidity profile in the cloudy

states without reducing the retrieval grid to uphold correlations between the layers. In the particular case analyzed here, however, saturation was not recorded by the sounding in the first cloud layer. In order to avoid introducing artificial gradients to the humidity profile by forcing saturation to the cloud layer, the cloudy $\boldsymbol{x}_i$ states were set to the un-saturated sounding measurement within each iteration. As expected, the information content in each cloud layer thus reduces to zero (see Fig. 5.18c). Yet, as could be expected, the resulting in-cloud retrieval uncertainty increases as the calculation of $\mathbf{S}_i$ (see Eq. (3.3.3)) is disrupted due to the fact that $\mathbf{K}_i$ is calculated before $\boldsymbol{x}_i$ is forced to the observed radiosonde profile. Therefore, the in-cloud retrieval error is no longer comparable to the other configurations. As opposed to the reduced retrieval grid in configuration (*iii*), however, the correlations between the states allows the measurement's information to be transferred to non-cloudy retrieval states. Therefore, the information content increases slightly by 0.2 and 0.1 DFS between and just above the upper cloud layer, respectively (see Fig. 5.18c). This increase of information content corresponds to a retrieval uncertainty decrease of up to 9.2 percentage points at 1400 m and 4.2 percentage points at 3000 m compared to the initial MWR+DAR+RL concept (configuration (*ii*)), respectively (Fig. 5.18b).

As opposed to adding the DAR DWR measurements to the observation vector, the in-cloud humidity could be obtained from the DWR measurements using a direct inversion approach such as presented by Roy et al. (2020). Thus, as opposed to adding the DAR DWR measurements to the observation vector $\boldsymbol{y}$, the directly inverted humidity measurements DARρ_v could instead be added to $\boldsymbol{y}$ with their associated uncertainty, here assumed to be $1.0\,\mathrm{g\,m^{-3}}$. This adjusted configuration (*v*) leads to increasing DFS by 0.6 and 1.1 in the lower and upper cloud layer, respectively (see Fig. 5.18c). The sub-cloud layer uncertainty is driven by the RL measurements, while the reduced DAR uncertainty in comparison to configuration (*ii*) acts most on the in-cloud uncertainty, reducing the optimal to prior uncertainty ratio by 18.1 and 33.3 percentage points at 600 and 2000 m, respectively, as seen in Fig. 5.18b. Between the cloud layers, the improvement is most pronounced above the first cloud between 800 and 1200 m, and below the second cloud layer between 1700 and 1900 m. Here, at 900 and 1800 m, respectively, the uncertainty is further reduced by 6.0 and 11.4 percentage points compared to the initial MWR+DAR+RL configuration (*ii*).

Of course, this effect strongly depends on the measurement uncertainties of the direct inverted humidity profile from the DAR observations. Further studies will investigate the relation between the assumed DWR error and DAR ρ_v error, as a

DWR uncertainty of 0.56 dB might not correspond to a direct inversion error of $1.0\,\mathrm{g\,m^{-3}}$ using the method by Roy et al. (2020). In the theoretical case of the DAR ρ_v error converging towards 0, the uncertainty would further reduce with simultaneous information gain. This theoretical configuration would then imitate an in-cloud saturation constraint while upholding the state correlations and uncertainty calculation.

5.5 Summary and Discussion

The synthetic analysis of the synergy concept potential was expanded to more realistic, increasingly complex cloudy scenarios based on selected cases observed during the EUREC^{4}A campaign. Three representative water vapor and cloud scenarios were chosen to test the synergy concept for the expected scene variability at BCO:
(i) a daily observed scene characterized by a single shallow cumulus cloud layer forming at LCL;
(ii) a double-layered liquid cloud scenario with a shallow cumulus cloud layer based at LCL, topped by a stratiform liquid outflow trapped under the trade inversion; and
(iii) a scene with an elevated moisture enclosure forming in the dry subsidence zone above the trade inversion, associated with the formation of an altocumulus layer. Synthetic MWR and DAR G2 observations were generated using the forward model PAMTRA, including assumptions about the DSD as well as the liquid content partitioning and cloud phase.

A standard retrieval approach using a sounding climatology was selected in order to investigate the vertical information distribution and synergistic benefits in the different scenarios. In all three cases, a synergistic error reduction and information content increase compared to a MWR-only or DAR-only retrieval can be noted above each cloud layer, and within the upper parts of each cloud layer. More specifically, in case of the (i) single-layer cloud scenario, the synergistic error reduces by up to 10.3 and 8.1 percentage points compared to the MWR-only and DAR-only configuration, respectively. This effect is expected to increase with a thicker cloud layer, as more DWR observations add more information to the in-cloud retrieval, which redistributes the MWR information to above the cloud layer where no DAR measurements are available.

In the double-layered cloud scenario (ii), the area above the upper cloud experienced the highest benefits, with errors decreasing by up to 11.1 percentage points and the information content increasing by 0.3 DFS above the upper cloud compared to the MWR-only configuration, respectively. In this case, all information content below the second cloud layer originates from the DAR observations. In total, the overall synergistic DFS increase by 1.0 and 1.6 DFS compared to the MWR- and DAR-only configurations. In the presence of an elevated moisture layer in case (iii), none of the configurations resolve the humidity gradients of the advected moisture in the free troposphere. An information content increase of 0.1 DFS between the cloud layers compared to the MWR-only setup results in a reduction of the synergistic partial water vapor amount overestimation of $0.2\,\mathrm{kg\,m^{-2}}$ compared to the sounding amount. In the second cloud layer, the synergistic configuration's retrieval information content increases by 0.2 and 0.5 DFS compared to the MWR- or DAR-only configuration.

Though specific to the particular retrieval solutions, the analysis of the retrieved water vapor amounts revealed in all cases no synergistic impact to the total water vapor compared to the MWR-only derived IWV, which showed a discrepancy of less than $0.5\,\mathrm{kg\,m^{-2}}$ in all cases. Yet the analysis of the partially integrated water vapor amounts revealed that the synergistic configuration improved the representation particularly between and above the cloud layers compared to the MWR-only retrieval, corresponding to the heights of increased information content. As seen in the EUREC^{4}A sounding data in Sec. 3.1.2, the largest water vapor variability is expected around the cloud layer forming around LCL (as seen in all three considered scenarios), and around the trade inversion, often characterized by a cloud layer trapped below the inversion as seen in scenario 2. Concluding on research question 3, the synergistic retrieval in the selected cases enhances the information content and reduces the retrieval uncertainty in the upper parts and above each of these cloud layers associated with the zones of enhanced water vapor variability.

The presented results, however, are affected by additional uncertainties due to the assumptions made about the DSD, LWP and LWC, particularly when partitioning the LWP to the respective cloud in case of multiple cloud layers. In a modified retrieval concept, these uncertainties can be accounted for by including the forward model error matrix $\mathbf{S}_b$ (Rodgers, 2000) to the measurement uncertainty matrix $\mathbf{S}_e$. In-situ measurements made during EUREC^{4}A can help constraining the DSD and LWC assumptions and uncertainties for the respective cloud conditions. While full-cloud profiling was assumed in the retrieval analysis, the reflectivity signal of

the thin stratiform outflow might in reality be below the radar sensitivity threshold as shown in Fig. 5.3. In order to overcome this constraint in a real application, the radar integration time could be increased as the stratiform outflow layers tend to be quite stationary (Nuijens et al., 2014). Future instrumentation's sensitivity is expected to increase with increasing transmitter powers.

In order to further constrain the retrieval to the observed conditions, independent observations could be used to customize the prior profile $\boldsymbol{x}_a$ and covariances $\mathbf{S}_a$ to the expected conditions. In particular a more precise knowledge of the trade inversion height and its associated humidity gradient would constrain the possible humidity profile solutions and the resulting partitioning of dry tropospheric versus moist boundary layer water vapor amount. As such observations are not available and, thus, cannot be included through the observation vector $\boldsymbol{y}$, a modified prior based on independent measurements of e.g. IWV or $\rho_{2\mathrm{m}}$ could be used constrain the retrieval to the expected conditions by reducing the covariances in the correct heights through a threshold-based approach. First analyses of the EUREC^{4}A BCO soundings signalized that an IWV-threshold of $33.70\,\mathrm{kg\,m^{-2}}$ or $\rho_{2\mathrm{m}}$-threshold of $17.68\,\mathrm{g\,m^{-3}}$ could be applied in order to sort the sounding profiles used for determining the climatological prior profile $\boldsymbol{x}_a$ and covariances $\mathbf{S}_a$ in order to influence the height of the humidity gradient and maximum covariance peak as seen in Fig. 5.19.

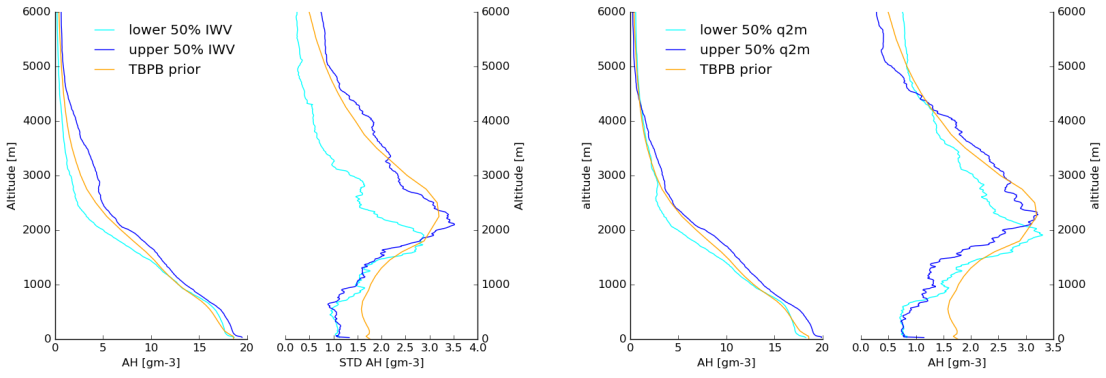

Figure 5.19 – Mean and standard deviation profile of absolute humidity measurements where (a) IWV was below (cyan) or above (blue) a median IWV-threshold of $33.70\,\mathrm{kg\,m^{-2}}$; and (b) $\rho_{2\mathrm{m}}$ was below (cyan) or above (blue) a median $\rho_{2\mathrm{m}}$-threshold of $17.68\,\mathrm{g\,m^{-3}}$, calculated for 182 ascending soundings at BCO during EUREC^{4}A . The climatological prior based on the GAIA soundings was added for reference (orange).

A limitation of this approach would include limited convergence in case the actual conditions differ from the prior predictions and, thus, temporal gaps when used

on an operational basis. By including a Kalman-filter as discussed in Foth and Pospichal (2017) for a MWR and Raman lidar synergy, the prior could be adjusted by additional Raman lidar measurements while accounting for the uncertainty in those measurements. Future studies could analyze the impacts of the threshold-based and Kalman-filter approach to the synergistic benefit and retrieved profile accuracy with a special focus on improving the height of the humidity gradient.

The question whether and where the synergistic retrieval can add more information to the retrieved state when reconstructing the atmospheric humidity profile between two operational soundings spaced by 24 hours was analyzed based on the same scenarios, assessing research question 4. In an adjusted retrieval approach, the prior profile was determined by a temporal interpolation at 12 hours past the initial, and 12 hours before the next operational sounding. Sounding data available from the EUREC^{4}A field study revealed the highest temporal variability in a 24-hour window around LCL and the trade inversion. Resolving research question 4, the information added from the synergy is enhanced in the areas of highest water vapor variability, where the error of the interpolated profile is largest. For example, the synergistic information content around the trade inversion in scenario 2 is enhanced by up to 0.2 DFS compared to the MWR-only configuration, accompanied by an uncertainty reduction of 6.1 percentage points just above cloud top. This increase of information content leads to an improved representation of the free tropospheric water vapor amount above the cloud layer of 3.6 $\mathrm{kg\,m^{-2}}$ compared to the interpolated prior amount, specific to this case and solution.

Compared to the retrieval configuration using a climatological prior, the synergistic information content gain is reduced to 0.2 - 0.6 DFS, as expected, as the prior represents the expected conditions better. Yet, when reconstructing an atmospheric state, this method seems to be more suitable, as humidity gradients could be resolved due to the more accurate prior conditions. The method of including Raman lidar measurements in order to derive a more accurate prior through a Kalman-filter approach as presented in Foth and Pospichal (2017) could be expanded to this synergy concept to further improve the reconstruction of the atmospheric conditions. In order to further generalize the effect on the derived partial water vapor amounts, the case study examples will be expanded to a larger statistics, e.g. using the whole EUREC^{4}A sounding dataset. Further studies will also include the analysis of the added information at other temporal interpolation points, and will include the effects of the spatial distance of BCO to GAIA, motivated by the mid-latitude analyses

presented in Löhnert et al. (2007). The method introduced therein to analyze the potential of the synergy for data assimilation or now-casting applications could additionally be tested for this synergy concept.

Expanding the synergy concept to other available measurements at BCO, the impacts of adding synthetic Raman lidar (RL) observations to the observation vector $\boldsymbol{y}$ have been assessed in order to quantify the synergistic benefits for the sub-cloud layer, and in order to evaluate modified retrieval setups to optimize the retrieval performance between and above the cloud layers as summarized in research question 5. As expected, the additional RL measurements dominate the retrieval in the sub-cloud layer as analyzed for the three EUREC^{4}A scenarios, determining the shape of the sub-cloud profile. The MWR+DAR+RL configuration shows increased sub-cloud layer DFS of 0.8 - 1.3 DFS, and a reduced optimal to prior uncertainty ratio of 13.6 – 26.2 percentage points compared to the MWR+DAR synergy when assuming a RL error of 1.0 g m^{-3}. The synergistic benefits enhance in the case of a higher cloud base due to a larger number of added RL measurements. Due to correlations, the uncertainty in the lowest cloud layer is also reduced, more precisely by 3.8 – 10.1 percentage points compared to the MWR+G2 setup. As expected, the synergistic benefit is sensitive to the RL measurement error, and decreases the synergistic sub-cloud benefit to 0.4 DFS and error reduction to 5.9 percentage points compared to the initial MWR+G2 configuration when assuming an error of 2.5 g m^{-3}. As the synergistic benefits strongly vary depending on the instrument-specific RL uncertainty which strongly depends on daytime solar signal contamination and temporal integration, a thorough error quantification is indispensable for more realistic measurement conditions.

In order to investigate how the retrieval concept using the same measurements could be modified in order to enhance the retrieval performance in the cloud-free areas between and above the cloud layer, several theoretical concept modification tools were evaluated based on scenario 2. Specifically, different configurations of the observation vector $\boldsymbol{y}$ and the forward parameter $\boldsymbol{b}$, as well as a retrieval saturation constraint tool have been compared to the standard MWR+DAR and MWR+DAR+RL configurations based on the resulting information gain and uncertainty decrease between and above the cloud layers. Out of all assessed configurations, the retrieval uncertainty between the cloud layers is most decreased compared to the initial MWR+DAR+RL configuration around the cloud edges in case RL and DAR humidity profiles obtained from direct inversion methods complement the MWR TBs in

the observation vector. Then the retrieval uncertainty e.g. at 1900 m is reduced by 11.4 percentage points compared to the initial MWR+DAR+RL configuration. Careful error evaluation regarding the consistency between DWR uncertainty and direct inversion humidity error is required in further studies to confirm this result. Imposing the knowledge of the in-cloud humidity profile through a saturation constraint yields to decreasing errors between the cloud layers around 1500 m, but is not feasible in reality, as the temperature profile would not be known. Including this constraint into a combined temperature and humidity retrieval such as presented in Löhnert et al. (2007) would allow further analyses. None of the evaluated modified concepts led to increasing information content or significantly reduced retrieval uncertainty above the cloud layer. Concluding on research question 5, additional RL measurements dominate the sub-cloud layer retrieval, while a modified approach of including low-uncertainty DAR and RL measurements to the observation vector could decrease the retrieval uncertainty additionally between the cloud layers compared to the MWR+DAR+RL retrieval configuration.

A combined humidity and temperature retrieval could be realized by expanding the observation vector with temperature sensitive V-band HATPRO TBs, e.g. obtained in elevation scans (Crewell and Löhnert, 2007). Adding an additional 90 GHz-channel to the retrieval would foster the derivation of the LWP without reducing the available information content for the water vapor states. In order to overcome potential radar sensitivity constraints, different radar frequencies could be selected, e.g. lower down on the wing of the 183 GHz absorption line. While lower frequencies would decrease the differential signal amplitude, decreased signal attenuation along the beam path would ensure full-cloud profiling also in case of multiple cloud layers. In order to reduce the uncertainty of water vapor amount available in the moist and dry troposphere, a question central to model evaluation (e.g. Holloway and Neelin, 2009), a modified retrieval concept could be evaluated in a future study. The state vector $\boldsymbol{x}$ could be reduced to retrieve the partial water vapor amount below, in, and above the cloud layer, as well as humidity gradients at the respective boundaries. Forward model parameters could include proxies for the mixedness of the sub-cloud layer, for the humidity gradient throughout the cloud layer, as well as for the height of the trade inversion. An additional measurement of the trade inversion height would further help to allocate the humidity to the correct tropospheric layer.

The results of this study are limited by some important factors. First, the analysis is based on three selected cases, which represent the observed variability, but cannot

cover all possible atmospheric conditions. An increased number of scenarios will be analyzed in order to draw conclusions based on a statistical sample larger than the here presented analyses, which is crucial for profound conclusions regarding the precision of the derived partial water vapor amounts. More precisely, all soundings launched at BCO can be combined with cloud macro- and microphysical properties as derived from the Cloudnet dataset in order to simulate a larger number of realistic conditions, covering a wider range of the expected water vapor and cloud variability. Secondly, the presented synergy concept has not been tested on real data. Real measurements would include additional error sources e.g. due to different volumes observed due to different field of view sizes. For a concept evaluation under real conditions, VIPR could be run e.g. in close vicinity of a multi-channel K-band MWR like the HATPRO. Thirdly, current G-band radar sensitivity thresholds might inhibit full-cloud profiling, and, thus, reduce the synergistic benefits in tropical moist conditions. Alternative applications of the synergy concept to overcome this application constraint will be further discussed in the following chapter based on an outlook on the air-/spaceborne application, and the application in a drier environment.

6 Outlook: Changing Perspectives

The analyses discussed earlier in this thesis were centered around the potential of the synergy concept for a ground-based deployment in the trades which suggested synergistic benefits for the MWR+G2 combination above each cloud layer for the analyzed scenarios. Yet the simulated measurements and results also indicated potential radar signal saturation constraints given currently available G-band technology such as described in Roy et al. (2020) or Cooper et al. (2018). Therefore, this chapter will present and discuss outlook ideas regarding other potential synergy applications based on first idealized forward simulated measurements for an airborne application on HALO in the trade environment (Sec. 6.1), and for a ground-based application in the Arctic at Ny-Ålesund, Spitsbergen (Sec. 6.2).

6.1 Airborne Application

In order to get an idea of what potential G-band airborne measurements for the scenarios presented in chapter 5 might look like, simulations of a nadir-loooking instrument deployed e.g. on HALO have been generated by modifying the strategy described in Sec. 3.2 and Sec. 5.1. Motivated by typical flight altitudes used during the NARVAL studies (Stevens et al., 2019), measurements were generated for an aircraft flying at 8000 m altitude over an ocean surface. The vertical radar range resolution was assumed to be 150 m with a reflectivity sensitivity threshold of -50 dBz at 1 km, decreasing with distance squared. Partial volume filling effects were prevented by setting the cloud boundaries to simulation grid levels, adjusting them to the closest grid level maximum 50 m higher or lower.

In order to account for the background emissions in the simulations (also see Sec. 2.1), further assumptions had to be made in the forward simulations regarding the surface conditions and emission ϵ. As ocean surface emissivity depends on sea roughness and foam coverage, the FAST microwave Emissivity Model (FASTEM,

Liu et al., 2011), implemented in PAMTRA, uses the surface wind speed to account for the induced differences compared to a calm sea surface (Mech et al., 2020). In the simulations, the lowest radiosonde levels of each respective scenario have been averaged to estimate the ground wind speed. SST was estimated based on the lowest respective radiosonde temperature measurements.

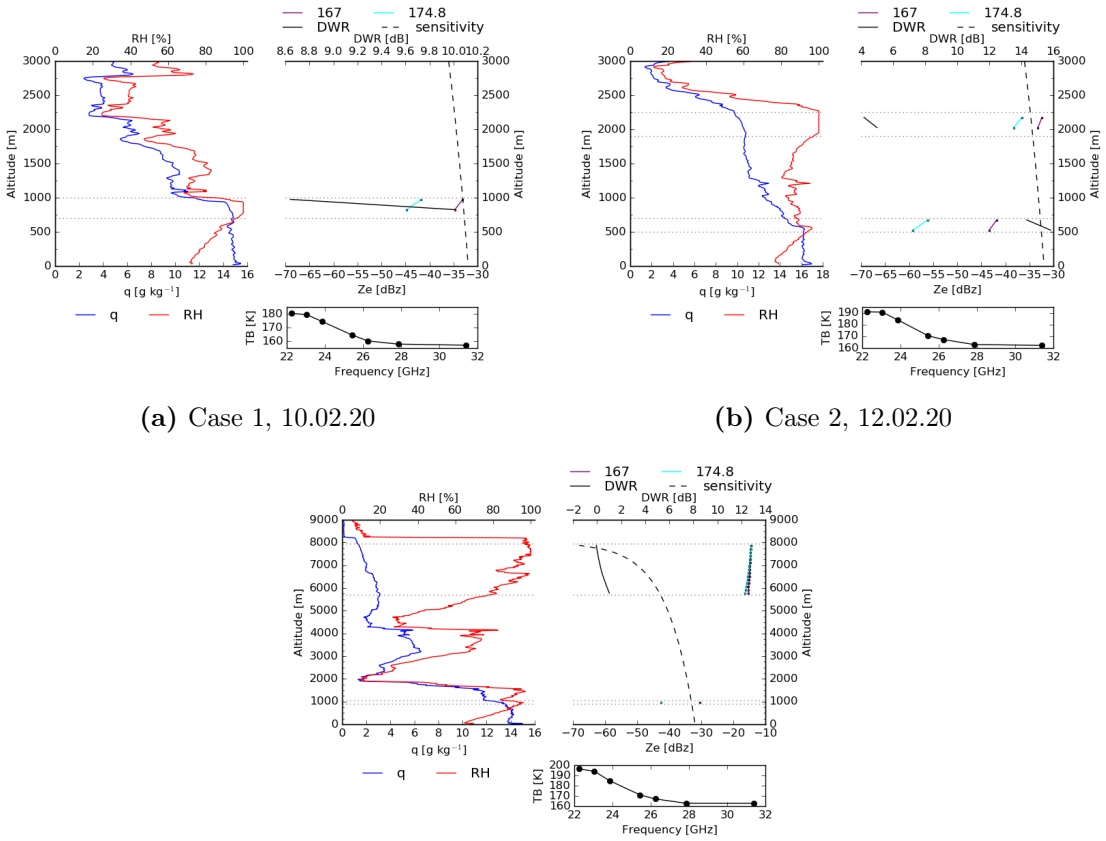

(a) Case 1, 10.02.20

(b) Case 2, 12.02.20

(c) Case 3, 13.02.20

Figure 6.1 – Sounding specific (blue) and relative humidity (red) (left panel) as well as simulated MWR TBs (black) and G-band reflectivities at 167 GHz (purple) and 174.8 GHz (cyan) with resulting DWR profile (black) (right panel), simulated for an airborne deployment with flight altitude of 8 km for (a) scenario 1, 10.02.20, (b) scenario 2, 12.02.20, and (c) scenario 3, 13.02.20.

At a flight altitude of 8000 m, the shallow clouds forming around LCL would not be detected by the radar in any of the simulated scenarios, assuming a −50 dBz sensitivity threshold 1 km below the aircraft. The signal at 167 GHz would be detected throughout the upper cloud layer in scenario 2, while the 174.8 GHz-signal would be saturated. The radar signal in both frequencies would penetrate the ice cloud in scenario 3, but the resulting differential DWR signal would be within the assumed noise range. In reality, DSDs, IWP and LWP might vary, affecting the

simulated reflectivities. Higher cloud altitudes due to higher LCL or trade inversion heights might additionally facilitate cloud detection.

In order to increase the radar sensitivity, the true signal integration time could be increased to e.g. 1 s, an integration time used by the HAMP-MIRA radar on HALO (Mech et al., 2014; Ewald et al., 2019). Yet longer integration times would enlarge the horizontal footprint size due to aircraft movements. For example, assuming VIPR's beam width of 0.24° (Roy et al., 2020), a HALO true ground speed of around 190 m s^{-1}, and a flight altitude of 8 km, the longer axis of the resulting elliptical footprint at ground would reach about 260 m. Depending on the respective horizontal variability of the water vapor field, however, larger footprints might only induce little uncertainties when the radar signals are used exclusively for water vapor profiling or estimation of partial water vapor contents. During the circle patterns performed in EUREC^{4}A, the total water vapor amounts generally changed little between 2 dropsondes launched within a 5-minute window or 58 km spatial distance. In the presence of cold pools, however, or on the edge of advected moisture layers, a higher horizontal resolution might be desired to resolve horizontal moisture gradients. An alternative decreased vertical resolution of larger than the here assumed 150 m would also increase the sensitivity, but this decreasing resolution might impair the quantification of dry versus moist tropospheric water vapor amount, and the associated gradient around the trade inversion.

Increasing radar sensitivities could also be reached by flying on lower altitude levels. The radar signal simulated at a flight altitude of 5 km would detect the upper cloud layer in scenario 2, while the low cloud would not be profiled (not shown). In scenario 1, only the signal at 167 GHz would penetrate the cloud layer. Potential flight patterns could include altitude changes depending on the cloud scenes in order to incorporate the detection of higher occurring moisture layers. In a real application, however, the deployment of the instrument would also be limited to high enough altitudes where the clear-sky ground return signal would not be too strong for the instrument receiver electronics. Higher flight levels, like FL320 (around 9800 m) on which HALO's circle flight pattern during EUREC^{4}A was flown, however, would require more powerful transmitted signals to reach sufficient sensitivities.

A benefit of an airborne deployment compared to a ground-based installation is the derivation of the water vapor amount between ground and aircraft in clear-sky scenarios due to the ground return signal. For a successful retrieval, however, the optimal estimation would need to incorporate the ground

emissivity. Further synergies, e.g. with the IR camera deployed during EUREC^{4}A on HALO (`http://eurec4a.eu/platforms/halo`), could offer an additional observation of the SST. The synergy concept discussed in this thesis could be realized by combining the radar measurements with the HAMP radiometers (Mech et al., 2014; Schnitt et al., 2017; Jacob et al., 2019). The synergy could be further extended by including all or some of the 26 HAMP passive channels, which would allow and improve a simultaneous LWP retrieval, particularly when including the 90 GHz channel (Crewell and Löhnert, 2007). HAMP's passive G-band channels could offer additional information to the retrieval in the dry free troposphere above the trade inversion (e.g. Zuidema et al., 2012a). Yet additional error sources would arise due to mis-matching footprints and footprint sizes, and aircraft movement. In case of increased radar sensitivities, these airborne observations could e.g. be used to evaluate satellite retrievals based on the observations by the Microwave Humidity Sounder (MHS) on the Meteorological Operational Satellite (MetOP), or SSMI/S on the DMSP satellites.

6.2 Dry Arctic Environment

Drier water vapor conditions as observed in the Arctic would reduce G-band signal attenuation compared to the moist conditions in the trades. At Ny-Ålesund (NYA), Spitsbergen, IWV amounts do not exceed 8 or 20 $\mathrm{kg\,m^{-2}}$ in the winter and summer months, respectively (Nomokonova et al., 2020), promising dry conditions year-round. A prevalent cloud type frequently observed at NYA are mixed-phase stratiform clouds (MPC) (Gierens et al., 2020) which have various lifetimes varying between hours and days (Shupe et al., 2006; de Boer et al., 2009; Morrison et al., 2012). MPC are prevalent across the whole Arctic region (Shupe, 2011; Mioche et al., 2015), are commonly associated with temperature or specific humidity inversions occurring above cloud top (e.g. Curry et al., 1996; Naakka et al., 2018; Devasthale et al., 2011; Sedlar et al., 2012); their cloud properties are crucial for quantifying cloud radiative effects (Sun and Shine, 1994; Shupe and Intrieri, 2004; Ebell et al., 2020). The role of specific humidity inversions in providing moisture for the formation and maintenance of MPC layers has been identified in modelling (Solomon et al., 2011, 2014) and observational (Sedlar et al., 2012) studies. A full understanding of the small-scale interplay between enhanced humidity at cloud top and cloud properties and lifetime, however, would require more detailed observations of both humidity

profiles and cloud properties (Egerer et al., 2020). As a deployment of a G-band radar has been evaluated as promising in simulations for ice-cloud conditions in high latitudes (Battaglia and Kollias, 2019), this instrument could provide the needed continuous water vapor profiles, particularly when operated in synergy with a MWR.

A suitable case to simulate G-band radar reflectivity measurements for these typical MPC conditions is given by the remote sensing and sounding measurements on 08.03.2017 at AWIPEV station, NYA, maintained by the Alfred Wegener Institute Helmholtz Centre for Polar and Marine Research (AWI) and the Polar Institute Paul Emile Victor (PEV). While ceilometer and MWR have been operational since 2011 (Maturilli and Ebell, 2018), a W-band radar was added to the suite of remote sensing instruments in 2016 (Küchler et al., 2017; Gierens et al., 2020)[1]. Based on these measurements, the Cloudnet algorithm (Illingworth et al., 2007) provides e.g. a cloud target classification product based on these instruments (Nomokonova et al., 2019). Radiosonde profiles are usually available every 24 hours (Maturilli and Kayser, 2017).

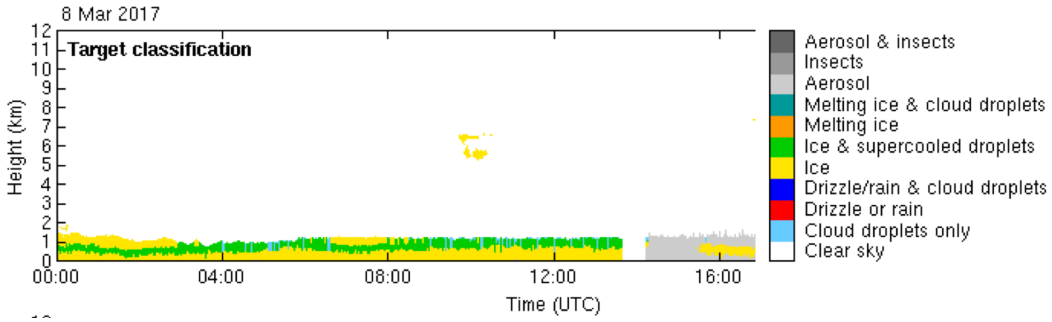

Figure 6.2 – Cloudnet cloud target classification at Ny-Ålesund on 08.03.2017.

As seen in Fig. 6.2 in the illustrated Cloudnet target classification data, on 08.03.17 a long-lasting stratiform mixed-phase cloud persisted throughout most of the day dissolving around 14:00UTC. Both the Cloudnet measurements as well as the sounding profile depicted in Fig. 6.3 report the layer between between 900 and 1300 m. Above cloud top, a temperature inversion is located up to 1550 m. The temperature inversion is associated with increasing humidity right above cloud top, and an additional moisture layer forming between 1500 and 2000 m, advected through westerly winds as recorded by the sounding which match the results found in Gierens

[1]Data copyright with AWI and University of Cologne, supported by the Transregional Collaborative Research Center (TR 172) project "Arctic Amplification: Climate Relevant Atmospheric and Surface Processes, and Feedback Mechanisms (AC)[3]".

et al. (2020). The recorded conditions were quite dry with an IWV of 3.5 kg m^{-2} as measured by the sounding.

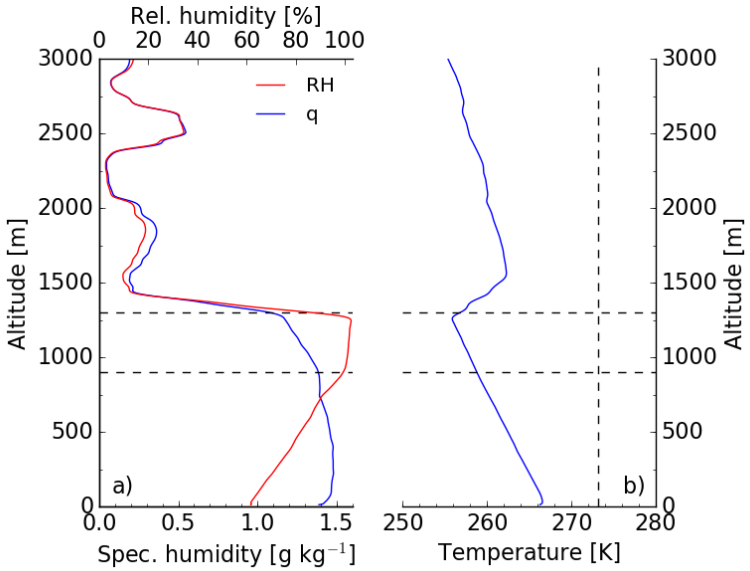

Figure 6.3 – Profile of (a) specific (blue) and relative (red) humidity, as well as (b) temperature recorded by sounding launched at Ny-Ålesund on 08.03.2017 for the 12 UT time, with cloud base and top level (dashed black) as identified from Cloudnet observations.

In order to gain initial insights into expected ground-based measurements, synthetic radar measurements were generated by the PAMTRA model based on the sounding profile (also see Sec. 3.2). In order to model the cloud parameters, idealized climatological literature values were attributed, as the HATPRO was not operational. Gierens et al. (2020) found a LWP of 42 g m^{-2} and an IWP of 16 g m^{-2} for low-level MPC in comparable synoptic situations at NYA based on 2.5 years of data. According to the airborne in-situ observations of several flight campaigns in the Svalbard region, Mioche et al. (2017) find that LWC increases throughout the MPC layer due to condensational growth processes, while IWC does not show a a significant vertical variability. In the simulations, liquid hydrometeors were distributed following a log-normal PSD with $r_{eff} = 5.0\,\mu m$ and $\sigma = 0.3$ (Ebell et al., 2020), while a mono-disperse ice PSD was calculated based on the mass mixing ratio input (Mech et al., 2020).

With these specific micro- and macrophysical cloud assumptions, the simulated reflectivities of -15.4 (-17.3) decrease to −16.3 dBz (−18.5 dBz) throughout the cloud layer at 167 and 174.8 GHz, respectively. The radar signal, thus, would not be attenuated in case the radar system had a reflectivity sensitivity threshold of

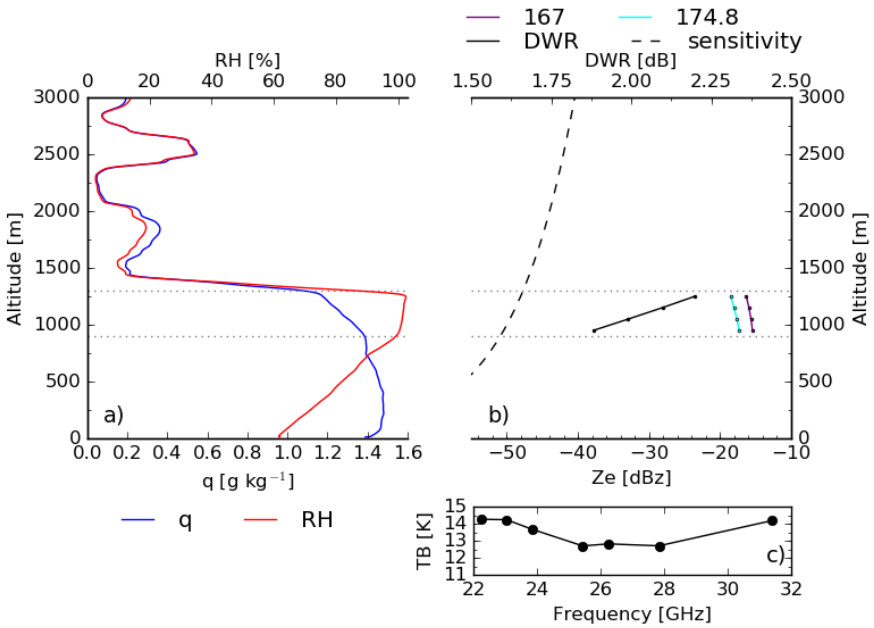

Figure 6.4 – Ny-Ålesund 08.03.17, 10:46 UTC: (a) Sounding specific (blue) and relative humidity (red) profiles, as well as simulated (b) G-band reflectivities at 167 GHz (purple) and 174.8 GHz (cyan) with resulting DWR profile (black), and (c) MWR TBs (black). The estimated G-band radar sensitivity at each radar range gate is added (dashed) in (b).

−50 dBz at 1000 m. From the simulated reflectivities, DWR signals of 1.9 - 2.2 dB result. As the considered case is fairly dry, the DWR amplitude and signal dynamic range are expected to increase in case of moister conditions as observed e.g. in the summer months.

Of course the simulated radar measurements strongly depend on the PSD and cloud phase distribution assumptions, particularly in the case of MPC, where the distribution of phases is not yet fully understood. Depending on the phase, temperature, and size of the hydrometeors, liquid and ice particle attenuation varies as a function of height throughout the cloud layer as shown in Battaglia and Kollias (2019). Potential Mie scattering effects due to various ice particles in the radar volumes could introduce differential scattering signals. Therefore, as opposed to the DWR signal obtained in the pure liquid clouds as discussed earlier in this thesis, the signal can, thus, not be directly related to water vapor differential attenuation. A modified retrieval approach would need to either make assumptions about the PSD through the forward model parameters with their associated errors, or would need to include the suitable states like LWC or IWC as well as PSD parameters (Maahn and Löhnert, 2017). Additional measurements that could deliver

the necessary information could include passive high-frequency channels, as available in the Microwave radar/radiometer for Arctic Clouds Mirac-P instrument (Mech et al., 2019); the actual reflectivities; a third radar wavelength (Gaussiat et al., 2003); or spectra from Doppler cloud radar measurements (Verlinde et al., 2013; Gierens, 2020).

Additional simulated measurements covering the variability of observed water vapor and cloud conditions at Ny-Ålesund would provide a more complete picture of the expected conditions. In a future simulation study, the differential scattering effects at the G2 frequencies, but also at varying frequency spacings, can be quantified for different PSDs. Co-located airborne cloud in-situ measurements such as performed during the ACLOUD/PASCAL field study (Wendisch et al., 2019; Ehrlich et al., 2019) or the MOSAIC expeditions (`http://mosaic-expedition.org`) can help to further constrain the PSD assumptions made in the forward model. Then, based on a theoretical feasibility study, the potential for expanding the synergy concept of combining MWR and G-band radar to the dry arctic environment could be assessed, e.g. with a special focus on the interplay between MPC lifetime and properties and humidity structure.

7 Conclusion and Discussion

Water vapor and cloud feedback processes manifest one of the largest sources of uncertainty in global climate prediction models. The water vapor structure is fundamental for clouds, convection and circulation processes, particularly in the tropical trade wind maritime regions where observations are scarce, and clouds are small but ubiquitous. Short- and long-term observations based on intensive field study operations or continuous observatory observations, respectively, are needed to advance process understanding and to evaluate model parametrization and performance. Yet global observation systems lack continuous, high-resolution water vapor observations of the atmospheric structure. Ground-based remote sensing applications suffer from saturation at cloud base in case of visible/infrared instruments, or lack of vertical resolution in case of passive microwave sounders, which penetrate clouds.

Therefore, in this thesis, a novel synergistic retrieval concept of combining dual-frequency radar and MWR measurements has been conceptualized, developed and evaluated for typical trade wind conditions based on synthetic feasibility studies. The proposed synergy concept combines the advantages of each instrument: while the MWR is most sensitive to the integrated column water vapor amount and can provide coarsely resolved water vapor profiles, the differential radar measurements constrain the retrieval of sub-cloud layer water vapor amount, as well as the profile in the cloud layer(s). The 2 m absolute humidity $\rho_{2\mathrm{m}}$, as well as measurements of the cloud boundaries further constrain the retrieval. The Dual-Wavelength Ratio (DWR) of two radar frequency pairs were analyzed: a pair of available Ka- and W-band radars e.g. at BCO (KaW), and a pair of G-band frequencies (167.0 and 174.8 GHz, G2), motivated by the first Differential Absorption Radar (DAR) prototype (Roy et al., 2020). Synthetic measurements were generated using the PAMTRA forward model (Mech et al., 2020) based on radiosonde thermodynamic profiles from Barbados, while assumptions regarding the cloud DSD and LWC were made based on climatological information. A random noise error was added to the measurements to simulate

calibration uncertainties. No radar sensitivity threshold was applied to the synthetic observations.

An optimal estimation retrieval method (Rodgers, 2000) was chosen to assess the synergistic benefits of the instrument combination based on the accuracy of the retrieved profiles and partial water amounts, the retrieval uncertainty of the optimal solution, and the information content through the Degrees of Freedom for Signal (DFS). The logarithmic absolute humidity profile was retrieved on a height grid with decreasing vertical resolution throughout the troposphere, as well as the LWP. The synergistic observation vector comprised MWR TBs, radar DWRs and $\rho_{2\mathrm{m}}$ measurements, and varied for the single-instrument configurations. The PAMTRA model was used as forward model, linking atmospheric state and remote sensing measurement. A climatological prior profile and its associated covariances were used as prior to constrain the retrieval solution space. The measurement error covariances were assumed to be un-correlated.

Based on an idealized single-layered cloud scenario, the synergistic benefits of each combination were assessed based on a case study analysis as well as a sample of statistical moisture conditions. The synergistic benefits of combining MWR+KaW and MWR+G2 and their vertical dependency were investigated in research question 1. The analyses revealed that the MWR+G2 combination showed a higher synergistic potential than the MWR+KaW combination. The MWR+KaW configuration only showed marginal improvements in water vapor DFS of 7.5 % compared to the MWR-only approach, which is related to the DWR signal ambiguity between water vapor and liquid attenuation at the respective frequencies. Meanwhile, in the MWR+G2 combination, the total synergistic DFS are on average enhanced by 1.2 DFS; 1 DFS for the sub-cloud partial water vapor amount, and 0.2 additional DFS above the cloud layer compared to the MWR-only retrieval. The MWR+G2 retrieval information content in the sub- and in-cloud layer is driven by the radar measurements, while the MWR measurements constrain the retrieval above the cloud layer. Corresponding to the gain in information content, the synergistic retrieval uncertainty decreases particularly in the sub- and in-cloud layer, reaching a minimum of 1.0 gm^{-3} below LCL, which corresponds to a reduction of 28 % compared to the MWR-only uncertainty.

The sensitivity of the synergistic potential to the assumed measurement and forward model parameter errors, prior uncertainties and to the radar sensitivity was analyzed in order to assess research question 2. Doubling the DWR uncertainty

to ΔDWR = 1.13 dB led to increasing uncertainties of 0.1 g m^{-3} below and in the cloud layer. Highly intercalibrated radar measurements with a resulting ΔDWR of 0.1 dB led to a substantial improvement of up to 1.0 g m^{-3} right below cloud top compared to the initial MWR+G2 configuration. Doubling the MWR uncertainty increased the retrieval error above the cloud layer by 0.1 g m^{-3}. Varying the forward model parameters such as the DSD, r_{eff}, or assumed LWC profile only marginally impacted the synergistic benefits, and, in future studies, could be incorporated into the retrieval through the forward model parameter covariance matrix $\mathbf{S}_b$. The magnitude of the prior covariances did not impact the retrieval uncertainty as long as the prior correlations were preserved. If DWR measurements are not available throughout the whole vertical extent of the cloud due to radar reflectivity sensitivity constraints, the synergistic benefits reduce and approach the MWR-only uncertainty.

Expanding the synthetic single-layered cloud scenario to more realistic and increasingly complex cloud conditions, the MWR+G2 retrieval performance was theoretically assessed in three simulated scenarios based on measurements during the EUREC^{4}A campaign. The MWR+KaW synergy was not further analyzed due to the reduced synergy benefits regarding the water vapor states. Representing the expected water vapor variability at BCO in trade wind driven conditions, the analyses comprised simulated measurements of a single-layered cloud case forming at LCL (scenario 1); a double-layered cloud case with a cloud layer forming at LCL and a stratiform outflow layer forming below the trade inversion (scenario 2); and a shallow convective cloud forming at LCL topped by an altocumulus cloud associated with an elevated moisture layer above the trade inversion (scenario 3).

Assessing research question 3, the synergistic benefits in the three selected cases were analyzed regarding the coincidence with the layers associated with the highest water vapor variability. The results analyzing the more complex cloud conditions confirm the results of the single-layered cloud scenario as, in all three cases, the MWR+G2 total information content is increased by up to 1.0 DFS compared to the MWR-only configuration, and the highest synergistic impact is observed above each respective cloud layer. More specifically, in the double-layered cloud scenario 2, the increased information content originates purely from the DAR measurements in the sub- and in-cloud layers, as well as between the cloud layers. A synergistic increase of 0.2 and 0.3 DFS compared to the MWR-only configuration is observed in and above the upper cloud layer, reducing the optimal to prior uncertainty ratio above the upper cloud by up to 11.1 percentage-points. While it is not expected for the

synergy to resolve sharp humidity gradients, the results suggest that the discrepancy between the retrieved partial water vapor amounts and the sounding reduces in the levels of increased information content for the specific analyzed cases. Resolving research question 3, the results suggest that the synergy enhances the information content and reduces the retrieval error particularly in the vertical layers associated with the highest vertical variability found around LCL and the trade inversion.

In a modified retrieval approach, the added information of the synergy to reconstructing the atmospheric humidity conditions between two 24-hour spaced operational radiosondes was assessed for the three selected scenarios. Research question 4 specifically asked whether and where the synergy adds information compared to the temporally interpolated sounding profile. The prior profile was adjusted to the temporally interpolated profile of the soundings 12 hours prior and after the respective analyzed case, while the prior covariances then describe the error and correlations of this interpolation. Similarly to the analyses based on a climatological sounding prior, the retrieval in the sub- and in-cloud layers is driven by the DAR measurements, while synergistic information gain above the upper cloud is only seen in the presence of a second liquid cloud layer forming below the trade inversion. The total gain of DFS compared to the MWR-only setup is decreased to 0.2 – 0.6 DFS, as expected as the prior conditions represent the expected atmospheric state better. Within a 24-hour window, the humidity is expected to vary most around LCL and the trade inversion as seen from the EUREC^{4}A sounding dataset. The synergy improves the information content by 0.1 DFS at those heights compared to the MWR-only retrieval. The double-layered liquid cloud scenario shows that the retrieved free tropospheric water vapor amount agrees by up to 3.6 $\mathrm{kg\,m^{-2}}$ better with the observed sounding amount than the interpolated prior. An analysis based on a larger statistical sample will evaluate the findings for a larger variety of conditions.

Research question 5 investigated how additional Raman lidar (RL) measurements improve the retrieval performance in the sub-cloud layer, and how the MWR+DAR+RL retrieval concept can be varied to optimize the information content between and above the cloud layers. Analyses of all three scenarios confirmed the expectation of improved retrieval sub-cloud layer performance as, compared to the initial MWR+G2 configuration, the sub-cloud DFS increases by 0.8 – 1.3 DFS, and the sub-cloud optimal to prior uncertainty ratio decreases by 13.6 – 26.2 percentage points, respectively. Due to correlations, only the lowest cloud layer benefits from the improved sub-cloud layer performance as retrieval uncertainties are further reduced

by 3.8 – 10.1 percentage points compared to the MWR+G2 configuration at cloud base. The synergistic sub-cloud information increase is sensitive to the assumed RL measurement error, and decreases by 70 % when increasing the RL error from $1.0\,\mathrm{g\,m^{-3}}$ to $2.5\,\mathrm{g\,m^{-3}}$.

By varying the observation vector and forward model parameter configuration, different retrieval configurations were evaluated to optimize the synergistic retrieval performance. Based on a double-layered cloud scenario, the analyses revealed that including humidity profiles obtained from a direct inversion retrieval such as presented in Roy et al. (2020) would additionally decrease the retrieval uncertainty between the cloud layers by up to 11.4 percentage-points around the cloud edges compared to the initial configuration including the DWR measurements. An in-cloud saturation constraint led to a decreasing retrieval uncertainty between the cloud layers by up to 9.2 percentage-points compared to the initial MWR+DAR+RL setup. This constraint would not be applicable in reality, however, as the temperature profile would not be precisely known. No additional uncertainty decrease was observed above the upper cloud layer for any modified retrieval setup.

Concluding on all research questions, the presented analyses revealed small but consistent uncertainty reductions and information content increases, particularly above each cloud layer and between cloud layers compared to a MWR-only retrieval. Limitations of the analyses will be discussed, and future research will be summarized in the following pages.

The feasibility of the presented synergy concept can only be evaluated based on real data, for example by operating the VIPR (Roy et al., 2020) instrument in close vicinity of a HATPRO MWR at a ground-based remote sensing observatory like BCO. There, independent water vapor measurements can be used for retrieval evaluation purposes, e.g. through radiosonde ascents, or continuous humidity measurements on a weather mast for the lowest boundary layer height levels. As the MWR+KaW synergy did not add a significant amount of information to the synergy regarding water vapor profiling, future studies could include the synergistic potential for improved LWC profiling, expanding on previous studies by Hogan et al. (2005); Tridon et al. (2020); Zhu et al. (2019). That way, the uncertainty regarding the partitioning of the LWP in multiple-layered cloud scenarios could also be quantified. For a successful real application, however, further sources of uncertainty will need to be quantified, including partial beam-filling effects, mis-matched instrument beams e.g. due to horizontal spacing between the instruments (e.g. Küchler and Löhnert,

2019), or instrument-specific intercalibration effects. Careful error source analyses will have to evaluate the consistency of the theoretically derived synergistic benefits when assessing real measurements.

A major limitation of the presented study includes the assumption that the radar signal penetrates throughout the whole cloud layer. Assuming a radar sensitivity of −50 dBz at 1 km height with a vertical grid resolution of 150 m would in reality only allow the detection of cloud base in about a third of the simulated cases in Sec. 4.3. Yet, as shown in Sec. 4.5.2, the synergistic benefits strongly depend on the vertical availability of the differential radar measurements, and converge with the MWR-only uncertainties in case the signal is saturated. While it is expected that radar transmitting powers will increase in future G-band systems (personal communication, R. Roy), extended integration times would also improve the sensitivity given that the observed cloud conditions only change little within the respective integration window. Further synthetic studies could include the analysis of a different, less attenuated radar frequency pair in the G-band such as proposed by Lebsock et al. (2015), who analyzed a pair of frequencies at 160 and 170 GHz for spaceborne deployment. Lower frequencies would result in lower signal attenuation, but would simultaneously decrease the dynamic range of the differential signal. A tunable frequency range would allow the radar to be adjustable to the specific atmospheric conditions in different moisture environments.

Additional forward model errors could be induced into the optimal estimation due to absorption model uncertainties as summarized in Cimini et al. (2018). Further studies will have to quantify the effects of vertically correlated measurement uncertainties regarding the vertical radar measurement error in the measurement error covariance matrix $\mathbf{S}_e$. In a future application of this synergy optimal estimation concept, the forward model parameter error matrix $\mathbf{S}_b$ can additionally be quantified to account for DSD variety and for the fact that the realistic temperature and pressure profiles might not be available, and would have to be replaced e.g. by climatological mean profiles. In the trades, however, the temperature profile varies little on a daily basis and does not experience a strong diurnal variation (Vial et al., 2019); thus, the expected additional uncertainty is low. Alternatively, the temperature profile could be retrieved by adding it to the state vector. The MWR V-band TBs available in the HATPRO instrument could provide temperature-profile sensitive measurements, particularly when an elevation-scanning technique is applied (Crewell and Löhnert,

2007). Through the inclusion of a saturation constraint as done in Löhnert et al. (2008), the retrieval could be further constrained to reality within the cloud layers.

Modified retrieval setups could incorporate Raman lidar measurements such as shown in Sec. 5.4. Particularly in a night-time deployment, where the BCO RL measurements are most accurate and are below uncertainties of $1.0\,\mathrm{g\,kg^{-1}}$ (Schulz and Stevens, 2018), the inclusion of profiles available from direct inversion retrievals would be beneficial for the derivation of the water vapor profile between two cloud layers. Further studies could also investigate the addition of different passive channels to optimize the retrieval information content. Optimizing schemes as discussed in Lipton (2003) or Collard (2007) for spaceborne applications could be implemented to the synergy. In order to further condition the prior to the expected conditions, a threshold-based approach using independent $\rho_{2\mathrm{m}}$ or IWV measurements could be included to customize the prior profile and covariances, and, thus, condition the retrieval further to the expected conditions. Alternatively, the prior could also be constrained through a Kalman-filter approach such as presented in Foth and Pospichal (2017) who find increasing retrieval accuracies when using RL clear-sky measurements for a Kalman-filter prior in a combined MWR+RL retrieval. Regarding a deployment in the trades, a different retrieval approach could be tested in order to optimize the partitioning of the retrieved moist boundary layer and dry free tropospheric water amount. Assuming the presence of a cloud layer capped by the inversion, a modified retrieval approach could instead of the full profile retrieve the partial water vapor amount in the sub-, in- and above-cloud layer, as well as the humidity gradients throughout and above the cloud layer. Assumptions about the well-mixedness of the sub-cloud layer could further condition the retrieval. This modified approach, if successful, could further benefit studies intending to quantify the available water vapor amount in the dry free troposphere, a parameter crucial for e.g. determining cloud radiative effects (Spencer and Braswell, 1997).

In reality, nature provides a higher variety of atmospheric conditions than considered in the presented analyses, and the range of considered atmospheric conditions needs to be increased. An expanded analysis could incorporate all sounding profiles launched during the EUREC^{4}A field study, using the simultaneous BCO and Cloudnet observations to simulate the corresponding conditions and measurements. With an increased number of simulations, more statistically thorough results could be drawn regarding the synergistic potential of deriving accurate water vapor profiles and partial water vapor amounts. More diverse conditions could include drizzling virga,

larger cloud particles, or mixed-phase cloud occurrences. In all of these cases, Mie scattering effects could lead to differential scattering signals affecting the differential radar reflectivity measurements, and the associated errors.

The synergistic concept is not limited to the ground-based application, as water vapor profile observations are equally needed over remote areas e.g. over the oceans. First simulations were made in Sec. 6.1 for an airborne perspective of the synergy concept, modelling e.g. an application within HALO's remote-sensing instrument suite deployed during EUREC^{4}A (Stevens et al., 2019). The simulated measurements suggest that at a flight altitude of 8 km and with an assumed instrument sensitivity of -50 dBz at 1 km range, however, the boundary layer clouds forming at LCL would not be detected by the radar considering the same scenarios as before. Increased integration times would improve the sensitivities, but widen the instrument's horizontal footprint size, introducing errors due to partial beam filling effects due to the small cloud sizes. If sensitivity constraints were overcome, the passive HAMP-channels, including passive G-band channels (Mech et al., 2014), could further expand the synergistic options in order to e.g. close measurement gaps between dropsonde launches. When applied from the air- or spaceborne perspective, the integrated water vapor amount could also be derived in clear-sky cases due to the ground return signal. In this case, further assumptions on the ground reflectance would have to be made (e.g. Lebsock et al., 2015; Millán et al., 2016).

In order to overcome the potential reflectivity constraints when deploying a G-band radar in moist conditions with shallow clouds, a potential application in the dry Arctic environment might be feasible. As presented in Sec. 6.2, first idealized ground-based simulations for a typical case as observed in Ny-Ålesund, Spitsbergen, showed that the resulting reflectivity signals would be above assumed sensitivity thresholds, which motivates further studies analyzing the resulting synergy benefits. Continuous water vapor profiling observations would enable further studies regarding the dependence between specific humidity inversions and mixed-phase cloud lifetime and properties.

Yet in the presence of ice hydrometeors or large liquid droplets, differential scattering impacts might manifest an additional source of signal to the DWR signal, which a retrieval would have to account for. A modified retrieval approach would need to incorporate more thorough assumptions about the phase and PSD, or would need to incorporate these parameters as retrieval states. Observations that could be added to the synergy in order to constrain the solution could e.g. be radar Doppler spectra as proposed by Verlinde et al. (2013) or Gierens (2020).

Co-located remote sensing and in-situ observations such as performed during the ACLOUD/PASCAL (Wendisch et al., 2019; Ehrlich et al., 2019) or the MOSAIC field study (`http://mosaic-expedition.org`) will contribute to further quantifying the link between macro- and microphysical cloud properties.

A successful implementation of the synergy concept would be beneficial for many evaluation studies. Even though radar observations have been challenging to include into numerical forecasting through data assimilation methods (e.g. Fabry and Meunier, 2020), an operational deployment of the synergy could provide an evaluation dataset for further developments. Future satellite missions, such as the planned EarthCARE measurements (Illingworth et al., 2015b) and their retrievals, could be evaluated with ground-based data. In the trades, the retrieval benefits of a synergistic deployment with improved radar sensitivities coincide with the vertical areas of highest water vapor variability; thus, continuous observations of the water vapor structure and associated cloud formation would contribute to modelling evaluation, e.g. to solve the questions raised regarding the interplay of convection and cloud processes and their associated parametrizations.

The presented theoretical analyses and results based on synthetic measurements suggest a small but consistent improvement compared to current existing water vapor profiling methods. As opposed to methods operating in the optical or infrared spectrum, this synergistic concept allows water vapor to be retrieved throughout and above multiple cloud layers in a physically consistent way. Compared to a MWR-only retrieval configuration, the retrieval information content is enhanced, while the retrieval uncertainty is decreased above each respective cloud layer. The enhanced retrieval information content suggests improved derivation of the partial respective water vapor amounts below, between, in and above the cloud layers. Further synthetic evaluation studies will expand the feasibility analysis to a larger statistics, including a larger variety of observed atmospheric conditions also in different moisture environments. Based on the results, the application of the concept to real measurements can be evaluated, even if additional error sources need to be quantified and current radar sensitivities need to be further improved for an application in tropical moist conditions. Whether or not the presented synergy concept can fully close the observational gap of continuous, high vertical resolution water vapor profiling across different climatological conditions remains an open question, but the presented feasibility studies provide a base for future investigations.

Since Aristotle's work more than 2000 years ago, scientific understanding has advanced fundamentally regarding the understanding of the role of clouds and water vapor in meteorology. Today's scientific community has emancipated itself in many ways from the general opinion of even the 1940's when clouds were thought of a subject suitable "for a little girl to study" (NASA Earth Observatory (2004): Carl-Gustav Rossby to Joanne Simpson in response to her wish to pursue a doctorate in studying clouds)[1]. Improved modelling and enhanced observational technology, including synergies of different observational methods, will both advance the understanding of water vapor and clouds in the Earth's climate, and will contribute to spreading fascination to more generations of scientists and dreamers to come.

[1]Joanne Simpson née Gerould later became the first woman in the US to earn a PhD in Meteorology in 1949 for her pioneering work on tropical cumulus clouds.

A Appendix

A.1 Atmospheric Soundings During the EUREC^{4}A Field Study

The following manuscript gives an overview of the sounding measurements during the EUREC^{4}A field study as published in Stephan et al. (2020). Sec. A1 introduces the motivation of the sounding activity, while technical details of the measurements at the five different launching stations and the data processing are discussed in Sec. A2. Sec. A3 gives an overview of the measured conditions, analysing differences between ascending and descending soundings, as well as the observed synoptic conditions. Sec. A4 summarises the findings, and data availability is summarised in Sec. A5.

Sabrina Schnitt organised and led the sounding measurements and organisation at BCO during EUREC^{4}A and conceptualised the manuscript structure with the leading authors. She prepared Fig. 9 as well as most analyses and text in Sec. A3.2, and supported the data processing.

https://doi.org/10.5194/essd-2020-174
Preprint. Discussion started: 5 August 2020

Open Access Earth System Science Data Discussions

Ship- and island-based atmospheric soundings from the 2020 EUREC^{4}A field campaign

Claudia Christine Stephan[1], Sabrina Schnitt[2], Hauke Schulz[1], Hugo Bellenger[3], Simon P. de Szoeke[4], Claudia Acquistapace[2,*], Katharina Baier[1,*], Thibaut Dauhut[1,*], Rémi Laxenaire[5,*], Yanmichel Morfa-Avalos[1,*], Renaud Person[6,7,*], Estefanía Quiñones Meléndez[4,*], Gholamhossein Bagheri[8,+], Tobias Böck[2,+], Alton Daley[9,+], Johannes Güttler[10,+], Kevin C. Helfer[11,+], Sebastian A. Los[12,+], Almuth Neuberger[1,+], Johannes Röttenbacher[13,+], Andreas Raeke[14,+], Maximilian Ringel[1,+], Markus Ritschel[1,+], Pauline Sadoulet[15,+], Imke Schirmacher[16,+], M. Katharina Stolla[1,+], Ethan Wright[5,+], Benjamin Charpentier[17], Alexis Doerenbecher [18], Richard Wilson[19], Friedhelm Jansen[1], Stefan Kinne[1], Gilles Reverdin[20], Sabrina Speich[3], Sandrine Bony[3], and Bjorn Stevens[1]

[1]Max Planck Institute for Meteorology, Hamburg, Germany
[2]Institute for Geophysics and Meteorology, University of Cologne, Cologne, Germany
[3]LMD/IPSL, CNRS, ENS, École Polytechnique, Institut Polytechnique de Paris, PSL, Research University, Sorbonne Université, Paris, France
[4]College of Earth, Ocean, and Atmospheric Sciences, Oregon State University, Corvallis, Oregon, USA
[5]Center for Ocean-Atmospheric Prediction Studies, Florida State University, Tallahassee, Florida, USA
[6]Sorbonne Université, CNRS, IRD, MNHN, INRAE, ENS, UMS 3455, OSU Ecce Terra, Paris, France
[7]Sorbonne Université, CNRS, IRD, MNHN, UMR7159 LOCEAN-IPSL, Paris, France
[8]Laboratory for Fluid Physics, Pattern Formation and Biocomplexity, Max Planck Institute for Dynamics and Self-Organization, Göttingen, Germany
[9]Caribbean Institute for Meteorology and Hydrology, Husbands, St. James, Barbados
[10]Max Planck Institute for Dynamics and Self-Organization, 37077 Göttingen, Germany
[11]Department of Geoscience and Remote Sensing, Delft University of Technology, Delft, The Netherlands
[12]Department of Earth and Planetary Sciences, University of New Mexico, Albuquerque, New Mexico, USA
[13]Institute for Meteorology, University of Leipzig, Leipzig, Germany
[14]Deutscher Wetterdienst, Seewetteramt Hamburg, Seeschiffahrtsberatung - Bordwetterdienst, Hamburg, Germany
[15]Météo-France, Bordeaux, France
[16]University of Hamburg, Hamburg, Germany
[17]Meteomodem, Ury, France
[18]Météo-France and CNRS: CNRM-UMR 3589, 42 Av. G. Coriolis, 31057 Toulouse Cedex, France
[19]Sorbonne Universite, LATMOS/IPSL, INSU/CNRS, Paris, France
[20]LOCEAN, SU/CNRS/IRD/MNHN, Sorbonne Université, Paris, France
[*]These authors contributed equally to this work.
[+]These authors also contributed equally to this work.

Correspondence: Claudia C. Stephan (claudia.stephan@mpimet.mpg.de)

Abstract. To advance the understanding of the interplay among clouds, convection, and circulation, and its role in climate change, the EUREC^{4}A and ATOMIC field campaigns collected measurements in the western tropical Atlantic during January and February 2020. Upper-air radiosondes were launched regularly (usually 4-hourly) from a network consisting of the Barbados Cloud Observatory (BCO) and four ships within 51–60 °W, 6–16 °N. From January 8 to February 19, a total of

https://doi.org/10.5194/essd-2020-174
Preprint. Discussion started: 5 August 2020

Open Access Earth System Science Data Discussions

812 radiosondes measured wind, temperature and relative humidity. In addition to the ascent, the descent was recorded for 82 % of the soundings. The soundings sampled changes in atmospheric pressure, winds, lifting condensation level, boundary layer depth, and vertical distribution of moisture associated with different ocean surface conditions, synoptic variability, and mesoscale convective organization. Raw (Level-0), quality-controlled 1-second (Level-1), and vertically gridded (Level-2) data in NetCDF format (Stephan et al., 2020) are available to the public at AERIS (https://doi.org/10.25326/62). The methods of data collection and post-processing for the radiosonde data set are described here.

1 Introduction

A number of scientific experiments have focused on the trade-cumulus boundary layer over the tropical Atlantic Ocean. The Barbados Oceanographic Meteorological Experiment (BOMEX 1969; Kuettner and Holland, 1969), Atlantic Trade-Wind Experiment (ATEX 1969; Augstein et al., 1973), Atlantic Stratocumulus Transition Experiment (ASTEX 1992; Albrecht et al., 1995), and Rain in Shallow Cumulus Over the Ocean (RICO 2006; Rauber et al., 2007) experiment measured thermodynamic and wind profiles of the Atlantic trade regime (reviewed by Baker, 1993). With these profiles as initial and environmental conditions, models of the cumulus clouds explain their interaction with the environment (e.g. Arakawa and Schubert, 1974; Albrecht et al., 1979; Krueger, 1988; Tiedtke, 1989; Albrecht, 1993; Bretherton, 1993; Xue et al., 2008; vanZanten et al., 2011).

Arrayed networks of soundings have been used to characterize the interaction of clouds, convection, and the synoptic environment. In many examples, they have been used to diagnose tendencies of the heat, mass, and moisture budgets for the tropical atmosphere (e.g. Reed and Recker, 1971; Yanai et al., 1973; Nitta and Esbensen, 1974; Lin and Johnson, 1996; Mapes et al., 2003; Johnson and Ciesielski, 2013). These experiments in the deep tropics monitored the synoptic (100–1000 km) variations of vertical motion and moisture convergence as context for the evolution of the ensemble of convective clouds observed within their sounding networks.

These sounding arrays measure horizontal divergence, which is used to estimate mean large-scale vertical motion. In DYCOMS-II, Lenschow et al. (2007) used stacked flight circles to estimate subsidence on a fine scale relevant to marine stratocumulus clouds. Studying the variations of mesoscale ($\sim$100 km) organization of the trade wind shallow cumulus clouds likewise requires fine horizontal resolution. The Next-Generation Aircraft Remote Sensing for Validation Studies (NARVAL; Stevens et al., 2016, 2019; Bony and Stevens, 2019) demonstrated that circles of dropsondes released from aircraft above the shallow clouds reliably measure a snapshot of vertical motion.

The shallow trade cumulus clouds over the tropical Atlantic Ocean are a focus also of the Elucidating the Role of Clouds-Circulation Coupling in Climate Campaign (EUREC^{4}A; Bony et al., 2017) and associated campaigns, i.e, the Atlantic Tradewind

https://doi.org/10.5194/essd-2020-174
Preprint. Discussion started: 5 August 2020

Open Access Earth System Science Data Discussions

Ocean–Atmosphere Mesoscale Interaction Campaign (ATOMIC) [1]. The experimental design of EUREC^{4}A involved 85 dropsonde circles from aircraft flights combined with regular around-the-clock upper air observations from surface-launched radiosondes. The regular sampling from surface-launched radiosondes complemented the mesoscale vertical velocity measurements from dropsonde circles by continuously measuring time-height profiles of the atmosphere, synoptic variability for an extended time period, and diurnal variability. Radiosondes sampled when research aircraft were not flying, notably at night.

Between January 8 and February 19, 2020, 812 radiosondes were launched from Barbados and the northwestern tropical Atlantic Ocean east of Barbados. A focus of the campaign was on shallow cumulus clouds, their radiative effects, and their response to the large-scale environment, contributing progress toward the World Climate Research Programme's Grand Challenge on Clouds, Circulation and Climate Sensitivity (Bony et al., 2015). Other EUREC^{4}A investigations focus on air-sea interactions due to ocean mesoscale eddies, cloud microphysical processes, and the effect of shallow convection on the distribution of winds. The present paper introduces the radiosonde observations and their resulting data sets.

Radiosondes were launched from Barbados and four research vessels. The island-based launches took place at the Barbados Cloud Observatory (BCO; 59.43 °W, 13.16 °N), situated at Deebles Point on the windward coast of Barbados. Surface and remote sensing observations at BCO have been in operation since April 1, 2010 (Stevens et al., 2016).

Four research vessels launched radiosondes over the northwestern tropical Atlantic east of Barbados (51–60 °W, 6–16 °N) during EUREC^{4}A: two German research vessels, *Maria S. Merian* (hereafter *Merian*) and *Meteor*, a French research vessel, *L'Atalante* (hereafter *Atalante*), and a United States research vessel, *Ronald H. Brown* (hereafter *Brown*). The BCO and the research vessels all measured surface meteorology and deployed various other measurements for remote sensing of clouds and the atmospheric boundary layer.

In Section 2 we describe the measurement strategy for the coordinated EUREC^{4}A radiosonde network, the data collection procedures for each platform, and the post-processing steps that were applied to create the final data set. Section 3 shows an overview and some characteristics of the data and is followed by a summary in Section 4. The *Atalante* additionally launched a different type of sonde, which is described in the appendix.

2 Sounding measurements

2.1 The EUREC^{4}A sounding network

The number of launches per day as well as the dates of regular observations (Fig. 1) differ from platform to platform, reflecting availability of ships and personnel. Soundings supported specific research interests on each platform, in addition to the coordinated EUREC^{4}A sounding network. We designed the radiosonde network to optimize the joint contribution of all platforms to the overarching goals of EUREC^{4}A. Sounding platforms were usually spaced to optimally sample the scales of the synoptic circulation. The *Meteor* remained nearly stationary at a longitude of 57 °W and moved within a meridional corridor between 12.0–14.5 °N to support coordinated aircraft measurements in its vicinity (Fig. 2a). The *Brown* occupied a southwest-northeast

[1] Because the sounding network and EUREC^{4}A comprised many projects, or component campaigns, we refer to the union of these simply as EUREC^{4}A.

https://doi.org/10.5194/essd-2020-174
Preprint. Discussion started: 5 August 2020

Open Access Earth System Science Data Discussions

transect along the direction of the climatological surface trade winds, and approximately orthogonal to *Meteor*'s sampling line. The *Brown*'s transect between the BCO (59.43 °W, 13.16 °N) and the Northwest Tropical Atlantic Station for air-sea flux measurements buoy (NTAS) at 51.02 °W, 14.82 °N (Fig. 2b) sampled airmasses upwind of the BCO that move westward with the climatological easterly trade winds within 12.5–14.5 °N. This elongated region between BCO and NTAS is referred to as the 70 'Trade-wind Alley'. The *Merian* and *Atalante* ventured southward to a minimum latitude of ∼6.5 °N to observe oceanic and atmospheric variability associated with Brazil Ring Current Eddies as they tracked northwestward along the corridor referred to as 'Boulevard des Tourbillons'. The *Atalante* and *Merian* thus often form the southern points of the radiosonde network (Fig. 2c, d).

Aircraft operations included a circular flight pattern of 180–200 km diameter centered at ∼13.3 °N, ∼-57.7 °E. Dropsondes 75 were deployed along the circle to estimate the area-averaged mass divergence, as described in Bony and Stevens (2019). To sample larger scales than represented by this circle, we aimed at 4-hourly soundings from all five stations while platforms were separated by more than 200 km. The launch frequency was reduced when such a separation could not be maintained or when vessels left the key region of the network, i.e. moved south of 12 °N. These scenarios occurred from time to time in order to support other measurements. Figure 3 shows that the network sampled large scales for 30 consecutive days.

80 To increase the number of vertical profiles, we recorded the ascent as well as the descent of the radiosondes. Except for the *Brown*, balloons were equipped with parachutes, which nearly match fall speeds to balloon ascent speeds. Given that a typical ascent takes about 90 min, a radiosonde was sampling the air somewhere above each platform nearly continuously during regular operation. All platforms deployed Vaisala RS41-SGP radiosondes and used Vaisala MW41 ground station software to record and process the sounding data. To start a sounding, a radiosonde sensor was placed on the ground station for an 85 automated ground check initialization procedure, which took about 5–6 min. The frequency at which the radiosonde transmits its signal to the receiver was set manually to a designated value for each platform (listed in Table 1) to avoid radio interference.

The default launch times were 0245, 0645, 1045, 1445, 1845, and 2245 UTC, to have radiosondes reach 100 hPa at standard synoptic times (00 and 12 UTC). Departures from this schedule occurred due to a variety of reasons, including defective radiosondes, balloon bursts before the launch, collisions of ascending radiosondes with other on board instrumentation, and 90 air traffic safety. In the following section, we describe specific issues and aspects of the launch procedure particular to each platform.

2.1.1 Barbados Cloud Observatory (BCO)

The BCO is located at the eastern-most point of Barbados (59.43 °W, 13.16 °N) and thus directly exposed to easterly trade winds from the ocean. The BCO launched 182 sondes, of which 162 measured descents. Radiosondes were prepared inside an 95 air-conditioned office container with air temperature and relative humidity adjusted to 20 °C and 60 %, respectively. Balloons were prepared outside and placed into a launcher whose size provided rough guidance for achieving the desired filling level (Fig. 4a). Launches were coordinated with Barbados Air Traffic Control, which delayed soundings up to 15 min. Surface conditions obtained from the weather station observations at the BCO were entered into the software after automatic release detection.

https://doi.org/10.5194/essd-2020-174
Preprint. Discussion started: 5 August 2020

Open Access Earth System Science Data Discussions

2.1.2 R/V *Meteor*

The *Meteor* launched 203 sondes and collected data for 167 descents during the EUREC^{4}A core period (January 8 to February 19). Eight additional ascents and descents, respectively, were recorded after February 20. Radiosondes were prepared inside a laboratory on the top deck of the ship with the antenna placed on the roof. Before February 9 the soundings were launched from the container of the German Weather Service (DWD) on the port side at the stern of the ship (Fig. 4b). This container had a marker to indicate the optimum fill level of the balloons.

On February 9 the DWD launcher broke and a launcher of the type shown in Fig. 4a was used, located at the stern of the ship. An awning over the balloon indicated the fill level. Ground data were obtained from on-board instruments of the DWD. In addition to sondes launched by the EUREC^{4}A science crew, the DWD launched one radiosonde per day. The 31 ascending DWD sondes launched during the EUREC^{4}A core period, plus an additional eight after February 20, are included in the Level-1 and Level-2 data sets, described in Section 2.3.

2.1.3 R/V *Ronald H. Brown* (*Brown*)

The *Brown* released 170 sondes and collected data for 159 descents. The radiosondes were initialized and ground-checked inside an air-conditioned laboratory. Near-surface measurements were recorded from the ship's meteorological sensors via the ship computer system display. The ground station antenna was located on the aft 02 deck railing above the staging bay. Initialized radiosonde sensor packages were placed for 1–5 min on the main deck to equilibrate to ambient environmental conditions and check GPS reception and telemetry. The balloons were filled by hand in the staging bay (Fig. 4d), which was mostly sheltered. Operators avoided unnecessary contact with the balloon body but restrained it by hand if the wind was strong.

On leg 1 (January 8–24) at night, less helium was used to reduce the buoyancy of the balloons in order to achieve lower ascent rates and better resolve the fine-scale vertical structure of the atmosphere.The ascent rate for day launches was 4.4$\pm$0.5 m s^{-1}; for night launches, ascent was about 12 % slower, 3.9$\pm$0.6 m s^{-1}. After January 24, the same target ascent rate was used for day and night, and operators obtained consistent balloon volumes by timing the filling.

Balloons were launched from a location on the deck to minimize the effect of the ship and obstructions on the sounding. The ship usually turned or slowed to improve the relative wind for the sounding. The relative wind carried the sounding away from the ship, but the ship's aerodynamic wake made the first $\sim$5 s of the balloon's flight unpredictable. The sounding was sometimes launched up to 10 min earlier or later to accommodate other ship operations.

2.1.4 R/V *L'Atalante* (*Atalante*)

The *Atalante* launched 139 Vaisala sondes and measured 138 descents. A coordinated sounding phase was performed with the *Merian* to increase the temporal resolution from January 30 at 2045 UTC to February 2 at 1645 UTC around 52–54 °W and 6–8 °N. During this period launching times were shifted by 2 hours aboard the *Atalante* (0045, 0445, 0845, 1245, 1645, 2045 UTC) while the *Merian* launched at regular times. In addition to the Vaisala soundings, 47 sondes of MeteoModem type M10

https://doi.org/10.5194/essd-2020-174
Preprint. Discussion started: 5 August 2020

Open Access Earth System Science Data Discussions

were launched from the *Atalante* to measure the lower atmosphere across mesoscale sea surface temperature (SST) fronts, as detailed in the appendix.

The radiosondes were prepared aft of the bridge. This open space was right next to the top building of the ship, which may have affected measurements at low levels. Before launching, operators asked the bridge for direction change if necessary and possible. The balloons were launched by hand from the rear deck of the bridge, where the launcher was situated (Fig. 4e). The Vaisala antenna was installed on the roof top. Surface measurements were obtained from local measurements on board. At the beginning of the campaign a frequency of 401.0 MHz was selected, which later on had to be switched to 401.2 MHz because of radio interference at 400.9 MHz from an unknown source. This interference caused loss of signal for two radiosondes during their ascent. When a previous sounding was not terminated at the launch time of a subsequent sounding, a frequency of 400.7 MHz was selected.

The *Atalante* experienced substantial instabilities of the Vaisala acquisition system at the initialization step of the system (system location unavailable) and with the reception of the GPS signal by the Vaisala antenna and radiosondes. These problems required multiple restarts of the software and the acquisition system (between 1 and 8 times), creating delays between 10 min and 1 h. However, they did not affect the quality of the soundings. The operators checked the cables and replaced the GPS antenna of the Vaisala system with an antenna that had a larger DC voltage range (15 V instead of 4 V). Nevertheless, the problems persisted during the cruise with the need to restart the system several times before each launch.

2.1.5 R/V *Maria S. Merian* (*Merian*)

The *Merian* launched 118 sondes and recorded 38 descents. Fewer sondes were launched on the *Merian* than other platforms (Fig. 1) due to difficulties and priority of *Atalante* sondes when the ships were close to one another. The radio signal was often lost using the first antenna location, which the team suspected was due to blocking by the chimney. A new location improved the reception of the signal.

The *Merian* was equipped with a launch container (Fig. 4c). The helium fill level was decided by inflating the balloon until it reached the upper edge of the launch container. During the day, temperatures in the container rose considerably higher then ambient, but the container was well ventilated as the launch was prepared, such that the instruments experienced typical temperatures of 28–31 °C during synchronization, with only few exceptions. Nonetheless, the residual warming could be a source of bias relative to the surface meteorology observations and persist for tens of meters after the launch. Near-surface data were taken from ship measurements.

2.2 Real-time sounding data distribution

Sounding observations distributed in real-time over the Global Telecommunication System (GTS) improve atmospheric analyses for initializing and verifying weather forecasts, and improve subsequent reanalyses. Therefore, we aimed to disseminate as much of the full 1-second resolution radiosonde data from the EUREC^{4}A campaign as possible over the GTS. Radiosonde data (ascent and descent) from the *Atalante* (114 reports during the campaign) and the BCO (60 reports in February) were sent to the GTS through a Météo-France entry point. This allowed their assimilation in numerical weather prediction (NWP)

https://doi.org/10.5194/essd-2020-174
Preprint. Discussion started: 5 August 2020

Open Access Earth System Science Data Discussions

systems. Most of the *Brown* data were sent to the US National Center for Environmental Prediction (NCEP). From here they were ingested into US Weather Service and Navy NWP systems, yet not European ones. None of the data from the *Merian* and *Meteor* could be transmitted to the GTS by satellite internet. However, during EUREC^{4}A, 29 daily ascent soundings from the *Meteor* were sent to the GTS via the EUMETNET Automated Shipboard Aerological Program (E-ASAP), at around 1630 UTC.

World Meteorological Organization Binary Universal Form for the Representation of meteorological data (BUFR) were submitted to the GTS and exchanged among the platforms during the EUREC^{4}A campaign. BUFR supports ascending soundings (BUFR 309057), descending soundings (BUFR 309056, since BUFR Table version 31.0.0), and dropsondes released from aircraft (BUFR 309053). The Vaisala MW41 sounding software writes quality-controlled BUFR files. The sounding instruments measure relative humidity, but the BUFR files only contain the derived dew point temperature. We obtain the relative humidity from the dew point by inverting the dew point formula exactly.

2.3 Quality control and data formats

The Vaisala RS41 temperature and humidity measurements are highly robust and accurate, even in cloudy environments. The humidity sensor is actively heated to prevent water condensation and frost formation on the sensor surface. The Vaisala MW41 software writes proprietary .mwx binary files which are ZIP-archives that contain both the raw as well as the processed measurements. These data make up our Level-0 data set. We also provide Level-1 and Level-2 data, which we describe in the following. Our assignment of levels for the data sets adheres to the standards laid out in Ciesielski et al. (2012).

2.3.1 Level-1 data

Level-1 data in NetCDF format are quality controlled and averaged to 1-second resolution from the Level-0 data. Because the pressure, temperature and humidity are measured with a different sensor (PTU) than wind and position, the data are synchronized to the PTU time. This synchronization is done by the Vaisala MW41 software and the results are included in the Level-0 archive files. The Level-1 data were processed from these results.

The Vaisala MW41 sounding system applies a radiation correction to daytime temperature measurements by subtracting increments that vary as a function of pressure and solar zenith angle. The uncertainty of the radiation correction is typically less than 0.2 °C in the troposphere; uncertainty gradually increases in the stratosphere.

The Vaisala system applies algorithms to adjust for time lags of the RS41 sensors. At 10 hPa the response time of the temperature sensor is 2.5 s for an ascent speed of 6 m s^{-1}. At $18\,\mathrm{km}$ ($75\,\mathrm{hPa}$) with a temperature lapse rate of 0.01 °C m^{-1} and an ascent rate varying from 3 to 9 m s^{-1}, the remaining uncertainty in the temperature reading due to time lag is 0.02 °C. At lower altitudes the uncertainty is even smaller. A time-lag correction is also applied to measurements of humidity. The response time of the humidity sensor is dependent on the ambient temperature. For example, at an ascent rate of 6 m s^{-1} and at 1000 hPa it is $<$0.3 s for +20 °C and $<$10 s for -40 °C. The remaining combined uncertainty during the sounding is 4 % relative humidity.

https://doi.org/10.5194/essd-2020-174
Preprint. Discussion started: 5 August 2020

Open Access Earth System Science Data Discussions

After time-lag adjustments, the Vaisala MW41 quality control algorithm detects outliers and smooths the data to reduce noise. Our software (Schulz, 2020a) reads the processed Vaisala mwx, and MeteoModem BUFR files, and converts them to self-describing NetCDF files. We also add the ascent or descent rate, calculated from the geopotential height and time information between consecutive measurements, to the NetCDF files. The resolution of the measurements is 1 s. The resulting NetCDF files are the Level-1 data set distributed here.

2.3.2 Level-2 data

To facilitate scientific analyses, Level-2 data are provided on a common altitude grid with bin sizes of $10\,\mathrm{m}$, by averaging the Level-1 data. Mean temperature, wind components, position, and logarithm of pressure are directly averaged within bins. Relative humidity is calculated from the mean of the Level-1 water vapor mixing ratio, calculated from the water vapor pressure formula of Hardy (1998), which is also used by the ASPEN software for EUREC^{4}A dropsonde measurements.

In case of missing data within a sounding, we linearly interpolate gaps of up to $50\,\mathrm{m}$. Gaps larger than $50\,\mathrm{m}$, as well as data below $40\,\mathrm{m}$ in our Level-2 data set originating from the ship soundings, are filled with missing values. Yoneyama et al. (2002) found ship influences on radiosonde measurements to extend no further than $40\,\mathrm{m}$ above the deck. For descending soundings the raw data near the surface are missing as the signal is lost due to Earth's curvature at $300\,\mathrm{m}$ to $800\,\mathrm{m}$ above mean sea level. The median of the lowest descent measurement is at $340\,\mathrm{m}$.

3 Data characteristics

3.1 Ascending versus descending soundings

We begin with an examination of instrument ascent and descent speeds for the different platforms (Fig. 5). The median ascent speed in the mid-to-upper troposphere is between 4.5 and 5 m s^{-1} for radiosondes launched from the BCO, *Atalante* and *Merian* (Fig. 5a, g, i). Radiosondes launched from the *Meteor* and the *Brown* ascended at slightly smaller rates of about 4 m s^{-1} (Fig. 5c, e). For all platforms and at all altitudes the 10th and 90th percentiles are roughly symmetric about the median ascent rate and fall mostly within ± 1 m s^{-1} of the median. Radiosondes from the *Atalante* and *Merian* appear to have experienced stronger updrafts in the upper troposphere. This is consistent with sampling the more convectively-active conditions in the south, where there is a warmer ocean surface, more precipitable water, deeper convection and a greater chance of land influences. Above $20\,\mathrm{km}$, the median ascent rate and the spread in ascent rates increase for all platforms.

Descent speeds exhibit a much stronger functional dependence on altitude (Fig. 5b, d, f, h, j). For platforms that employed parachutes (BCO, *Meteor*, *Atalante* and *Merian*), descent rates decrease towards the ground to a minimum of about 5 m s^{-1} in the lowest kilometers. Instruments without a parachute from the *Brown* have descent rates of sightly less than 15 m s^{-1} in the lowest few kilometers. The positive skewness of the distributions associated with stations that used parachutes is due to descending radiosondes with broken or detached parachutes, or with unexpected behavior of the torn balloon remains. With

https://doi.org/10.5194/essd-2020-174
Preprint. Discussion started: 5 August 2020

Open Access Earth System Science Data Discussions

the exponential decrease of air density with altitude, descent rates increase non-linearly and rapidly with altitude, exceeding 20 m s^{-1} between 20–25 km when parachutes were used and exceeding 40 m s^{-1} in case of the *Brown*.

Fig. 6 compares the measurements of horizontal wind speed, air temperature and relative humidity between ascending and descending soundings. We do not expect perfect agreement between ascending and descending soundings, for several reasons. First, the instruments drift substantial horizontal distances and hence systematically sample a downwind location (as illustrated in Fig. 11f for the BCO). Second, there are variable time lags of the order of a couple of hours between ascending and descending measurements. We also note that the number of descent profiles available for computing statistics is in some cases substantially smaller than the number of ascent profiles (Fig. 1). The numbers of available measurements are again listed on the left hand side of Fig. 6. All quantities shown in Fig. 6 are computed from matched ascent-descent pairs of the same instrument.

Measurements of horizontal wind speeds do not show statistically significant differences between ascent and descent (the mean lies within the 95 % confidence intervals), with the exception of the *Brown*. Here, wind speeds at around 20 km altitude are stronger for the ascent. This systematic difference could be related to excessively rapid descent rates. Similar results are found for measurements of air temperature (Fig. 6b, d, f, h, j). In case of the *Brown*, stratospheric temperature observations during descent are warmer by more than 1 °C, suggesting a bias due to high descent rates. The same bias exists for the other platforms, but the effect is smaller and not statistically significant at the 95 % confidence level. Differences in relative humidity are not statistically significant inside the troposphere.

3.2 Synoptic conditions

We first present the synoptic situation for the region defined by the *Meteor* and the BCO soundings. Our initial analysis focuses on the soundings for these two platforms because they define a more or less fixed geographic area – radiosondes launched from the *Meteor* were almost all launched between 12.5 °N and 14.5 °N along 57.15 °W – bounding the subdomain that was most intensively sampled. A comparison between twelve BCO soundings with coincident and nearly co-located ship-based soundings (ships were positioned just offshore of the BCO) showed no evidence (Fig. A4) of a systematic influence of the island on the BCO soundings. Hence, the BCO soundings appear representative of the western most boundary of the marine measurement area. Focusing on a fixed region during the period of most intensive airborne operations, between January 20 and February 17, also provides a reference for quantifying differences in soundings taken outside of this region, or time period, as is discussed at the end of this subsection.

Synoptic differences among variables believed to be important for patterns of low-level cloudiness suggest that: (i) the *Meteor* and the BCO sample the same synoptic environment; and (ii) that changes in the environment can usefully be described by week-to-week variability over the four weeks starting on Monday, January 20. Fig. 7 shows that the lower-tropospheric stability, the near surface winds, the lifting condensation level (LCL) of near-surface air, and the hydrolapse associated with the depth of the trade-wind layer, as measured from the *Meteor* or BCO soundings, track each other well. Fig. 8 further illustrates that the LCL tracks well the lowest cloud bases as measured by the *Meteor* ceilometer. Week-to-week variations as deduced from the soundings of either platform show the first and last week to be characterized by a deeper moist layer, and lessened lower tropospheric stability, the latter primarily explained by changes in the potential temperature at 700 hPa.

https://doi.org/10.5194/essd-2020-174
Preprint. Discussion started: 5 August 2020

Open Access Earth System Science Data Discussions

The two week period starting on January 27 has a much shallower trade-wind layer and stronger stability. Near surface winds vary somewhat out of phase with the moisture variability, with winds stronger in the second half of the four week period, and weaker in the first half. The LCL shows very little synoptic variability.

Cloud observations are also included in Fig. 7. Reports of mid-level (C_M) and high-level (C_H) clouds are derived from 3 hourly SYNOP observations reported by the Barbados Meteorological Service at Grantley Adams International Airport. If a reported mid or high-level cloud type was persistent through the day (more than three reports) it is included via its WMO cloud symbol[2] in Fig. 7. Notable are mid-level clouds that coincide with the deepening of the marine layer, particularly during the period at the end where a layer of altocumulus (C_M = 4) persisted for several days (Fig. 8). Observations of low clouds (C_L) indicated that C_L=8 and C_L=2 where the dominant low-level clouds; both evident on almost every day with little evidence of synoptic variability. This is also evident from the *Meteor* ceilometer measurements (Fig. 8). For this reason, in Fig. 7 we instead identify days when particular patterns of mesoscale variability were in evidence. We adopted the four patterns, Sugar, Gravel, Flowers, Fish following Stevens et al. (2020) and whether or not one particular pattern was identified was taken from a cloud classification activity organized by one of the authors (H. Schulz). These patterns suggest that the moist initial period has the satellite presentation of Fish, and that the period of increased lower-tropospheric stability and strengthening winds on February 2 was associated with the pattern Flowers, consistent with the analysis of Bony et al. (2020).

To give a better impression of the synoptic variability, the period identified with the Fish pattern, between January 22–24, is investigated further. The visible satellite imagery from MODIS on Aqua (Fig. 9a) illustrates the large-scale characteristics of the observed Fish cloud pattern, covering the BCO and the northern latitudes of the observations region. The pattern resembles a spine in a surrounding cloud-free area and was accompanied by unseasonably large amounts of surface precipitation. Fig. 9b illustrates the moistening of the atmosphere and the deepening of the boundary layer, as measured at the BCO, over the course of this event. Between January 20–26, the increase of integrated moisture up to $55\,\mathrm{kg\,m^{-2}}$ coincides well with the deepening moist layer, thus also with changes in cloud top height and trade wind inversion height. Before and after the event, the inversion layer height was around $2\,\mathrm{km}$ (Fig. 7), and the boundary layer was characterized by a mixture of Gravel and Sugar, albeit the latter not on a scale that lent itself to identification from the satellite imagery. During the peak of the event on January 22 and 23, the moisture layer deepened up to 5 km. While the Fish cloud pattern passed over BCO, the pressure in the boundary layer decreased by up to 4 hPa (see Fig. 11e) and the temperature in the upper middle troposphere ($6\,\mathrm{km}$ to $8\,\mathrm{km}$) showed a slight positive anomaly (see Fig. 11a). The rain intensity, measured at BCO with a Vaisala WXT-520 ground station, peaked at $15\,\mathrm{mm\,h^{-1}}$, and precipitation events were persistent, in contrast to the short rain showers more typical of the dry season (Stevens et al., 2016). Bony et al. (2020) found that the Fish cloud pattern often occurs under weaker surface trade wind speeds below 8 m $\mathrm{s^{-1}}$; the sounding data confirm this, as the measured wind speeds lie well below this threshold in the lower boundary layer, e.g. Fig. 7.

Given that the vertical structure of the humidity field appears to be a strong indicator of synoptic variability, time-height humidity plots for all of the platforms are used to explore the coherence of synoptic conditions sampled by individual platforms. This analysis (Fig. 10) shows that soundings from the *Brown*, which moved around more, but stayed mostly north of 12.5 °N

[2]These symbols are taken from the 2017 edition (Table 14) of the WMO Cloud Atlas (www.wmocloudatlas.org).

https://doi.org/10.5194/essd-2020-174
Preprint. Discussion started: 5 August 2020

Open Access Earth System Science Data Discussions

and east of the *Meteor*, sampled a similar synoptic environment. The *Merian* and *Atalante* however were further south and their soundings show a humidity structure and evolution that is less coherent than seen by the ships in the Trade-wind Alley. Based on this finding and because performing the same analysis for any one station does not change the big picture, we composite the soundings from all of the platforms north of 12.5 °N. Figure 11 shows the temporal evolution of atmospheric conditions for the full period of data coverage averaged north of 12.5 °N, i.e., over the Trade-wind Alley. Before January 22 the mid-troposphere is relatively cool and zonal winds in the upper troposphere are strong. From January 22 onward the observational domain experienced warmer temperatures, weaker upper-tropospheric westerlies, as well as weaker easterlies near the surface. Positive pressure anomalies first appear in the upper troposphere and reach the surface at the end of January when a ridge starts to dominate the area. Surface and upper-tropospheric winds strengthen again after February 6 when the positive pressure anomaly fades. A strong moistening of the mid and upper levels is seen around February 13, which coincides with a directional change of the meridional winds at these levels, favoring the aforementioned extensive and persistent altocumulus cloud layer (Fig. 7).

Most differences between the structure of the atmosphere within the Trade-wind Alley (North of 12.5 °N) and the 'Boulevard des Tourbillons' (southern corridor) are confined to the structure of the lower-tropospheric humidity. South of 12.5 °N, the atmosphere was on average much more humid in the lower and middle troposphere, as shown in Fig. 12. This humidity anomaly is not persistent, as dry conditions, similar to those observed north of 12.5 °N, were also present; it can rather be associated with more frequent periods of a deep moist layer and deeper convection, for example as observed during the period around January 29 (see Fig. 10). Additional, albeit less substantial differences (not shown), are that middle-upper troposphere relative humidities (between 7 km to 10 km) are actually somewhat drier in the South. There is very little evidence of systematic differences in the temperature structure between the northern and southern soundings, except for a hint of enhanced stability in the upper troposphere (11 km to 15 km) in the North. Over the 'Boulevard des Tourbillons', the depth of the near surface easterly layer is 1 km to 2 km shallower and between 5 km to 15 km, the westerlies have a stronger northerly component.

4 Summary

The EUREC^{4}A field campaign during January–February 2020 included among its wide range of observational platforms an extensive radiosonde network, consisting of the Barbados Cloud Observatory and four research vessels. 182 radiosondes of type RS41-SGP were successfully launched in a regular manner between January 16 and February 17 from the BCO, 203 between January 18 and February 19 from the *Meteor*, 170 between January 8 and February 12 from the *Brown*, 139 between January 21 and February 16 from the *Atalante*, and 118 between January 20 and February 19 from the *Merian*. In addition, 47 MeteoModem radiosondes of type M10 were launched from the *Atalante* during intensive observational periods to sample variability associated with sea surface temperature fronts. These are described in the appendix.

We made data at three stages publicly available. Level-0 data contain the raw .mwx binary files, which can be read and processed with the MW41 software. Level-1 data were subject to Vaisala's standard quality control algorithm, which detects outliers in the profiles, performs a smoothing to reduce noise, and applies time-lag and radiation corrections. The Level-1 file

https://doi.org/10.5194/essd-2020-174
Preprint. Discussion started: 5 August 2020

Open Access Earth System Science Data Discussions

format is NetCDF with a temporal resolution of 1 s. To facilitate scientific analyses, Level-2 data are vertically gridded by averaging Level-1 data in 10-m bins. All soundings, ascending and descending, from each platform were collected into one NetCDF file for the Level-2 data.

The *Meteor* and the *Brown* followed nearly-orthogonal sampling lines, mostly in the latitude band 12.5–14.5 °N, whereas the *Atalante* and *Merian* sampled conditions further to the south. It was a central goal of EUREC^{4}A to better understand the formation and feedbacks of different patterns of shallow cumulus clouds. We were fortunate that Nature provided us with a wide variety of cloud conditions, which are reflected in the radiosonde data. The six weeks of sounding data at high temporal resolution should render the radiosonde data described herein useful for a large variety of scientific analyses.

5 Code and data availability

Raw Level-0 data consist of single files per sounding in .mwx. format, which combine ascent and descent from each instrument. Quality-controlled Level-1 data consist of single files per sounding in NetCDF format, with separate files for ascent and descent. Level-2 data are stored in a single file per station and include data on a 10-m vertical resolution grid, including all available ascents and descents. Ascent and descent can be distinguished by a flag that indicates the direction. All data (Stephan et al., 2020) are archived and freely available for public access at AERIS (https://doi.org/10.25326/62). Our software, which we used to convert to NetCDF format is also publicly available (Schulz, 2020a; https://doi.org/10.5281/zenodo.3907257) and uses the ecCodes library (https://github.com/ecmwf/eccodes).

Appendix A: Extra soundings on board the *Atalante*

In addition to the regular Vaisala soundings, further soundings were performed from the *Atalante* primarily to sample the lower atmosphere across sea surface temperature (SST) fronts associated with oceanic mesoscale dynamics. An independent radiosonde receiver was used to not interfere with the regular soundings depicted in this article. MeteoModem M10 radiosondes were chosen for availability and cost. In order to decide the period of intensive sampling using these sondes, we first identified on a daily basis the ocean mesoscale eddies and currents by applying the TOEddies detection algorithm (Laxenaire et al., 2018) to the Ssalto/Duacs Near Real Time (NRT) altimeter products (Absolute Dynamic Topography – ADT – and the associated surface geostrophic velocities; Ablain et al., 2017, Taburet et al., 2019).

These data were successively analyzed together with the Near Real Time (NRT) SST produced by Collecte Localisation Satellites (CLS), the ship's ThermoSalinoGraph (TSG) 5 m-depth temperature measurements, and ARPEGE and ECMWF forecasts in order to decide in real time the launching strategy. The NRT CLS SST is produced as a 1-day average, high-resolution product, which is a simple data average of the satellite measurements taken over the previous day, and has a resolution of 0.02 ° in latitude and longitude. This product may have local gaps due to the presence of clouds or missing data.

https://doi.org/10.5194/essd-2020-174
Preprint. Discussion started: 5 August 2020

Open Access Earth System Science Data Discussions

Precisely setting the sounding periods was difficult because the satellite observations were only available for the previous day with additional uncertainties in the location of SST fronts due to cloud screening. Furthermore, this strategy was defined in coordination with the *Merian* to take into account the oceanographic observation goals common to both ships.

The first targeted and intensive radiosonde observation leg took place on January 26. 11 MeteoModem sondes were launched while crossing a SST front associated with a relatively cold filament (-0.5 to -1 °C SST anomaly) steered from the Guyana coast by a mesoscale anticyclonic eddy (Fig. A1a). During this leg, the ship crossed a front of about 0.5 °C extending over 30 km with near surface wind of 6–7 m s^{-1} magnitude and 60°–70° direction. During this leg the ship was heading eastward, almost into the wind. Figure A1a shows the February 25 SST map, chosen as clouds prevented retrievals on the following day. According to the satellite product, one would have expected to meet the front further east. Fortunately, a first diagonal transect during the night provided us with the actual front location.

The second targeted and intensive radiosonde observation leg took place on February 2–3. This leg lasted for about 24 hours during which 28 MeteoModem radiosondes were launched while the ship was zigzagging in order to sample several times the northeastern edge of a cool SST anomaly of nearly -1 °C associated with coastal upwelling off the Suriname and French Guyana coast (Fig. A1b). During this leg, the ship was moving westward and sampled SST variations of 0.3–1 °C extending over 50–60 km. At this time the near surface wind was variable in direction, 40°–80°, and relatively strong (8–11 m s^{-1}).

The remaining MeteoModem radiosondes were launched on few diverse occasions: two were launched in the center of the warm core of a second eddy on January 27. Another radiosonde was launched under a convective system on February 10. The last four launches took place in cloud streets on February 17.

We used M10 GPS radiosondes with an SR10 station and EOSCAN (1.4.200306) software. Only ascent data are available for these soundings as no parachute was used and most of the launches were stopped manually at about 10 km height to increase the sampling frequency of the lower atmosphere in regions characterized by SST fronts. Launch frequencies reached up to one sounding every 40 min during the intensive launch periods. Therefore, several radiosondes were emitting at the same time, so frequencies had to be changed within the 400.4–403.4 MHz band to avoid interference. M10 radiosondes measure relative humidity and temperature, from which dew point temperature is deduced. The altitude and horizontal displacements of the radiosondes are measured by GPS and are used to diagnose the horizontal wind components. The pressure is deduced from the altitude and the surface station pressure measurement, using the hydrostatic approximation. Our published data formats, NetCDF and ASCII formatted files (.cor files), both contain data reported every second. Note that in Level-1 data, constructed from BUFR reports that do not contain relative humidity, the latter is deduced from the dew point temperature using the Magnus-Tetens formula and might therefore slightly differ from the value in the raw .cor files that provide the direct measurement of the radiosondes.

Figure A2 illustrates the outcome of these targeted and intensive radiosonde observations with results from the February 2–3 intensive observation period (Fig. A1b). Profile color (Fig. A2a–c) denotes the SST measured by the ship at the time of the launch (Fig. A2d). Blue (red) profiles are thus on the cold (warm) side of the SST front. These profiles are from raw data (level-0) and no attempt was made to validate, correct or remove doubtful data such as the surprisingly cold layer between 800–900 m altitude that can be seen in one of the blue potential temperature profiles (Fig. A2a). No attempt has either been

https://doi.org/10.5194/essd-2020-174
Preprint. Discussion started: 5 August 2020

Open Access Earth System Science Data Discussions

made to disentangle diurnal or synoptic scale variability from the imprint of the SST front on the lower atmosphere. However, one can note that the warm side of the SST front was sampled mostly during nighttime (local noon at 1530 UTC, nighttime from 22–10 UTC). There is a clear tendency for warmer boundary layers over the warm side of the front than over the cold side (Fig. A2a). On the other hand, the height of the mixed layer, that can be defined as near homogeneous potential temperature layers close to the surface, tends to be deeper over the cold side than over the warm side. This contrasts with results obtained over stronger SST fronts from observation (Ablain et al., 2014) and modeling studies (e.g., Kilpatrick et al., 2013; Redelsperger et al., 2019) and suggests that the lower atmosphere does not solely respond to the SST gradient. Over the cold side, wind speed tends to decrease with altitude (Fig. A2b). Over the warm side, and despite a larger variability from a profile to another, the wind speed tends to be more homogeneous in the vertical than on the cold side. Because the mixed layer depth is shallower over the warm side, it is however difficult to interpret this as the result of a stronger vertical turbulent mixing. Overall, near surface wind speed tends to be slightly weaker on the warm side than on the cold side. There is also a noticeable change in wind direction throughout the boundary layer from E-NE over the warm side to NE over the cold side (Fig. A2c).

Finally, we provide a first assessment of the quality of MeteoModem M10 measurements based on the *Atalante* soundings, as also Vaisala soundings were launched during the intensive MeteoModem periods. We compare MeteoModem and Vaisala wind, temperature and relative humidity profiles for 8 pairs of soundings that were launched within 25 min (Fig. A3). Choosing such a small time period certainly limits the number of difference profiles that can be computed, but it ensures that the two radiosondes sampled comparable situations. Mean difference profiles and corresponding standard deviations are computed on 100 m bins. Neither horizontal wind components (Fig. A3a, b) nor temperature (Fig. A3c) show any clear bias, although the differences between MeteoModem and Vaisala can be a few m s^{-1} for the wind components (standard deviation of about 0.5–1 m s^{-1}) and about 1 °C for temperature (standard deviation of about 0.1–0.2 °C). On the other hand, despite a large noise below 4 km height, relative humidity shows a rather homogeneous moist bias of about 5 % (1–5 % standard deviation) in MeteoModem measurements compared with Vaisala (Fig. A3d). No correction was applied, neither to the temperature nor to the relative humidity measurements. In particular, corrections for the relative humidity seem necessary but are still a matter of research. An example of such corrections, developed for soundings in the continental mid-latitude can be found in Dupont et al. (2020).

Author contributions. Sandrine Bony and Bjorn Stevens designed the sounding strategy, which was then refined and realized in cooperation with Claudia C. Stephan and Simon P. de Szoeke. Sabrina Speich (cruise lead *Atalante*) designed, with Gilles Reverdin, and managed the measurements on board the *Atalante*. Stefan Kinne (cruise lead *Meteor*) and Friedhelm Jansen (responsible for BCO operations) managed the logistics of purchasing and transporting the radiosonde equipment. Benjamin Charpentier and Richard Wilson processed the MeteoModem data. Alexis Doerenbecher investigated the data flow through the GTS. The majority of radiosonde launches were performed by Gholamhossein Bagheri, Tobias Böck, Alton Daley, Johannes Güttler, Kevin C. Helfer, Sebastian A. Los, Almuth Neuberger, Andreas Raeke, Maximilian Ringel, Markus Ritschel, Johannes Röttenbacher, Pauline Sadoulet, Imke Schirmacher, M. Katharina Stolla and Ethan Wright. Claudia Acquistapace, Katharina Baier, Thibaut Dauhut, Rémi Laxenaire, Yanmichel Morfa-Avalos, Renaud Person and Estefanía Quiñones Meléndez played a leading role in the experimental execution. Hugo Bellenger and Simon P. de Szoeke contributed to the design of the radiosonde

https://doi.org/10.5194/essd-2020-174
Preprint. Discussion started: 5 August 2020

Open Access Earth System Science Data Discussions

network. Hauke Schulz and Sabrina Schnitt processed, quality-checked and analyzed the data. Claudia C. Stephan prepared the manuscript with contributions from all co-authors.

Competing interests. There are no competing interests.

Disclaimer. TEXT

Acknowledgements. We acknowledge Olivier Garrouste and Axel Roy from Météo-France for lending the MeteoModem station and launcher and their technical assistance, and Thierry Jimonet and Météo-France Guadeloupe for their help. We would like to thank Rudolf Krockauer and Tanja Kleinert (DWD), Bruce Ingleby (ECMWF) and Jeff Ator (NOAA) for helping to track the radiosonde data sent to the GTS. We would like to thank Sophie Bouffies-Cloché (IPSL) and Florent Beucher (MF) for making ECMWF and ARPEGE forecasts available in real time. We thank Philippe Robbe, captain of the French *Atalante*, and the crew that helped us in completing successfully all the planned observations. We are grateful to Doris Jördens for the technical support with the Vaisala equipment, and to Ingo Lange, Harald Budweg, and Rudolf Krockauer for their help with training our operators. We would like to thank the numerous volunteers performing launches at BCO, and Andreas Kopp, Joachim Ribbe, Klaus Reus, Diego Lange, Alex Kellmann and Nicolas Geyskens for launches on the research vessels. We would like to express our special gratitude to Angela Gruber for resolving any problems before they became problems. The ceilometer data from the *Meteor* (Jansen, 2020b) and surface meterology data from the BCO (Jansen, 2020a) are publicly available. We acknowledge the use of imagery from the NASA Worldview application (https://worldview.earthdata.nasa.gov), part of the NASA Earth Observing System Data and Information System (EOSDIS). The Ssalto/Duacs altimeter products were produced and distributed by the Copernicus Marine and Environment Monitoring Service (CMEMS) (http://www.marine.copernicus.eu). The Collecte Localisation Satellites (CLS) SST and Chlorophylle-a catsat products (https://www.catsat.com/ocean-data/) were made available to us during the cruise in the framework of the Données et Services pour l'Océan (ODATIS) French national data infrastructure. The *Atalante* cruise was funded under the EUREC^{4}A-OA project by the following French institutions: the national INSU-CNRS program LEFE; the French Research Fleet; Ifremer; CNES; the Department of Geosciences of ENS through the Chaire Chanel program; MétéoFrance. Vaisala radiosondes were funded by the Max Planck Society, and the US National Oceanic and Atmospheric Administration Ocean and Atmospheric Research grant number NA19OAR4310375. MeteoModem radiosondes were funded thanks to Caroline Muller by the European Research Council (ERC) under the European Union's Horizon 2020 research and innovation programme (Project CLUSTER, grant agreement No. 805041). Claudia C. Stephan was supported by the Minerva Fast Track Program of the Max Planck Society.

https://doi.org/10.5194/essd-2020-174
Preprint. Discussion started: 5 August 2020

Open Access Earth System Science Data Discussions

References

Ablain, M., Legeais, J., Prandi, P., Marcos, M., Fenoglio-Marc, L., Dieng, H., Benveniste, J., and Cazenave, A.: Satellite altimetry-based sea level at global and regional scales, Surv. Geophys., 38, 7–31, https://doi.org/10.1007/s10712-016-9389-8, 2017.

Ablain, Y., Tomita, H., Cronin, M., and Bond, N. A.: Atmospheric pressure response to mesoscale sea surface temperature variations in the Kuroshio Extension region: In situ evidence, J. Geophys. Res. Atmos., 119, 8015–8031, https://doi.org/10.1002/2013JD021126, 2014.

Albrecht, B. A.: Effects of precipitation on the thermodynamic structure of the trade wind boundary layer, J. Geophy. Res. Atm., 98, 7327–7337, https://doi.org/10.1029/93JD00027, 1993.

Albrecht, B. A., Betts, A. K., Schubert, W. H., and Cox, S. K.: Model of the thermodynamic structure of the trade-wind boundary layer: Part I. Theoretical formulation and sensitivity tests, J. Atmos. Sci., 36, 73–89, https://doi.org/10.1175/1520-0469(1979)036<0073:MOTTSO>2.0.CO;2, 1979.

Albrecht, B. A., Bretherton, C. S., Johnson, D., Scubert, W. H., and Frisch, A. S.: The Atlantic Stratocumulus Transition Experiment—ASTEX, Bull. Amer. Meteor. Soc., 76, 889–904, https://doi.org/10.1175/1520-0477(1995)076<0889:TASTE>2.0.CO;2, 1995.

Arakawa, A. and Schubert, W. H.: Interaction of a cumulus cloud ensemble with the large-scale environment, Part I, J. Atmos. Sci., 31, 674–701, https://doi.org/10.1175/1520-0469(1974)031<0674:IOACCE>2.0.CO;2, 1974.

Augstein, E., Riehl, H., Ostapoff, F., and Wagner, V.: Mass and energy transports in an undisturbed Atlantic trade-wind flow, Mon. Wea. Rev., 101, 101–111, https://doi.org/10.1175/1520-0493(1973)101<0101:MAETIA>2.3.CO;2, 1973.

Baker, M.: Trade Cumulus Observations, in: The representation of cumulus convection in numerical models, edited by Emanuel, K. A. and Raymond, D. J., Meteorological Monographs, pp. 29–37, Amer. Meteor. Soc., Boston, MA, https://doi.org/10.1007/978-1-935704-13-3_3, 1993.

Bolton, D.: The computation of equivalent potential temperature, Mon. Wea. Rev., 108, 1046–1053, https://doi.org/10.1175/1520-0493(1980)108<1046:TCOEPT>2.0.CO;2, 1980.

Bony, S. and Stevens, B.: Measuring area-averaged vertical motions with dropsondes, J. Atmos. Sci., 76, 767–783, https://doi.org/10.1175/JAS-D-18-0141.1, 2019.

Bony, S., Stevens, B., Frierson, D. M. W., Jakob, C., Kageyama, M., Pincus, R., Shepherd, T. G., Sherwood, S. C., Siebesma, A. P., Sobel, A. H., Watanabe, M., and Webb, M. J.: Clouds, circulation and climate sensitivity, Nature Geosci., 8, 261, https://doi.org/10.1038/ngeo2398, 2015.

Bony, S., Stevens, B., Ament, F., Bigorre, S., Chazette, P., Crewell, S., Delanoë, J., Emanuel, K., Farrell, D., Flamant, C., Gross, S., Hirsch, L., Karstensen, J., Mayer, B., Nuijens, L., Ruppert, J. H., Sandu, I., Siebesma, P., Speich, S., Szczap, F., Totems, J., Vogel, R., Wendisch, M., and Wirth, M.: EUREC4A: A field campaign to elucidate the couplings between clouds, convection and circulation, Surv. Geophys., 38, 1529–1568, https://doi.org/10.1007/s10712-017-9428-0, 2017.

Bony, S., Schulz, H., Vial, J., and Stevens, B.: Sugar, gravel, fish and flowers: Dependence of mesoscale patterns of trade-wind clouds on environmental conditions, Geophys. Res. Lett., n/a, https://doi.org/10.1029/2019GL085988, 2020.

Bretherton, C. S.: Understanding Albrecht's model of trade cumulus cloud fields, J. Atmos. Sci., 50, 2264–2283, https://doi.org/10.1175/1520-0469(1993)050<2264:UAMOTC>2.0.CO;2, 1993.

Ciesielski, P. E., Haertel, P. T., Johnson, R. H., Wang, J., and Loehrer, S. M.: Developing high-quality field program sounding datasets, Bull. Amer. Met. Soc., 93, 325–336, https://doi.org/10.1175/BAMS-D-11-00091.1, 2012.

https://doi.org/10.5194/essd-2020-174
Preprint. Discussion started: 5 August 2020

Open Access Earth System Science Data Discussions

Dupont, J.-C., Haeffelin, M., Badosa, J., Clain, G., Raux, C., and Vignelles, D.: Characterization and corrections of relative humidity measurement from Meteomodem M10 radiosondes at mid-latitude stations, J. Atm. and Oceanic Technol., https://doi.org/10.1175/JTECH-D-18-0205.1, 2020.

Hardy, B.: ITS-90 formulations for vapor pressure, frostpoint temperature, dewpoint temperature, and enhancement factors in the range–100 to+ 100 C, in: The proceedings of the third international symposium on Humidity & Moisture, Teddington, London, England, pp. 1–8, 1998.

Jansen, F.: Surface meteorology Barbados Cloud Observatory, https://doi.org/10.25326/54, https://doi.org/10.25326/54, 2020a.

Jansen, F.: Ceilometer measurements RV Meteor, https://doi.org/10.25326/53, https://doi.org/10.25326/53, 2020b.

Johnson, R. H. and Ciesielski, P. E.: Structure and properties of Madden–Julian Oscillations deduced from DYNAMO sounding arrays, J. Atmos. Sci., 70, 3157–3179, https://doi.org/10.1175/JAS-D-13-065.1, 2013.

Kilpatrick, T., Schneider, N., and Qiu, B.: Boundary layer convergence induced by strong winds across a midlatitude SST front, J. Climate, 11, 1698–1718, https://doi.org/10.1175/JCLI-D-13-00101.1, 2013.

Krueger, S. K.: Numerical simulation of tropical cumulus clouds and their interaction with the subcloud layer, J. Atmos. Sci., 45, 2221–2250, https://doi.org/10.1175/1520-0469(1988)045<2221:NSOTCC>2.0.CO;2, 1988.

Kuettner, J. P. and Holland, J.: the BOMEX project, Bull. Amer. Meteor. Soc., 50, 394–403, https://doi.org/10.1175/1520-0477-50.6.394, 1969.

Laxenaire, R., Speich, S., Blanke, B., Chaigneau, A., Pegliasco, C., and Stegner, A.: Anticyclonic eddies connecting the western boundaries of Indian and Atlantic Oceans, J. Geophys. Res. Oceans, 123, 7651–7677, https://doi.org/10.1029/2018JC014270, 2018.

Lenschow, D. H., Savic-Jovcic, V., and Stevens, B.: Divergence and vorticity from aircraft air motion measurements, J. Atm. Ocean. Tech., 24, 2062–2072, https://doi.org/10.1175/2007JTECHA940.1, 2007.

Lin, X. and Johnson, R. H.: Heating, moistening, and rainfall over the western Pacific warm pool during TOGA COARE, J. Atmos. Sci., 53, 3367–3383, https://doi.org/10.1175/1520-0469(1996)053<3367:HMAROT>2.0.CO;2, 1996.

Mapes, B. E., Ciesielski, P. E., and Johnson, R. H.: Sampling errors in Rawinsonde-array budgets, J. Atmos. Sci., 60, 2697–2714, https://doi.org/10.1175/1520-0469(2003)060<2697:SEIRB>2.0.CO;2, 2003.

Nitta, T. and Esbensen, S.: Heat and moisture budget analyses using BOMEX data, Mon. Wea. Rev., 102, 17–28, https://doi.org/10.1175/1520-0493(1974)102<0017:HAMBAU>2.0.CO;2, 1974.

Rauber, R. M., Ochs, H. T., Di Girolamo, L., Göke, S., Snodgrass, E., Stevens, B., Knight, C., Jensen, J. B., Lenschow, D. H., Rilling, R. A., Rogers, D. C., Stith, J. L., Albrecht, B. A., Zuidema, P., Blyth, A. M., Fairall, C. W., Brewer, W. A., Tucker, S., Lasher-Trapp, S. G., Mayol-Bracero, O. L., Vali, G., Geerts, B., Anderson, J. R., Baker, B. A., Lawson, R. P., Bandy, A. R., Thornton, D. C., Burnet, E., Brenguier, J.-L., Gomes, L., Brown, P. R. A., Chuang, P., Cotton, W. R., Gerber, H., Heikes, B. G., Hudson, J. G., Kollias, P., Krueger, S. K., Nuijens, L., O'Sullivan, D. W., Siebesma, A. P., and Twohy, C. H.: Rain in shallow cumulus over the ocean: The RICO Campaign, Bull. Amer. Meteor. Soc., 88, 1912–1928, https://doi.org/10.1175/BAMS-88-12-1912, 2007.

Redelsperger, J.-L., Bouin, M.-N., Pianezze, J., Garnier, V., and Marié, L.: Impact of a sharp, small-scale SST front on the marine atmospheric boundary layer on the Iroise Sea: Analysis from a hectometric simulation, Quart. J. Roy. Meteor. Soc., 145, 3692–3714, https://doi.org/10.1002/qj.3650, 2019.

Reed, R. J. and Recker, E. E.: Structure and properties of synoptic-scale wave disturbances in the equatorial western Pacific, J. Atmos. Sci., 28, 1117–1133, 1971.

Schulz, H.: EUREC4A radiosonde software, https://doi.org/10.5281/zenodo.3923087, 2020a.

https://doi.org/10.5194/essd-2020-174
Preprint. Discussion started: 5 August 2020

Open Access Earth System Science Data Discussions

Schulz, H.: Meso-scale cloud organizaiton during EUREC^{4}A, Earth Sys. Sci. Data, xx, to be submitted, 2020b.

Stephan et al., C. C.: Radiosonde measurements from the EUREC4A field campaign, https://doi.org/10.25326/62, https://doi.org/10.25326/62, 2020.

Stevens, B., Farrell, D., Hirsch, L., Jansen, F., Nuijens, L., Serikov, I., Brügmann, B., Forde, M., Linne, H., Lonitz, K., and Prospero, J. M.: The Barbados Cloud Observatory: Anchoring investigations of clouds and circulation on the edge of the ITCZ, Bull. Amer. Met. Soc., 97, 787–801, https://doi.org/10.1175/BAMS-D-14-00247.1, 2016.

Stevens, B., Ament, F., Bony, S., Crewell, S., Ewald, F., Gross, S., Hansen, A., Hirsch, L., Jacob, M., Kölling, T., Konow, H., Mayer, B., Wendisch, M., Wirth, M., Wolf, K., Bakan, S., Bauer-Pfundstein, M., Brueck, M., Delanoë, J., Ehrlich, A., Farrell, D., Forde, M., Gödde, F., Grob, H., Hagen, M., Jäkel, E., Jansen, F., Klepp, C., Klingebiel, M., Mech, M., Peters, G., Rapp, M., Wing, A. A., and Zinner, T.: A high-altitude long-range aircraft configured as a cloud observatory: The NARVAL expeditions, Bull. Amer. Meteor. Soc., 100, 1061–1077, https://doi.org/10.1175/BAMS-D-18-0198.1, 2019.

Stevens, B., Bony, S., Brogniez, H., Hentgen, L., Hohenegger, C., Kiemle, C., L'Ecuyer, T. S., Naumann, A. K., Schulz, H., Siebesma, P. A., Vial, J., Winker, D. M., and Zuidema, P.: Sugar, gravel, fish and flowers: Mesoscale cloud patterns in the trade winds, Quart. J. Roy. Meteor. Soc., 146, 141–152, https://doi.org/10.1002/qj.3662, 2020.

Taburet, G., Sanchez-Roman, A., Ballarotta, M., Pujol, M.-I., Legeais, J.-F., Fournier, F., Faugere, Y., and Dibarboure, G.: DUACS DT2018: 25 years of reprocessed sea level altimetry products, Ocean Sci., 15, 1207–1224, https://doi.org/10.5194/os-15-1207-2019, 2019.

Tiedtke, M.: A comprehensive mass flux scheme for cumulus parameterization in large-scale models, Mon. Wea. Rev., 117, 1779–1800, https://doi.org/10.1175/1520-0493(1989)117<1779:ACMFSF>2.0.CO;2, 1989.

vanZanten, M. C., Stevens, B., Nuijens, L., Siebesma, A. P., Ackerman, A. S., Burnet, F., Cheng, A., Couvreux, F., Jiang, H., Khairoutdinov, M., Kogan, Y., Lewellen, D. C., Mechem, D., Nakamura, K., Noda, A., Shipway, B. J., Slawinska, J., Wang, S., and Wyszogrodzki, A.: Controls on precipitation and cloudiness in simulations of trade-wind cumulus as observed during RICO, J. Adv. Model. Earth Sys., 3, https://doi.org/10.1029/2011MS000056, 2011.

Xue, H., Feingold, G., and Stevens, B.: Aerosol effects on clouds, precipitation, and the organization of shallow cumulus convection, J. Atmos. Sci., 65, 392–406, https://doi.org/10.1175/2007JAS2428.1, 2008.

Yanai, M., Esbensen, S., and Chu, J.-H.: Determination of bulk properties of topical cloud clusters from large-scale heat and moisture budgets, J. Atmos. Sci., 30, 611–627, https://doi.org/10.1175/1520-0469(1973)030<0611:DOBPOT>2.0.CO;2, 1973.

Yoneyama, K., Hanyu, M., Sueyoshi, S., Yoshiura, F., and Katsumata, M.: Radiosonde observation from ships in the tropical region, JAMSTECR, 45, 2002.

https://doi.org/10.5194/essd-2020-174
Preprint. Discussion started: 5 August 2020

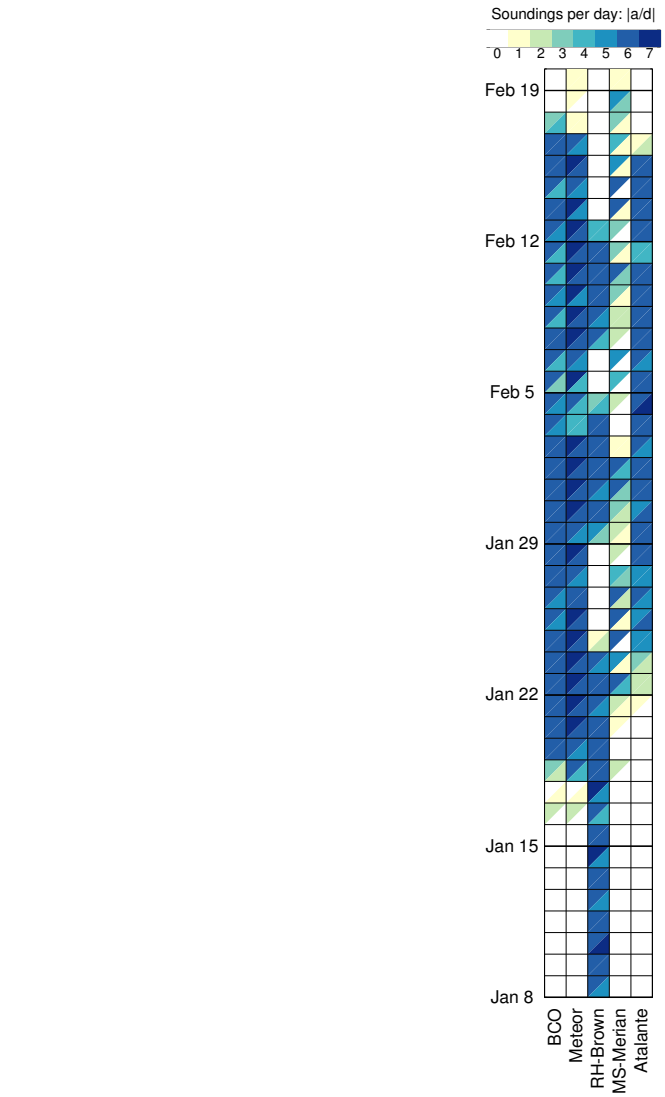

Figure 1. Daily number of ascending (upper left triangles) and descending (lower right triangles), respectively, soundings associated with each platform.

https://doi.org/10.5194/essd-2020-174
Preprint. Discussion started: 5 August 2020

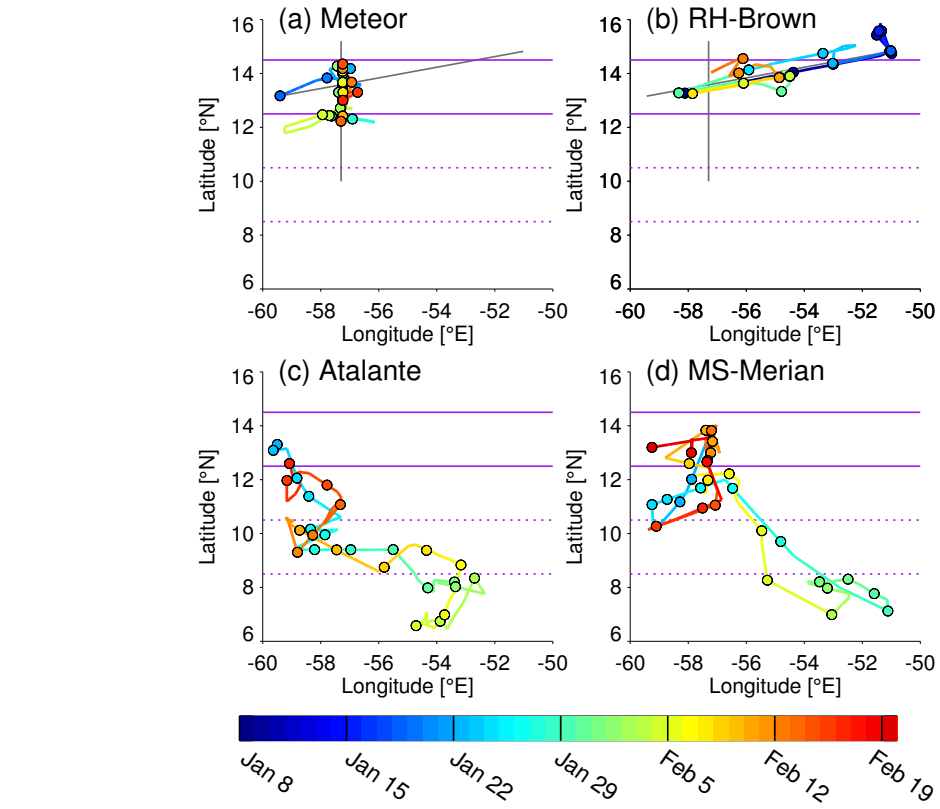

Figure 2. Routes and launch coordinates of radiosondes for the four research vessels colored by date. Circles mark the locations of the first radiosonde launch on each day. The gray lines in (a) and (b) mark the nearly orthogonal lines that were sampled by the *Meteor* (North–South) and the *Brown* (West–East). Purple lines mark the northern (12.5–14.5 °N; solid) and southern (8.5–10.5 °N; dashed) latitude bands that we later use to define a North (Trade-wind Alley) and South (Boulevard des Tourbillons) domain.

https://doi.org/10.5194/essd-2020-174
Preprint. Discussion started: 5 August 2020

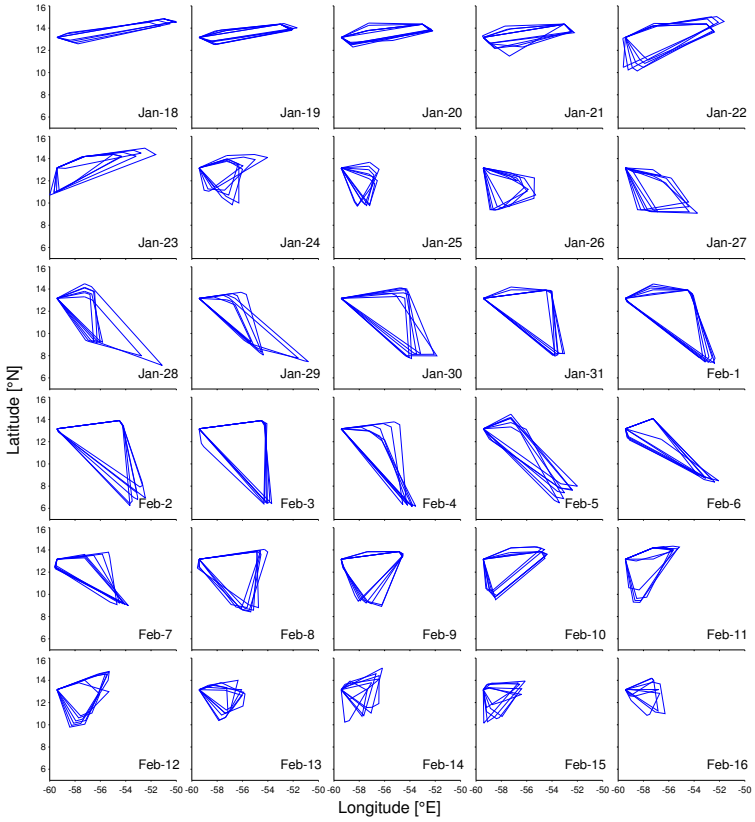

Figure 3. For each day between Jan-18 and Feb-16, 4-hourly polygons mark the outer bounds of the radiosonde network. Polygon vertices correspond to starting locations of either ascending or descending soundings that occurred within ±2 hours of a fixed time.

https://doi.org/10.5194/essd-2020-174
Preprint. Discussion started: 5 August 2020

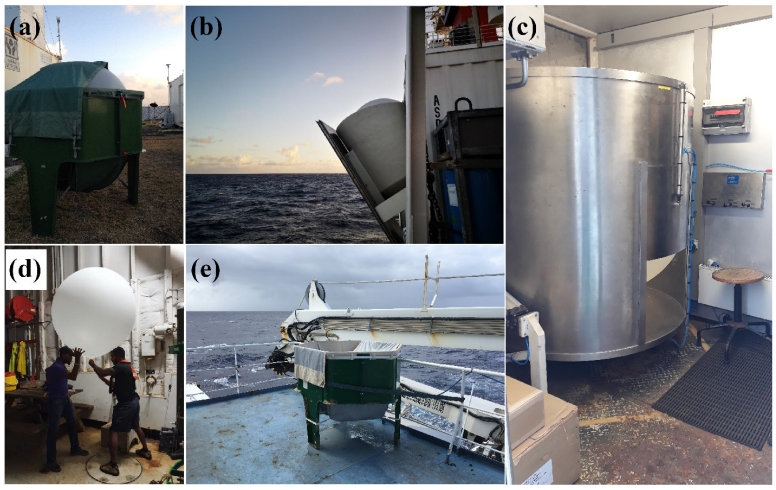

Figure 4. Photographs of the (a) launcher with balloon at the BCO, (b) DWD launcher with balloon on board the *Meteor*, (c) launch container with balloon on board the *Merian*, (d) manual balloon filling procedure on board the *Brown*, (e) empty launcher on board the *Atalante*.

https://doi.org/10.5194/essd-2020-174
Preprint. Discussion started: 5 August 2020

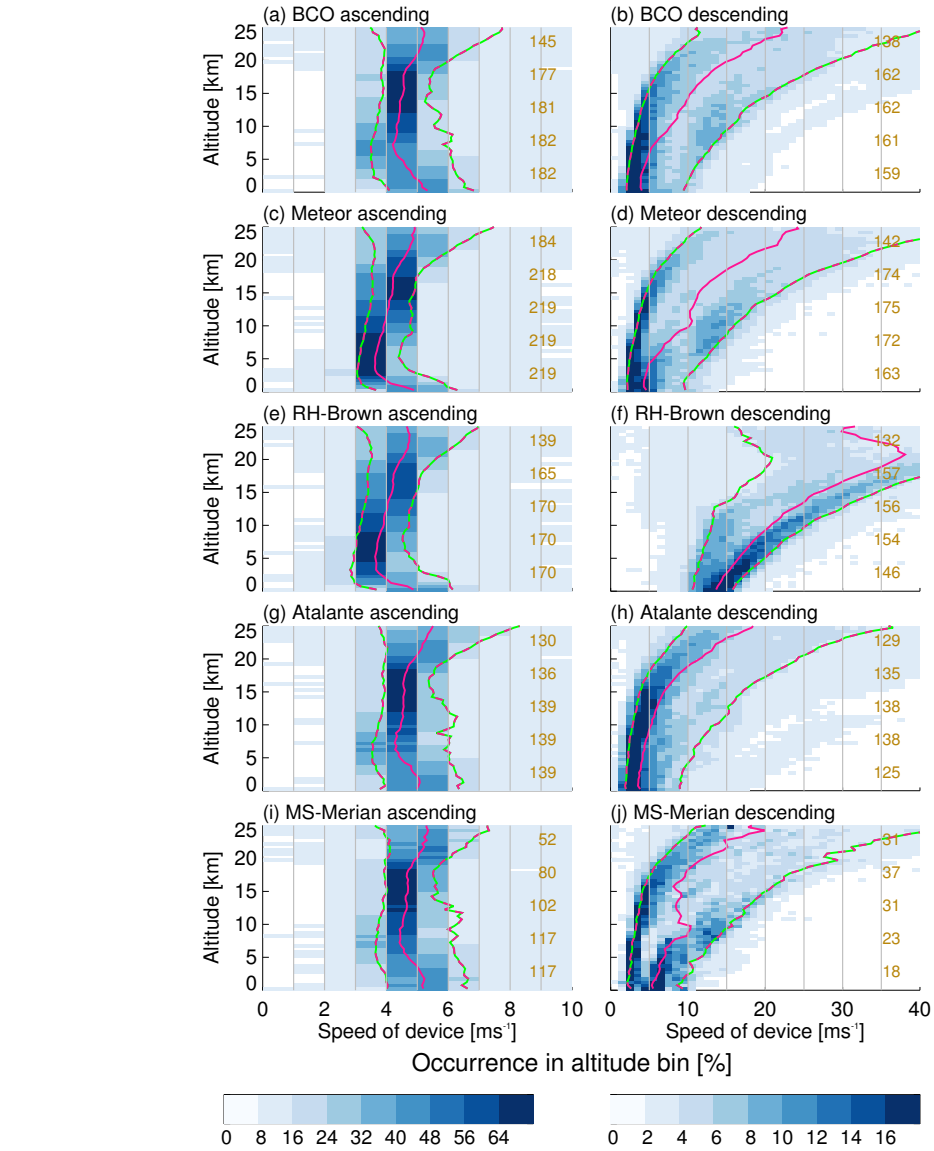

Figure 5. Instrument (left) ascent and (right) descent speeds as a function of height. The sum of occurrence frequencies in each altitude bin is 100 %. The pink line shows the median profiles and the pink-green lines show the 10th and the 90th percentiles, respectively. Altitude bins are 500 m deep and speed bins are 1 m s^{-1} wide. The numbers of radiosondes that crossed the corresponding height-levels (2.5, 7.5, 12.5, 17.5 and 22.5 km, respectively) are shown in each panel.

https://doi.org/10.5194/essd-2020-174
Preprint. Discussion started: 5 August 2020

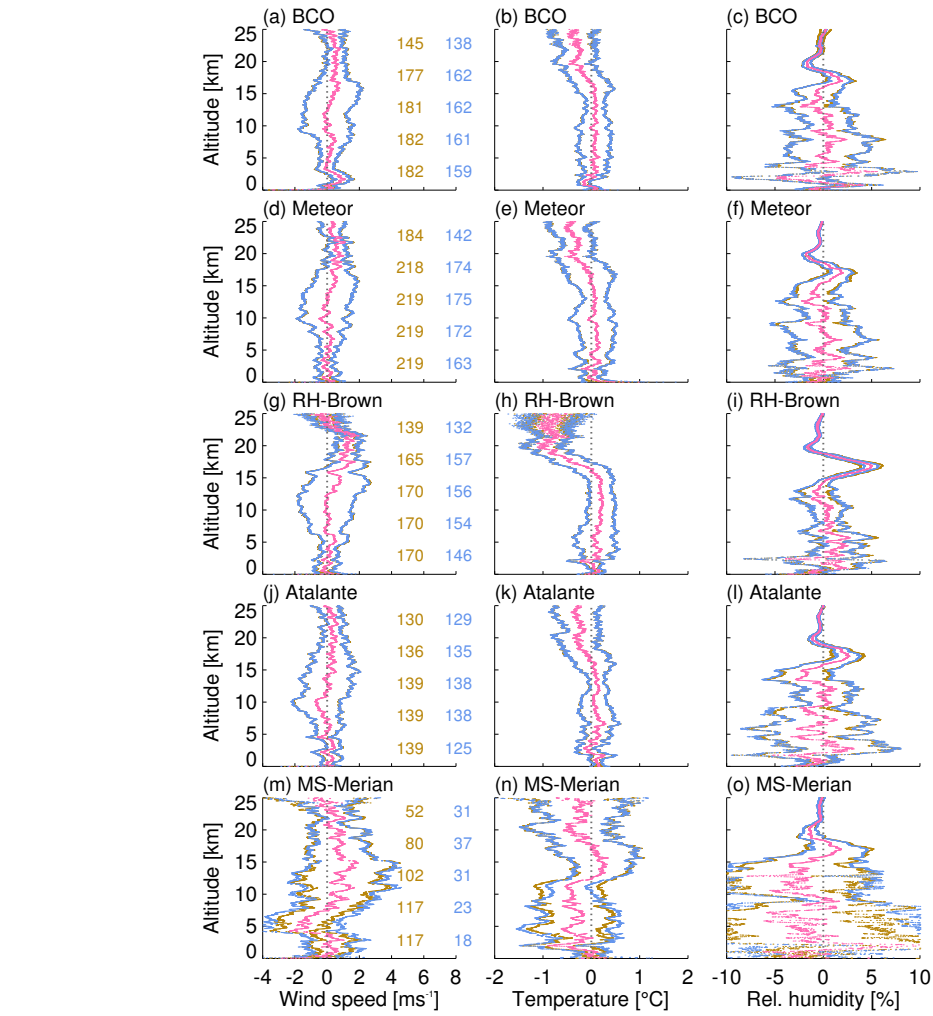

Figure 6. Comparison of (left) horizontal wind speed, (middle) air temperature, and (right) relative humidity, measured during ascent and descent. The pink dots show the time-averaged values during ascent minus the time-averaged values during descent. Brown (blue) dots show the 95 % confidence intervals for ascent (descent). Numbers inside the panels on the left-hand side show the counts of ascending (brown) and descending (blue) radiosondes that crossed the corresponding height-levels (2.5, 7.5, 12.5, 17.5 and 22.5 km, respectively.)

https://doi.org/10.5194/essd-2020-174
Preprint. Discussion started: 5 August 2020

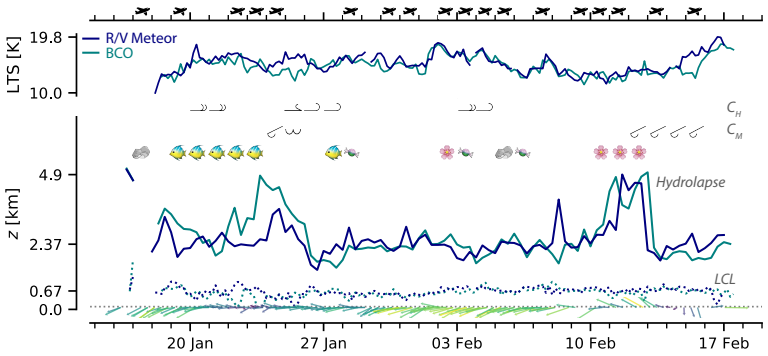

Figure 7. Synoptic overview of period and region of intensive aircraft measurements. Plotted is the potential temperature at 700 hPa, the height of the hydrolapse, defined as the mean height of a running 500 m range in which mean relative humidity first drops below 30 %, the lifting condensation level (LCL) and the wind vector averaged over the lower 200 m. Winds are 12 h median values, other quantities are resampled on a 4 h interval, with median values plotted except for the LCL where minimum values are plotted. For the wind vectors the maximum and minimum wind speeds are $12.3\,\mathrm{m\,s^{-1}}$ and $2.0\,\mathrm{m\,s^{-1}}$, respectively. Tick marks denote maximum and minimum θ_{700}, and maximum and median height of *Meteor* hydrolapse and the mean height of the LCL (*Meteor*). Also shown are days when aircraft with dropsondes were flying, the synoptic cloud observations of mid-level (C_M) and high (C_H) clouds with the associated WMO cloud-sybmol (Table 14 of 2017 World Meteorological Organization Cloud Atlas, https://cloudatlas.wmo.int/en/home.html) that predominated for that day. Cloud types are taken from the Barbados Meteorological Service SYNOP reports. Days on which a mesoscale pattern of shallow convection, following the classification activity of Schulz (2020b), was readily identified are indicated by the emojis for Fish, Sugar (candy), Flowers or Gravel (rocks).

https://doi.org/10.5194/essd-2020-174
Preprint. Discussion started: 5 August 2020

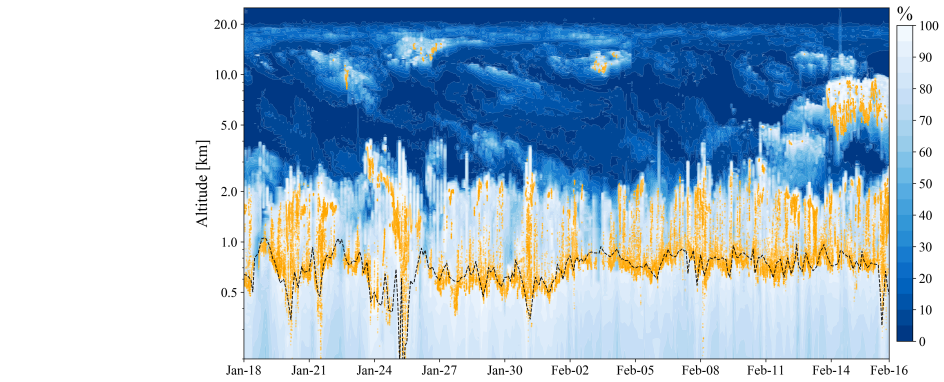

Figure 8. Comparison between ascending soundings and ceilometer measurements on the *Meteor*. The relative humidity from radiosonde measurements is shown in blue-to-white shading. The black dashed line represents the lifting condensation level calculated based on Bolton (1980). Cloud base heights as observed by the ceilometer are marked with orange dots. The vertical axis is chosen to be logarithmic for better visibility of the moisture distribution near the surface. The time-axis for the soundings uses launch time. The temporal resolution of the ceilometer data is 10 s. Low-altitude relative humidity profiles (300 m to 800 m) of the descending soundings were recovered by assuming a dry adiabat temperature and a constant humidity profile.

https://doi.org/10.5194/essd-2020-174
Preprint. Discussion started: 5 August 2020

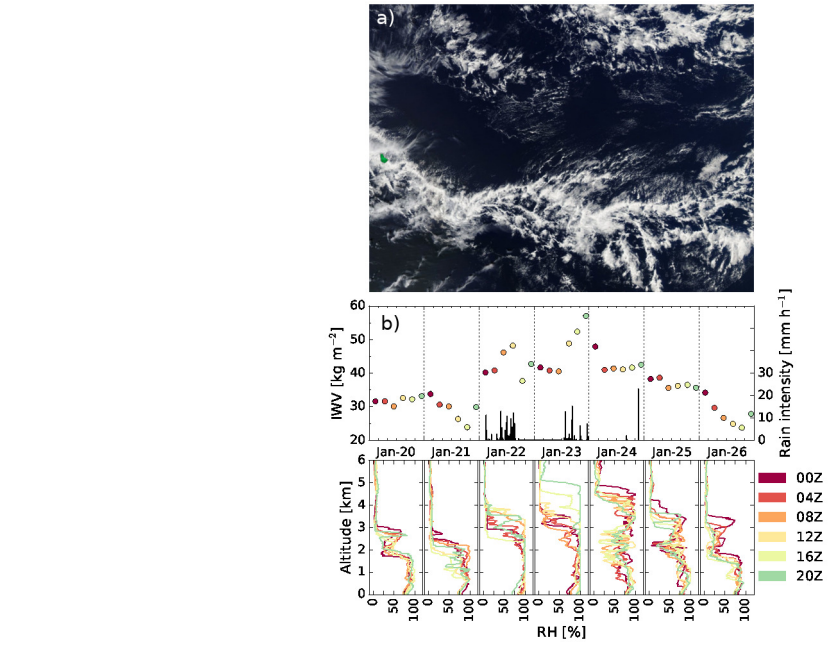

Figure 9. Fish cloud pattern passing Barbados between January 22–24, 2020. (a) MODIS-Aqua scene from January 22. The image covers 9–18 °N, 48–60 °W with Barbados shown in artificial green. (b) Temporal evolution of relative humidity (lower panel) and integrated water vapor (IWV; upper panel, color-coded) as measured by the BCO soundings January 20–26. Profiles and calculated IWV values are color-coded according to the nearest hour of the sounding reaching 100 hPa. The upper panel also shows a one-minute running mean of rain intensity recorded at BCO (black).

https://doi.org/10.5194/essd-2020-174
Preprint. Discussion started: 5 August 2020

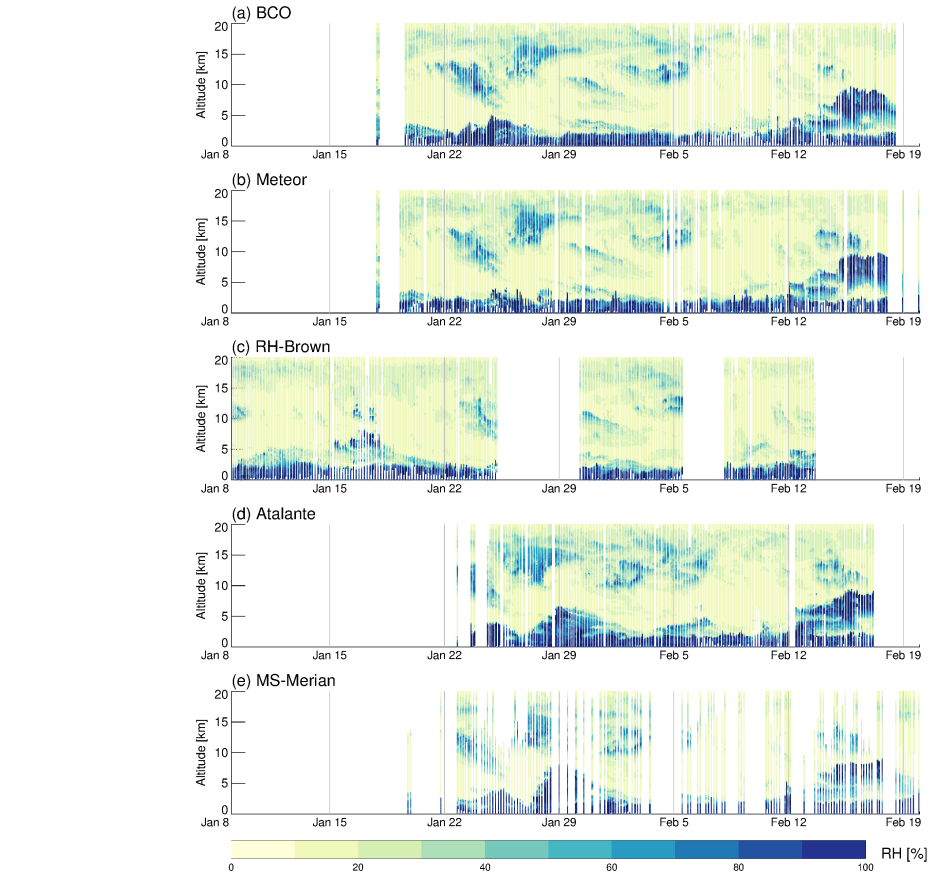

Figure 10. Time-height series of relative humidity measurements from all platforms. The plot combines ascending and descending soundings.

https://doi.org/10.5194/essd-2020-174
Preprint. Discussion started: 5 August 2020

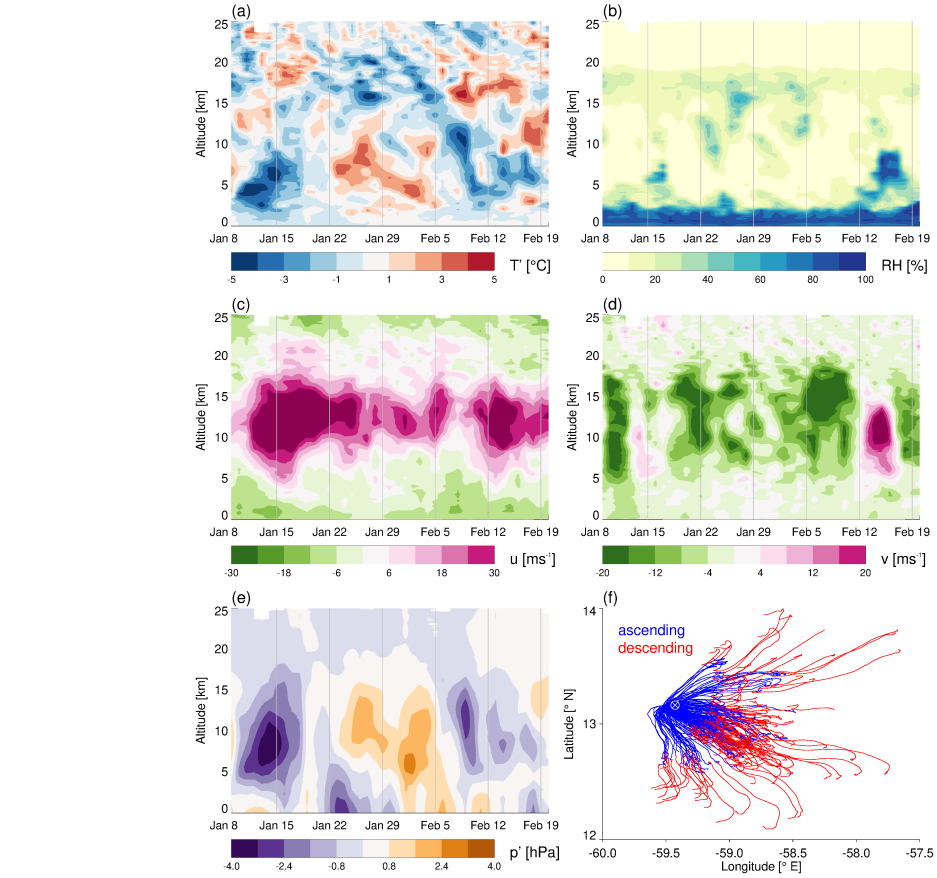

Figure 11. (a-e) Time-height cross sections of daily (a) temperature anomaly, (b) relative humidity, (c) zonal wind, (d) meridional wind and (e) pressure anomaly computed from ascending soundings north of 12.5 °N. The data combine 182 soundings from the BCO, 169 from the *Brown*, 150 from the *Meteor*, 28 from the *Merian* and 4 from the *Atalante*. Anomalies are defined as deviations from the time average at each altitude. (f) The horizontal trajectories of ascending and descending, respectively, radiosondes launched from the BCO.

https://doi.org/10.5194/essd-2020-174
Preprint. Discussion started: 5 August 2020

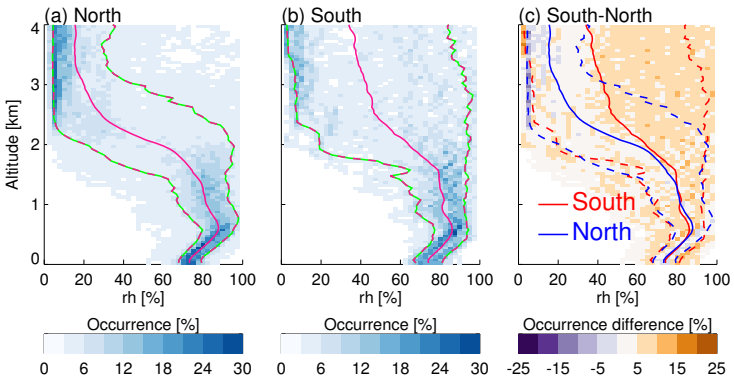

Figure 12. Occurrences of relative humidity as a function of height below 4 km for all soundings launched between January 26 and February 12 (437 profiles). The sum of occurrence frequencies in each altitude bin is 100 %. Altitude bins are 50 m deep and each x-axis contains 40 bins. North (panel a) designates soundings from the northern (12.5–14.5 °N; 261 profiles) latitude band, and South designates soundings from southern (8.5–10.5 °N, 63 profiles) latitude band. Solid lines show the mean profiles in each region and dashed lines the 10th and the 90th percentiles. Only data from ascending radiosondes are used in this comparison.

https://doi.org/10.5194/essd-2020-174
Preprint. Discussion started: 5 August 2020

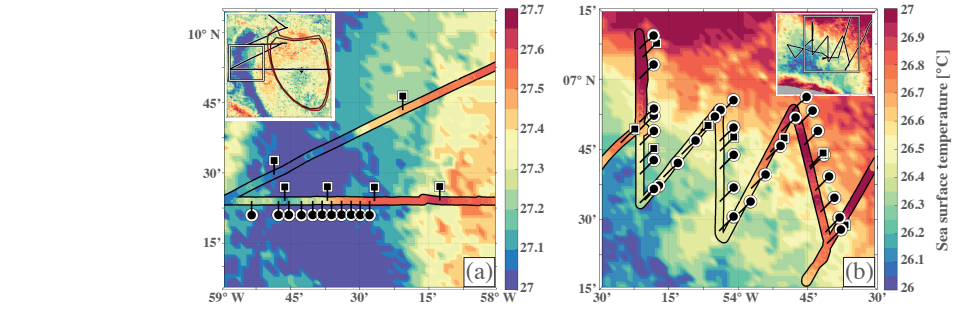

Figure A1. Maps of CLS SST (°C) for (a) January 25, 2020, and (b) February 2, 2020, with the *Atalante* track during the first (January 26) and second (February 2–3) intensive leg, respectively. The color shows the SST measured by the ship's ThermoSalinoGraph (TSG) at 5 m depth and the ticks show the location of Vaisala (squares) and MeteoModem (circles) radiosonde launches. Inserts in the upper corners, where the black lines indicate the ship's course, show the larger scale view of the corresponding scenes with the geographical imprint indicated by white squares. In the panel insert a, the closed contours and the black diamond indicate, respectively, the edges of an anticyclonic eddy and the position of its center.

https://doi.org/10.5194/essd-2020-174
Preprint. Discussion started: 5 August 2020

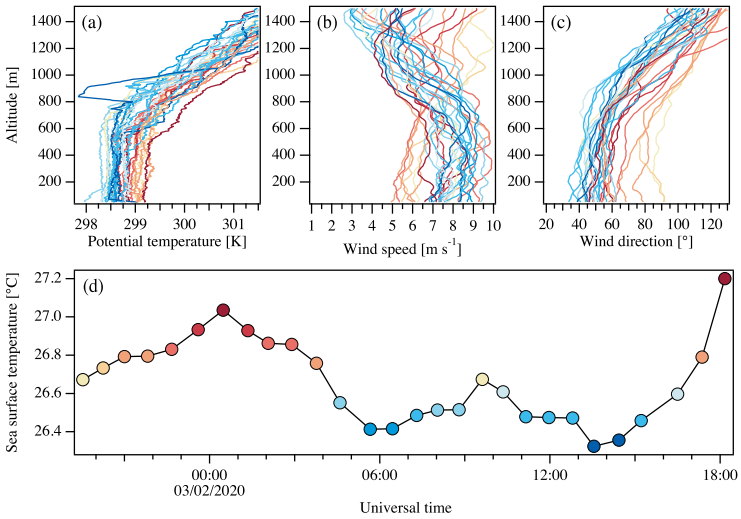

Figure A2. Vertical profiles (50–1500 m) from MeteoModem M10 sondes launched during the second targeted intensive radiosonde period (Figure A1b) for (a) potential temperature, horizontal wind (b) speed and (c) direction, and (d) the corresponding SST time series from the *Atalante* TSG with each circle corresponding to a MeteoModem launch. Colors are indicative of the SST (°C) at the time of each launch. Vertical profiles are built from Level-0 raw measurements.

https://doi.org/10.5194/essd-2020-174
Preprint. Discussion started: 5 August 2020

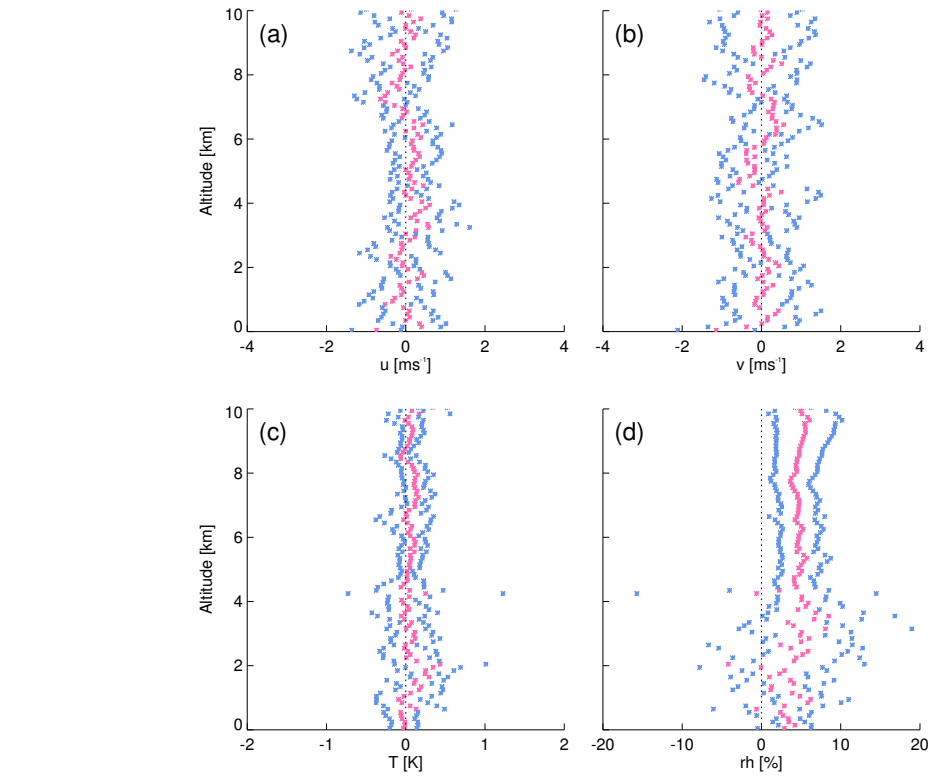

Figure A3. For *Atalante* soundings launched within ±25 min, the mean difference MeteoModem-Vaisala (pink) and ±1 standard deviation (blue) computed on 8 difference profiles with a vertical resolution of 100 m. Shown are difference profiles for (a) zonal wind, (b) meridional wind, (c) temperature, and (d) relative humidity.

https://doi.org/10.5194/essd-2020-174
Preprint. Discussion started: 5 August 2020

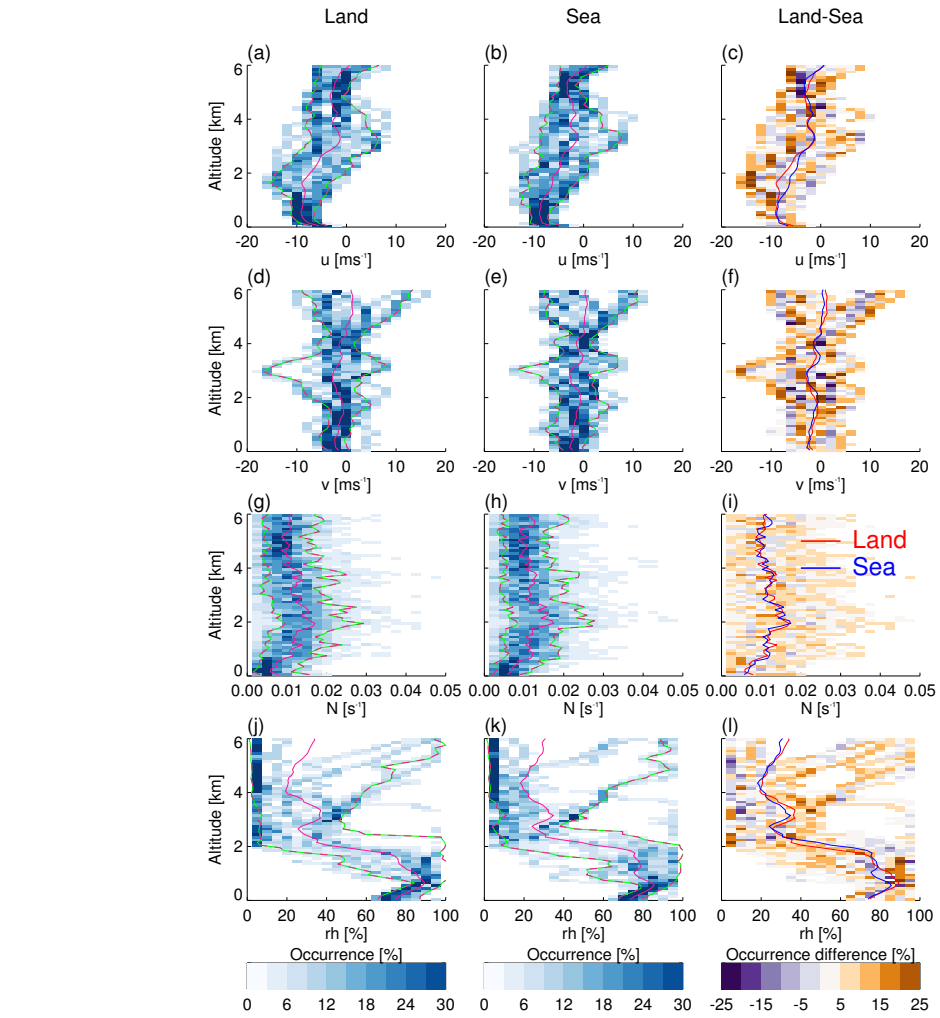

Figure A4. As Fig. 12, but instead of comparing different regions, we here compare ascending soundings launched from BCO with ascending soundings launched within $\pm 90\,\mathrm{min}$ from nearby ships (within 1° longitude to the east and $\pm 1°$ latitude of BCO, resulting in 12 matching soundings). Altitude bins are $100\,\mathrm{m}$ deep and there are 20 bins on the x-axis.

https://doi.org/10.5194/essd-2020-174
Preprint. Discussion started: 5 August 2020

Open Access Earth System Science Data Discussions

Table 1. For each platform the rows list (1) the numbers of recorded ascending soundings, (2) the numbers of recorded descending soundings, (3) the first date of data coverage, (4) the last date of data coverage, (5) whether or not parachutes were used, (6) the station altitude relative to sea level, (7) the GPS antenna offset relative to the station, (8) the launch site offset relative to the station, (9) the surface barometer offset relative to the station, (10) the frequency used to transmit the signal from the radiosonde to the antenna.

	BCO	*Meteor*		*Brown*	*Atalante*	*Merian*
		MPI-M	DWD			
Number ascents	182	180[1]	39[1]	170	139	118
Number descents	162	175[1]	-	159	138	38
Start date	Jan 16	Jan 16	Jan 18	Jan 8	Jan 21	Jan 18
End date	Feb 17	Mar 1	Feb 26	Feb 12	Feb 16	Feb 19
Use of parachutes	yes	yes	no	no	yes	yes
Station altitude (msl)	25.0	16.9	5.4	4.3	13.1	10.4
GPS antenna offset (m)	4.3	2.5	3	5.5	2.6	1.6
Launch site offset (m)	0.0	-11.5, -14.2[2]	0.0, -2.7[2]	0.5	-0.6	0.0
Surface barometer offset (m)	1.0	-16.9	-5.4	-4.3	0.2	0.6
Frequency (MHz)	400.2	401.5	403.0	400.5	400.7 – 401.2	402.0

[1]includes 8 additional soundings after Feb 20, 0 UTC
[2]Feb 9, 18 UTC - Feb 20, 0 UTC

Bibliography

Abbott, C. G. and F. E. Fowle, 1908: Recent determination of the solar constant of radiation. *Terrestrial Magnetism and Atmospheric Electricity*, **13 (2)**, 79–82, doi:10.1029/TE013i002p00079.

Abel, S. J. and B. J. Shipway, 2007: A comparison of cloud-resolving model simulations of trade wind cumulus with aircraft observations taken during RICO. *Quarterly Journal of the Royal Meteorological Society*, **133 (624)**, 781–794, doi:10.1002/qj.55.

Ackerman, T. P. and G. M. Stokes, 2003: The Atmospheric Radiation Measurement Program. *Physics Today*, **56 (1)**, 38–44, doi:10.1063/1.1554135.

Andersson, E., E. Hólm, P. Bauer, A. Beljaars, G. A. Kelly, A. P. McNally, A. J. Simmons, J.-N. Thépaut, and A. M. Tompkins, 2007: Analysis and forecast impact of the main humidity observing systems. *Quarterly Journal of the Royal Meteorological Society*, **133 (627)**, 1473–1485, doi:10.1002/qj.112.

Arakawa, A., 2004: The Cumulus Parameterization Problem: Past, Present, and Future. *Journal of Climate*, **17 (13)**, 2493–2525, doi:10.1175/1520-0442(2004)017<2493:RATCPP>2.0.CO;2.

Arrhenius, S., 1896: On the influence of carbonic acid in the air upon the temperature of the ground. *The London, Edinburgh, and Dublin Philosophical Magazine and Journal of Science*, **41 (251)**, 237–276, doi:10.1080/14786449608620846.

Augstein, E., H. Schmidt, and F. Ostapoff, 1974: The vertical structure of the atmospheric planetary boundary layer in undisturbed trade winds over the Atlantic Ocean. *Boundary-Layer Meteorology*, **6 (1)**, 129–150, doi:10.1007/BF00232480.

Barrera-Verdejo, M., S. Crewell, U. Löhnert, E. Orlandi, and P. D. Girolamo, 2016: Ground-based lidar and microwave radiometry synergy for high vertical resolution absolute humidity profiling. *Atmospheric Measurement Techniques*, **9 (8)**, 4013–4028, doi:10.5194/amt-9-4013-2016.

Battaglia, A. and P. Kollias, 2019: Evaluation of differential absorption radars in the 183GHz band for profiling water vapour in ice clouds. *Atmospheric Measurement Techniques*, **12 (6)**, 3335–3349, doi:10.5194/amt-12-3335-2019.

Battaglia, A., C. D. Westbrook, S. Kneifel, P. Kollias, N. Humpage, U. Löhnert, J. Tyynelä, and G. W. Petty, 2014: G band atmospheric radars: new frontiers in cloud physics. *Atmospheric Measurement Techniques*, **7 (6)**, 1527–1546, doi:10.5194/amt-7-1527-2014.

Battan, L. J., 1973: *Radar Observation of the Atmosphere*. The University of Chicago Press, Chicago, IL.

Bauer, P., A. Thorpe, and G. Brunet, 2015: The quiet revolution of numerical weather prediction. *Nature*, **525 (7567)**, 47–55, doi:10.1038/nature14956.

Betts, A. K. and B. A. Albrecht, 1987: Conserved Variable Analysis of the Convective Boundary Layer Thermodynamic Structure over the Tropical Oceans. *Journal of the Atmospheric Sciences*, **44 (1)**, 83–99, doi:10.1175/1520-0469(1987)044<0083:CVAOTC>2.0.CO;2.

Blumberg, W. G., D. D. Turner, U. Löhnert, and S. Castleberry, 2015: Ground-Based Temperature and Humidity Profiling Using Spectral Infrared and Microwave Observations. Part II: Actual Retrieval Performance in Clear-Sky and Cloudy Conditions. *Journal of Applied Meteorology and Climatology*, **54 (11)**, 2305–2319, doi:10.1175/JAMC-D-15-0005.1.

Bobak, J. and C. Ruf, 2000: Improvements and complications involved with adding an 85-GHz channel to cloud liquid water radiometers. *IEEE Transactions on Geoscience and Remote Sensing*, **38 (1)**, 214–225, doi:10.1109/36.823914.

Bony, S. and J.-L. Dufresne, 2005: Marine boundary layer clouds at the heart of tropical cloud feedback uncertainties in climate models. *Geophysical Research Letters*, **32 (20)**, doi:10.1029/2005GL023851.

Bony, S. and B. Stevens, 2019: Measuring Area-Averaged Vertical Motions with Dropsondes. *Journal of the Atmospheric Sciences*, **76 (3)**, 767–783, doi:10.1175/JAS-D-18-0141.1.

Bony, S., R. Colman, V. M. Kattsov, R. P. Allan, C. S. Bretherton, J.-L. Dufresne, A. Hall, S. Hallegatte, M. M. Holland, W. Ingram, D. A. Randall, B. J. Soden, G. Tselioudis, and M. J. Webb, 2006: How Well Do We Understand and Evaluate Climate Change Feedback Processes? *Journal of Climate*, **19 (15)**, 3445–3482, doi:10.1175/JCLI3819.1.

Bony, S., B. Stevens, D. M. W. Frierson, C. Jakob, M. Kageyama, R. Pincus, T. G. Shepherd, S. C. Sherwood, A. P. Siebesma, A. H. Sobel, M. Watanabe, and M. J. Webb, 2015: Clouds, circulation and climate sensitivity. *Nature Geoscience*, **8 (4)**, 261–268, doi:10.1038/ngeo2398.

Bony, S., B. Stevens, F. Ament, S. Bigorre, P. Chazette, S. Crewell, J. Delanoë, K. Emanuel, D. Farrell, C. Flamant, S. Gross, L. Hirsch, J. Karstensen, B. Mayer, L. Nuijens, J. H. Ruppert, I. Sandu, P. Siebesma, S. Speich, F. Szczap, J. Totems, R. Vogel,

M. Wendisch, and M. Wirth, 2017: EUREC4A: A Field Campaign to Elucidate the Couplings Between Clouds, Convection and Circulation. *Surveys in Geophysics*, **38 (6)**, 1529–1568, doi:10.1007/s10712-017-9428-0.

Boucher, O., A. Randall, P. Artaxo, C. Bretherton, G. Feingold, P. Forster, V.-M. Kerminen, Y. Kondo, H. Liao, U. Lohmann, P. Rasch, S. Saktheesh, S. Sherwood, B. Stevens, and X. Zhang, 2013: Clouds and Aerosols. *Climate Change 2013: The Physical Science Basis. Contribution of Working Group I to the Fifth Assessment Report of the Intergovernmental Panel on Climate Change*, T. F. Stocker, D. Qin, G.-K. Plattner, M. Tignor, S. K. Allen, J. Boschung, A. Nauels, Y. Xia, V. Bex, and P. M. Midgley, Eds., Cambridge University Press, Cambridge, United Kingdom and New York, NY, USA.

Bretherton, C. S., P. N. Blossey, and C. R. Jones, 2013: Mechanisms of marine low cloud sensitivity to idealized climate perturbations: A single-LES exploration extending the CGILS cases. *Journal of Advances in Modeling Earth Systems*, **5 (2)**, 316–337, doi:10.1002/jame.20019.

Bretherton, C. S., P. N. Blossey, and M. Khairoutdinov, 2005: An Energy-Balance Analysis of Deep Convective Self-Aggregation above Uniform SST. *Journal of the Atmospheric Sciences*, **62 (12)**, 4273–4292, doi:10.1175/JAS3614.1.

Bretherton, C. S., M. E. Peters, and L. E. Back, 2004: Relationships between Water Vapor Path and Precipitation over the Tropical Oceans. *Journal of Climate*, **17 (7)**, 1517–1528, doi:10.1175/1520-0442(2004)017<1517:RBWVPA>2.0.CO;2.

Brient, F., T. Schneider, Z. Tan, S. Bony, X. Qu, and A. Hall, 2016: Shallowness of tropical low clouds as a predictor of climate models' response to warming. *Climate Dynamics*, **47 (1)**, 433–449, doi:10.1007/s00382-015-2846-0.

Brueck, M., L. Nuijens, and B. Stevens, 2015: On the Seasonal and Synoptic Time-Scale Variability of the North Atlantic Trade Wind Region and Its Low-Level Clouds. *Journal of the Atmospheric Sciences*, **72 (4)**, 1428–1446, doi:10.1175/JAS-D-14-0054.1.

Cadeddu, M., D. Turner, and J. Liljegren, 2009: A Neural Network for Real-Time Retrievals of PWV and LWP From Arctic Millimeter-Wave Ground-Based Observations. *IEEE Transactions on Geoscience and Remote Sensing*, doi:10.1109/TGRS.2009.2013205.

Cess, R. D., et al., 1990: Intercomparison and interpretation of climate feedback processes in 19 atmospheric general circulation models. *Journal of Geophysical Research: Atmospheres*, **95 (D10)**, 16 601–16 615, doi:10.1029/JD095iD10p16601.

Charney, J. G., A. Arakawa, D. J. Baker, B. Bolin, R. E. Dickinson, R. M. Goody, C. E. Leith, H. M. Stommel, and C. I. Wunsch, 1979: Carbon Dioxide and Climate: A Scientific Assessment. Tech. rep., National Academy of Sciences, Woods Hole, Massachusetts.

Chen, C.-T., E. Roeckner, and B. J. Soden, 1996: A Comparison of Satellite Observations and Model Simulations of Column-Integrated Moisture and Upper-Tropospheric Humidity. *Journal of Climate*, **9 (7)**, 1561–1585, doi:10.1175/1520-0442(1996)009<1561:ACOSOA>2.0.CO;2.

Cimini, D., P. W. Rosenkranz, M. Y. Tretyakov, M. A. Koshelev, and F. Romano, 2018: Uncertainty of atmospheric microwave absorption model: impact on ground-based radiometer simulations and retrievals. *Atmospheric Chemistry and Physics*, **18 (20)**, 15 231–15 259, doi:10.5194/acp-18-15231-2018.

Cimini, D., O. Caumont, U. Löhnert, L. Alados-Arboledas, R. Bleisch, T. Huet, M. E. Ferrario, F. Madonna, O. Maier, G. Pace, and R. Posada, 2012: An International Network of Ground-Based Microwave Radiometers for the Assimilation of Temperature and Humidity Profiles into NWP Models. *Proceedings of 9th International Symposiumon Tropospheric Profiling*, L'Aquila,Italy, 4.

Collard, A. D., 2007: Selection of IASI channels for use in numerical weather prediction. *Quarterly Journal of the Royal Meteorological Society*, **133 (629)**, 1977–1991, doi:10.1002/qj.178.

Cooper, K. B., R. Rodriguez Monje, L. Millán, M. Lebsock, S. Tanelli, J. V. Siles, C. Lee, and A. Brown, 2018: Atmospheric Humidity Sounding Using Differential Absorption Radar Near 183 GHz. *IEEE Geoscience and Remote Sensing Letters*, **15 (2)**, 163–167, doi:10.1109/LGRS.2017.2776078.

Crewell, S. and U. Löhnert, 2003: Accuracy of cloud liquid water path from ground-based microwave radiometry 2. Sensor accuracy and synergy. *Radio Science*, **38 (3)**, doi:10.1029/2002RS002634.

Crewell, S. and U. Löhnert, 2007: Accuracy of Boundary Layer Temperature Profiles Retrieved With Multifrequency Multiangle Microwave Radiometry. *IEEE Transactions on Geoscience and Remote Sensing*, **45 (7)**, 2195–2201, doi:10.1109/TGRS.2006.888434.

Curry, J. A., J. L. Schramm, W. B. Rossow, and D. Randall, 1996: Overview of Arctic Cloud and Radiation Characteristics. *Journal of Climate*, **9 (8)**, 1731–1764, doi:10.1175/1520-0442(1996)009<1731:OOACAR>2.0.CO;2.

Davison, J. L., R. M. Rauber, L. Di Girolamo, and M. A. LeMone, 2013: A Revised Conceptual Model of the Tropical Marine Boundary Layer. Part I: Statistical Characterization of the Variability Inherent in the Wintertime Trade Wind Regime over the Western Tropical Atlantic. *Journal of the Atmospheric Sciences*, **70 (10)**, 3005–3024, doi:10.1175/JAS-D-12-0321.1.

De Angelis, F., D. Cimini, U. Löhnert, O. Caumont, A. Haefele, B. Pospichal, P. Martinet, F. Navas-Guzmán, H. Klein-Baltink, J.-C. Dupont, and J. Hocking, 2017: Long-term observations minus background monitoring of ground-based brightness temperatures from a microwave radiometer network. *Atmospheric Measurement Techniques*, **10 (10)**, 3947–3961, doi:10.5194/amt-10-3947-2017.

de Boer, G., E. W. Eloranta, and M. D. Shupe, 2009: Arctic Mixed-Phase Stratiform Cloud Properties from Multiple Years of Surface-Based Measurements at Two High-Latitude Locations. *Journal of the Atmospheric Sciences*, **66 (9)**, 2874–2887, doi:10.1175/2009JAS3029.1.

Derbyshire, S. H., I. Beau, P. Bechtold, J.-Y. Grandpeix, J.-M. Piriou, J.-L. Redelsperger, and P. M. M. Soares, 2004: Sensitivity of moist convection to environmental humidity. *Quarterly Journal of the Royal Meteorological Society*, **130 (604)**, 3055–3079, doi:10.1256/qj.03.130.

Devasthale, A., J. Sedlar, and M. Tjernström, 2011: Characteristics of water-vapour inversions observed over the Arctic by Atmospheric Infrared Sounder (AIRS) and radiosondes. *Atmospheric Chemistry and Physics*, **11 (18)**, 9813–9823, doi:10.5194/acp-11-9813-2011.

Dufresne, J.-L. and S. Bony, 2008: An Assessment of the Primary Sources of Spread of Global Warming Estimates from Coupled Atmosphere–Ocean Models. *Journal of Climate*, **21 (19)**, 5135–5144, doi:10.1175/2008JCLI2239.1.

Durre, I., R. S. Vose, and D. B. Wuertz, 2006: Overview of the Integrated Global Radiosonde Archive. *Journal of Climate*, **19 (1)**, 53–68, doi:10.1175/JCLI3594.1.

Ebell, K., U. Löhnert, E. Päschke, E. Orlandi, J. H. Schween, and S. Crewell, 2017: A 1-D variational retrieval of temperature, humidity, and liquid cloud properties: Performance under idealized and real conditions. *Journal of Geophysical Research: Atmospheres*, **122 (3)**, 1746–1766, doi:10.1002/2016JD025945.

Ebell, K., T. Nomokonova, M. Maturilli, and C. Ritter, 2020: Radiative Effect of Clouds at Ny-Ålesund, Svalbard, as Inferred from Ground-Based Remote Sensing Observations. *Journal of Applied Meteorology and Climatology*, **59 (1)**, 3–22, doi:10.1175/JAMC-D-19-0080.1.

Ebell, K., E. Orlandi, A. Hünerbein, U. Löhnert, and S. Crewell, 2013: Combining ground-based with satellite-based measurements in the atmospheric state retrieval: Assessment of the information content. *Journal of Geophysical Research: Atmospheres*, **118 (13)**, 6940–6956, doi:10.1002/jgrd.50548.

Egerer, U., A. Ehrlich, M. Gottschalk, R. A. J. Neggers, H. Siebert, and M. Wendisch, 2020: Case study of a humidity layer above Arctic stratocumulus using balloon-borne turbulence and radiation measurements and large eddy simulations. *Atmospheric Chemistry and Physics Discussions*, 1–27, doi:10.5194/acp-2020-584.

Ehrlich, A., M. Wendisch, C. Lüpkes, M. Buschmann, H. Bozem, D. Chechin, H.-C. Clemen, R. Dupuy, O. Eppers, J. Hartmann, A. Herber, E. Jäkel, E. Järvinen, O. Jourdan, U. Kästner, L.-L. Kliesch, F. Köllner, M. Mech, S. Mertes, R. Neuber, E. Ruiz-Donoso, M. Schnaiter, J. Schneider, J. Stapf, and M. Zanatta, 2019: A comprehensive in situ and remote sensing data set from the Arctic CLoud Observations Using airborne measurements during polar Day (ACLOUD) campaign. *Earth System Science Data*, **11 (4)**, 1853–1881, doi:10.5194/essd-11-1853-2019.

Ellis, S. M. and J. Vivekanandan, 2010: Water vapor estimates using simultaneous dual-wavelength radar observations. *Radio Science*, **45 (5)**, doi:10.1029/2009RS004280.

Ewald, F., S. Groß, M. Hagen, L. Hirsch, J. Delanoë, and M. Bauer-Pfundstein, 2019: Calibration of a 35 GHz airborne cloud radar: lessons learned and intercomparisons with 94 GHz cloud radars. *Atmospheric Measurement Techniques*, **12 (3)**, 1815–1839, doi:10.5194/amt-12-1815-2019.

Fabry, F., C. Frush, I. Zawadzki, and A. Kilambi, 1997: On the Extraction of Near-Surface Index of Refraction Using Radar Phase Measurements from Ground Targets. *Journal of Atmospheric and Oceanic Technology*, **14 (4)**, 978–987, doi:10.1175/1520-0426(1997)014<0978:OTEONS>2.0.CO;2.

Fabry, F. and V. Meunier, 2020: Why Are Radar Data so Difficult to Assimilate Skillfully? *Monthly Weather Review*, **148 (7)**, 2819–2836, doi:10.1175/MWR-D-19-0374.1.

Finger, F. G. and F. J. Schmidlin, 1991: Upper-Air Measurements and Instrumentation Workshop. *Bulletin of the American Meteorological Society*, **72 (1)**, 50–56, doi:10.1175/1520-0477-72.1.50.

Foote, E., 1856: Circumstances Affecting the Heat of Sun's Rays. *American Journal of Science and Arts*, **XXII (LXVI)**, 382–383.

Foth, A. and B. Pospichal, 2017: Optimal estimation of water vapour profiles using a combination of Raman lidar and microwave radiometer. *Atmospheric Measurement Techniques*, **10 (9)**, 3325–3344, doi:10.5194/amt-10-3325-2017.

Friedman, H. A., G. Conrad, and J. D. McFadden, 1970: ESSA research flight facility aircraft participation in the Barbados Oceanographic and Meteorological Experiment. *Bulletin of the American Meteorological Society*, **51 (9)**, 822–835, doi:10.1175/1520-0477(1970)051<0822:ERFFAP>2.0.CO;2.

Frisinger, H. H., 1972: Aristotle and his "Meteorologica". *Bulletin of the American Meteorological Society*, **53 (7)**, 634–638, doi:10.1175/1520-0477(1972)053<0634:AAH>2.0.CO;2.

Frisinger, H. H., 1973: Aristotle's legacy in meteorology. *Bulletin of the American Meteorological Society*, **54 (3)**, 198–204, doi:10.1175/1520-0477(1973)054<0198:ALIM>2.0.CO;2.

Gaussiat, N., H. Sauvageot, and A. J. Illingworth, 2003: Cloud Liquid Water and Ice Content Retrieval by Multiwavelength Radar. *Journal of Atmospheric and Oceanic Technology*, **20 (9)**, 1264–1275, doi:10.1175/1520-0426(2003)020<1264:CLWAIC>2.0.CO;2.

Geer, A. J., N. Bormann, K. Lonitz, P. Weston, R. Forbes, and S. J. English, 2019: Recent progress in all-sky radiance assimilation. *ECMWF Newsletter*, **161**, 20–25, doi:10.21957/mb31c8ag74.

Geer, A. J., F. Baordo, N. Bormann, P. Chambon, S. J. English, M. Kazumori, H. Lawrence, P. Lean, K. Lonitz, and C. Lupu, 2017: The growing impact of satellite observations sensitive to humidity, cloud and precipitation. *Quarterly Journal of the Royal Meteorological Society*, **143 (709)**, 3189–3206, doi:10.1002/qj.3172.

Gierens, R., 2020: Observations of Arctic low-level mixed-phase clouds at Ny-Alesund: Characterization and insights gained by high-resolution Doppler radar. Ph.D. thesis, Universität zu Köln, Köln, Germany.

Gierens, R., S. Kneifel, M. D. Shupe, K. Ebell, M. Maturilli, and U. Löhnert, 2020: Low-level mixed-phase clouds in a complex Arctic environment. *Atmospheric Chemistry and Physics*, **20 (6)**, 3459–3481, doi:10.5194/acp-20-3459-2020.

Gutleben, M., S. Groß, M. Wirth, C. Emde, and B. Mayer, 2019: Impacts of Water Vapor on Saharan Air Layer Radiative Heating. *Geophysical Research Letters*, **46 (24)**, 14 854–14 862, doi:10.1029/2019GL085344.

Görsdorf, U., V. Lehmann, M. Bauer-Pfundstein, G. Peters, D. Vavriv, V. Vinogradov, and V. Volkov, 2015: A 35-GHz Polarimetric Doppler Radar for Long-Term Observations of Cloud Parameters—Description of System and Data Processing. *Journal of Atmospheric and Oceanic Technology*, **32 (4)**, 675–690, doi:10.1175/JTECH-D-14-00066.1.

Güldner, J. and D. Spänkuch, 2001: Remote Sensing of the Thermodynamic State of the Atmospheric Boundary Layer by Ground-Based Microwave Radiometry. *Journal of Atmospheric and Oceanic Technology*, **18 (6)**, 925–933, doi:10.1175/1520-0426(2001)018<0925:RSOTTS>2.0.CO;2.

Hansen, J., A. Lacis, D. Rind, G. Russell, P. Stone, I. Fung, R. Ruedy, and J. Lerner, 1984: Climate Sensitivity: Analysis of Feedback Mechanisms. *Climate Processes and Climate*

Sensitivity, American Geophysical Union (AGU), 130–163.

Hartmann, D. L., M. E. Ockert-Bell, and M. L. Michelsen, 1992: The Effect of Cloud Type on Earth's Energy Balance: Global Analysis. *Journal of Climate*, **5 (11)**, 1281–1304, doi:10.1175/1520-0442(1992)005<1281:TEOCTO>2.0.CO;2.

Hartmann, D. L., A. M. G. Klein Tank, M. Rusicucci, L. V. Alexander, B. Broenniman, Y. Charabi, F. J. Dentener, E. J. Dlugokencky, D. R. Easterling, A. Kaplan, B. J. Soden, P. W. Thorne, M. Wild, P. M. Zhai, and E. Kent, 2013: Observations: Atmosphere and Surface. *Climate Change 2013: The Physical Science Basis. Contribution of Working Group I to the Fifth Assessment Report of the Intergovernmental Panel on Climate Change*, T. F. Stocker, D. Qin, G.-K. Plattner, M. Tignor, S. K. Allen, J. Boschung, A. Nauels, Y. Xia, V. Bex, and P. M. Midgley, Eds., Cambridge University Press, Cambridge, 159–254.

Held, I. M. and B. J. Soden, 2000: Water Vapor Feedback and Global Warming. *Annual Review of Energy and the Environment*, **25 (1)**, 441–475, doi:10.1146/annurev.energy.25.1.441.

Held, I. M. and B. J. Soden, 2006: Robust Responses of the Hydrological Cycle to Global Warming. *Journal of Climate*, **19 (21)**, 5686–5699, doi:10.1175/JCLI3990.1.

Hogan, R. J., N. Gaussiat, and A. J. Illingworth, 2005: Stratocumulus Liquid Water Content from Dual-Wavelength Radar. *Journal of Atmospheric and Oceanic Technology*, **22 (8)**, 1207–1218, doi:10.1175/JTECH1768.1.

Holland, J. Z., 1970: preliminary report on the BOMEX sea-air interaction program. *Bulletin of the American Meteorological Society*, **51 (9)**, 809–821, doi:10.1175/1520-0477(1970)051<0809:PROTBS>2.0.CO;2.

Holloway, C. E. and J. D. Neelin, 2009: Moisture Vertical Structure, Column Water Vapor, and Tropical Deep Convection. *Journal of the Atmospheric Sciences*, **66 (6)**, 1665–1683, doi:10.1175/2008JAS2806.1.

Holloway, C. E., A. A. Wing, S. Bony, C. Muller, H. Masunaga, T. S. L'Ecuyer, D. D. Turner, and P. Zuidema, 2017: Observing Convective Aggregation. *Surveys in Geophysics*, **38 (6)**, 1199–1236, doi:10.1007/s10712-017-9419-1.

Hulme, M., 2009: On the origin of 'the greenhouse effect': John Tyndall's 1859 interrogation of nature. *Weather*, **64 (5)**, 121–123, doi:10.1002/wea.386.

Illingworth, A. J., D. Cimini, C. Gaffard, M. Haeffelin, V. Lehmann, U. Löhnert, E. J. O'Connor, and D. Ruffieux, 2015a: Exploiting Existing Ground-Based Remote Sensing Networks to Improve High-Resolution Weather Forecasts. *Bulletin of the American Meteorological Society*, **96 (12)**, 2107–2125, doi:10.1175/BAMS-D-13-00283.1.

Illingworth, A. J., R. J. Hogan, E. J. O'Connor, D. Bouniol, M. E. Brooks, J. Delanoé, D. P. Donovan, J. D. Eastment, N. Gaussiat, J. W. F. Goddard, M. Haeffelin, H. K. Baltink, O. A. Krasnov, J. Pelon, J.-M. Piriou, A. Protat, H. W. J. Russchenberg, A. Seifert, A. M. Tompkins, G.-J. van Zadelhoff, F. Vinit, U. Willén, D. R. Wilson, and C. L. Wrench, 2007: Cloudnet: Continuous Evaluation of Cloud Profiles in Seven Operational Models Using Ground-Based Observations. *Bulletin of the American Meteorological Society*, **88 (6)**, 883–898, doi:10.1175/BAMS-88-6-883.

Illingworth, A. J., H. W. Barker, A. Beljaars, M. Ceccaldi, H. Chepfer, N. Clerbaux, J. Cole, J. Delanoë, C. Domenech, D. P. Donovan, S. Fukuda, M. Hirakata, R. J. Hogan, A. Huenerbein, P. Kollias, T. Kubota, T. Nakajima, T. Y. Nakajima, T. Nishizawa, Y. Ohno, H. Okamoto, R. Oki, K. Sato, M. Satoh, M. W. Shephard, A. Velázquez-Blázquez, U. Wandinger, T. Wehr, and G.-J. van Zadelhoff, 2015b: The EarthCARE Satellite: The Next Step Forward in Global Measurements of Clouds, Aerosols, Precipitation, and Radiation. *Bulletin of the American Meteorological Society*, **96 (8)**, 1311–1332, doi:10.1175/BAMS-D-12-00227.1.

IPCC, 2013: *Climate Change 2013: The Physical Science Basis. Contribution of Working Group I to the Fifth Assessment Report of the Intergovernmental Panel on Climate Change*. Cambridge University Press, Cambridge, United Kingdom and New York, NY, USA.

Jackson, R., 2020: Eunice Foote, John Tyndall and a question of priority. *Notes and Records: the Royal Society Journal of the History of Science*, **74 (1)**, 105–118, doi:10.1098/rsnr.2018.0066.

Jacob, M., F. Ament, M. Gutleben, H. Konow, M. Mech, M. Wirth, and S. Crewell, 2019: Investigating the liquid water path over the tropical Atlantic with synergistic airborne measurements. *Atmospheric Measurement Techniques*, **12 (6)**, 3237–3254, doi:10.5194/amt-12-3237-2019.

Jakob, C., 2010: Accelerating Progress in Global Atmospheric Model Development through Improved ParameterizationsChallenges, Opportunities, and Strategies. *Bulletin of the American Meteorological Society*, **91 (7)**, 869–876, doi:10.1175/2009BAMS2898.1.

Jung, E., B. A. Albrecht, G. Feingold, H. H. Jonsson, P. Chuang, and S. L. Donaher, 2016: Aerosols, clouds, and precipitation in the North Atlantic trades observed during the Barbados aerosol cloud experiment-Part 1: Distributions and variability. *Atmospheric Chemistry and Physics*, **16 (13)**, 8643–8666, doi:10.5194/acp-16-8643-2016.

Keeling, C. D., 1960: The Concentration and Isotopic Abundances of Carbon Dioxide in the Atmosphere. *Tellus*, **12 (2)**, 200–203, doi:10.1111/j.2153-3490.1960.tb01300.x.

Klingebiel, M., V. P. Ghate, A. K. Naumann, F. Ditas, M. L. Pöhlker, C. Pöhlker, K. Kandler, H. Konow, and B. Stevens, 2019: Remote Sensing of Sea Salt Aerosol below Trade Wind Clouds. *Journal of the Atmospheric Sciences*, **76 (5)**, 1189–1202, doi:10.1175/JAS-D-18-0139.1.

Küchler, N., S. Kneifel, P. Kollias, and U. Löhnert, 2018: Revisiting Liquid Water Content Retrievals in Warm Stratified Clouds: The Modified Frisch. *Geophysical Research Letters*, **45 (17)**, 9323–9330, doi:10.1029/2018GL079845.

Küchler, N., S. Kneifel, U. Löhnert, P. Kollias, H. Czekala, and T. Rose, 2017: A W-Band Radar–Radiometer System for Accurate and Continuous Monitoring of Clouds and Precipitation. *Journal of Atmospheric and Oceanic Technology*, **34 (11)**, 2375–2392, doi:10.1175/JTECH-D-17-0019.1.

Küchler, N. and U. Löhnert, 2019: Radar–Radiometer-Based Liquid Water Content Retrievals of Warm Low-Level Clouds: How the Measurement Setup Affects Retrieval Uncertainties. *IEEE Journal of Selected Topics in Applied Earth Observations and Remote Sensing*, **12 (5)**, 1355–1361, doi:10.1109/JSTARS.2019.2908414.

Lamer, K., P. Kollias, A. Battaglia, and S. Preval, 2020: Mind the gap – Part 1: Accurately locating warm marine boundary layer clouds and precipitation using spaceborne radars. *Atmospheric Measurement Techniques*, **13 (5)**, 2363–2379, doi:10.5194/amt-13-2363-2020.

Lamer, K., P. Kollias, and L. Nuijens, 2015: Observations of the variability of shallow trade wind cumulus cloudiness and mass flux. *Journal of Geophysical Research: Atmospheres*, **120 (12)**, 6161–6178, doi:10.1002/2014JD022950.

Lebsock, M. D., K. Suzuki, L. F. Millán, and P. M. Kalmus, 2015: The feasibility of water vapor sounding of the cloudy boundary layer using a differential absorption radar technique. *Atmospheric Measurement Techniques*, **8 (9)**, 3631–3645, doi:10.5194/amt-8-3631-2015.

Lhermitte, R., 1990: Attenuation and Scattering of Millimeter Wavelength Radiation by Clouds and Precipitation. *Journal of Atmospheric and Oceanic Technology*, **7 (3)**, 464–479, doi:10.1175/1520-0426(1990)007<0464:AASOMW>2.0.CO;2.

Liljegren, J., S.-A. Boukabara, K. Cady-Pereira, and S. Clough, 2005: The effect of the half-width of the 22-GHz water vapor line on retrievals of temperature and water vapor profiles with a 12-channel microwave radiometer. *IEEE Transactions on Geoscience and Remote Sensing*, **43 (5)**, 1102–1108, doi:10.1109/TGRS.2004.839593.

Liou, K., 2002: *An Introduction to Atmospheric Radiation*, International Geophysics Series, Vol. 84. 2d ed., Academic Press, Elsevier, San Diego, California.

Lipton, A., 2003: Satellite sounding channel optimization in the microwave spectrum. *IEEE Transactions on Geoscience and Remote Sensing*, **41 (4)**, 761–781, doi:10.1109/TGRS.2003.810926.

Liu, Q., F. Weng, and S. J. English, 2011: An Improved Fast Microwave Water Emissivity Model. *IEEE Transactions on Geoscience and Remote Sensing*, **49 (4)**, 1238–1250, doi:10.1109/TGRS.2010.2064779.

Lock, A. P., 2009: Factors influencing cloud area at the capping inversion for shallow cumulus clouds. *Quarterly Journal of the Royal Meteorological Society*, **135 (641)**, 941–952, doi:10.1002/qj.424.

Löhnert, U. and S. Crewell, 2003: Accuracy of cloud liquid water path from ground-based microwave radiometry 1. Dependency on cloud model statistics. *Radio Science*, **38 (3)**, doi:10.1029/2002RS002654.

Löhnert, U., S. Crewell, O. Krasnov, E. O'Connor, and H. Russchenberg, 2008: Advances in Continuously Profiling the Thermodynamic State of the Boundary Layer: Integration of Measurements and Methods. *Journal of Atmospheric and Oceanic Technology*, **25 (8)**, 1251–1266, doi:10.1175/2007JTECHA961.1.

Löhnert, U., S. Crewell, and C. Simmer, 2004: An Integrated Approach toward Retrieving Physically Consistent Profiles of Temperature, Humidity, and Cloud Liquid Water. *Journal of Applied Meteorology*, **43 (9)**, 1295–1307, doi:10.1175/1520-0450(2004)043<1295:AIATRP>2.0.CO;2.

Löhnert, U., S. Crewell, C. Simmer, and A. Macke, 2001: Profiling Cloud Liquid Water by Combining Active and Passive Microwave Measurements with Cloud Model Statistics. *Journal of Atmospheric and Oceanic Technology*, **18 (8)**, 1354–1366, doi:10.1175/1520-0426(2001)018<1354:PCLWBC>2.0.CO;2.

Löhnert, U., E. v. Meijgaard, H. K. Baltink, S. Groß, and R. Boers, 2007: Accuracy assessment of an integrated profiling technique for operationally deriving profiles of temperature, humidity, and cloud liquid water. *Journal of Geophysical Research: Atmospheres*, **112 (D4)**, doi:10.1029/2006JD007379.

Löhnert, U., D. D. Turner, and S. Crewell, 2009: Ground-Based Temperature and Humidity Profiling Using Spectral Infrared and Microwave Observations. Part I: Simulated Retrieval Performance in Clear-Sky Conditions. *Journal of Applied Meteorology and Climatology*, **48 (5)**, 1017–1032, doi:10.1175/2008JAMC2060.1.

Löhnert, U., J. H. Schween, C. Acquistapace, K. Ebell, M. Maahn, M. Barrera-Verdejo, A. Hirsikko, B. Bohn, A. Knaps, E. O'Connor, C. Simmer, A. Wahner, and S. Crewell, 2015: JOYCE: Jülich Observatory for Cloud Evolution. *Bulletin of the American*

Meteorological Society, **96 (7)**, 1157–1174, doi:10.1175/BAMS-D-14-00105.1.

Maahn, M. and U. Löhnert, 2017: Potential of Higher-Order Moments and Slopes of the Radar Doppler Spectrum for Retrieving Microphysical and Kinematic Properties of Arctic Ice Clouds. *Journal of Applied Meteorology and Climatology*, **56 (2)**, 263–282, doi:10.1175/JAMC-D-16-0020.1.

Maahn, M., D. D. Turner, U. Löhnert, D. J. Posselt, K. Ebell, G. G. Mace, and J. M. Comstock, 2020: Optimal Estimation Retrievals and Their Uncertainties: What Every Atmospheric Scientist Should Know. *Bulletin of the American Meteorological Society*, 1–34, doi:10.1175/BAMS-D-19-0027.1.

Malkus, J. S., 1958: On the structure of the trade wind moist layer. *Papers in Physical Oceanography and Meteorology*, **XIII (2)**, 1–47, doi:10.1575/1912/1065.

Marotzke, J., C. Jakob, S. Bony, P. A. Dirmeyer, P. A. O'Gorman, E. Hawkins, S. Perkins-Kirkpatrick, C. L. Quéré, S. Nowicki, K. Paulavets, S. I. Seneviratne, B. Stevens, and M. Tuma, 2017: Climate research must sharpen its view. *Nature Climate Change*, **7 (2)**, 89–91, doi:10.1038/nclimate3206.

Maschwitz, G., U. Löhnert, S. Crewell, T. Rose, and D. D. Turner, 2013: Investigation of ground-based microwave radiometer calibration techniques at 530 hPa. *Atmospheric Measurement Techniques*, **6 (10)**, 2641–2658, doi:10.5194/amt-6-2641-2013.

Maturilli, M. and K. Ebell, 2018: Twenty-five years of cloud base height measurements by ceilometer in Ny-Ålesund, Svalbard. *Earth System Science Data*, **10 (3)**, 1451–1456, doi:10.5194/essd-10-1451-2018.

Maturilli, M. and M. Kayser, 2017: Arctic warming, moisture increase and circulation changes observed in the Ny-Ålesund homogenized radiosonde record. *Theoretical and Applied Climatology*, **130 (1)**, 1–17, doi:10.1007/s00704-016-1864-0.

Mech, M., L.-L. Kliesch, A. Anhäuser, T. Rose, P. Kollias, and S. Crewell, 2019: Microwave Radar/radiometer for Arctic Clouds (MiRAC): first insights from the ACLOUD campaign. *Atmospheric Measurement Techniques*, **12 (9)**, 5019–5037, doi:10.5194/amt-12-5019-2019.

Mech, M., M. Maahn, S. Kneifel, D. Ori, E. Orlandi, P. Kollias, V. Schemann, and S. Crewell, 2020: PAMTRA 1.0: A Passive and Active Microwave radiative TRAnsfer tool for simulating radiometer and radar measurements of the cloudy atmosphere. *Geoscientific Model Development Discussions*, 1–34, doi:10.5194/gmd-2019-356.

Mech, M., E. Orlandi, S. Crewell, F. Ament, L. Hirsch, M. Hagen, G. Peters, and B. Stevens, 2014: HAMP – the microwave package on the High Altitude and LOng range research aircraft (HALO). *Atmospheric Measurement Techniques*, **7 (12)**, 4539–4553, doi:10.5194/amt-7-4539-2014.

Medeiros, B. and L. Nuijens, 2016: Clouds at Barbados are representative of clouds across the trade wind regions in observations and climate models. *Proceedings of the National Academy of Sciences*, **113 (22)**, 6102–6104, doi:10.1073/pnas.ss11322.

Meneghini, R., L. Liao, and L. Tian, 2005: A Feasibility Study for Simultaneous Estimates of Water Vapor and Precipitation Parameters Using a Three-Frequency Radar. *Journal of Applied Meteorology*, **44 (10)**, 1511–1525, doi:10.1175/JAM2302.1.

Mie, G., 1908: Beiträge zur Optik trüber Medien, speziell kolloidaler Metallösungen. *Annalen der Physik*, **4 (25)**, 377–445.

Miles, N. L., J. Verlinde, and E. E. Clothiaux, 2000: Cloud Droplet Size Distributions in Low-Level Stratiform Clouds. *Journal of the Atmospheric Sciences*, **57 (2)**, 295–311, doi:10.1175/1520-0469(2000)057<0295:CDSDIL>2.0.CO;2.

Millán, L., M. Lebsock, N. Livesey, and S. Tanelli, 2016: Differential absorption radar techniques: water vapor retrievals. *Atmospheric Measurement Techniques*, **9 (6)**, 2633–2646, doi:10.5194/amt-9-2633-2016.

Mioche, G., O. Jourdan, M. Ceccaldi, and J. Delanoë, 2015: Variability of mixed-phase clouds in the Arctic with a focus on the Svalbard region: a study based on spaceborne active remote sensing. *Atmospheric Chemistry and Physics*, **15 (5)**, 2445–2461, doi:10.5194/acp-15-2445-2015.

Mioche, G., O. Jourdan, J. Delanoë, C. Gourbeyre, G. Febvre, R. Dupuy, M. Monier, F. Szczap, A. Schwarzenboeck, and J.-F. Gayet, 2017: Vertical distribution of microphysical properties of Arctic springtime low-level mixed-phase clouds over the Greenland and Norwegian seas. *Atmospheric Chemistry and Physics*, **17 (20)**, 12 845–12 869, doi:10.5194/acp-17-12845-2017.

Morrison, H., G. de Boer, G. Feingold, J. Harrington, M. D. Shupe, and K. Sulia, 2012: Resilience of persistent Arctic mixed-phase clouds. *Nature Geoscience*, **5 (1)**, 11–17, doi:10.1038/ngeo1332.

Naakka, T., T. Nygård, and T. Vihma, 2018: Arctic Humidity Inversions: Climatology and Processes. *Journal of Climate*, **31 (10)**, 3765–3787, doi:10.1175/JCLI-D-17-0497.1.

NASA Earth Observatory, 2004: Joanne Simpson. URL: `https://earthobservatory.nasa.gov/features/Simpson/simpson2.php`, Publisher: NASA Earth Observatory; accessed online 2020-09-19.

Naumann, A. K. and C. Kiemle, 2020: The vertical structure and spatial variability of lower-tropospheric water vapor and clouds in the trades. *Atmospheric Chemistry and Physics*, **20 (10)**, 6129–6145, doi:10.5194/acp-20-6129-2020.

Nehrir, A. R., C. Kiemle, M. D. Lebsock, G. Kirchengast, S. A. Buehler, U. Löhnert, C.-L. Liu, P. C. Hargrave, M. Barrera-Verdejo, and D. M. Winker, 2017: Emerging Technologies and Synergies for Airborne and Space-Based Measurements of Water Vapor Profiles. *Surveys in Geophysics*, **38 (6)**, 1445–1482, doi:10.1007/s10712-017-9448-9.

Nomokonova, T., K. Ebell, U. Löhnert, M. Maturilli, and C. Ritter, 2020: The influence of water vapor anomalies on clouds and their radiative effect at Ny-Ålesund. *Atmospheric Chemistry and Physics*, **20 (8)**, 5157–5173, doi:10.5194/acp-20-5157-2020.

Nomokonova, T., K. Ebell, U. Löhnert, M. Maturilli, C. Ritter, and E. O'Connor, 2019: Statistics on clouds and their relation to thermodynamic conditions at Ny-Ålesund using ground-based sensor synergy. *Atmospheric Chemistry and Physics*, **19 (6)**, 4105–4126, doi:10.5194/acp-19-4105-2019.

Nuijens, L., B. Medeiros, I. Sandu, and M. Ahlgrimm, 2015: The behavior of trade-wind cloudiness in observations and models: The major cloud components and their variability. *Journal of Advances in Modeling Earth Systems*, **7 (2)**, 600–616, doi:10.1002/2014MS000390.

Nuijens, L., I. Serikov, L. Hirsch, K. Lonitz, and B. Stevens, 2014: The distribution and variability of low-level cloud in the North Atlantic trades. *Quarterly Journal of the Royal Meteorological Society*, **140 (684)**, 2364–2374, doi:10.1002/qj.2307.

Nuijens, L. and A. P. Siebesma, 2019: Boundary Layer Clouds and Convection over Subtropical Oceans in our Current and in a Warmer Climate. *Current Climate Change Reports*, **5 (2)**, 80–94, doi:10.1007/s40641-019-00126-x.

Nuijens, L., B. Stevens, and A. P. Siebesma, 2009: The Environment of Precipitating Shallow Cumulus Convection. *Journal of the Atmospheric Sciences*, **66 (7)**, 1962–1979, doi:10.1175/2008JAS2841.1.

Nörenberg, D., 2008: Development of ground equipment for atmospheric propagation conditions assessment from 10 up to 90 GHz fre- quency bands (ATPROP). Software documentation ESA CON- TRACT 19839/06/NL/GLC, Institute for Geophysics and Meteorolgy, University of Cologne, and Radiometer Physics GmbH, Meckenheim.

Petty, G. W., 2006: *A first course in Atmospheric Radiation*. 2d ed., Sundog Publishing, Madison, Wisconsin.

Pierce, D. W., T. P. Barnett, E. J. Fetzer, and P. J. Gleckler, 2006: Three-dimensional tropospheric water vapor in coupled climate models compared with observations from the AIRS satellite system. *Geophysical Research Letters*, **33 (21)**, doi:10.1029/2006GL027060.

Pierrehumbert, R. T., 1995: Thermostats, Radiator Fins, and the Local Runaway Greenhouse. *Journal of the Atmospheric Sciences*, **52 (10)**, 1784–1806,

doi:10.1175/1520-0469(1995)052<1784:TRFATL>2.0.CO;2.

Pincus, R., A. Beljaars, S. A. Buehler, G. Kirchengast, F. Ladstaedter, and J. S. Whitaker, 2017: The Representation of Tropospheric Water Vapor Over Low-Latitude Oceans in (Re-)analysis: Errors, Impacts, and the Ability to Exploit Current and Prospective Observations. *Surveys in Geophysics*, **38 (6)**, 1399–1423, doi:10.1007/s10712-017-9437-z.

Posselt, D. J., J. Kessler, and G. G. Mace, 2017: Bayesian Retrievals of Vertically Resolved Cloud Particle Size Distribution Properties. *Journal of Applied Meteorology and Climatology*, **56 (3)**, 745–765, doi:10.1175/JAMC-D-16-0276.1.

Rauber, R. M. and S. W. Nesbitt, 2018: *Radar meteorology: a first course*. 1st ed., Advancing weather and climate science series, John Wiley & Sons, Inc., Hoboken, NJ.

Rauber, R. M., et al., 2007: Rain in Shallow Cumulus Over the Ocean: The RICO Campaign. *Bulletin of the American Meteorological Society*, **88 (12)**, 1912–1928, doi:10.1175/BAMS-88-12-1912.

Rieck, M., L. Nuijens, and B. Stevens, 2012: Marine Boundary Layer Cloud Feedbacks in a Constant Relative Humidity Atmosphere. *Journal of the Atmospheric Sciences*, **69 (8)**, 2538–2550, doi:10.1175/JAS-D-11-0203.1.

Riehl, H. and J. S. Malkus, 1957: On the heat balance and maintenance of circulation in the trades. *Quarterly Journal of the Royal Meteorological Society*, **83 (355)**, 21–29, doi:10.1002/qj.49708335503.

Rinehart, R. E., 2010: *Radar for Meteorologists*. 5th ed., Rinehart Publications, Nevada Missouri USA.

Rodgers, C. D., 2000: *Inverse Methods for Atmospheric Sounding: Theory and Practice*. World Scientific.

Rose, T., S. Crewell, U. Löhnert, and C. Simmer, 2005: A network suitable microwave radiometer for operational monitoring of the cloudy atmosphere. *Atmospheric Research*, **75 (3)**, 183–200, doi:10.1016/j.atmosres.2004.12.005.

Ross, R. J. and W. P. Elliott, 2001: Radiosonde-Based Northern Hemisphere Tropospheric Water Vapor Trends. *Journal of Climate*, **14 (7)**, 1602–1612, doi:10.1175/1520-0442(2001)014<1602:RBNHTW>2.0.CO;2.

Roy, R. J., M. Lebsock, L. Millán, and K. B. Cooper, 2020: Validation of a G-Band Differential Absorption Cloud Radar for Humidity Remote Sensing. *Journal of Atmospheric and Oceanic Technology*, **37 (6)**, 1085–1102, doi:10.1175/JTECH-D-19-0122.1.

Roy, R. J., M. Lebsock, L. Millán, R. Dengler, R. Rodriguez Monje, J. V. Siles, and K. B. Cooper, 2018: Boundary-layer water vapor profiling using differential absorption radar. *Atmospheric Measurement Techniques*, **11 (12)**, 6511–6523, doi:10.5194/amt-11-6511-2018.

Schnitt, S., U. Löhnert, and R. Preusker, 2020: Potential of Dual-Frequency Radar and Microwave Radiometer Synergy for Water Vapor Profiling in the Cloudy Trade-Wind Environment. *Journal of Atmospheric and Oceanic Technology*, **accepted**, 1–53, doi:10.1175/JTECH-D-19-0110.1.

Schnitt, S., E. Orlandi, M. Mech, A. Ehrlich, and S. Crewell, 2017: Characterization of Water Vapor and Clouds During the Next-Generation Aircraft Remote Sensing for Validation (NARVAL) South Studies. *IEEE Journal of Selected Topics in Applied Earth Observations and Remote Sensing*, **10 (7)**, 3114–3124, doi:10.1109/JSTARS.2017.2687943.

Schotland, R. M., 1966: Some observations of the vertical profile of water vapor by means of a laser optical radar(Measurement and theory, including signal to noise and transfer function calculations, of atmospheric water vapor using ruby laser optical radar). *1966.*, University of Michigan, Ann Arbor, Proceedings of 4th Symposium on Remote Sensing of the Environment, Vol. 271, 273–283.

Schröder, M., M. Lockhoff, L. Shi, T. August, R. Bennartz, H. Brogniez, X. Calbet, F. Fell, J. Forsythe, A. Gambacorta, S.-p. Ho, E. R. Kursinski, A. Reale, T. Trent, and Q. Yang, 2019: The GEWEX Water Vapor Assessment: Overview and Introduction to Results and Recommendations. *Remote Sensing*, **11 (3)**, 251, doi:10.3390/rs11030251.

Schulz, H. and B. Stevens, 2018: Observing the Tropical Atmosphere in Moisture Space. *Journal of the Atmospheric Sciences*, **75 (10)**, 3313–3330, doi:10.1175/JAS-D-17-0375.1.

Schulz, J., P. Schluessel, and H. Grassl, 1993: Water vapour in the atmospheric boundary layer over oceans from SSM/I measurements. *International Journal of Remote Sensing*, **14 (15)**, 2773–2789, doi:10.1080/01431169308904308.

Sedlar, J., M. D. Shupe, and M. Tjernström, 2012: On the Relationship between Thermodynamic Structure and Cloud Top, and Its Climate Significance in the Arctic. *Journal of Climate*, **25 (7)**, 2374–2393, doi:10.1175/JCLI-D-11-00186.1.

Sherwood, S., M. J. Webb, J. D. Annan, K. C. Armour, P. M. Forster, J. C. Hargreaves, G. Hegerl, S. A. Klein, K. D. Marvel, E. J. Rohling, M. Watanabe, T. Andrews, P. Braconnot, C. S. Bretherton, G. L. Foster, Z. Hausfather, A. S. v. d. Heydt, R. Knutti, T. Mauritsen, J. R. Norris, C. Proistosescu, M. Rugenstein, G. A. Schmidt, K. B. Tokarska, and M. D. Zelinka, 2020: An assessment of Earth's climate sensitivity using multiple lines of evidence. *Reviews of Geophysics*, **n/a (n/a)**, e2019RG000 678, doi:10.1029/2019RG000678.

Sherwood, S. C., S. Bony, and J.-L. Dufresne, 2014: Spread in model climate sensitivity traced to atmospheric convective mixing. *Nature*, **505 (7481)**, 37–42, doi:10.1038/nature12829.

Sherwood, S. C., R. Roca, T. M. Weckwerth, and N. G. Andronova, 2010: Tropospheric water vapor, convection, and climate. *Reviews of Geophysics*, **48 (2)**, doi:10.1029/2009RG000301.

Shupe, M. D., 2011: Clouds at Arctic Atmospheric Observatories. Part II: Thermodynamic Phase Characteristics. *Journal of Applied Meteorology and Climatology*, **50 (3)**, 645–661, doi:10.1175/2010JAMC2468.1.

Shupe, M. D. and J. M. Intrieri, 2004: Cloud Radiative Forcing of the Arctic Surface: The Influence of Cloud Properties, Surface Albedo, and Solar Zenith Angle. *Journal of Climate*, **17 (3)**, 616–628, doi:10.1175/1520-0442(2004)017<0616:CRFOTA>2.0.CO;2.

Shupe, M. D., S. Y. Matrosov, and T. Uttal, 2006: Arctic Mixed-Phase Cloud Properties Derived from Surface-Based Sensors at SHEBA. *Journal of the Atmospheric Sciences*, **63 (2)**, 697–711, doi:10.1175/JAS3659.1.

Siebert, H., M. Beals, J. Bethke, E. Bierwirth, T. Conrath, K. Dieckmann, F. Ditas, A. Ehrlich, D. Farrell, S. Hartmann, M. A. Izaguirre, J. Katzwinkel, L. Nuijens, G. Roberts, M. Schäfer, R. A. Shaw, T. Schmeissner, I. Serikov, B. Stevens, F. Stratmann, B. Wehner, M. Wendisch, F. Werner, and H. Wex, 2013: The fine-scale structure of the trade wind cumuli over Barbados; an introduction to the CARRIBA project. *Atmospheric Chemistry and Physics*, **13 (19)**, 10 061–10 077, doi:10.5194/acp-13-10061-2013.

Smagorinsky, J., 1963: General Circulation Experiments With The Primitive Equations I. The Basic Experiment. *Monthly Weather Review*, **91 (3)**, 99–164, doi:10.1175/1520-0493(1963)091<0099:GCEWTP>2.3.CO;2.

Sohn, B.-J. and E. A. Smith, 2003: Explaining Sources of Discrepancy in SSM/I Water Vapor Algorithms. *Journal of Climate*, **16 (20)**, 3229–3255, doi:10.1175/1520-0442(2003)016<3229:ESODII>2.0.CO;2.

Solheim, F., J. R. Godwin, E. R. Westwater, Y. Han, S. J. Keihm, K. Marsh, and R. Ware, 1998: Radiometric profiling of temperature, water vapor and cloud liquid water using various inversion methods. *Radio Science*, **33 (2)**, 393–404, doi:10.1029/97RS03656.

Solomon, A., M. D. Shupe, O. Persson, H. Morrison, T. Yamaguchi, P. M. Caldwell, and G. de Boer, 2014: The Sensitivity of Springtime Arctic Mixed-Phase Stratocumulus Clouds to Surface-Layer and Cloud-Top Inversion-Layer Moisture Sources. *Journal of the Atmospheric Sciences*, **71 (2)**, 574–595, doi:10.1175/JAS-D-13-0179.1.

Solomon, A., M. D. Shupe, P. O. G. Persson, and H. Morrison, 2011: Moisture and dynamical interactions maintaining decoupled Arctic mixed-phase stratocumulus in the presence of a humidity inversion. *Atmospheric Chemistry and Physics*, **11 (19)**, 10 127–10 148, doi:10.5194/acp-11-10127-2011.

Spencer, R. W. and W. D. Braswell, 1997: How Dry is the Tropical Free Troposphere? Implications for Global Warming Theory. *Bulletin of the American Meteorological Society*, **78 (6)**, 1097–1106, doi:10.1175/1520-0477(1997)078<1097:HDITTF>2.0.CO;2.

Stankov, B. B., 1998: Multisensor Retrieval of Atmospheric Properties. *Bulletin of the American Meteorological Society*, **79 (9)**, 1835–1854, doi:10.1175/1520-0477(1998)079<1835:MROAP>2.0.CO;2.

Steinke, S., S. Eikenberg, U. Löhnert, G. Dick, D. Klocke, P. Di Girolamo, and S. Crewell, 2015: Assessment of small-scale integrated water vapour variability during HOPE. *Atmospheric Chemistry and Physics*, **15 (5)**, 2675–2692, doi:10.5194/acp-15-2675-2015.

Stephan, C. C., et al., 2020: Ship- and island-based atmospheric soundings from the 2020 EUREC^{4}A field campaign. *Earth System Science Data Discussions*, 1–35, doi:10.5194/essd-2020-174.

Stephens, G., D. Winker, J. Pelon, C. Trepte, D. Vane, C. Yuhas, T. L'Ecuyer, and M. Lebsock, 2018: CloudSat and CALIPSO within the A-Train: Ten Years of Actively Observing the Earth System. *Bulletin of the American Meteorological Society*, **99 (3)**, 569–581, doi:10.1175/BAMS-D-16-0324.1.

Stephens, G. L., 2005: Cloud Feedbacks in the Climate System: A Critical Review. *Journal of Climate*, **18 (2)**, 237–273, doi:10.1175/JCLI-3243.1.

Stephens, G. L., D. G. Vane, R. J. Boain, G. G. Mace, K. Sassen, Z. Wang, A. J. Illingworth, E. J. O'connor, W. B. Rossow, S. L. Durden, S. D. Miller, R. T. Austin, A. Benedetti, and C. Mitrescu, 2002: The Cloudsat Mission and the A-Train: A New Dimension of Space-Based Observations of Clouds and Precipitation. *Bulletin of the American Meteorological Society*, **83 (12)**, 1771–1790, doi:10.1175/BAMS-83-12-1771.

Stevens, B., , and coauthors, 2020a: EUREC4A. *in prep; to be submitted to AGU Advances.*

Stevens, B., 2004: Atmospheric moist convection. *Annual Review of Earth and Planetary Sciences*, **33 (1)**, 605–643, doi:10.1146/annurev.earth.33.092203.122658.

Stevens, B. and S. Bony, 2013: What Are Climate Models Missing? *Science*, **340 (6136)**, 1053, doi:10.1126/science.1237554.

Stevens, B., H. Brogniez, C. Kiemle, J.-L. Lacour, C. Crevoisier, and J. Kiliani, 2017: Structure and Dynamical Influence of Water Vapor in the Lower Tropical Troposphere. *Surveys in Geophysics*, **38 (6)**, 1371–1397, doi:10.1007/s10712-017-9420-8.

Stevens, B., A. S. Ackerman, B. A. Albrecht, A. R. Brown, A. Chlond, J. Cuxart, P. G. Duynkerke, D. C. Lewellen, M. K. Macvean, R. A. J. Neggers, E. Sánchez, A. P. Siebesma, and D. E. Stevens, 2001: Simulations of Trade Wind Cumuli under a Strong Inversion. *Journal of the Atmospheric Sciences*, **58 (14)**, 1870–1891, doi:10.1175/1520-0469(2001)058<1870:SOTWCU>2.0.CO;2.

Stevens, B., D. Farrell, L. Hirsch, F. Jansen, L. Nuijens, I. Serikov, B. Brügmann, M. Forde, H. Linne, K. Lonitz, and J. M. Prospero, 2016: The Barbados Cloud Observatory: Anchoring Investigations of Clouds and Circulation on the Edge of the ITCZ. *Bulletin of the American Meteorological Society*, **97 (5)**, 787–801, doi:10.1175/BAMS-D-14-00247.1.

Stevens, B., et al., 2019: A High-Altitude Long-Range Aircraft Configured as a Cloud Observatory: The NARVAL Expeditions. *Bulletin of the American Meteorological Society*, **100 (6)**, 1061–1077, doi:10.1175/BAMS-D-18-0198.1.

Stevens, B., S. Bony, H. Brogniez, L. Hentgen, C. Hohenegger, C. Kiemle, T. S. L'Ecuyer, A. K. Naumann, H. Schulz, P. A. Siebesma, J. Vial, D. M. Winker, and P. Zuidema, 2020b: Sugar, gravel, fish and flowers: Mesoscale cloud patterns in the trade winds. *Quarterly Journal of the Royal Meteorological Society*, **146 (726)**, 141–152, doi:10.1002/qj.3662.

Sun, Z. and K. P. Shine, 1994: Studies of the radiative properties of ice and mixed-phase clouds. *Quarterly Journal of the Royal Meteorological Society*, **120 (515)**, 111–137, doi:10.1002/qj.49712051508.

Tian, L., G. M. Heymsfield, L. Li, and R. C. Srivastava, 2007: Properties of light stratiform rain derived from 10- and 94-GHz airborne Doppler radars measurements. *Journal of Geophysical Research: Atmospheres*, **112 (D11)**, doi:10.1029/2006JD008144.

Tiedtke, M., 1989: A Comprehensive Mass Flux Scheme for Cumulus Parameterization in Large-Scale Models. *Monthly Weather Review*, **117 (8)**, 1779–1800, doi:10.1175/1520-0493(1989)117<1779:ACMFSF>2.0.CO;2.

Tobin, I., S. Bony, and R. Roca, 2012: Observational Evidence for Relationships between the Degree of Aggregation of Deep Convection, Water Vapor, Surface Fluxes, and Radiation. *Journal of Climate*, **25 (20)**, 6885–6904, doi:10.1175/JCLI-D-11-00258.1.

Toporov, M. and U. Löhnert, 2020: Synergy of Satellite- and Ground-Based Observations for Continuous Monitoring of Atmospheric Stability, Liquid Water Path, and Integrated Water Vapor: Theoretical Evaluations Using Reanalysis and Neural Networks. *Journal of Applied Meteorology and Climatology*, **59 (7)**, 1153–1170, doi:10.1175/JAMC-D-19-0169.1.

Trenberth, K. E., J. Fasullo, and L. Smith, 2005: Trends and variability in column-integrated atmospheric water vapor. *Climate Dynamics*, **24 (7)**, 741–758, doi:10.1007/s00382-005-0017-4.

Tridon, F., A. Battaglia, and S. Kneifel, 2020: How to estimate total differential attenuation due to hydrometeors with ground-based multi-frequency radars? *Atmospheric Measurement Techniques Discussions*, 1–29, doi:10.5194/amt-2020-159.

Turner, D. D., B. M. Lesht, S. A. Clough, J. C. Liljegren, H. E. Revercomb, and D. C. Tobin, 2003: Dry Bias and Variability in Vaisala RS80-H Radiosondes: The ARM Experience. *Journal of Atmospheric and Oceanic Technology*, **20 (1)**, 117–132, doi:10.1175/1520-0426(2003)020<0117:DBAVIV>2.0.CO;2.

Turner, D. D. and U. Löhnert, 2014: Information Content and Uncertainties in Thermodynamic Profiles and Liquid Cloud Properties Retrieved from the Ground-Based Atmospheric Emitted Radiance Interferometer (AERI). *Journal of Applied Meteorology and Climatology*, **53 (3)**, 752–771, doi:10.1175/JAMC-D-13-0126.1.

Tyndall, J., 1859: On the transmission of heat of different qualities through gases of different kinds. *Proceedings of the Royal Institution*, **3**, 155–158.

Ulaby, F. T., 2014: *Microwave radar and radiometric remote sensing*. The University of Michigan Press, Ann Arbor.

Vaisala, 2012: Vaisala Weather Transmitter WXT520. URL: `https://www.vaisala.com/sites/default/files/documents/M210906EN-C.pdf`, accessed online 2020-09-19.

Verlinde, J., M. P. Rambukkange, E. E. Clothiaux, G. M. McFarquhar, and E. W. Eloranta, 2013: Arctic multilayered, mixed-phase cloud processes revealed in millimeter-wave cloud radar Doppler spectra. *Journal of Geophysical Research: Atmospheres*, **118 (23)**, 13,199–13,213, doi:10.1002/2013JD020183.

Vial, J., S. Bony, B. Stevens, and R. Vogel, 2017: Mechanisms and Model Diversity of Trade-Wind Shallow Cumulus Cloud Feedbacks: A Review. *Surveys in Geophysics*, **38 (6)**, 1331–1353, doi:10.1007/s10712-017-9418-2.

Vial, J., R. Vogel, S. Bony, B. Stevens, D. M. Winker, X. Cai, C. Hohenegger, A. K. Naumann, and H. Brogniez, 2019: A New Look at the Daily Cycle of Trade Wind Cumuli. *Journal of Advances in Modeling Earth Systems*, **11 (10)**, 3148–3166, doi:10.1029/2019MS001746.

Vömel, H., H. Selkirk, L. Miloshevich, J. Valverde-Canossa, J. Valdés, E. Kyrö, R. Kivi, W. Stolz, G. Peng, and J. A. Diaz, 2007: Radiation Dry Bias of the Vaisala RS92 Humidity Sensor. *Journal of Atmospheric and Oceanic Technology*, **24 (6)**, 953–963, doi:10.1175/JTECH2019.1.

Wagner, T. J., P. M. Klein, and D. D. Turner, 2018: A New Generation of Ground-Based Mobile Platforms for Active and Passive Profiling of the Boundary Layer. *Bulletin of the American Meteorological Society*, **100 (1)**, 137–153, doi:10.1175/BAMS-D-17-0165.1.

Webb, M. J. and A. P. Lock, 2013: Coupling between subtropical cloud feedback and the local hydrological cycle in a climate model. *Climate Dynamics*, **41 (7)**, 1923–1939, doi:10.1007/s00382-012-1608-5.

Webster, E. W., 2020: The Internet Classics Archive | Meteorology by Aristotle. URL: `http://classics.mit.edu/Aristotle/meteorology.html`, accessed online 2020-07-12.

Wendisch, M., et al., 2019: The Arctic Cloud Puzzle: Using ACLOUD/PASCAL Multiplatform Observations to Unravel the Role of Clouds and Aerosol Particles in Arctic Amplification. *Bulletin of the American Meteorological Society*, **100 (5)**, 841–871, doi:10.1175/BAMS-D-18-0072.1.

Westwater, E. R., 1978: The accuracy of water vapor and cloud liquid determination by dual-frequency ground-based microwave radiometry. *Radio Science*, **13 (4)**, 677–685, doi:10.1029/RS013i004p00677.

Westwater, E. R., S. Crewell, and C. Mätzler, 2004: A review of surface-based microwave and millimeter-wave radiometric remote sensing of the troposphere. *URSI Radio Science Bulletin*, **2004 (310)**, 59–80, doi:10.23919/URSIRSB.2004.7909438.

Winker, D. M., J. Pelon, J. A. Coakley, S. A. Ackerman, R. J. Charlson, P. R. Colarco, P. Flamant, Q. Fu, R. M. Hoff, C. Kittaka, T. L. Kubar, H. Le Treut, M. P. Mccormick, G. Mégie, L. Poole, K. Powell, C. Trepte, M. A. Vaughan, and B. A. Wielicki, 2010: The CALIPSO MissionA Global 3D View of Aerosols and Clouds. *Bulletin of the American Meteorological Society*, **91 (9)**, 1211–1230, doi:10.1175/2010BAMS3009.1.

WMO, 2014: Statement Of Guidance For Global Numerical Weather Prediction. URL: `https://www.wmo.int/pages/prog/www/OSY/SOG/SoG-Global-NWP.pdf`, accessed online 2020-09-19.

WMO, T. Oakley, H. Vömel, and L. Wei, 2011: *WMO Intercomparison of High Quality Radiosonde Systems*, WMO/TD, Vol. 107. WMO, Geneva.

Wulfmeyer, V., R. M. Hardesty, D. D. Turner, A. Behrendt, M. P. Cadeddu, P. D. Girolamo, P. Schlüssel, J. V. Baelen, and F. Zus, 2015: A review of the remote sensing of lower tropospheric thermodynamic profiles and its indispensable role for the understanding and the simulation of water and energy cycles. *Reviews of Geophysics*, **53 (3)**, 819–895, doi:10.1002/2014RG000476.

Wyant, M. C., C. S. Bretherton, and P. N. Blossey, 2009: Subtropical Low Cloud Response to a Warmer Climate in a Superparameterized Climate Model. Part I: Regime Sorting and Physical Mechanisms. *Journal of Advances in Modeling Earth Systems*, **1 (3)**, doi:10.3894/JAMES.2009.1.7.

Zhu, Z., K. Lamer, P. Kollias, and E. E. Clothiaux, 2019: The Vertical Structure of Liquid Water Content in Shallow Clouds as Retrieved From Dual-Wavelength Radar Observations. *Journal of Geophysical Research: Atmospheres*, **124 (24)**, 14 184–14 197, doi:10.1029/2019JD031188.

Zuidema, P., D. Leon, A. Pazmany, and M. Cadeddu, 2012a: Aircraft millimeter-wave passive sensing of cloud liquid water and water vapor during VOCALS-REx. *Atmospheric Chemistry and Physics*, **12 (1)**, 355–369, doi:10.5194/acp-12-355-2012.

Zuidema, P., Z. Li, R. J. Hill, L. Bariteau, B. Rilling, C. Fairall, W. A. Brewer, B. Albrecht, and J. Hare, 2012b: On Trade Wind Cumulus Cold Pools. *Journal of the Atmospheric Sciences*, **69 (1)**, 258–280, doi:10.1175/JAS-D-11-0143.1.

Acknowledgments

Part of this study was funded by the HD(CP)^2 project that is funded by the German Federal Ministry of Education and Research (BMBF) within the framework program "Research for Sustainable Development (FONA)" under grant number 01LK1502E. Thank you to the Graduate School of Geosciences (GSGS) at University of Cologne for providing travel funds including various conferences and the research stay at Barbados.

Uli, Susanne, Bjorn and René, your time, support, advice, and mentoring over the past years has been invaluable. Many thanks for our many scientific discussions and for supervising this thesis.

Thank you, Vera, Claudia, Kerstin, Marek, Davide, Bernhard, Birger for all the scientific and non-scientific support and advice. Karin, thank you for all your help!

Thanks to Jürgen Fischer for allowing me to join the group and providing office space at FUB. To all the WeW staff, thanks for taking in a ground-based microwave person into your spaceborne optical remote sensing world, and thanks for the many fruitful scientific and non-scientific discussions on the balcony. Nicole, thanks for the many answers to all my questions, and special thanks to Jan for the countless cooking adventures in the institute's kitchen!

Mario and Friedel, thanks for the many lasting Barbados memories, with and without radiosondes. Theresa, thanks for all the great moments during the NCAR summer school, in Hamburg, and during EUREC^{4}A.

Rosa - we made it! Thanks for your endless support not only but particularly in the weeks before handing in.

Elena, Hannah-Jo, Julian, Wiebke, Miri, Jörg, Antonia, Yannick: thanks for all your couches and making Köln to my 2nd home in the past years.

Barbara, Peter, Lili, Oli, Jutta, Henry, Leonie, Stephanie, Alex, Gitta, thank you for all your support.

Daphne - thanks for being an endless source of inspiration and creativity.

Selbstständigkeitserklärung:

Hiermit versichere ich an Eides statt, dass ich die vorliegende Dissertation selbstständig und ohne die Benutzung anderer als der angegebenen Hilfsmittel und Literatur angefertigt habe. Alle Stellen, die wörtlich oder sinngemäßaus veröffentlichten und nicht veröffentlichten Werken dem Wortlaut oder dem Sinn nach entnommen wurden, sind als solche kenntlich gemacht. Ich versichere an Eides statt, dass diese Dissertation noch keiner anderen Fakultät oder Universität zur Prüfung vorgelegen hat; dass sie - abgesehen von unten angegebenen Teilpublikationen und eingebundenen Artikeln und Manuskripten - noch nicht veröffentlicht worden ist sowie, dass ich eine Veröffentlichung der Dissertation vor Abschluss der Promotion nicht ohne Genehmigung des Promotionsausschusses vornehmen werde. Die Bestimmungen dieser Ordnung sind mir bekannt. Darüber hinaus erkläre ich hiermit, dass ich die Ordnung zur Sicherung guter wissenschaftlicher Praxis und zum Umgang mit wissenschaftlichem Fehlverhalten der Universität zu Köln gelesen und sie bei der Durchführung der Dissertation zugrundeliegenden Arbeiten und der schriftlich verfassten Dissertation beachtet habe und verpflichte mich hiermit, die dort genannten Vorgaben bei allen wissenschaftlichen Tätigkeiten zu beachten und umzusetzen. Ich versichere, dass die eingereichte elektronische Fassung der eingereichten Druckfassung vollständig entspricht.

Berlin, 21.09.2020

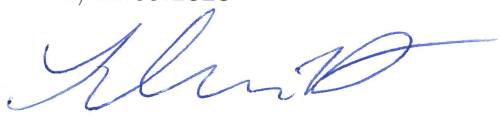

Sabrina Schnitt

Teilpublikationen:

- Schnitt, S., U. Löhnert, and R. Preusker, 2020: Potential of Dual-Frequency Radar and Microwave Radiometer Synergy for Water Vapor Profiling in the Cloudy Trade-Wind Environment. *Journal of Atmospheric and Oceanic Technology*, **accepted**, 1–53, doi:10.1175/JTECH-D-19-0110-1

- Stephan, C. C., Schnitt, S., Schulz, H., Bellenger, H., de Szoeke, S. P., Acquistapace, C. Baier, K. Dauhut, T. , Laxenaire, R., Morfa-Avalos, Y., Person, R., Quiñones Meléndez, E., Bagheri, G., Böck, T., Daley, A., Güttler, J., Helfer, K. C., Los, S. A., Neuberger, A., Röttenbacher, J., Raeke, A., Ringel, M., Ritschel, M., Sadoulet, P., Schirmacher, I., Stolla, M. K., Wright, E., Charpentier, B., Doerenbecher, A., Wilson, R., Jansen, F., Kinne, S., Reverdin, G., Speich, S., Bony, S., Stevens, B., 2020: Ship- and island-based atmospheric soundings from the 2020 EUREC^{4}A field campaign. *Earth System Science Data Discussions*, **2020**, 1–35, doi: 10.5194/essd-2020-174

Hinweis zur Archivierung

Die für diese Dissertation gewonnenen Primärdaten und die zu Reproduzierbarkeit der in der Dissertation dargestellten Ergebnisse genutzten Datenanalysen und Versuchsprotokolle sind im digitalen Archivsystem des Instituts für Geophysik und Meteorologie der Universität zu Köln gesichert und dort auf Anfrage verfügbar.